STRUCTURAL AND THERMOCHEMICAL INVESTIGATIONS OF MULTIPLY CHARGED TRANSITION METAL ION COMPLEXES WITH WATER AND WITH AMINO ACIDS

by

Rebecca Ann Coates

A dissertation submitted to the faculty of
The University of Utah
in partial fulfillment of the requirements for the degree of

Doctor of Philosophy

Department of Chemistry

The University of Utah

December 2017

The University of Utah Graduate School

STATEMENT OF DISSERTATION APPROVAL

The dissertation of **Rebecca Ann Coates**

has been approved by the following supervisory committee members:

Peter Armentrout	, Chair	**8/10/2017** Date Approved
Michael Morse	, Member	**8/10/2017** Date Approved
Joel Miller	, Member	**8/10/2017** Date Approved
Jan Miller	, Member	**8/10/2017** Date Approved
Ryan Steele	, Member	**8/10/2017** Date Approved

and by **Cynthia Burrows** , Chair/Dean of

the Department/College/School of **Chemistry**

and by David B. Kieda, Dean of The Graduate School.

ABSTRACT

Guided ion beam tandem mass spectrometry is used to obtain the kinetic energy dependent cross sections for collision-induced dissociation of hydrated transition metal complexes of $Ni^{2+}(H_2O)_x$, $x = 4 – 11$, $Co^{2+}(H_2O)_x$, $x = 5 – 11$, and $CoOH^+(H_2O)_x$, $x = 1 – 4$. The resulting cross sections obtained for each reactant ion are analyzed using statistical models to yield 0 K bond dissociation energies (BDEs). The primary dissociation pathway for these three systems is the loss of a single water followed by sequential water loss at higher energies. The charge separation process, $M^{2+}(H_2O)_x \rightarrow MOH^+(H_2O)_m + H^+(H_2O)_{x-m-1}$, is also observed for particular sized complexes in the $M^{2+}(H_2O)_x$ studies. Threshold analyses determine the charge separation pathway to be energetically favored over water loss at $x = 4$ for Ni^{2+} and $x = 6$ for Co^{2+}. For collision induced dissociation of $CoOH^+(H_2O)_x$ complexes, the loss of OH becomes a competitive dissociative pathway to the loss of water at $x = 1$. Combining the experimental HO-$Co^+(H_2O)$ and water loss BDEs from $CoOH^+(H_2O)_x$ with those for $Co^+(H_2O)_y$ from literature, BDEs for the loss of OH from $CoOH^+(H_2O)_x$ are also derived. Theoretical geometry optimizations and single point energy calculations are performed on reactant and product complexes using several levels of theory to obtain thermochemistry for comparison to experiment.

Structural characterization of gas-phase ions of cysteine (Cys), cysteine methyl ester (CysOMe) and serine (Ser) complexed to zinc and cadmium dications is investigated by infrared multiple photon dissociation (IRMPD) action spectroscopy using

a free electron laser in combination with theoretical calculations. IRMPD spectra are measured for $[Zn(CysH)]^+$, $[Cd(CysH)]^+$, $[Zn(CysOMeH)]^+$, $[Cd(CysOMeH)]^+$, $CdCl^+(CysOMe)$, $[Zn(SerH)CH_3CN]^+$and $CdCl^+(Ser)$ complexes. The measured action spectra are compared to linear absorption spectra calculated at the B3LYP/6-311+G(d,p) level (Zn^{2+} complexes) and B3LYP/def2-TZVP levels (Cd^{2+} complexes) to identify the structures of the experimentally observed species. On the basis of these experiments and calculations, all complexes examined here adopt a tridentate binding coordination of the amino acid to the metal.

For Oriana,

My best friend and loyal companion.

I work hard so that you may have a better life.

TABLE OF CONTENTS

ACKNOWLEDGEMENTS

Foremost, I would like to express my sincere gratitude to my advisor Dr. Peter Armentrout for his continued support of my research, for his patience, understanding, and immense knowledge. His mentorship and encouragement were paramount in providing a well-rounded experience for me to grow as a chemist. For everything you've done, Peter, I thank you.

I would also like to thank all the past and present Armentrout group members. Specifically, to Chris McNary, my first friend in Utah and my trusted colleague. Also, thank you to Georgia Boles and Fan Yang for being ideal lab and office mates. Completing this work would have been all the more difficult were it not for their help in the lab, moral support, and friendship.

A major highlight of my graduate research career has been traveling to the Netherlands for our collaborative research opportunities at the FELIX facility. Fruitful research aside, I thank the stellar FELIX staff for these lasting memories.

I would like to acknowledge my awesome, brave and cheerful family for the endless love and support they have provided me through my entire life. I am very grateful to my adventure partner for his patience, love and unwavering encouragement during these years.

Lastly, the National Science Foundation generously provided funding for the work presented in this dissertation, Grants CHE-1359769 and PIRE-0730072.

CHAPTER 1

INTRODUCTION AND OVERVIEW

1.1 Background

Many transition metals are nutritionally essential for humans, animals, micro-organisms, and plants. As many of these metals are ubiquitous in nature, either deficiency or toxicity can occur with either too little or too much essential metal intake. Although many transition metals are naturally present, the anthropogenic release from the progress of industrialization and commercial uses cause various concentrations of these metals with toxic and even carcinogenic consequences.[1-5] One of the primary means of exposure for the general population is as a metal contaminant in drinking water. For the efficient removal of these metal pollutants in bulk aqueous environments, a complete understanding of the hydrated metal ion at the microscopic level is first required. The transition metal ions of interest chosen for the first part of this dissertation are Ni^{2+} and Co^{2+}, both of which are essential metals for biological function. However, these metals are also listed as potential contaminants under the EPA Safe Drinking Water Act.[6]

For the past decade, the Armentrout group has studied gas-phase hydrated metal ions by threshold collision-induced dissociation (TCID) for $M^+(H_2O)_x$ where M^+ = Ti to Cu;[7] and $M^{2+}(H_2O)_x$ where M = Fe,[8] Cu,[9] Zn,[10-11] and Cd[12-13] using a guided ion beam tandem mass spectrometer coupled to an electrospray ionization source (ESIGIBMS).

This experimental technique coupled with quantum chemical calculations allows us to gain accurate thermochemical information for the dissociative behavior as well as insight into the structural conformation of the hydrated metal complexes. The work presented in this dissertation examines the TCID of $M^{2+}(H_2O)_x$ complexes for M = Ni and Co, where x = 4 – 11 and x = 5 – 11, respectively. The dominant dissociative process in these complexes for all observed x is loss of a single neutral water molecule, reaction 1.1,

$$M^{2+}(H_2O)_x \rightarrow M^{2+}(H_2O)_{x-1} + H_2O \quad (1.1)$$

followed by the sequential loss of additional water molecules at higher energies. For both hydrated metal systems, certain specific complexes are also observed to undergo a dissociative charge separation process, reaction 1.2.

$$M^{2+}(H_2O)_x \rightarrow MOH^{+}(H_2O)_m + H^{+}(H_2O)_{x-m-1} \quad (1.2)$$

Modeling the competition of the water loss versus charge separation reactions allows us to determine the critical size at which reaction 1.2 becomes energetically favorable over reaction 1.1 for both $Ni^{2+}(H_2O)_x$ and $Co^{2+}(H_2O)_x$ systems. Concurrently, reaction 1.2 is observed to occur during the formation of $M^{2+}(H_2O)_x$ complexes such that we independently measure the binding energies for $CoOH^{+}(H_2O)_x$, for x = 1 – 4. Experimental dehydration and extracted dehydroxylation energies are obtained for the $CoOH^{+}(H_2O)_x$ complexes. The kinetic energy-dependent cross sections for $Ni^{2+}(H_2O)_x$, $Co^{2+}(H_2O)_x$, and $CoOH^{+}(H_2O)_x$ systems are modeled to yield 0 K bond dissociation energies (BDEs), which are compared to theoretically predicted energetics.

If metal ions become mobile in water they can subsequently be introduced to biological systems. Metals ions cannot be destroyed as they make their way through the

body, but are instead spread throughout and are easily ligated.[14] This raises the question, once *in vivo*, how do metal ions interact with biological ligands? The latter part of this dissertation aims to answer the fundamentals of this question using infrared multiple photon dissociation (IRMPD) spectroscopy to gain structural insight into complexes of Zn^{2+} and Cd^{2+} bound to single amino acids. Zinc is an essential nutrient, found as the metal center in several metalloproteins,[15-16] whereas cadmium is highly toxic, a known carcinogen, nonbiodegradable, and can replace zinc in many biological systems.[17-18] The structural assignment of the metallated amino acids is determined by comparing experimental IR spectra generated to linear absorption spectra predicted by theory.

1.2 Overview

Chapter 2 outlines the instrumentation used in the present work. Chapters 3 – 5 utilized the ESI-GIBMS. The work in Chapters 6 and 7 was performed using a Fourier-transform ion cyclotron resonance (FT-ICR)[19-21] mass spectrometer coupled to the Free Electron Laser for Infrared eXperiments (FELIX)[22] beam line. Raw data conversion techniques for both CID and IRMPD data are also outlined in Chapter 2. Additionally, each chapter (3 – 7) presents the respective experimental procedures, data collection techniques, methods for converting raw data into cross sections or IR spectra, and theoretical methods utilized. Methods for modeling cross sections for single, sequential, and competitive dissociations to yield thermochemical information are outlined in Chapters 3 – 5.

Chapter 3 details the collision-induced dissociation experiments for $Ni^{2+}(H_2O)_x$, where $x = 4 – 11$, resulting in the first experimentally determined BDEs for $x = 4$ and 5.

Use of an in-source fragmentation technique allowed for the control of the population of ground and excited isomer reactant ions. As a result, speculative thermochemistry for excited isomers of the $x = 4 – 6$ complexes are also obtained. A detailed theoretical study into the structures and predicted BDEs of the $Ni^{2+}(H_2O)_x$ complexes is also presented using several levels of theory for comparison to experiment. Calculated rate-limiting transition states for reaction 1.2 are compared to experimental threshold measurements for dissociative charge separation processes. The work in Chapter 3 has been published.[23]

Chapter 4 is a continuation of the hydrated 3d transition metals studies, with the experimental and theoretical investigation of $Co^{2+}(H_2O)_x$ complexes, $x = 5 – 11$, sequential binding energies. Because different levels of theory disagree on the ground structure (GS) conformation, analysis of the experimental cross sections is examined for the different conformations to address the ambiguity in the assignment of the coordination number for Co^{2+}. The competition between reactions 1.1 and 1.2 is also examined, and rate-limiting transition states for the charge separation process are calculated and compared to experimental threshold measurements of the reaction barrier height. Results from this study give evidence to establish a new critical size for the charge separation of $Co^{2+}(H_2O)_x$. This work is under preparation for publication.

Chapter 5 presents studies on the $CoOH^+(H_2O)_x$ system, where TCID experiments are performed to obtain hydration energies for $x = 1 – 4$. Hydroxylation energies are also extracted by Hess's Law from combining bond enthalpies of $CoOH^+(H_2O)_x$-H_2O and $Co^+(H_2O)_x$-H_2O.[7] Theoretical calculations are performed to provide structures for the reactant and product ions, and to generate bond energies for comparison to the experimental values. The work in Chapter 5 has been published.[24]

Chapters 6 and 7 introduce work done in collaborative efforts with the FELIX Facility at Radboud University, a free electron user facility in the Netherlands. The IRMPD studies aim to interpret why Zn^{2+} preferentially binds to the amino acids histidine (His)[25] and cysteine (Cys), by gaining insight into the structural binding motif of the metal ion to the amino acid. Metallated Cys and cysteine methyl ester (CysOMe) are studied in Chapter 6. To determine zinc's binding preference for Cys and His, we have extended the IRMPD studies to observe structural conformation changes when these residues are replaced with other amino acids including glutamine (Gln),[26] glutamic acid (Glu),[27] and asparagine (Asn).[28] Chapter 7 examines metallated serine (Ser) as it differs from Cys only by the replacement of oxygen for the sulfur in the side-chain. To identify the structures of the experimentally observed gas-phase species, the measured action spectra are compared to calculated linear absorption spectra. The work in these chapters has been published.[29-30]

1.3 Future Work

Experimental thresholds presented in Chapters 3 – 5 of this work are extracted from modeling of either the primary or sequential products only. However, because of the limited range of complexes generated in the source for Chapter 5, we are interested in investigating whether modeling the tertiary and quaternary sequential products might provide useful thermodynamic information. However, our modeling program is programmed to examine only primary and secondary ligand loss channels. Therefore, the thermochemistry should be taken from the relative thresholds and we would treat the $Co^{2+}(H_2O)_{x-2}$ and $Co^{2+}(H_2O)_{x-3}$ product cross sections as if they were the primary and

sequential dissociation products, respectively, ignoring the true dominant primary and secondary channels. From the $Co^{2+}(H_2O)_5$ CID product cross sections, this would allow us to obtain an upper limit for the BDEs of $Co^{2+}(H_2O)_3$ and $Co^{2+}(H_2O)_2$. Should this approach yield accurate thermochemical information, it will be advantageous to try and utilize this process to model the quinary sequential product with hopes of determining the $Co^{2+}(H_2O)$ BDE. To test the accuracy of this approach we aim to first model the tertiary, quaternary and quinary processes from the $x = 11$ reactants, for which primary and secondary threshold data are available for comparison ($x = 9$, 8, and 7, respectively). The tertiary and quaternary sequential modeling approach has been previously examined for $Cu^{2+}(H_2O)_x$, in which it was determined a correction factor of ~0.2 eV need to be applied to the tertiary BDEs to be within reasonable agreement to primary BDEs.[9]

It was discovered in the CID $Ni^{2+}(H_2O)_x$ and $Co^{2+}(H_2O)_x$ studies (presented in Chapter 3 and 4) that the conditions of the source can be changed to alter the reactant ion population distribution and eliminate generation of hydroxides or protonated water species, reaction 1.2. Subsequently, we advantageously adjust these conditions such that the dications are instead eliminated to study the $CoOH^+(H_2O)_x$ preferentially (Chapter 5). The motivation behind this technique is to reduce contamination of nearly isobaric complexes, which has previously complicated $Fe^{2+}(H_2O)_x$ CID cross sections for $x = 5$ and 11.[8] This method of preferential reactant ion selection/deselection is being applied in collaborative studies initiated for the investigation of $Mn^{2+}(H_2O)_x$, $FeOH^+(H_2O)_x$ and $SnOH^+(H_2O)_x$ by CID and theoretical studies. The method for deselecting $Ni^{2+}(H_2O)_x$ reactant complexes and studying the $NiOH^+(H_2O)_x$ complexes would be a worthwhile

study to initiate in the future. Such a study would allow periodic trends in the hydration and hydroxylation of $MOH^+(H_2O)_x$ complexes to be examined.

1.4 References

(1) Nriagu, J. O.; Pacyna, J. M., Quantitative Assessment of Worldwide Contamination of Air, Water and Soils by Trace Metals. *Nature* **1988,** *333*, 134-9.

(2) Chang, L. W., Toxicology of Metals. In *Toxicology of Metals*, Lewis Publishers: Boca Raton, 1996; pp 245-246.

(3) Richens, D. T., *The Chemistry of Aqua Ions*. John Wiley and Sons, Inc: New York, 1997; p 540 - 567.

(4) Barceloux, D. G., Cobalt. *J. Toxicol. Clin. Toxicol.* **1999,** *37*, 201-206.

(5) Grandjean, P., Human Exposure to Nickel. *IARC Sci Publ* **1984,** *53*, 469-85.

(6) EPA. (1974). 93rd Congress: Safe Drinking Water Act.

(7) Dalleska, N. F.; Honma, K.; Sunderlin, L. S.; Armentrout, P. B., Solvation of Transition Metal Ions by Water. Sequential Binding Energies of $M^+(H_2O)_x$ (x = 1 - 4) for M = Ti - Cu Determined by Collision-Induced Dissociation. *J. Am. Chem. Soc.* **1994,** *116*, 3519-3528.

(8) Hofstetter, T. E.; Armentrout, P. B., Threshold Collision-Induced Dissociation and Theoretical Studies of Hydrated Fe(II): Binding Energies and Coulombic Barrier Heights. *J. Phys. Chem. A* **2013,** *117*, 1110-1123.

(9) Sweeney, A. F.; Armentrout, P. B., Hydrated Copper Ion Chemistry: Guided Ion Beam and Computational Investigation of $Cu^{2+}(H_2O)_n$ (n = 7-10) Complexes. *Eur. J. Mass Spectrom. (Chichester, Eng)* **2015,** *21*, 497-516.

(10) Cooper, T. E.; Carl, D. R.; Armentrout, P. B., Hydration Energies of Zinc (II): Threshold Collision-induced Dissociation Experiments and Theoretical Studies. *J. Phys. Chem. A* **2009,** *113*, 13727–13741.

(11) Cooper, T. E.; Armentrout, P. B., An Experimental and Theoretical Investigation of the Charge Separation Energies of Hydrated Zinc (II): Redefinition of the Critical Size. *J. Phys. Chem. A* **2009,** *113*, 13742–13751.

(12) Cooper, T. E.; Armentrout, P. B., Threshold Collision-induced Dissociation of Hydrated Cadmium (II): Experimental and Theoretical Investigation of the Binding Energies for $Cd^{2+}(H_2O)_n$ Complexes (n = 4 – 11). *Chem. Phys. Lett.* **2010,** *486*, 1-6.

(13) Cooper, T. E.; Armentrout, P. B., Sequential Bond Energies and Barrier Heights for the Water Loss and Charge Separation Dissociation Pathways of $Cd^{2+}(H_2O)_n$, n = 3-11. *J. Chem. Phys.* **2011,** *134*, 114308.

(14) Center for Disease Control Department of Health and Human Services. (2004). Public Health Statement Cobalt. *Agency for Toxic Substances and Disease Registry.* https://www.atsdr.cdc.gov/.

(15) Spiro, T. G., *Zinc Enzymes*. J. Wiley: New York, 1983; p ix, 359 p.

(16) Kimura, E., Roles of Zinc(II) Ion in Zinc Enzymes. *Pure & Appl. Chem.* **1993,** *65*, 355.

(17) Berg, J. M.; Shi, Y., The Galvanization of Biology: A Growing Appreciation for the Roles of Zinc. In *Science*, 1996; Vol. 271, pp 1081-1085.

(18) M. Huang; D. Krepkiy; Hu, W. W.; D. H. Petering, *J. Inorg. Biochem.* **2004,** *98*, 775-785.

(19) Polfer, N. C.; Oomens, J.; Moore, D. T.; von Helden, G.; Meijer, G.; Dunbar, R. C., Infrared Spectroscopy of Phenylalanine Ag(I) and Zn(II) Complexes in the Gas Phase. *J. Am. Chem. Soc.* **2006,** *128*, 517-525.

(20) Valle, J. J.; Eyler, J. R.; Oomens, J.; Moore, D. T.; van der Meer, A. F. G.; von Heldon, G.; Meijer, G.; Hendrickson, C. L.; Marshall, A. G.; Blakney, G. T., Free Electron Laser-Fourier Transform Ion Cyclotron Resonance Mass Spectrometry Facility for Obtaining Infrared Multiphoton Dissociation Spectra of Gaseous Ions. *Rev. Sci. Instrum.* **2005,** *76*, 023103.

(21) Polfer, N. C. J. O., Reaction Products in Mass Spectrometry Elucidated with Infrared Spectroscopy. *Phys. Chem. Chem. Phys.* **2007,** *9*, 3804-3817.

(22) Oepts, D. v. d. M., A.F.G.; van Amersfoort, P.W. , The Free-Electron-Laser User Facility FELIX. *Infrared Phys. Technol.* **1995,** *36*, 297-308.

(23) Coates, R. A.; Armentrout, P. B., Thermochemical Investigations of Hydrated Nickel Dication Complexes by Threshold Collision-Induced Dissociation and Theory. *J. Phys. Chem. A* **2017,** *121*, 3629-3646.

(24) Coates, R. A.; Armentrout, P. B., Binding Energies of Hydrated Cobalt Hydroxide Ion Complexes: A Guided Ion Beam and Theoretical Investigation. *J. Chem. Phys.* **2017,** *147*, 064305.

(25) Hofstetter, T. E.; Howder, C.; Berden, G.; Oomens, J.; Armentrout, P. B., Structural Elucidation of Biological and Toxicological Complexes: Investigation of Monomeric and Dimeric Complexes of Histidine with Multiply Charged Transition Metal (Zn and Cd) Cations using IR Action Spectroscopy. *J. Phys. Chem. B* **2011,** *115*, 12648-12661.

(26) Boles, G. C.; Coates, R. A.; Berden, G.; Oomens, J.; Armentrout, P. B., Experimental and Theoretical Investigations of Infrared Multiple Photon Dissociation Spectra of Glutamine Complexes with Zn^{2+} and Cd^{2+}. *J. Phys. Chem. B* **2015,** *119*, 11607-17.

(27) Boles, G. C.; Owen, C. J.; Berden, G.; Oomens, J.; Armentrout, P. B., Experimental and theoretical investigations of infrared multiple photon dissociation spectra of glutamic acid complexes with Zn^{2+} and Cd^{2+}. *Phys. Chem. Chem. Phys.* **2017,** *19*, 12394-12406.

(28) Boles, G. C.; Coates, R. A.; Berden, G.; Oomens, J.; Armentrout, P. B., Experimental and Theoretical Investigations of Infrared Multiple Photon Dissociation Spectra of Asparagine Complexes with Zn^{2+} and Cd^{2+} and Their Deamidation Processes. *J. Phys. Chem. B* **2016,** *120*, 12486-12500.

(29) Coates, R. A.; McNary, C. P.; Boles, G. C.; Berden, G.; Oomens, J.; Armentrout, P. B., Structural Characterization of Gas-Phase Cysteine and Cysteine Methyl Ester Complexes With Zinc and Cadmium Dications By Infrared Multiple Photon Dissociation Spectroscopy. *Phys. Chem. Chem. Phys.* **2015,** *17*, 25799-808.

(30) Coates, R. A.; Boles, G. C.; McNary, C. P.; Berden, G.; Oomens, J.; Armentrout, P. B., Zn^{2+} and Cd^{2+} Cationized Serine Complexes: Infrared Multiple Photon Dissociation Spectroscopy and Density Functional Theory Investigations. *Phys. Chem. Chem. Phys.* **2016,** *18*, 22434-45.

CHAPTER 2

EXPERIMENTAL METHODS AND DATA ANALYSIS

2.1 Collision-Induced Dissociation Experiments

The hydrated transition metal ion experiments described in Chapters 3, 4, and 5 were performed using a guided ion beam tandem mass spectrometer with an electrospray ionization source (ESI-GIBMS), shown in Figure 2.1, which has been described in detail previously.[1-3] The GIBMS consists of four main regions: ESI source, magnetic momentum analyzer, octopole ion guide and reaction cell, and a quadrupole mass filter and Daly detector. The ions are generated using an ESI source,[3] which comprises a stainless-steel electrospray needle, a heated capillary, an 88 plate radiofrequency (rf) ion funnel,[4] and an rf hexapole ion guide. A 10^{-4} M solution of the metal salt in neat water is delivered through the electrospray stainless-steel needle with a flow rate of 0.05 − 0.10 L/h and a voltage of 2.0 − 2.2 kV applied to the needle to ionize the complexes. The ions enter a capillary following the spray which is heated to 80 °C to promote desolvation of large droplets and has a small applied potential, typically <15 V. After emerging from the capillary, the ions are collected in the ion funnel (IF), increasing signal intensity,[5-6] and are pulled through the IF by a gentle DC gradient, typically ~10 V, so as to avoid collisional heating. At the end of the IF, the ions are injected into an rf-only hexapole ion guide which traps the ions in the radial direction using an rf amplitude set to 250 V peak

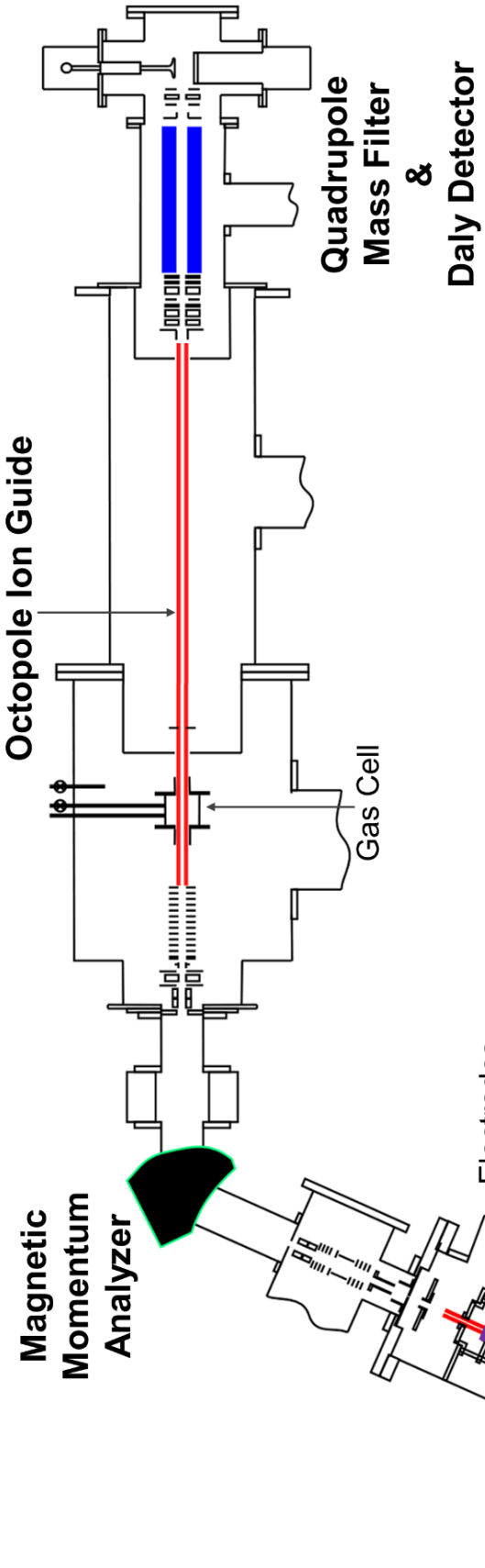

Figure 2.1. Schematic of the guided ion beam tandem mass spectrometer (GIBMS)

to peak. Here, the ions undergo sufficient thermalizing collisions, $>10^4$ collisions with the ambient gas (predominantly air and water),[7] as they drift through the hexapole to bring them to a Maxwell Boltzmann distribution of ro-vibrational states at room temperature.[3,7-10] A set of DC electrodes set in between the hexapole rods are utilized as an in-source fragmentation technique to increase the signal intensity of smaller complexes by fragmenting larger complexes with increasing electrode voltage.[11] The position of the electrodes relative to the end of the hexapole allows the newly formed smaller complexes to rethermalize as they drift to the end of the hexapole, demonstrated previously[11-13] and in this work. This electrode fragmentation technique is used to preferentially form smaller complex sizes of $Ni^{2+}(H_2O)_x$, $Co^{2+}(H_2O)_x$, and $CoOH^{+}(H_2O)_x$ as explicitly outlined in Chapters 3, 4 and 5, respectively.

The thermalized ions are extracted from the hexapole and focused into the magnetic momentum analyzer for selection of the desired reactant ion by its mass-to-charge ratio (m/z). The reactant ions are then decelerated to a known kinetic energy relative to the hexapole in the ion source, V_{lab}, and focused into an rf octopole ion guide[14] where the ions are trapped radially. Reactant ions pass through a collision gas cell which surrounds part of the octopole containing xenon (at low pressures varying between 0.05 and 0.20 mTorr). Xenon is used as the collision gas for inducing dissociation as it is large, monatomic, chemically unreactive, and polarizable, thereby providing efficient kinetic to internal energy transfer upon collision.[15-16] After the collision cell, unreacted reactant and product ions drift out of the octopole, where they are focused into a quadrupole mass filter and then detected utilizing a Daly type detector.[17]

2.1.1 Data reduction and analysis. Ion intensities are converted to absolute cross sections, which correspond to the probability of a reaction to occur, using a Beer's Law relationship seen in eq 2.1.

$$I = I_0 \exp(-\sigma_{tot} \rho l) \tag{2.1}$$

Here, I is the reactant ion intensity of the transmitted ion beam (after the collision cell), I_0 is the reactant ion intensity before the collision cell, σ_{tot} is the total cross section, ρ is the number density of xenon in the collision cell, and l is the effective path length of the gas cell (8.6 cm). The rf field of the octopole ensures very few ions are lost by scattering, such that $I - I_0 = \Sigma I_j$, the sum all product intensities. The product intensity of channel j is converted to a cross section by eq 2.2.

$$\sigma_j = \sigma_{tot} \left(\frac{I_j}{\sum I_j} \right) \tag{2.2}$$

By subtracting ion intensities without collision gas in the cell from those with collision gas in the cell, background collisions and detector noise are removed from the cross sections. Experiments are performed at three different pressures of Xe in the collision cell (typically about 0.05, 0.10, and 0.20 mTorr) so that the cross sections could be extrapolated to zero pressure. This ensures single collision conditions by rigorously removing effects arising from multiple collisions,[18-19] which are particularly significant in the present systems for higher order water losses and the charge separation channels. Absolute cross sections have an uncertainty of ±20% (10% uncertainties for pressure measurement and 10% for collision cell length).[20]

The energy of the reactants in the lab frame, V_{Lab}, is converted to the relative center-of-mass (CM) energy using $E_{CM} = z \times V_{Lab} \times m/(m + M)$, where z is the number of charges on the ion, m is the mass of the neutral reactant Xe, and M is the mass of the ionic reactant. The absolute energy zero and kinetic energy distribution of the reactant ions are determined using a retarding potential technique.[1] The derivative of the normalized ion intensities is fit to a Gaussian distribution to obtain the absolute zero of energy as well as the distribution of reactant ion kinetic energies.

Accurate thermochemical results for the loss of a single ligand from a reactant ion are extracted from the zero-pressure kinetic energy dependent cross sections using the modified line-of-centers (LOC) model for bimolecular collisions, eq 2.3.

$$\sigma_j(E) = \sigma_0 \sum g_i\left(E + E_i - E_{0,j}\right)^n / E \qquad (2.3)$$

In this expression, σ_0 is an energy independent scaling factor, E is the relative translational energy of the reactants, $E_{0,j}$ is the reaction threshold at 0 K for channel j, and n is an adjustable fitting parameter that characterizes the energy deposition during collision.[2] The summation is over the ro-vibrational states of the reactants having excitation energies E_i and populations g_i, where $\sum g_i = 1$. The number of ro-vibrational states are counted using the Beyer-Swinehart-Stein-Rabinovitch algorithm,[21-24] and a Maxwell-Boltzmann distribution at 300 K is used to describe the populations g_i. Before comparison with the data, the model is also convoluted over the kinetic energy distributions of the reactants.[1] As the size of the reactant ions increases, those with energy in excess of the dissociation threshold may not have time to dissociate within the experimental time of flight, $\tau \approx 5 \times 10^{-4}$ s.[25] Accordingly, larger kinetic energies are

required to dissociate the ion within the time scale of the experiment and the apparent thresholds increase to higher energies. This kinetic shift in the threshold can be accounted for by incorporating Rice-Ramsperger-Kassel-Marcus (RRKM) statistical theory[25,26-27] for unimolecular dissociation into eq 2.3, as seen in eq 2.4.[28]

$$\sigma_j(E) = \left(\frac{n\sigma_{0,j}}{E}\right) \sum g_i \int_{E_{0,j}-E_i}^{E} \left[\frac{k_j(E^*)}{k_{tot}(E^*)}\right] (E-\varepsilon)^{n-1} P_{D1} d(\varepsilon) \qquad (2.4)$$

Here, ε is the energy deposited into internal modes of the reactant ion during collision at a relative translational energy, E. The internal energy of the energized molecule (EM) after collision is $E^* = \varepsilon + E_i$. This value is integrated over all possible deposited energies leading to dissociation and is used to calculate the total unimolecular dissociation rate coefficient, $k_{tot}(E^*) = \Sigma\, k_j(E^*)$. $P_{D1} = 1 - \exp[-k_{tot}(E^*)\,\tau]$ is the probability of dissociation of the EM to occur within the experiment time scale. Should the EM dissociate within the time frame, the integration of eq 2.4 recovers eq 2.3. Modeling competitive dissociative pathways is achieved by eq 2.4 through the incorporation of the $k_j(E^*)/k_{tot}(E^*)$ factor. The RRKM unimolecular rate coefficient is defined by eq 2.5,

$$k_{tot}(E^*) = \sum k_j(E^*) = \sum d_j N_j^{\dagger}\left(E^* - E_{0,j}\right)/h\rho(E^*) \qquad (2.5)$$

where d_j is the reaction degeneracy for channel j given by the ratio of the rotational symmetry numbers (reactant/products),[25] $N_j^{\dagger}(E^* - E_{0,j})$ is the number of ro-vibrational states of the transition state (TS) for channel j at an energy $E^* - E_{0,j}$ above the reaction barrier, and $\rho(E^*)$ is the density of states for the ro-vibrational levels of the EM at E^*. The rotational constants and vibrational frequencies of the EM and TSs are taken from quantum chemical calculations (detailed in Chapters 3, 4, and 5).

Sequential dissociations are also modeled in Chapters 3, 4, and 5 in order to obtain thermochemical information on smaller complexes not directly accessible from the ESI source. Thresholds for secondary dissociation are modeled in conjunction with modeling the single water loss channel by a statistical approach combining eq 4 with the probability for further dissociation, eq 2.6,

$$P_{D2} = 1 - e^{-k_2(E_2^*)\tau} \tag{2.6}$$

where E_2^* is the internal energy of the product ion undergoing sequential dissociation. This energy is determined by energy conservation, $E_2^* = E^* - E_{0,j} - T_1 - E_L$, where T_1 is the translational energy of the primary products and E_L is the internal energy of the neutral product. Statistical assumptions are used to assign the distributions of each of these quantities, thereby allowing calculation of the secondary dissociation rate constant, k_2.[29] Because the uncertainties in the energy distribution increase for every neutral ligand lost, the sequential model is typically limited to single primary product channels such that no designation of the individual primary reaction channel j is included in eq 2.6. Equations 2.3, 2.4, or 2.6 are used to analyze the experimental cross sections, reproducing the data over extended energy and magnitude ranges by optimizing the fitting parameters, $\sigma_{0,j}$, $E_{0,j}$, and n by a nonlinear least squares criterion. The uncertainties in these parameters are ascertained by including variations associated with modeling several independent experimental cross sections, scaling the theoretical vibrational frequencies by ±10%, varying the n value by ±0.1, scaling the experimental time of flight up and down by a factor of two, and including the uncertainty in the absolute energy scale (±0.05 eV, lab).

2.2 Infrared Multiple Photon Dissociation Experiments

Metallated amino acid experiments described in Chapters 6 and 7 were performed at the FELIX Facility of Radboud University in the Netherlands using the free electron laser for infrared experiments (FELIX) beam line.[30] A 4.7 T Fourier transform ion cyclotron resonance (FT-ICR) mass spectrometer[31-33] is used to measure the IRMPD spectra. Solutions of 1.0 mM amino acid with 1.0 mM zinc nitrate or cadmium chloride in 50:50 MeOH:H_2O solution are used to generate metallated amino acid ions by a Micromass Z-spray ESI source, operated in the positive ion mode, with a flow rate of 3 - 10 µL/min and ~2.9 kV. Ions generated by the ESI source are accumulated in a linear hexapole rf trap at approximately 10^{-3} Torr for 5 - 7 s before being pulse extracted through a quadrupole bender. After pulse extraction from the trap, ions are guided to the ICR cell using rf and dc electric fields via a 1.0-meter-long octopole ion guide. Capturing the ions is achieved using gated re-referencing of the ions' dc bias potential on the octopole to avoid the need for a gas pulse and to avoid collisional heating of the ions.[31] Once trapped in the ICR cell, the ions are allowed to cool radiatively to room temperature for up to 0.4 s at 10^{-8} Torr.[34] The ion of interest is mass isolated using a stored waveform inverse Fourier transform (SWIFT) excitation pulse.[35-36] These isolated ions are irradiated with FELIX for 3 - 5 s at a 5 or 10 Hz macropulse repetition rate (energy up to 45 mJ per pulse and the bandwidth is 0.5% of the central frequency). In addition to the FELIX beam, a secondary laser beam from a 35-W continuous wave CO_2-laser can be introduced into the ICR cell to interact with the stored ions.

2.2.1 Data reduction. The IRMPD spectra are generated by plotting the photofragmentation yield, eq 2.7,

$$Y = \Sigma I_F / (I_P + \Sigma I_F) \quad (2.7)$$

where I_P and I_F are the integrated intensities of the parent and fragment ion mass peaks, respectively, as a function of the wavenumber of the IR radiation after correcting for laser power. Infrared spectra obtained using IRMPD methods are comparable to those recorded using linear absorption techniques, in part because the spectra result from incoherent, rather than coherent, multiple photon excitation. Previous modeling studies have demonstrated the near-linear absorption character of IRMPD studies.[37-38]

2.3 References

(1) Ervin, K. M.; Armentrout, P. B., Translational Energy Dependence of $Ar^+ + XY \rightarrow ArX^+ + Y$ (XY = H_2, D_2, HD) from Thermal to 30 eV c.m. *J. Chem. Phys.* **1985,** *83*, 166.

(2) Muntean, F.; Armentrout, P. B., Guided Ion Beam Study of Collision-Induced Dissociation Dynamics: Integral and Differental Cross Sections. *J. Chem. Phys.* **2001,** *115*, 1213-1228.

(3) Moision, R. M.; Armentrout, P. B., An Electrospray Ionization Source for Thermochemical Investigation With the Guided Ion Beam Mass Spectrometer. *J. Am. Soc. Mass Spectrom.* **2007,** *18*, 1124.

(4) Kim, T.; Udseth, H. R.; Smith, R. D., Improved Ion Transmission From Atmospheric Pressure to High Vacuum Using a Multicapillary Inlet and Electrodynamic Ion Funnel Interface. *Anal. Chem.* **2000,** *72*, 5014.

(5) Shaffer, S. A.; Prior, D. C.; Anderson, G. A.; Udseth, H. R.; Smith, R. D., An Ion Funnel Interface for Improved Ion Focusing and Sensitivity Using Electrospray Ionization Mass Spectrometry. *Anal. Chem.* **1998,** *70*, 4111.

(6) Shaffer, S. A.; Tolmachev, A.; Prior, D. C.; Anderson, G. A.; Udseth, H. R.; Smith, R. D., Characterization of an Improved Electrodynamic Ion Funnel Interface for Electrospray Ionization Mass Spectrometry. *Anal. Chem.* **1999,** *71*, 2957.

(7) Moision, R. M.; Armentrout, P. B., An Electrospray Source for Thermochemical Investigation with the Guided Ion Beam Mass Spectrometer. *J. Am. Soc. Mass Spectrom.* **2007,** *18*, 1124-1134.

(8) Carl, D. R.; Moision, R. M.; Armentrout, P. B., Binding Energies for the Inner Hydration Shells Of Ca^{2+}: an Experimental and Theoretical Investigation of $Ca^{2+}(H_2O)_x$ Complexes (x=5-9). *Int. J. Mass Spectrom.* **2007,** *265*, 308.

(9) Carl, D. R.; Chatterjee, B. K.; Armentrout, P. B., Inner Shell Hydration Energies of Sr^{2+}. *J. Chem. Phys.* **2010,** *132*, 044303.

(10) Carl, D. R.; Moision, R. M.; Armentrout, P. B., Thermalized Ions from In-source Fragmentation. *J. Am Soc. Mass Spectrom.* **2009,** *20*, 2312.

(11) Carl, D. R.; Moision, R. M.; Armentrout, P. B., In-source Fragmentation Technique for the Production of Thermalized Ions. *J. Am. Soc. Mass Spectrom.* **2009,** *20*, 2312-2317.

(12) Carl, D. R.; Moision, R. M.; Armentrout, P. B., Binding Energies for the Inner Hydration Shells of Ca^{2+}: An Experimental and Theoretical Investigation of $Ca^{2+}(H_2O)_x$ Complexes (x = 5 – 9). *Int. J. Mass Spectrom.* **2007,** *265*, 308-325.

(13) Cooper, T. E.; Armentrout, P. B., Threshold Collision-Induced Dissociation of Hydrated Cadmium (II): Experimental and Theoretical Investigation of the Binding Energies for $Cd^{2+}(H_2O)_n$ Complexes (n = 4 – 11). *Chem. Phys. Lett.* **2010,** *486*, 1-6.

(14) Gerlich, D., Inhomogeneous rf Fields: A Versatile Tool for the Study of Processes with Slow Ions. *Adv. Chem. Phys.* **1992,** *82*, 1-176.

(15) Dalleska, N. F.; Honma, K.; Sunderlin, L. S.; Armentrout, P. B., Solvation of Transition Metal Ions by Water. Sequential Binding Energies of $M^+(H_2O)_x$ (x = 1-4) for M = Ti to Cu Determined by Collision-Induced Dissociation. *J. Am. Chem. Soc.* **1994,** *116*, 3519.

(16) Aristov, N.; Armentrout, P. B., Collision Induced Dissociation of Vanadium Monoxide Ion. *J. Phys. Chem.* **1986,** *90*, 5135–5140.

(17) Daly, N. R., Scintillation Type Mass Spectrometer Ion Detector. *Rev. Sci. Instrum.* **1960,** *31*, 264.

(18) Hales, D. A.; Lian, L.; Armentrout, P. B., Collision-Induced Dissociation of Nb_n^+ (n = 2 - 11): Bond Energies and Dissociation Pathways. *Int. J. Mass Spectrom. Ion Process.* **1990,** *102*, 269.

(19) Schultz, R. H.; Crellin, K. C.; Armentrout, P. B., The Sequential Bond Energies of $Fe(CO)_x^+$ (x = 1 - 5): Systematic Effects on Collision-Induced Dissociation Measurements. *J. Am. Chem. Soc.* **1991,** *113*, 8590-8601.

(20) Ervin, K. M.; Armentrout, P. B., Translational Energy Dependence of $Ar^+ + XY \rightarrow ArX^+ + Y$ (XY = H_2, D_2, HD) from Thermal to 30 eV c.m. *J. Chem. Phys.* **1985,** *83*, 166-189.

(21) Stein, S. E.; Rabinovich, B. S., On the Use of Exact State Counting Methods in RRKM Rate Calculations. *Chem. Phys. Lett.* **1977,** *49*, 1883.

(22) Beyer, T. S.; Swinehart, D. F., Algorithm 448: Number of Multiply-Restricted Partitions. *Comm. Assoc. Comput. Mach.* **1973,** *16*, 379.

(23) Stein, S. E.; Rabinovich, B. S., Accurate Evaluation of Internal Energy Level Sums and Densities Including Anharmonic Oscillators and Hindered Rotors. *J. Chem. Phys.* **1973,** *58*, 2438.

(24) Gilbert, R. G.; Smith, S. C., *Theory of Unimolecular and Recombination Reactions*. Blackwell Scientific: Oxford, 1990.

(25) Muntean, F.; Armentrout, P. B., Guided Ion Beam Study of Collision-Induced Dissociation Dynamics: Integral and Differental Cross Sections. *J. Chem. Phys.* **2001,** *115*, 1213-1228.

(26) Holbrook, K. A.; Pilling, M. J.; Robertson, S. H., *Unimolecular Reactions*. 2nd ed.; Wiley: New York, 1996.

(27) Truhlar, D. G.; Garrett, B. C.; Klippenstein, S. J., Current Status of Transition-State Theory. *J. Phys. Chem.* **1996,** *100*, 12771-12800.

(28) Rodgers, M. T.; Ervin, K. M.; Armentrout, P. B., Statistical Modeling of Collision-Induced Dissociation Thresholds. *J. Chem. Phys.* **1997,** *106*, 4499-4508.

(29) Armentrout, P. B., Statistical Modeling of Sequential Collision-induced Dissociation. *J. Chem. Phys.* **2007,** *126*, 234302.

(30) Oepts, D. v. d. M., A.F.G.; van Amersfoort, P.W. , The Free-Electron-Laser user facility FELIX. *Infrared Phys. Technol.* **1995,** *36*, 297-308.

(31) Polfer, N. C.; Oomens, J.; Moore, D. T.; von Helden, G.; Meijer, G.; Dunbar, R. C., Infrared Spectroscopy of Phenylalanine Ag(I) and Zn(II) Complexes in the Gas Phase. *J. Am. Chem. Soc.* **2006,** *128*, 517-525.

(32) Valle, J. J.; Eyler, J. R.; Oomens, J.; Moore, D. T.; van der Meer, A. F. G.; von Heldon, G.; Meijer, G.; Hendrickson, C. L.; Marshall, A. G.; Blakney, G. T., Free Electron Laser-Fourier Transform Ion Cyclotron Resonance Mass Spectrometry Facility For Obtaining Infrared Multiphoton Dissociation Spectra of Gaseous Ions. *Rev. Sci. Instrum.* **2005,** *76*, 023103.

(33) Polfer, N. C. J. O., Reaction Products in Mass Spectrometry Elucidated With Infrared Spectroscopy. *Phys. Chem. Chem. Phys.* **2007,** *9*, 3804-3817.

(34) Dunbar, R. C., Infrared Radiative Cooling of Isolated Polyatomic Molecules. *J. Chem. Phys.* **1989,** *90*, 7369-7375.

(35) Marshall, A. G.; Wang, T. C. L.; Ricca, T. L., Tailored Excitation for Fourier Transform Ion Cyclotron Resonance Mass Spectrometry. *J. Am. Chem. Soc.* **1985,** *107*, 7893-7897.

(36) Guan, S. H.; Marshall, A. G., Stored Waveform Inverse Fourier Transform (SWIFT) Ion Excitation in Trapped-Ion Mass Spectometry: Theory and Applications. *Int. J. Mass. Spectrom. Ion Process.* **1996,** *158*, 5-37.

(37) Polfer, N. C., Infrared Multiple Photon Dissociation Spectroscopy of Trapped Ions. *Chem. Soc. Rev.* **2011,** *40*, 2211-21.

(38) Oomens, J. S., B.G.; Meijer, G.; von Helden, G. , Gas-Phase Infrared Multiple Photon Dissociation Spectroscopy of Mass-Selected Molecular Ions. *IJMS* **2006,** *254*, 1-19.

CHAPTER 3

THERMOCHEMICAL INVESTIGATIONS OF HYDRATED NICKEL DICATION COMPLEXES BY THRESHOLD COLLISION-INDUCED DISSOCIATION AND THEORY

Reprinted with permission from Rebecca A. Coates and P. B. Armentrout, Thermochemical Investigations of Hydrated Nickel Dication Complexes by Threshold Collision-Induced Dissociation and Theory, *The Journal of Physical Chemistry A*, **2017** *121*, 3629-3646. DOI: 10.1021/acs.jpca.

THE JOURNAL OF PHYSICAL CHEMISTRY A

Article

pubs.acs.org/JPCA

Thermochemical Investigations of Hydrated Nickel Dication Complexes by Threshold Collision-Induced Dissociation and Theory

Rebecca A. Coates and P. B. Armentrout*

Department of Chemistry, University of Utah, 315 South 1400 East, Room 2020, Salt Lake City, Utah 84112, United States

Supporting Information

ABSTRACT: The experimental bond energies of $Ni^{2+}(H_2O)_x$ complexes, where x = 4−11, are determined by threshold collision-induced dissociation using a guided ion beam tandem mass spectrometer with an electrospray ionization source. The electrospray ionization source produces a distribution of $Ni^{2+}(H_2O)_x$ complexes, where an in-source fragmentation technique is employed to access the x = 4−6 complexes and control the population of excited isomers. The kinetic energy-dependent cross sections are modeled to yield 0 K bond energies for sequential loss of neutral water molecules, which are converted to 298 K binding energies. Analysis of the primary and secondary water losses from the $Ni^{2+}(H_2O)_x$ reactant ion complexes, x = 4−11, provide accurate thermochemistry for the hydration energies of Ni^{2+} and yield the first experimental values for x = 4 and 5 binding energies. Speculative thermochemistry for excited isomers of the x = 4−6 complexes is also obtained. Quantum chemical calculations explore the relative energies of possible geometries. Theoretical bond energies for ground structures are used for direct comparison with experimental values. Our experimental results agree well with previously calculated and experimentally obtained binding enthalpies as well as with the more extensive quantum chemical calculations performed here.

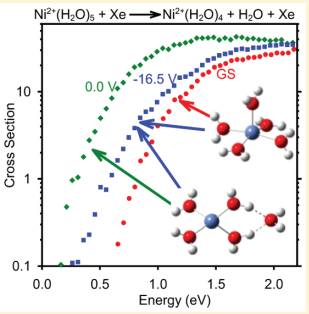

INTRODUCTION

Nickel (Ni) is a naturally occurring group 3d transition metal existing in various mineral forms and is present in all facets of the environment. Nickel plays a well-defined biological role as a trace nutrient in animals, plants, and bacteria.[1] Although biologically important, like so many other transition metals, nickel is heavily used in industry and can also be toxic in excess, being listed on the EPA Clean Water Act Priority Pollutant List.[2] Exposure via diet and drinking water provide most of the intake of nickel and nickel compounds, and once nickel enters the body, it is distributed to all organs.[1,3] Hence, understanding of the fundamental interactions of nickel and water can provide insight into effective strategies for removal of the pollutant and its delivery to needed biological sites.

Previously, our group has used threshold collision-induced dissociation (TCID) in tandem with theoretical calculations to investigate the hydration of alkaline earth and transition metal dications $M^{2+}(H_2O)_x$, where M = Mg,[4] Ca,[5,6] Sr,[7] Ba,[8] Fe,[9] Cu,[10,11] Zn,[12,13] and Cd.[14,15] These studies show that the sequential bond dissociation energies (BDEs), dissociation pathways, and ligand coordination behavior are dependent on the metal center as well as the number of water ligands surrounding the metal. Several other research groups have examined the hydration of multiply charged metals from both an experimental and a theoretical viewpoint. For nickel, Williams and co-workers used blackbody infrared radiative dissociation (BIRD) to directly measure hydration energies of $Ni^{2+}(H_2O)_x$ for x = 6−8, determining 0 K hydration energies of 100.8 ± 4.2, 73.6 ± 3.3, and 71.5 ± 2.9 kJ/mol, respectively.[16] Kebarle and co-workers used high-pressure mass spectrometry (HPMS) to measure the equilibrium for the hydration of the late first-row transition metals, Mn^{2+} through Zn^{2+}, determining ΔG_{300} for the processes;[17,18] however, for Ni^{2+}, these experiments were limited to water clusters sizes of x = 8−12. By assuming ΔS = 96 J/K mol, they determined an outer shell 298 K hydration energy of 63.2 kJ/mol at x = 8 (equivalent to 67.4 kJ/mol at 0 K, see below), somewhat less than the BIRD value. These studies have also sought to investigate the number of ligands that directly bind to the metal center before the second solvation shell forms, known as the coordination number (CN). For Ni^{2+}, CN equals 6, as determined by both infrared photodissociation spectroscopy[19] and a density functional theory (DFT) study of the low-lying isomers of $Ni^{2+}(H_2O)_x$ (x = 1−24).[20]

The present study extends our TCID studies to the hydration of Ni^{2+} by examining the sequential dissociation of $Ni^{2+}(H_2O)_x$ complexes, where x = 4−11. In agreement with our previous $M^{2+}(H_2O)_x$ studies, the dominant process observed is reaction 1, loss of a single water ligand

$$Ni^{2+}(H_2O)_x \rightarrow Ni^{2+}(H_2O)_{x-1} + H_2O \quad (1)$$

followed by sequential loss of additional water molecules. In addition, particular sized complexes are found to undergo dissociative charge separation processes, reaction 2.

Received: January 19, 2017
Revised: April 19, 2017
Published: April 25, 2017

DOI: 10.1021/acs.jpca.7b00635
J. Phys. Chem. A 2017, 121, 3629−3646

$$Ni^{2+}(H_2O)_x \rightarrow NiOH^+(H_2O)_m + H^+(H_2O)_{x-m-1} \quad (2)$$

In the nickel system, when the charge separation reaction 2 is observed, this threshold is found to be higher in energy than the primary water loss threshold for reaction 1, such that the competition between the two pathways does not affect the measured hydration energies, as discussed below. The phenomenon in reaction 2 for hydrated nickel dications has been studied previously to determine the critical size, x_{crit}, defined there as "the maximum number of ligands at which dissociative charge transfer is competitive with simple ligand loss."[21] Kebarle and co-workers reported a lower limit critical size for Ni^{2+} as $x_{crit} = 4$,[22] whereas Shvartzburg and Siu found $x_{crit} = 5$.[21] Previous TCID studies by Armentrout have determined 3d transition metal energy-dependent critical sizes for Fe^{2+} ($x_{crit} = 4$),[9] Cu^{2+} ($x_{crit} = 8$),[10] and Zn^{2+} ($x_{crit} = 7$).[13] In that work, it was suggested that the critical size be more precisely defined as "the largest value of x at which the charge separation is energetically favored over the loss of one water ligand."[13] Here, we also examine the critical size of $Ni^{2+}(H_2O)_x$ using the energy-dependent definition. Finally, in the case of the $x = 4-6$ systems, evidence for the production of excited isomers was found, and thermochemistry measured independently for these. Using TCID in conjunction with theoretical calculations, this study provides an in-depth look at the structures and binding interactions that form the inner and second hydration shells of this nickel dication.

EXPERIMENTAL AND COMPUTATIONAL METHODS

Experimental Procedures. Cross sections for the collision-induced dissociation (CID) of hydrated nickel dication complexes are measured using a guided ion beam tandem mass spectrometer (GIBMS), which has been described in detail previously.[23,24] The hydrated nickel dications, $Ni^{2+}(H_2O)_x$, are produced using an electrospray ionization (ESI) source,[25] which comprises a stainless steel electrospray needle, a heated capillary, an 88 plate radio-frequency (rf) ion funnel,[26] and an rf hexapole ion guide. The complexes are generated by electrospray ionization of 10^{-4} M $NiCl_2$ dilute water solution with a low flow rate of 0.08−0.10 L/h and a voltage of 2.0−2.2 kV applied to the electrospray needle. The capillary was heated to 80 °C to promote desolvation of large droplets, with an applied positive potential (14−17 V) set slightly larger than the voltage of the first plate of the ion funnel (12−15 V). The ions that emerge from the capillary are collected in the ion funnel. A 0.250″ diameter polished stainless steel disk (jet disrupter)[25,27] is located 20 plates from the first ion funnel plate to disperse the emitted jet stream in the ion funnel. The ions are pulled through the funnel by a dc-gradient, kept to only 10−15 V for these experiments, and injected into the hexapole ion guide. The rf of the hexapole ion guide traps the ions in the radial direction with an amplitude of 250 V peak-to-peak. In the past, an in-source fragmentation technique, utilizing negatively biased dc electrodes in between the hexapole rods and described in detail elsewhere,[28] was used to effectively enhance the signal intensity of smaller $M^{2+}(H_2O)_x$ complexes by fragmenting larger complexes. As will be seen below, at low electrode voltages, the ion beam showed evidence for multiple isomers of the selected $Ni^{2+}(H_2O)_x$ ($x < 7$) reactant ions. Here, the electrodes could be employed to fragment the higher energy isomers, either removing them or allowing them to "rehydrate" into low-energy isomers. Once past the electrodes, the ions undergo $>10^4$ collisions with ambient gas as they drift through the hexapole ion guide. Previous studies have shown that under the proper conditions, the ions emerging from the hexapole are thermalized to room temperature.[7,14,29,30] Although the ESI source directly generated $Ni^{2+}(H_2O)_x$ complexes, $x = 5-11$, the ion intensity for $x = 5-7$ could be greatly increased with use of the in-source fragmentation electrodes. At relatively high negative electrode voltages (−18 V), the $Ni^{2+}(H_2O)_4$ complex could be generated. No complex sizes smaller were observed as we believe the threshold for charge separation into singly charged hydrated nickel hydroxide and hydronium ions, reaction 2, is below the threshold for water loss, reaction 1, from $x = 4$ (see discussion below).

To further investigate the thermalization of the ions, a 5.1 cm long nitrogen gas cooling cell that surrounds the hexapole (15.2 cm total length) starting 2.5 cm from the inlet was added to the ESI/IF/6P source. Various pressures of nitrogen gas were added to the cell to alter the thermalization conditions, but no changes in the cross sections for $Ni^{2+}(H_2O)_x$ where $x = 4-6$ were observed.

The ions generated and thermalized in the source were extracted from the hexapole ion guide and focused into a magnetic sector momentum analyzer, where the desired reactant ion was mass selected. The reactant ions were then decelerated to a well-defined voltage relative to the ion source, V_{lab}, and focused into an rf octopole ion guide[31] where the ions were trapped radially. A collision gas cell (8.3 cm effective length), which surrounds the central part of the first of two octopoles (22.9 and 63.5 cm long), contained Xe at varying pressures (0.05−0.20 mTorr) that are low enough that single collision conditions dominate. Xenon was used as the collision gas to induce dissociation because it is heavy, monatomic, polarizable, and chemically unreactive.[32,33] After collision, product ions and remaining reactant ions drifted to the end of the octopole where they were extracted, mass selected using a quadrupole mass filter, and detected using a Daly detector.[34]

Ion intensities were converted to absolute cross sections as described previously with an uncertainty of ±20% (10% uncertainties each in pressure measurement and collision cell length).[24] The laboratory ion potential, V_{lab}, was converted to the relative kinetic energy in the center-of-mass (CM) frame by $E_{CM} = E_{lab} \times m/(m + M)$, where $E_{lab} = 2V_{lab}$ because the ions are doubly charged, m is the mass of the neutral collision gas, and M is the mass of the reactant ion. The absolute zero of energy and the kinetic energy distribution of the ion beam were determined using a retarding potential technique, in which the derivative of the normalized ion intensity was fit to a Gaussian distribution.[24] All energies below are reported in CM frame, unless noted otherwise.

Thermochemical Analysis. To produce accurate thermochemical data from the modeling of the CID process, several effects must be considered; multiple collisions, lifetime effects, and energy distributions. To ensure rigorous single collision conditions, cross sections were obtained at multiple Xe pressures, about 0.20, 0.10, and 0.05 mTorr, and extrapolated to zero pressure cross sections.[35,36] The zero-pressure extrapolated cross sections for dissociation of a reactant $Ni^{2+}(H_2O)_x$ complex are modeled using the empirical threshold model shown in eq 3:

$$\sigma_j(E) = \sigma_0 \sum g_i(E + E_i - E_{0,j})^n/E \quad (3)$$

DOI: 10.1021/acs.jpca.7b00635
J. Phys. Chem. A 2017, 121, 3629−3646

where σ_0 is an energy-independent scaling factor, E is the relative translational energy of the reactants, $E_{0,j}$ is the reaction threshold for channel j at 0 K, and n is an adjustable fitting parameter that describes the efficiency of the energy transfer upon collision.[23] The summation is over the ro-vibrational states of the reactants with excitation energies, E_i, and populations, g_i, where $\Sigma g_i = 1$. The number of ro-vibrational states was directly counted by the Beyer−Swinehart−Stein−Rabinovich algorithm to evaluate the internal energy distribution for the reactants.[37−40] A Maxwell−Boltzmann distribution at 300 K is used to compute the relative populations, g_i.

As the $Ni^{2+}(H_2O)_x$ ions become larger, those with energy in excess of the dissociation threshold may not have time to dissociate on the time scale of the experiment, $\tau \approx 5 \times 10^{-4}$ s.[23] This can lead to a kinetic shift in the energy threshold, which can be accounted for by incorporating Rice−Ramsperger−Kassel−Marcus (RRKM) statistical theory[40−42] for unimolecular dissociation into eq 3, as shown in eq 4.[43]

$$\sigma_j(E) = \left(\frac{n\sigma_{0,j}}{E}\right)\sum g_i \int_{E_{0,j}-E_i}^{E}\left[\frac{k_j(E^*)}{k_{tot}(E^*)}\right](E-\varepsilon)^{n-1}P_{D1}\,d(\varepsilon) \quad (4)$$

In eq 4, ε is the energy transferred into internal degrees of freedom of the reactant ion at a relative translational energy, E. The internal energy of the energized molecule after collision is $E^* = \varepsilon + E_i$, and $k_{tot}(E^*)$ is the total unimolecular dissociation rate coefficient. The rate coefficient is used to calculate a probability of dissociation, $P_{D1} = 1 - \exp[-k_{tot}(E^*)\tau]$. The RRKM unimolecular dissociation rate coefficient is defined by eq 5,

$$k_{tot}(E^*) = \sum k_j(E^*) = \sum d_j N_j^{\dagger}(E^* - E_{0,j})/h\rho(E^*) \quad (5)$$

where $k_j(E^*)$ is the rate coefficient for a single dissociation channel j, d_j is the reaction degeneracy calculated from the ratio of rotational symmetry numbers[40] of the reactants and products of channel j, $N_j^{\dagger}(E^* - E_{0,j})$ is the sum of the ro-vibrational states of the transition state (TS) at an energy $(E^* - E_{0,j})$ above the threshold for channel j, and $\rho(E^*)$ is the density of ro-vibrational states for the energized molecule at the energy available, E^*. When the rate of dissociation is much faster than the average experimental time scale, eq 4 reduces to eq 3. Equation 4 also accounts for the competition between multiple dissociation pathways using the $k_j(E^*)/k_{tot}(E^*)$ ratio.[43,44] Calculation of the RRKM unimolecular rate coefficients in eq 5 requires the ro-vibrational states of the energized molecule and TS. The molecular parameters for the energized molecule were taken from quantum chemical calculations of the reactant ion. For water loss, the TS was assumed to be loose with no reverse activation barrier, as the bond cleavage is heterolytic with all the charge remaining on the nickel containing fragment complex.[45] The water loss TS is product-like and treated in the phase space limit (PSL), such that it uses molecular parameters taken from quantum chemical calculations of the products.[43] Because the charge separation processes produce two singly charged species, there must be an associated Coulomb barrier along the reaction coordinate for this dissociation channel such that the charge separation TSs are tight. The rate-limiting TSs for charge separation are labeled according to the products formed in reaction 2, i.e., TS$[m + (x - m - 1)]$ where m is the number of waters attached to the $NiOH^+$ product and $(x - m - 1)$ is the number of waters attached to the H^+ product. Molecular parameters for these TSs are taken directly from the calculations described below.

For a given $Ni^{2+}(H_2O)_x$ complex size, a sequential dissociation model was employed to simultaneously analyze cross sections for the first and second water losses. Thresholds for sequential dissociation of a second water molecule were modeled with a statistical approach that has been shown to provide accurate thresholds for singly and doubly charged systems.[43,46] The bond dissociation energy (BDE) for the $Ni^{2+}(H_2O)_{x-1}$ complex is the difference between the thresholds of these two product cross sections. The model for sequential dissociation combines eq 4, the cross section of the primary dissociation product, with the probability for further dissociation given by eq 6

$$P_{D2} = 1 - e^{-k_2(E_2^*)\tau} \quad (6)$$

where E_2^* is the internal energy of the product ion undergoing sequential dissociation. This energy is determined by energy conservation, $E_2^* = E^* - E_{0,j} - T_1 - E_L$, where T_1 is the translational energy of the primary products and E_L is the internal energy of the neutral product. For the remainder of this article, representation of this sequential dissociation model that combines eqs 4 and 6 will be notated as eq 4 × 6.

The CID cross sections of eq 4 and eqs 4 × 6 were convoluted over the relative kinetic energy distributions of the $Ni^{2+}(H_2O)_x$ and Xe reactants for comparison with the experimental cross sections.[24] A nonlinear least-squares fitting procedure was used to optimize the fitting parameters in each model. The uncertainties associated with the fitting parameters, $\sigma_{0,j}$, n, and $E_{0,j}$, were determined from modeling multiple data sets and additional modeling of the cross sections by scaling the vibrational frequencies by ±10%, varying the best fit n value by ±0.1, scaling the experimental time-of-flight up and down by a factor of 2, and including the absolute uncertainty of the energy scale 0.05 eV (lab). Because all sources of energy are accounted for in these analyses, the measured thresholds, $E_{0,j}$, equal the BDE for the $Ni^{2+}(H_2O)_x$ or $Ni^{2+}(H_2O)_{x-1}$ complex at 0 K,[47] or the height of the charge separation barrier of reaction 2.

Computational Details. Possible geometries for $Ni^{2+}(H_2O)_x$ complexes were taken from previously examined geometries of $Zn^{2+}(H_2O)_x$ complexes,[12] which were determined using a simulated annealing procedure that combines annealing cycles and ab initio calculations.[48] Structures were optimized using density functional theory and the Gaussian09 suite of programs[49] at the B3LYP/6-31G(d) level of theory[50,51] using the "loose" keyword to utilize a large step size of 0.01 au and rms force constant of 0.0017 to ensure rapid geometry convergence. These structures were refined at a B3LYP/6-311+G(d,p) level, which was used for the final geometry optimizations as well as providing vibrational frequencies and rotational constants. Geometry optimizations utilizing empirical dispersion corrections were also determined at the B3LYP-GD3BJ/6-311+G(d,p) level.[52] Vibrational frequencies were scaled by 0.989[53] before being used in the modeling process to calculate zero point energy and thermal corrections. Single point energy calculations using the B3LYP/6-311+G(d,p) optimized geometries were performed at B3LYP, B3P86,[54] M06,[55] M06-GD3, and MP2(full)[56] (where full indicates correlation of all electrons) levels of theory using a 6-311+G(2d,2p) basis set and also at the B3LYP-GD3BJ/6-311+G(2d,2p)//B3LYP-GD3BJ/6-311+G(d,p) level. The relative energetics calculated from the single point calculations

DOI: 10.1021/acs.jpca.7b00635
J. Phys. Chem. A 2017, 121, 3629−3646

Table 1. Theoretical Relative Enthalpy (ΔH_0) and Free Energies (ΔG_{298}) (kJ/mol) for Distinct $Ni^{2+}(H_2O)_x$ Isomers[a]

x	complex (x,y,z)	B3LYP	B3LYP-GD3BJ	M06	MP2(full)
3	(3,0)	**0.0(0.0)**	**0.0(0.0)**	**5.0(7.0)**[b]	**0.0(0.0)**
	(2,1)_A	86.9(86.5)	90.6(90.3)	68.1(69.7)	100.9(100.5)
4	(4,0) C_s	**0.0(0.0)**	**0.0(0.0)**	**0.0(0.0)**	**0.0(0.0)**
	(4,0) D_4	95.1(94.4)	94.3(93.6)	38.5(37.8)	109.0(108.3)
	(3,1)_A	48.6(46.7)	53.5(51.5)	59.5(57.6)	71.8(69.9)
	(3,1)_AA	61.2(57.8)	62.4(59.0)	64.4(60.9)	72.3(68.9)
5	(5,0)	**0.0(0.0)**	**0.0(0.0)**	**0.0(0.0)**	**0.0(0.0)**
	(4,1)_AA	25.1(21.7)	28.8(25.4)	38.3(34.9)	36.6(33.2)
	(4,1)_A	28.6(27.8)	35.4(34.7)	48.5(47.7)	43.3(42.6)
6	(6,0)	**0.0(0.0)**	**0.0(0.0)**	**0.0(0.0)**	**0.0(0.0)**
	(5,1)_A_bA_b	15.3(10.6)	20.5(15.8)	33.3(28.6)	29.1(24.3)
	(5,1)_A_b	22.6(20.2)	30.5(28.0)	45.8(43.3)	38.6(36.2)
	(4,2)_4D_2AA	33.4(26.1)	42.5(35.2)	63.3(55.9)	59.3(51.9)
	(4,2)_3D_AA,A	61.1(55.5)	73.6(68.1)	104.3(98.8)	91.3(85.7)
7	(6,1)_AA	**0.0(0.0)**	**0.0(0.0)**	**0.0(0.0)**	**0.0(0.0)**
	(5,2)_2D,DD_2A_bA_b	2.9(0.5)	8.6(6.1)	19.2(16.7)	15.5(13.1)
	(4,3)_2D,2DD_3AA	30.3(25.1)	39.3(34.1)	55.5(50.3)	56.8(51.6)
8	(6,2)_4D_2AA_g	1.2(**0.0**)	0.9(**0.0**)	1.4(**0.0**)	2.4(**0.0**)
	(6,2)_2D,DD_2AA	**0.0**(1.1)	**0.0**(1.5)	**0.0**(1.0)	**0.0**(0.03)
	(5,3)_4D,DD_3AA_{ggg}	4.3(2.1)	9.9(8.1)	22.0(19.7)	17.8(14.5)
	(4,4)_4DD_4AA	29.3(24.5)	38.6(34.2)	51.8(46.9)	57.4(51.5)
9	(6,3)_6D_3AA	**0.0(0.0)**	**0.0(0.0)**	**0.0(0.0)**	**0.0(0.0)**
	(5,4)_4DD_4AA	4.2(2.8)	9.8(8.4)	20.6(19.2)	16.0(14.6)
	(4,5)_D,3DD_2AA,3A	56.0(58.5)	74.8(77.3)	105.9(108.2)	89.4(92.0)
10	(6,4)_4D,2DD_4AA C_2	**0.0(0.0)**	**0.0(0.0)**	**0.0(0.0)**	0.2(0.5)
	(6,4)_5D,DD_2AA,AAD_2,AA_2	2.9(2.5)	2.5(2.1)	4.8(4.4)	**0.0(0.0)**
	(5,5)_D,4DD_4AA,A	4.2(6.1)	14.6(16.5)	27.3(29.2)	19.2(21.6)
11	(6,5)_D,4DD_3AA,AAD_2,AA_2	**0.0**(1.3)	0.5(2.4)	**0.0**(0.6)	**0.0**(1.6)
	(6,4,1)_4D,2DD_3AA,AAD_A	1.0(4.2)	6.6(10.5)	6.2(8.7)	6.4(10.0)
	(6,5)_4D,2DD_AA,2AAD_2,2AA_2	0.6(**0.0**)	**0.0(0.0)**	1.4(**0.0**)	0.3(**0.0**)

[a]ΔG_{298} values are given in parentheses. Values are single point energies calculated at the level shown using a 6-311+G(2d,2p) basis set from geometries optimized at the B3LYP/6-311+G(d,p) level. Zero point energy corrections are included. Bold values represent the predicted ground structures (GS). [b]For these calculations, the (3,0)_C_{3h} isomer is the ground structure. See Table S2.

include zero point corrections to yield 0 K values as well as thermal corrections to the source temperature at 298 K. Basis set superposition errors (BSSE) were calculated for dissociation of the lowest energy structures at each level of theory in the full counterpoise (cp) limit.[57,58]

RESULTS

Overview of Theoretical Results. As described above, the geometry optimizations and frequency calculations for $Ni^{2+}(H_2O)_x$ (x = 1−11) complexes were calculated using a B3LYP/6-311+G(d,p) level of theory. For all complexes, the triplet spin state of the $3d^8$ configuration on nickel was found to be much more favorable energetically compared to a singlet spin state. Although experimental data for the $Ni^{2+}(H_2O)_x$ complexes where x = 1−3 were not attainable, their optimized structures were also calculated and are presented here for completeness. Important structural parameters of the B3LYP predicted ground structures are provided in Table S1 of the Supporting Information for $Ni^{2+}(H_2O)_x$, where x = 1−9. For the smaller complex sizes, $x \leq 6$, all levels of theory predict that all waters bind directly to the nickel dication for structures with the lowest relative energies. Table 1 reports relative energetics at 0 and 298 K for distinct low energy isomers of $x \geq 3$ complexes. Structures and relative energies at 0 and 298 K of all investigated isomers of $Ni^{2+}(H_2O)_x$ are given in Figure S1 and Table S2, respectively, of the Supporting Information. In Figure S1 and figures showing structures discussed below, intermolecular hydrogen bonds are visualized (as dashed lines) only between water ligands of different solvent shells in order to emphasize solvent shell growth. In all cases, these donor−acceptor hydrogen bonds *between* solvent shells have been measured as less than 2.0 Å, suggesting relatively strong electrostatic interactions. Longer-range, weaker electrostatic hydrogen-bonding interactions between ligands *within* a single solvent shell (2.9−3.6 Å) can be inferred from the orientation of the water molecules with respect to each other. (These longer range interactions are not explicitly shown as they make the shell structure difficult to see.)

To verify these qualitative conclusions, we determined the relative transition state energy for breaking these intermolecular hydrogen bonds *within* a single solvent shell compared to those *between* solvent shells using the (6,0) versus (6,1) GSs. The highly symmetrical (6,0) GS with T_h molecular symmetry exhibits long hydrogen bonds (3.0 Å) between the ligands of its single solvent shell (Figure 1). Rotating a single water ligand in this isomer breaks these interactions with two adjacent water ligands and requires 8.6−10.5 kJ/mol of energy at four levels of theory. In the analogous (6,1)_AA GS (Figure 2a), breaking a single hydrogen bond between the first and second shell ligands to form the (6,1)_A isomer required 13.3−15.3 kJ/mol. All levels of theory predict the long interactions within a solvent shell to be weaker than the shorter intersolvent shell hydrogen

DOI: 10.1021/acs.jpca.7b00635
J. Phys. Chem. A 2017, 121, 3629−3646

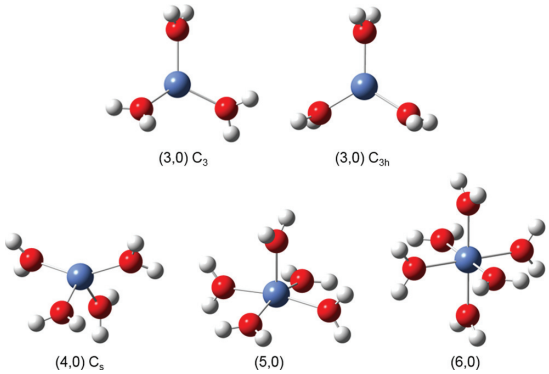

Figure 1. Geometries for the predicted ground structures of $Ni^{2+}(H_2O)_x$ complexes, where x = 3−6, as optimized at the B3LYP/6-311+G(d,p) level of theory.

bonds; B3LYP and MP2(full) levels predict a difference of 5.1 and 5.9 kJ/mol, respectively, whereas the B3P86 and M06 levels find 3.9 and 4.1 kJ/mol differences, respectively.

As complex sizes become larger than x = 6, we find that all ground structures have a coordination number of 6 and that additional water molecules do not interact directly with the nickel dication but begin forming outer solvent shells as hydrogen bonding between the water molecules becomes preferable. Nevertheless, structures having 4, 5, and 6 water inner shells were also investigated for cluster sizes $x \geq 5$. It can be noted that all levels of theory predict the same lowest energy isomers for x = 1−9 at both 0 and 298 K. However, for complexes of x = 10 and 11, the complexity of the possible arrangements of the large number of water ligands in the outer shells leads to differences among different levels of theory in their prediction of the ground structure. Thus, as shown in Table 1, there are two and three potential ground structures for x = 10 and 11, respectively.

We use an (x,y,z) nomenclature to describe the number of water molecules in the first (x), second (y), and third (z) solvent shells of each unique structure. To describe the hydrogen bonding of waters in the cluster, isomers are further denoted using an A/D nomenclature where a water molecule can be a single (A) or double (AA) hydrogen bond acceptor and/or single (D) or double (DD) hydrogen bond donor. To indicate waters that bridge between two different solvent shells, a subscript "2" is denoted on both the donor and acceptor (which is more easily visualized by example, see below). To further distinguish between structures with similar bonding schemes but differing geometric parameters, additions to the nomenclature may include: point group symmetries; the subscripts "a" or "b" to indicate if the bond connects to an axial or base ligand, respectively; series of oxygen−nickel dication−oxygen angles denoted as subscript "c" (cis) for angles <45°, "g" (gauche) for angles between 45° and 135°, and "t" (trans) for angles >135°.

Theoretical Geometries for $Ni^{2+}(H_2O)_x$ Complexes. Figure 1 shows the ground structures (GSs) for x = 3−6. Excited isomers are discussed in the Supporting Information, where they are shown in Figures S1. At x = 3, all levels of theory predict a (3,0) geometry for the ground structure (GS). B3LYP, B3LYP-GD3BJ, B3P86, and MP2(full) all calculate the C_3 isomer to be lowest in energy (Table 1). This GS exhibits a trigonal pyramidal geometry with ∠O−Ni−O of 115° as the water molecules tilt to participate in long (3.6 Å) hydrogen bonding with one another. The C_{3h} isomer lies 42−57 kJ/mol higher in energy at these levels of theory and exhibits no such H-bonding scheme as it is a trigonal planar geometry (∠O−Ni−O of 120°) with the water molecules perpendicular to the plane. M06 levels prefer this higher symmetry geometry and calculate the C_{3h} isomer as the lowest energy isomer by 7.0 kJ/mol energy at 298 K, Table S2.

For x = 4, the calculated GS geometry is (4,0) with C_s symmetry at all levels of theory. In this isomer, the water ligands have a seesaw structure with respect to the oxygen atoms, and the orientation of the ligands is dictated by long (3.1−3.2 Å) hydrogen bonding interactions. In the (3,1)_A structure (Figure S1), the fourth water ligand does not interact with the nickel dication but rather is promoted to a second solvent shell by accepting a single hydrogen bond. This structure was calculated as the GS according to Castro et al.;[20] however, the present study finds this isomer to be 46−70 kJ/mol higher in energy than (4,0) C_s at 298 K (Table 1).

It can be imagined that the $3d^8$ nickel dication might bind to four water molecules in a square-planar geometry, as favored for a singlet spin state, as opposed to the calculated seesaw geometry found for the triplet state GS. The triplet planar (4,0) isomer has D_4 symmetry (Figure S1), which increases the energy of the system with respect to the C_s isomer by 38−108 kJ/mol at 298 K. However, examination of the occupied molecular orbitals of the triplet state seesaw (4,0) GS shows that the singly occupied molecular orbitals (SOMO) put the electron density in octahedral e_g orbitals. Therefore, the best description of the (4,0) GS is a distorted octahedral geometry, which allows weak H-bonding interactions between adjacent ligands, as can be seen by the orientations of the waters in Figure 1. Thus, it would be expected that the inner shell ligands of the $Ni^{2+}(H_2O)_x$ complexes up to x = 6 will also adopt octahedral molecular geometries (as verified below), consistent with the triplet spin state compared to a square-planar singlet spin.

The $Ni^{2+}(H_2O)_5$ complex has a GS of (5,0) with C_{2v} symmetry at all levels of theory. This ground isomer has the water ligand oxygens in a square pyramidal structure with orientations determined by long hydrogen bonding interactions with all adjacent water ligands (2.9 Å for base-to-base, and 3.1 Å for axial-to-base). The SOMO for the (5,0) GS agrees with the evaluation made above for x = 4, where the hydrogen bonding orientation puts the electron density in the octahedral e_g MOs. Isomers where the fifth water is in the second hydration shell are higher in relative 298 K energy than the (5,0) isomer by 22−49 kJ/mol (Figure S1).

The calculated GS for $Ni^{2+}(H_2O)_6$ is a pseudo-octahedral (6,0) isomer with T_h symmetry at all levels of theory. In this octahedral configuration, Figure 1, the orientations of the ligands are again determined by long (3.0 Å) interligand hydrogen bonding occurring between the hydrogen atom of one ligand and the oxygen atom of a neighboring water unit. The lowest energy excited isomer is 5-coordinate, (5,1)_A_bA_b, and is higher in energy than the GS by 10−30 kJ/mol at 298 K.

Figure 2 shows the predicted ground structures for the $Ni^{2+}(H_2O)_{7\text{-}11}$ complexes. For the x = 7 complex, all levels of theory predict the ground structure to be (6,1)_AA with the oxygen of the seventh water doubly bound via two hydrogen bonds from neighboring octahedral inner shell water ligands, Figure 2a. The $Ni^{2+}(H_2O)_8$ ground isomer has a (6,2) geometry, but as the number of water ligands increases, so

DOI: 10.1021/acs.jpca.7b00635
J. Phys. Chem. A 2017, 121, 3629−3646

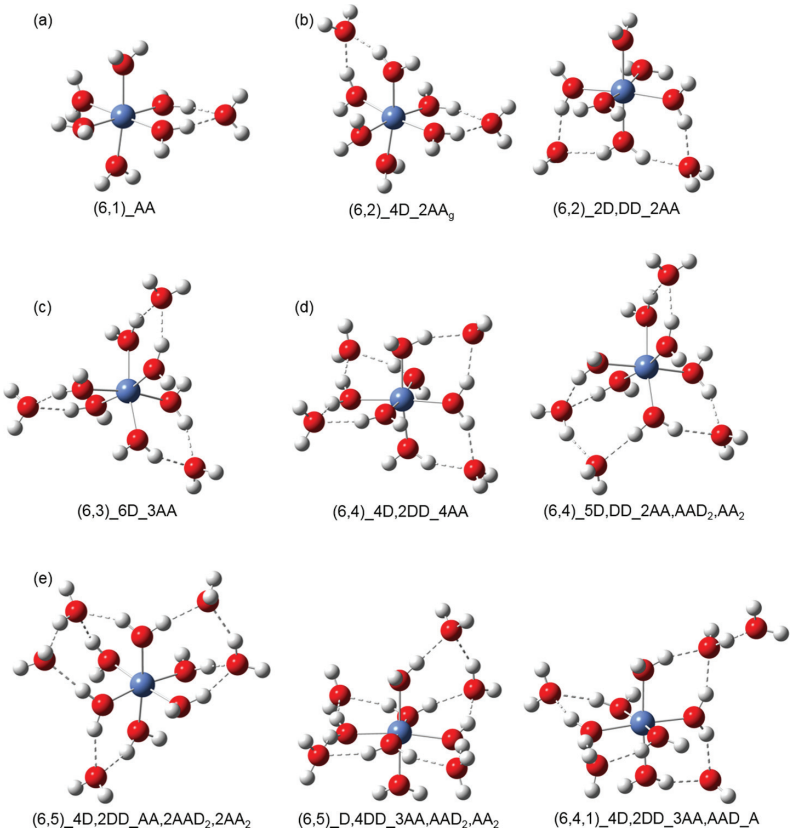

Figure 2. Geometries for the predicted ground structures of second solvent shell $Ni^{2+}(H_2O)_x$ complexes, where x = 7−11 are shown in parts (a)−(e), respectively, as optimized at the B3LYP/6-311+G(d,p) level of theory.

does the complexity in the arrangement of added water molecules, and temperature effects become apparent. At 0 K, all levels of theory calculate the (6,2)_2D,DD_2AA as the GS (by 0.3−2 kJ/mol), whereas at 298 K, all levels of theory predict the (6,2)_4D_2AA$_g$ isomer to be the lowest energy isomer, but only by 0.03−2 kJ/mol. As shown in Figure 2b, both of these (6,2) structures have two second-shell water ligands doubly hydrogen bonded to the inner solvent shell, but in the (6,2)_2D,DD_2AA structure, the two outer shell waters bind to the same inner shell water (DD). In $Ni^{2+}(H_2O)_9$, all levels of theory predict the GS to be a (6,3)_6D_3AA geometry with each of the six inner solvent shell waters donating only a single hydrogen bond to an outer solvent shell water, such that the second solvent shell water distances are maximized and bind in equivalent locations, Figure 2c.

Figure 2d shows the calculated lowest energy $Ni^{2+}(H_2O)_{10}$ complexes, both predicted to be 6-coordinate configurations. All levels of theory excluding MP2(full) predict that the GS structure is the (6,4)_4D,2DD_4AA isomer. This isomer has C_2 symmetry with the outer shell waters oriented in such a way that two of the outer solvent shell water ligands are adjacent to each other in plane with one inner solvent shell water shared between the two on the *xy* plane, while the other two water ligands are bound in the same adjacent fashion but in the *xz* plane. The MP2(full) GS configuration is (6,4)_5D,DD_2AA,AAD$_2$,AA$_2$, which is similar in geometry to the x = 9 (6,3)_6D_3AA isomer but the tenth water ligand (AA$_2$) accepts hydrogen bonds from both a first (A) and second (A$_2$) solvent shell water ligand. Both of these isomers are low-lying at all levels of theory, within 2 kJ/mol of one another.

For the $Ni^{2+}(H_2O)_{11}$ complex, three possible GSs are predicted depending on the level of theory and temperature, Figure 2e. All levels of theory predict that the 298 K GS isomer is the (6,5)_4D,2DD_AA,2AAD$_2$,2AA$_2$ structure where the two AA$_2$ ligands accept hydrogen bonds from both first and second solvent shell ligands of the (6,3)_6D_3AA structure. At 0 K, however, there is less agreement between the levels of theory as to the lowest energy isomer: B3LYP, M06, M06-GD3, and MP2(full) predict the (6,5)_D,4DD_3AA,AAD$_2$,AA$_2$ isomer, which has four in-plane second solvent shell water ligands and one AA$_2$ water binding to a second shell water and axial metal coordinated inner shell water. B3LYP-GD3BJ calculates the (6,5)_4D,2DD 298 K GS to also be the 0 K GS. B3P86 predicts the GS is the (6,4,1)_4D,2DD_3AA,AAD_A isomer, which is the (6,4) GS with the 11th water singly bound in a third solvent shell. An expanded detailed description of additional geometries for x = 3−11 can also be found in the Supporting Information.

Overall, all levels of theory predict coordination numbers of six for the first solvent shell for $Ni^{2+}(H_2O)_x$, x = 6−11. This agrees with previous hydration studies, including an infrared photodissociation study of $Ni^{2+}(H_2O)_{5-8}$ complexes performed

DOI: 10.1021/acs.jpca.7b00635
J. Phys. Chem. A 2017, 121, 3629−3646

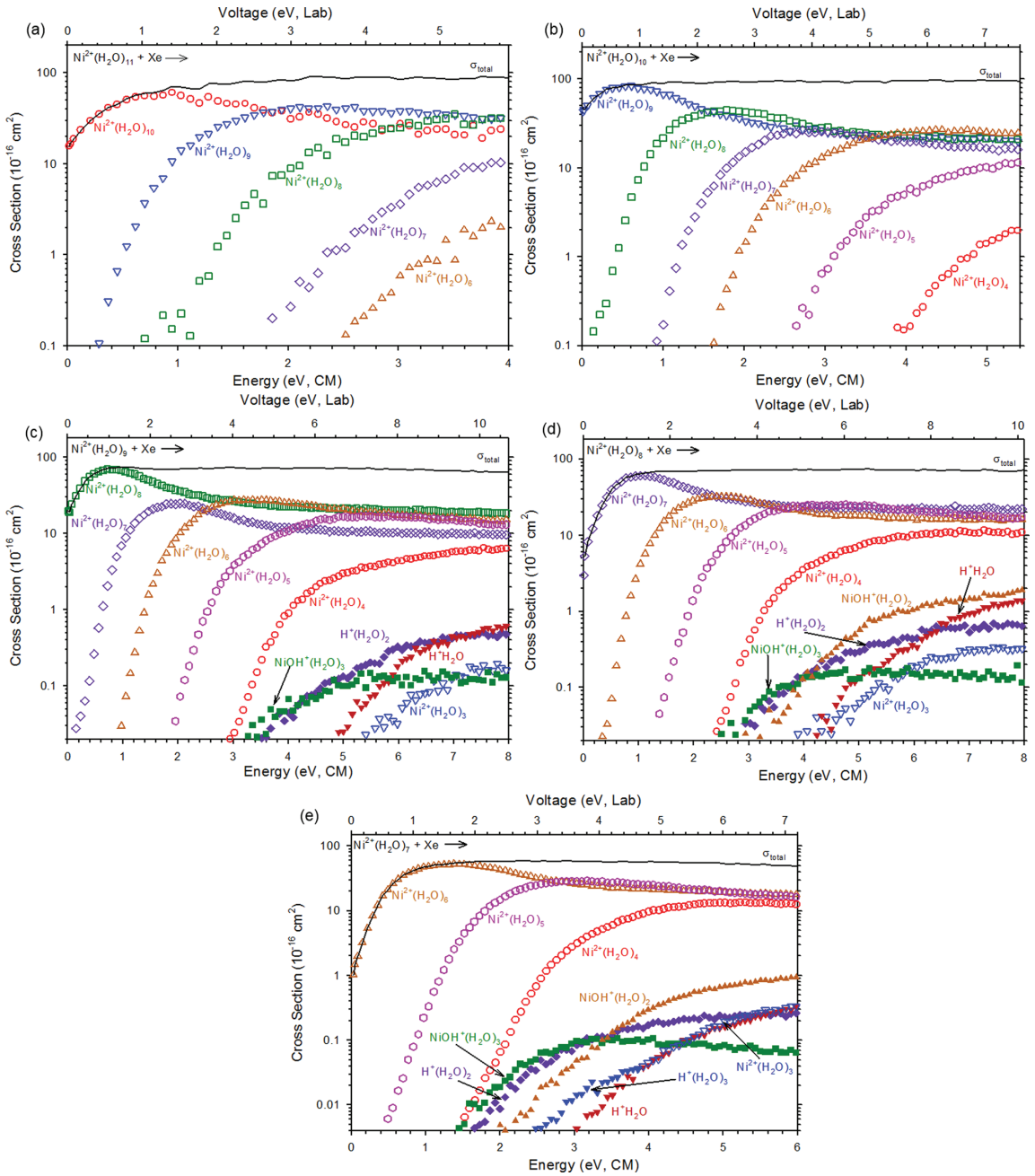

Figure 3. Cross sections for collision-induced dissociation of $Ni^{2+}(H_2O)_x$ where $x = 11-7$ (parts a–e) with Xe (~0.2 mTorr) as a function of kinetic energy in the center-of-mass frame (bottom *x*-axis) and applied voltage in the laboratory frame (top *x*-axis). Water loss products are represented by open symbols and charge separation products by closed symbols. In part e, note that the down blue triangles change from solid to open, which represents the cross sections for the near isobaric products $H^+(H_2O)_3$ (55.05 *m*/*z*) and $Ni^{2+}(H_2O)_3$ (55.98 *m*/*z*).

at 215 and 331 K, in which no indication of lower CN contributions were found at either temperature.[19]

Cross Sections for Threshold Collision-Induced Dissociation of $Ni^{2+}(H_2O)_{7-11}$. Experimental cross sections for the collision-induced dissociation of $Ni^{2+}(H_2O)_x$ with Xe (~0.2 mTorr) are shown in Figure 3 for $x = 7-11$. The major isotope of ^{58}Ni was used throughout the study. In all cases, the dominant dissociation pathway is the loss of a single water molecule, reaction 1. As the kinetic energy increases, this process is then followed by the sequential loss of additional water molecules. In all cases shown (as well as for the smaller complexes discussed below), the total cross sections reach a

DOI: 10.1021/acs.jpca.7b00635
J. Phys. Chem. A 2017, 121, 3629–3646

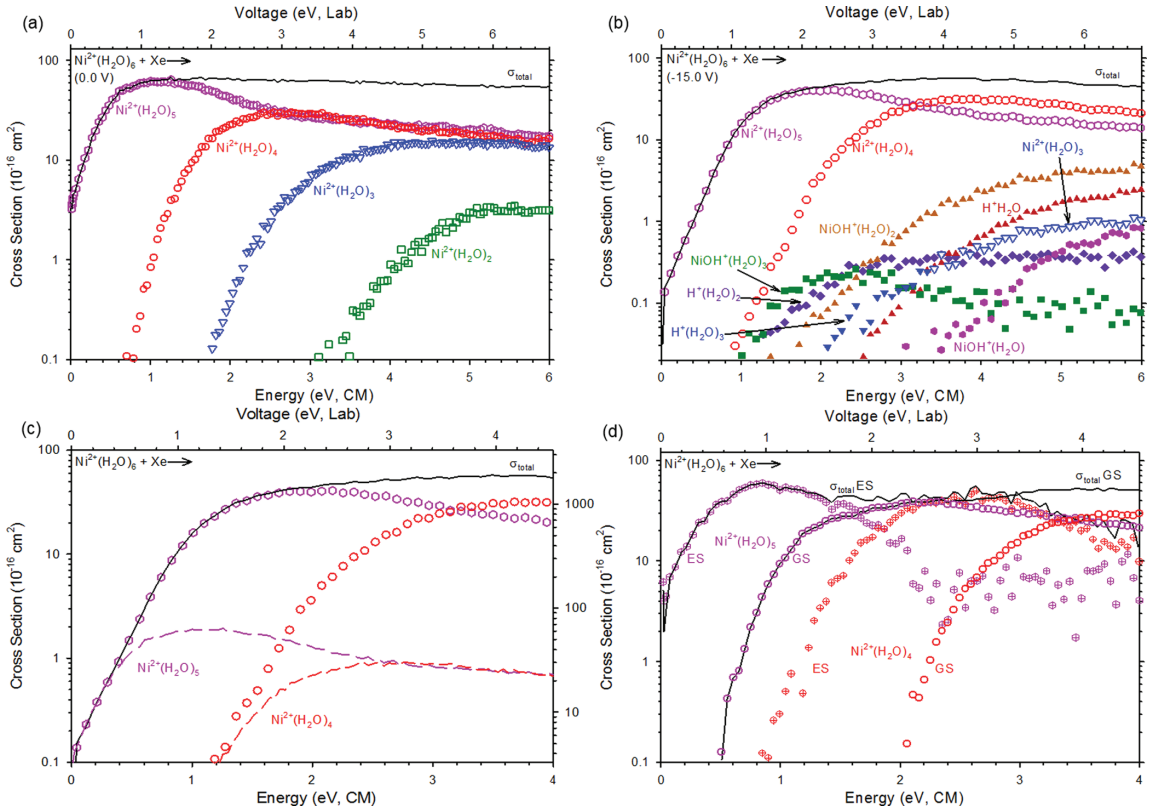

Figure 4. Cross sections for CID of $Ni^{2+}(H_2O)_6$ with Xe as a function of kinetic energy in the center-of-mass frame (bottom *x*-axis) and applied voltage in the laboratory frame (top *x*-axis). (a) Reaction conditions of 0.0 V electrodes and ~0.2 mTorr Xe. (b) Reaction conditions of −15.0 V electrodes and ~0.2 mTorr Xe. (c) Water loss product cross sections with Xe (~0.2 mTorr) with −15.0 V electrode (open symbols) and corresponding product cross sections using 0.0 V (dashed lines) reduced by a factor of 50. (d) Zero-pressure extrapolated and electrode extrapolated GS (open symbols) and ES (crossed symbols) for the primary and secondary product cross sections.

plateau, consistent with sequential dissociation processes. For x = 11 and 10, cross sections for losses of up to five and six water ligands, respectively, were characterized. For x = 9, cross sections for losses of six water molecules were again found. For both x = 9 and 10, it can be noted that the $Ni^{2+}(H_2O)_6$ product has a slightly enhanced cross section relative to its neighbors. In addition, products corresponding to the charge separation (CS) process, reaction 2, were observed for x = 9. It can be seen that the $NiOH^+(H_2O)_3$ and $H^+(H_2O)_2$ products rise from similar thresholds with similar magnitudes, meaning that these species must come from dissociation of the $Ni^{2+}(H_2O)_6$ product in reaction 7.

$$Ni^{2+}(H_2O)_6 \rightarrow NiOH^+(H_2O)_3 + H^+(H_2O)_2 \quad (7)$$

The apparent threshold for this CS reaction clearly exceeds that for loss of a water molecule from this complex to form $Ni^{2+}(H_2O)_5$, which explains why the CS cross section is so much smaller and rises less sharply than the cross section for water loss. In this regard, it is also useful to recognize that the CS processes are entropically disfavored as they must pass over a rate-limiting transition state corresponding to bringing the two incipient singly charged product ions together over a Coulombic barrier, whereas water loss processes always involve loose transition states.

For CID of $Ni^{2+}(H_2O)_8$, Figure 3d, loss of five water ligands and CS products was again characterized. The CS products are similar to x = 9, but now both $NiOH^+(H_2O)_2$ and H^+H_2O are observed at higher energy. Note that the sum of the $NiOH^+(H_2O)_3$ and $NiOH^+(H_2O)_2$ cross sections matches that of the sum of $H^+(H_2O)_2$ and $H^+(H_2O)$ in both magnitude and shape, suggesting that the smaller complexes are formed mainly by loss of water from the initially formed product ions of reaction 7. (Close inspection shows that the former sum is approximately 50% bigger than the latter, which we have previously demonstrated is because the products have appreciable kinetic energy that is released once they pass over the Coulombic barrier.[13] Momentum conservation dictates that the lighter products have a higher kinetic energy, such that they are less efficiently collected and detected.) The increased magnitude of the $NiOH^+(H_2O)_2$ cross section here compared to that formed from $Ni^{2+}(H_2O)_9$ suggests that there are contributions of both sequential loss of water from $NiOH^+(H_2O)_3$, and possibly the CS reaction 8

$$Ni^{2+}(H_2O)_5 \rightarrow NiOH^+(H_2O)_2 + H^+(H_2O)_2 \quad (8)$$

which becomes more evident for smaller reactant complexes. Again, the apparent threshold for the CS process is well above that for the competing loss of water from the dication complex.

DOI: 10.1021/acs.jpca.7b00635
J. Phys. Chem. A 2017, 121, 3629−3646

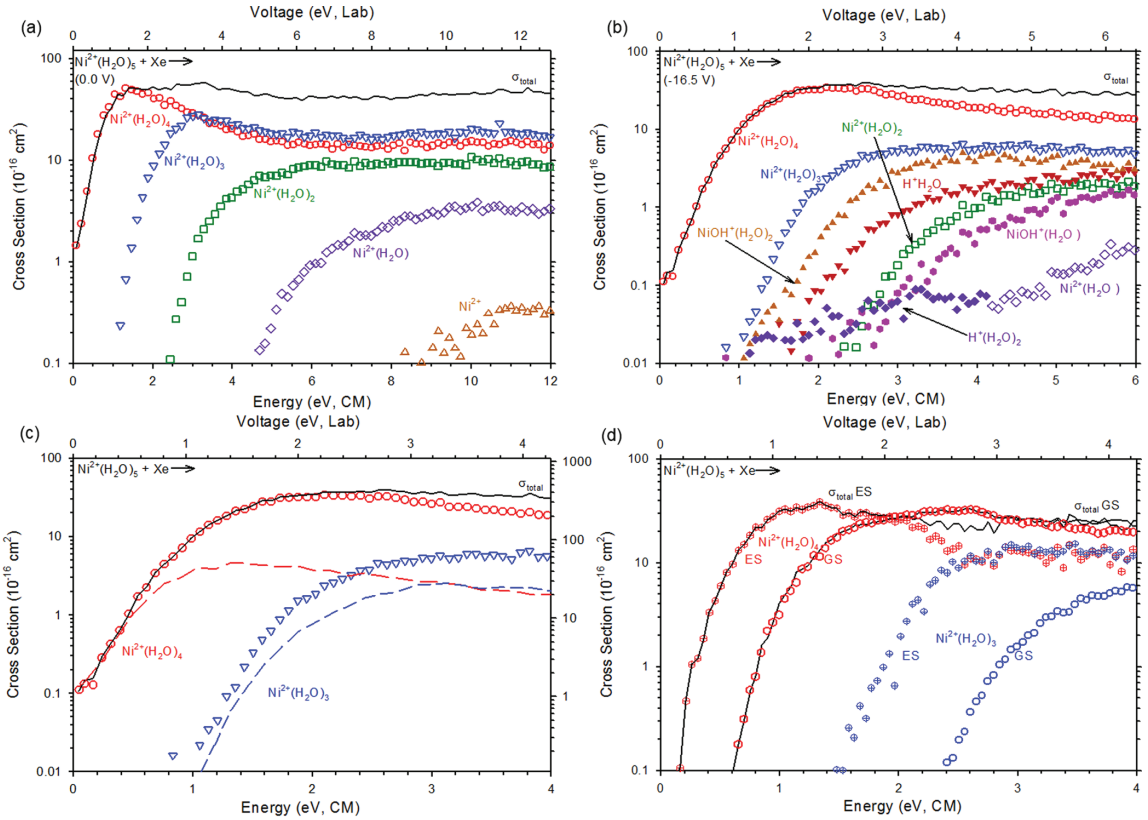

Figure 5. Cross sections for CID of $Ni^{2+}(H_2O)_5$ with Xe as a function of kinetic energy in the center-of-mass frame (bottom *x*-axis) and applied voltage in the laboratory frame (top *x*-axis). (a) Reaction conditions of 0.0 V electrodes and ~0.2 mTorr Xe. (b) Reaction conditions of −16.5 V electrodes and ~0.2 mTorr Xe. (c) Water loss product cross sections with Xe (~0.2 mTorr) with −16.5 V electrode (open symbols) and corresponding product cross sections using 0.0 V (dashed lines) reduced by a factor of 7. (d) Zero-pressure extrapolated and electrode-extrapolated GS (open symbols) and ES (crossed symbols) for the primary and secondary product cross sections.

Figure 3e shows the CID of $Ni^{2+}(H_2O)_7$, which follows the same product pathways as $Ni^{2+}(H_2O)_8$, exhibiting the loss of four water ligands and the same CS channels. Again, the dominant CS process is reaction 7, but close inspection (more evident on a linear cross section scale) shows that the $NiOH^+(H_2O)_2$ cross section has two components. The first is a higher energy feature starting near 3.2 eV that tracks with the decline in the $NiOH^+(H_2O)_3$. The second component is a lower energy feature that has an energy dependence that matches that for $H^+(H_2O)_3$ (with a magnitude of about 1/3). The $H^+(H_2O)_3$ and $Ni^{2+}(H_2O)_3$ products are nearly isobaric (within 1 *m*/*z*) and were not resolved experimentally. The single cross section collected for them, Figure 3e, has two features: the low energy onset attributed to formation of $H^+(H_2O)_3$ (55.05 *m*/*z*) and a higher energy feature starting near 4 eV attributed to $Ni^{2+}(H_2O)_3$ (55.98 *m*/*z*). These observations are evidence for the CS reaction 9.

$$Ni^{2+}(H_2O)_6 \rightarrow NiOH^+(H_2O)_2 + H^+(H_2O)_3 \qquad (9)$$

Again, none of the CS reactions observed have apparent thresholds below those for the competing water loss channels. Notably the data shown in Figure 3e was obtained by applying −10.0 V to the in-source electrodes, which maximized the signal of the $x = 7$ complex; however, similar results were obtained with no voltage on these electrodes.

Cross Sections for Threshold Collision-Induced Dissociation of $Ni^{2+}(H_2O)_{4-6}$. For $Ni^{2+}(H_2O)_6$, the CID results depend critically on the voltage applied to the in-source electrodes. Figure 4a,b show results obtained for 0 and −15.0 V, respectively. With no electrode voltage, Figure 4a, cross sections for losses of up to four water ligands were characterized and no CS channels were observed. If the electrode voltage is tuned to maximize the reactant signal, Figure 4b, the product channels for CID of $Ni^{2+}(H_2O)_6$ now exhibit the product pathways expected on the basis of the results for larger complexes, loss of up to three water ligands, and the same CS channels as seen for $Ni^{2+}(H_2O)_7$ with the addition of the higher energy $NiOH^+(H_2O)$.

A cursory inspection of the apparent thresholds for loss of water suggests they are somewhat higher in Figure 4b than a; however, it can be noticed that the shapes of these cross sections are identical at their lowest energies, such that the data at the high-electrode voltage have low energy features. This is illustrated in Figure 4c, where the 0 V electrode data for water loss have been reduced by a factor of 50 to compare directly with the same channels obtained at −15 V. These low-energy features are not the result of any pressure-dependent effects.

DOI: 10.1021/acs.jpca.7b00635
J. Phys. Chem. A 2017, 121, 3629−3646

Indeed, they become more prominent when the data at ~0.05, 0.10, and 0.20 mTorr of Xe are extrapolated to zero pressure.

We interpret this observation as follows. With no in-source fragmentation, the ion population is dominated by an ES of the complex that loses water readily, thereby suppressing the CS product channels. In-source fragmentation removes these excited structures leaving behind more stable structures, presumably the GS, which does permit the CS channels to occur, albeit inefficiently. We believe that both the ES and GS populations are thermalized, as many collisions occur past the fragmentation electrodes. Evidence for this conclusion comes from the zero-pressure extrapolated cross sections at 0 V on the electrodes, which again has a low-energy feature that is smaller in magnitude by a factor of 60 compared with that for −15 V electrode data (Figure S2). In this case, the low-energy feature is distinct in shape from the dominant feature, evidence that this feature cannot be explained simply by hot ions, but rather by a distinct population of excited species. In order to evaluate the true CID cross sections of these populations, one can simply subtract the cross sections shown in Figure 4c, leaving behind the CID cross sections for the GS. An equivalent but more comprehensive approach takes advantage of the fact that the cross sections shown in parts a and b of Figure 4 both comprise different populations of the ES and GS, with their ratios defined by the scaling factor used to make the cross sections equal at the lowest energy (in this case, 50:1 at 0.20 mTorr of Xe). In order to avoid the effects of secondary collisions, the 0 and −15 V electrode data were first extrapolated to zero-pressure conditions, yielding rigorous single collision cross sections. Then the zero-pressure data were extrapolated to 0% and 100% ES and GS, as shown in Figure 4d. Although this procedure is somewhat speculative, verification that it provides reasonable thermochemistry results can be obtained by comparison with the theoretical results, as discussed in detail below.

Figure 5 shows a similar evaluation of the $Ni^{2+}(H_2O)_5$ CID cross sections, with comparison of results taken at source electrode voltages of 0 V (part a) and −16.5 V (part b), which maximizes the reactant signal. Again, in the absence of in-source fragmentation, Figure 5a, losses of sequential water ligands down to the bare nickel dication were observed but no CS pathways. Increasing the negative electrode voltage was accompanied by the appearance of CS pathways, Figure 5b, a decrease in the magnitudes of the water loss product cross sections, and an increase in the apparent thresholds for water loss. The CS reaction 7 is no longer available such that the lowest energy CS channel is reaction 8 forming $NiOH^+(H_2O)_2 + H^+(H_2O)_2$ starting near 1 eV. The dominant CS process is reaction 10, which starts slightly higher in energy.

$$Ni^{2+}(H_2O)_4 \rightarrow NiOH^+(H_2O)_2 + H^+H_2O \quad (10)$$

As seen for larger complexes, water loss is still the dominant pathway, but loss of the second water to form $Ni^{2+}(H_2O)_3$ has a threshold and magnitude similar to that for the CS reactions. This comparison demonstrates that the CS reaction 10 probably has a lower threshold energy than water loss from $Ni^{2+}(H_2O)_4$; otherwise, this entropically disfavored reaction could not have a magnitude matching that of the more favorable water loss process. As for the $Ni^{2+}(H_2O)_6$ complex, the onsets for water loss cross sections in parts a and b of Figure 5 have the same shape, but now differ in magnitude by a factor of 7, as shown in Figure 5c. Using the same extrapolation procedure discussed above, zero-pressure extrapolated cross sections for ES and GS populations can be extracted and are shown in Figure 5d.

Dissociation of $Ni^{2+}(H_2O)_4$ is shown in Figure 6. This complex could only be generated in sufficient abundance for CID study by using the in-source electrodes, with maximum signal at −18.0 V. Here, only the loss of sequential water molecules down to the bare nickel dication are observed, and the CS processes do not appear. Results from the $x = 5$ complex suggest that the CS process 10 should be a competitive process with the loss of a single water from the $Ni^{2+}(H_2O)_4$ reactant ion. Clearly, the behavior shown in Figure 6 matches that for the $x = 5$ and 6 complexes without electrode voltages applied, suggesting that this reactant ion is also dominated by an ES complex. However, the ES and GS extrapolation method was not possible for the $Ni^{2+}(H_2O)_4$ reactant isomer as no $x = 4$ reactant ions were experimentally observed at 0 V electrode voltage.

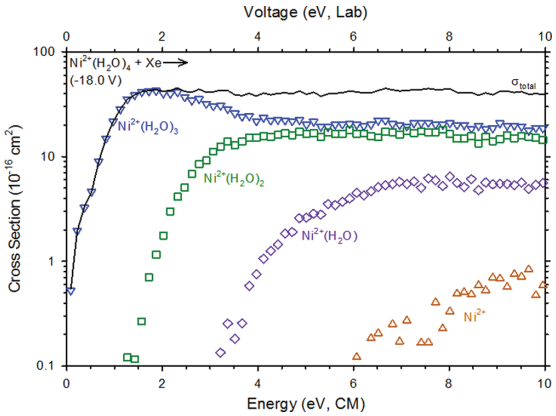

Figure 6. Cross sections for collision-induced dissociation of $Ni^{2+}(H_2O)_4$ with Xe (~0.2 mTorr) as a function of kinetic energy in the center-of-mass frame (bottom *x*-axis) and applied voltage in the laboratory frame (top *x*-axis). An in-source fragmentation electrode voltage of −18.0 V was employed.

Thermochemical Results for Primary Water Loss. Equations 3 and 4 were used to model the total reaction cross sections for water dissociation products for all $Ni^{2+}(H_2O)_x$ complexes observed. As noted above, the complexes are believed to be thermally equilibrated in the source, such that the model generally assumes the reactant isomer is the 298 K GS (or a specific excited structure) with an internal energy distribution of 298 K. The product isomer is assigned as the 0 K GS because previous studies have found our threshold analyses to be dominated by the lowest energy 0 K enthalpy species.[9,12] For this study, we analyzed the data using the appropriate GS complexes predicted by single point energies at any level of theory (Table 1), such that several different possibilities are explored for dissociation of $x = 10$ and 11. The optimum modeling parameters obtained are listed in Table 2, with all variations in the isomer possibilities for $x = 10$ and 11 included in Table S3. These different assumptions change the threshold energies obtained by only 0.01 and 0.02 eV, respectively. Threshold E_0 values were determined for the primary dissociation of each complex from modeling with (eq 4) and without (eq 3) including RRKM theory, which takes lifetime effects into account. Without including lifetime effects,

DOI: 10.1021/acs.jpca.7b00635
J. Phys. Chem. A 2017, 121, 3629−3646

Table 2. Optimized Parameters of eq 4 from Analysis of Total, Primary, and Secondary Cross Sections for Collision-Induced Dissociation of $Ni^{2+}(H_2O)_x$[a]

x	reactant	product	σ_0[b]	n[b]	E_0[b] (PSL) (eV)	E_0[c] (eV)	$\Delta S^{\ddagger}_{1000}$ (J/mol K)
4(ES)	(3,1)_A[d]	(3,0)	81.7(8.0)	0.8(0.3)	1.04(0.08)	1.07(0.13)	38(25)
	(3,1)_A[e]	(2,0)	63.2(9.3)	0.8(0.2)	2.58(0.07)		43(24)
5(GS)	(5,0)[d]	(4,0)	56.7(5.9)	0.8(0.1)	1.33(0.05)	1.46(0.12)	56(26)
	(5,0)[e]	(3,0)	38.2(6.3)	0.8(0.1)	2.94(0.09)		61(34)
	(5,0)[f]	TS[2 + 2]	38.6(2.7)	0.8(0.1)	1.76(0.06)	2.96(0.08)	46(16)
5(ES)	(4,1)[d]	(4,0)	60.9(5.6)	1.1(0.2)	0.88(0.06)	0.90(0.10)	75(4)
6(GS)	(6,0)[d]	(5,0)	71.4(6.0)	0.9(0.2)	1.17(0.07)	1.39(0.08)	49(22)
	(6,0)[e]	(4,0)	95.5(8.6)	0.9(0.1)	2.65(0.06)		58(36)
	(6,0)[f]	TS[3 + 2]	47.2(5.6)	0.9(0.2)	1.46(0.07)	2.75(0.10)	44(24)
6(ES)	(4,2)[d]	(5,0)	85.1(4.3)	1.5(0.6)	0.51(0.10)	0.59(0.12)	84(31)
7	(6,1)[d]	(6,0)	66.4(7.7)	0.9(0.2)	0.86(0.06)	1.00(0.11)	53(5)
	(6,1)[e]	(5,0)	66.5(4.7)	0.9(0.1)	2.20(0.09)		60(43)
8	(6,2)[d]	(6,1)	67.3(9.5)	1.0(0.2)	0.72(0.09)	0.92(0.12)	71(12)
	(6,2)[e]	(6,0)	63.3(4.9)	1.0(0.1)	1.57(0.06)		63(49)
9	(6,3)[d]	(6,2)	73.3(5.0)	1.0(0.1)	0.51(0.07)	0.87(0.10)	50(8)
	(6,3)[e]	(6,1)	69.5(2.8)	1.1(0.1)	1.32(0.04)		63(56)
10	(6,4)_4D,2DD[d]	(6,3)	82.5(2.4)	1.0(0.1)	0.47(0.03)	0.84(0.09)	66(4)
	(6,4)_4D,2DD[e]	(6,2)	80.4(5.1)	1.0(0.1)	1.18(0.05)		46(5)
	(6,4)_5D,DD[d]	(6,3)	80.9(5.0)	1.0(0.3)	0.46(0.03)	0.84(0.06)	51(38)
11	(6,5)_4D,2DD[d]	(6,4)_4D,2DD	97.4(3.7)	1.3(0.1)	0.42(0.04)	0.95(0.06)	71(29)
	(6,5)_4D,2DD[e]	(6,3)	96.3(29.0)	1.2(0.3)	1.18(0.10)		68(29)
	(6,5)_4D,2DD[d]	(6,4)_5D,DD	97.7(3.7)	1.2(0.1)	0.41(0.05)	0.94(0.06)	66(21)

[a]Uncertainties in parentheses. [b]Parameters for modeling with lifetime effects considered. [c]Parameters for modeling where lifetime effects are not included. [d]Single channel modeling of total cross section using eq 4. [e]Sequential modeling of primary and secondary cross sections using eqs 4 × 6. [f]Competitive analysis modeling of primary water loss and charge separation cross sections using eq 4.

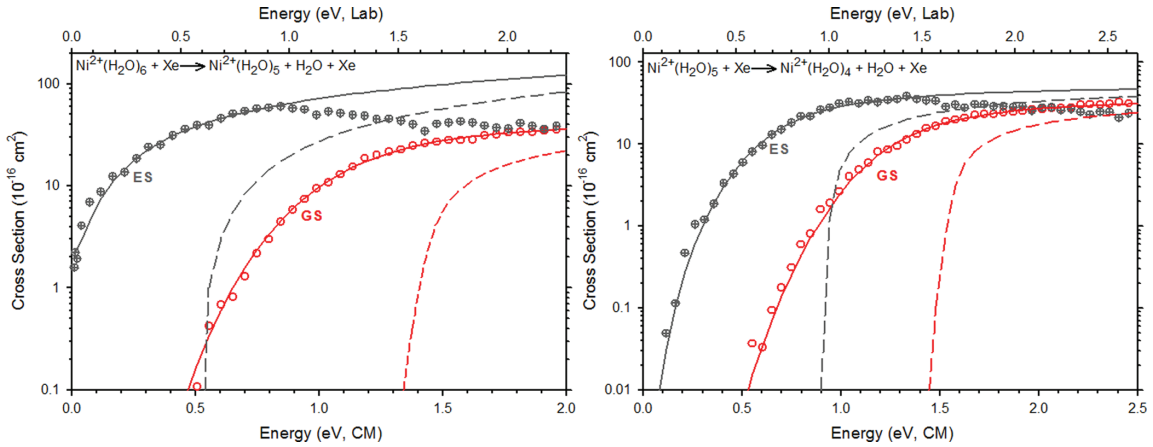

Figure 7. Analysis of zero-pressure and electrode extrapolated primary product cross sections for the excited state (ES, gray crossed circles) and ground state (GS, red circles) for collision-induced dissociation of $Ni^{2+}(H_2O)_6$ (left) and $Ni^{2+}(H_2O)_5$ (right) as a function of kinetic energy in the center-of-mass frame (bottom x-axis) and applied voltage in the laboratory frame (top x-axis). Solid lines show the best fits to the water loss cross sections convoluted over the kinetic and internal energy distributions of the neutral and ion. Dashed lines show the models in the absence of experimental kinetic energy broadening for reactants with an internal energy of 0 K. Optimized parameters for these fits are found in Table 2.

the primary threshold values are higher because of a kinetic shift that gradually increases from 0.03 eV for x = 4 to 0.53 eV for x = 11. These models reproduce the data nicely over extended energy ranges (at least 2 eV) and magnitudes (over 1 order of magnitude). This is shown in Figure 7 for x = 5 and 6 and in Figure S3 of the Supporting Information for x = 4, 7−11.

For the cases of $Ni^{2+}(H_2O)_5$ and $Ni^{2+}(H_2O)_6$, the total collision-induced dissociation cross sections for water loss from both the extrapolated ground structure (GS) and excited structure (ES) primary cross sections were modeled using eqs 3 and 4. Both sets of modeling parameters are included in Table 2. Further, our analysis of the CID of $Ni^{2+}(H_2O)_4$ is assigned to an ES species, for reasons described above.

For the GS reactant species, as the complex size increases from $Ni^{2+}(H_2O)_5$ to $Ni^{2+}(H_2O)_{11}$, the reaction thresholds for loss of a single water molecule consistently decrease. The largest decrease in consecutive GS threshold E_0 values is 0.31 eV for the x = 6 to x = 7 complexes, potentially consistent with

DOI: 10.1021/acs.jpca.7b00635
J. Phys. Chem. A 2017, 121, 3629−3646

the onset of the second solvent shell. Notably, the x = 5(ES) and 6(ES) threshold E_0 values are significantly lower than those of the GS species, as is evident in Figure 7. The reaction thresholds for the ES complexes also decrease monotonically from $Ni^{2+}(H_2O)_4$ to $Ni^{2+}(H_2O)_6$. These threshold energies are comparable to those for x = 7−11, which is consistent with the idea that these higher energy ES complexes may be assignable to structures containing a second-shell water ligand. In the case of $Ni^{2+}(H_2O)_4$, modeling parameters using several possible ES isomers are provided in Table S3 of the Supporting Information. These different isomer assumptions make little difference in the threshold energies obtained with a range of 1.04 to 1.14 eV. The (3,1)_A isomer was chosen as it provided the most positive entropy of activation, $\Delta S^{\ddagger}$, which represents the measure of looseness for the transition state for loss of water. Further, as will be seen below, the theoretical energetics for this isomer agree reasonably well with the experimental result.

To ascertain further information about all reaction pathways, we used competitive modeling procedures to obtain threshold information for the charge separation reactions 7 and 8 in competition with primary water loss channels from the corresponding thermalized reactants, x = 6 and 5, respectively. The optimum modeling parameters obtained are also listed in Table 2. The primary water loss PSL thresholds are unaffected when competing with the charge separation products. Consistent with the appearance of the CID cross sections, the competing charge separation products for reactions 7 and 8 are measured to have higher thresholds than their corresponding competing water loss products by 0.44 and 0.29 eV, respectively. These models are shown in Figure S4. Without including lifetime effects, the water loss products shift to higher threshold energies by only 0.13−0.22 eV (consistent with the loose PSL TS), whereas the charge separation products are significantly affected by lifetime and competition effects as they shift to higher thresholds by 1.2−1.3 eV (consistent with the tight TSs involved).

Thermochemical Results for Sequential Dissociation. Thermochemical results using the sequential model for analysis for x = 4−11 are also presented in Table 2. The sequential secondary water losses for all $Ni^{2+}(H_2O)_x$ complexes observed in this study were not complicated by any primary charge separation product thresholds, and thus, cross sections for primary and sequential dissociation products were simultaneously analyzed using eqs 4 and 4 × 6. The difference between the primary and secondary thresholds is used to calculate an independent measurement for the bond dissociation energy for $Ni^{2+}(H_2O)_{x-1}$ dissociating to $Ni^{2+}(H_2O)_{x-2}$ + H_2O. Figure 8 shows the sequential analysis of the GS primary and secondary cross sections for $Ni^{2+}(H_2O)_5$ and $Ni^{2+}(H_2O)_6$, as well as models of the total, primary, and secondary cross sections for $Ni^{2+}(H_2O)_8$, with those for x = 4, 7, 9−11 shown in Figure S3 of the Supporting Information. The figures show that the sequential analysis reproduces the product cross sections well over extended energy and magnitude ranges. Direct comparison of the models for the total cross sections versus the sequential models of the primary cross sections show that the analogous σ_0, n, and E_0 values are nearly identical with the threshold values within 0.03 eV in all cases. Thus, threshold energies for the primary water loss channels are basically unaffected by consideration of the secondary loss channel.

Conversion of 0 K Hydration Energies to 298 K. In all cases, the threshold energies obtained including lifetime effects

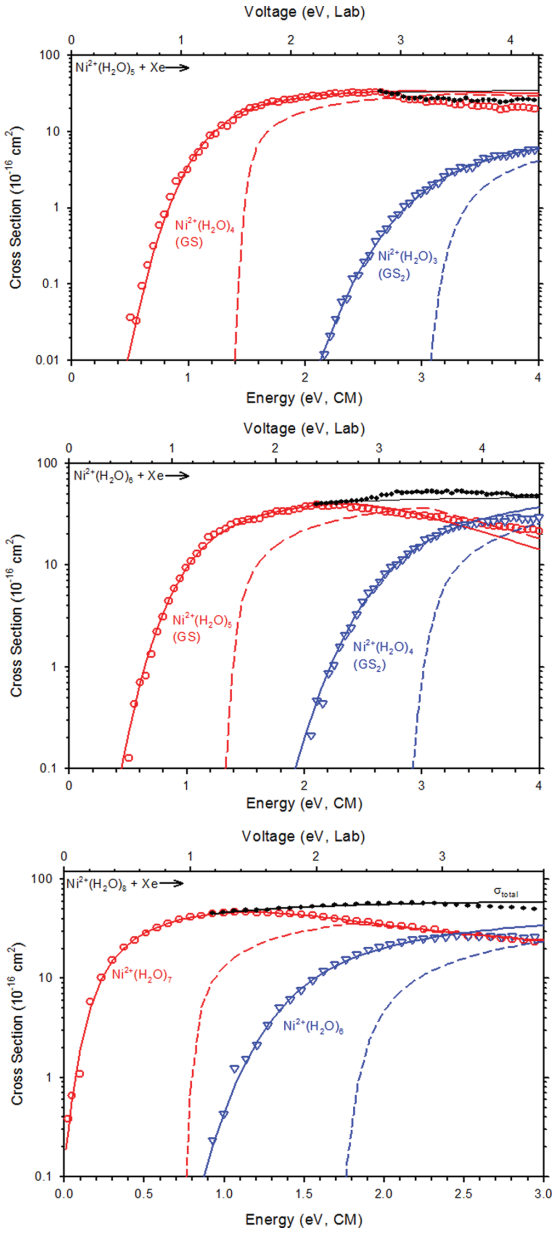

Figure 8. Zero pressure extrapolated cross sections for the CID of $Ni^{2+}(H_2O)_x$ with Xe for x = 5, 6, and 8. Solid lines show the best fits to the primary (open circles), secondary (open triangles), and total (closed circles) water loss cross sections using eqs 4 and 4 × 6 convoluted over the neutral and ion kinetic and internal energy distributions. The dashed lines show the model cross sections in the absence of experimental kinetic energy broadening for reactants with an internal energy of 0 K. Optimized parameters for these fits are found in Table 2.

are assigned as the 0 K bond energies. A rigid rotor/harmonic oscillator (RR/HO) approximation used the vibrational frequencies (scaled by 0.989) and rotational constants calculated at the B3LYP/6-311+G(d,p) level of theory to

DOI: 10.1021/acs.jpca.7b00635
J. Phys. Chem. A 2017, 121, 3629−3646

Table 3. Conversion of 0 K Thresholds to 298 K Enthalpies and Free Energies (kJ/mol) for $Ni^{2+}(H_2O)_x$[a]

x	reactant	product	ΔH_0[b]	$\Delta H_{298}-\Delta H_0$[c]	ΔH_{298}	$T\Delta S_{298}$[c]	ΔG_{298}
4(ES)	(3,1)	(3,0)	100.0(7.8)	3.3(0.7)	103.4(1.6)	33.6(3.8)	69.8(2.2)
5	(5,0)	(4,0)	128.4(5.1)	2.9(0.6)	131.3(2.3)	41.9(5.4)	89.4(3.1)
		TS[2 + 2]	140.5(6.8)	1.4(0.4)	141.9(0.5)	17.3(1.3)	124.7(2.4)
5(ES)	(4,1)	(4,0)	84.7(6.2)	5.9(0.6)	90.7(2.1)	45.6(1.2)	45.1(0.8)
6	(6,0)	(5,0)	113.1(6.6)	1.9(0.5)	115.0(0.6)	40.2(1.3)	74.8(0.8)
		TS[3 + 2]	170.2(5.7)	2.2(0.4)	172.5(0.6)	17.5(0.5)	154.6(2.1)
6(ES)	(4,2)	(5,0)	49.4(10.1)	7.9(0.5)	57.3(4.0)	46.6(6.0)	10.6(4.5)
7	(6,1)	(6,0)	83.2(4.3)	4.8(0.4)	88.0(0.4)	39.8(0.9)	48.1(0.5)
8	(6,2)	(6,1)	69.3(8.9)	4.2(0.4)	73.5(0.4)	43.3(1.0)	30.2(0.6)
9	(6,3)	(6,2)	49.3(6.3)	3.5(0.4)	52.8(0.5)	42.7(1.1)	10.1(0.7)
10	(6,4)_4D,2DD	(6,3)	45.5(2.7)	4.0(0.4)	49.6(0.4)	44.2(1.0)	5.4(0.6)
11	(6,5)_4D,2DD	(6,4)	40.4(3.5)	3.4(0.4)	43.8(0.5)	40.2(1.1)	3.6(0.7)

[a]Uncertainties in parentheses. [b]Values from Table 2. [c]Values are calculated from the vibrational frequencies and rotational constants calculated at the B3LYP/6-311+G(d,p) level of theory. Uncertainties are found by scaling the vibrational frequencies up and down by 10%.

Table 4. Comparison of Experimental,[a] Theoretical,[b] and Literature 0 K Hydration Enthalpies (kJ/mol) for $Ni^{2+}(H_2O)_x$

x	reactant	product	primary	secondary	BIRD[c]	HPMS[d]	B3LYP	B3LYP-GD3BJ	M06	MP2(full)	BPW91[e]
1	(1,0)	Ni^{2+}					428	434	423	370	472
2	(2,0)	(1,0)					340	345	346	324	347
3	(3,0)	(2,0)					224	234	225	223	222
	(2,1)	(2,0)		148 ± 8			137	143	162	122	
4	(4,0)	(3,0)		157 ± 9			177	187	191	185	[206][f]
4(ES)	(4,0) D_4	(3,0)	111 ± 6				87	97	152	80	98
4(ES)	(3,1)_A	(3,0)	100 ± 8				128	133	127	113	148
5	(5,0)	(4,0)	128 ± 5	142 ± 6			130	142	150	138	197 [139][f]
5(ES)	(4,1)	(4,0)	85 ± 6				85	92	84	80	
6	(6,0)	(5,0)	113 ± 7	129 ± 9	101 ± 4		108	121	132	118	103
6(ES)	(4,2)	(5,0)	49 ± 10				47	48	28	27	
7	(6,1)	(4,2)	83 ± 6	83 ± 5	74 ± 3		75	83	80	73	82
8	(6,2)	(6,1)	69 ± 9	78 ± 5	72 ± 3	73	78	85	84	77	82
9	(6,3)	(6,2)	49 ± 6	71 ± 5		73	74	81	80	75	74
10	(6,4)_4D,2DD	(6,3)	46 ± 3	74 ± 10		73	58	68	67	59	58
11	(6,5)_4D,2DD	(6,4)	40 ± 5			68	53	57	52	49	59
MADs[g]	primary			23	8	15	10	13	18	14	24 [14]
	secondary				15	8	11	8	11	12	16 [10]
	B3LYP						0	8	13	11	15 [11]
	MP2(full)						11	15	17	0	24 [19]

[a]Values from Table 2. [b]Theoretical values with cp correction. Single point energies calculated at the indicated level of theory using 6-311+G(2d,2p) basis set and zero point corrected. [c]Enthalpy values taken from ref 11 and adjusted to 0 K. [d]Free energy values taken from ref 12 and adjusted to 0 K. [e]BPW91/6-311+G(d,p) values taken from ref 15. [f]Bracketed values have been corrected by our excitation energy for the (3,1)_A isomer, see text. [g]Mean absolute deviations (MAD). Bracketed values include the x = 4 and 5 values corrected for (3,1)_A isomer excitation energy.

calculate $\Delta H_{298}-\Delta H_0$ and $T\Delta S_{298}$ values for dissociation. These conversion factors were used to convert the 0 K bond energies into 298 K bond enthalpies (ΔH_{298}) and to determine free energies (ΔG_{298}) of dissociation. These values are listed for $Ni^{2+}(H_2O)_x$, x = 4−11 in Table 3. The uncertainties in these conversions were obtained by scaling the vibrational frequencies up and down by 10%. It should be noted that some of the low vibrational frequencies correspond to torsional motions of the water ligands, and thus, the RR/HO approximations may not be accurate. The 298 K hydration enthalpies (ΔH_{298}) and free energies of dissociation (ΔG_{298}) track the 0 K hydration enthalpies (ΔH_0) as the values decrease monotonically with increasing number of water ligands.

Comparison of Experimental and Theoretical Bond Enthalpies for Ground Structures. Primary and secondary experimental 0 K hydration bond enthalpies for the loss of water from $Ni^{2+}(H_2O)_x$ (x = 3−11) complexes are compared in Table 4. Secondary bond enthalpies (obtained from differences between the primary and secondary thresholds) are higher than the values obtained from the corresponding primary thresholds. Specifically, the secondary bond enthalpies for x = 5(GS) and 6(GS) agree within 14−16 kJ/mol of their primary values, whereas x = 7 and 8 are nearly identical with the primary values (less than 10 kJ/mol difference) and the larger complexes x = 9 and 10 differ by larger amounts, 22 and 28 kJ/mol, respectively. Notably, the primary and secondary BDEs for x = 4 cannot be directly compared because these values are believed to correspond to different isomers. Namely, the sequential dissociation of $Ni^{2+}(H_2O)_5$ is presumed to reflect (5,0) → (4,0) + H_2O → (3,0) + $2H_2O$, whereas the primary dissociation of $Ni^{2+}(H_2O)_4$ is believed to correspond to the (3,1) → (3,0) + H_2O. This assumption can be checked via comparison with theory, as detailed below.

Table 4 also includes theoretical 0 K hydration bond enthalpies for the loss of water from $Ni^{2+}(H_2O)_x$ (x = 1−11) complexes. Theoretical values at the B3P86//B3LYP and M06-

DOI: 10.1021/acs.jpca.7b00635
J. Phys. Chem. A 2017, 121, 3629−3646

GD3//B3LYP levels and all levels without BSSE corrections can be found in Table S4 of the Supporting Information. Our experimental values agree well with B3LYP//B3LYP, B3LYP-GD3BJ//B3LYP-GD3BJ, B3P86//B3LYP (Table S4), MP2(full)//B3LYP calculated 0 K hydration enthalpies with MADs of 10−14 kJ/mol for primary water loss, as shown in Figure 9 for the B3LYP and MP2(full) values. Agreement is

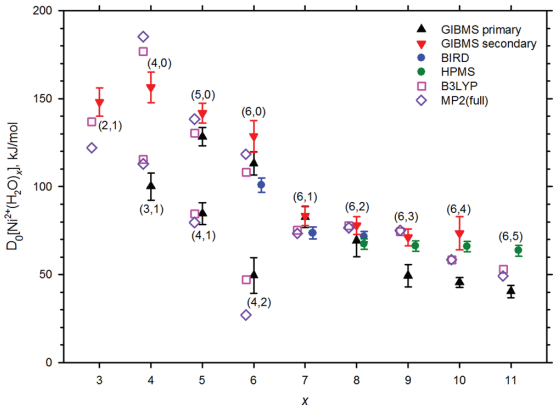

Figure 9. Comparison of experimental primary (black solid triangles) and secondary (red solid inverted triangles) 0 K bond energies with theoretical B3LYP/6-311+G(2d,2p)//B3LYP/6-311+G(d,p) (open pink squares) and MP2(full)/6-311+G(2d,2p)//B3LYP/6-311+G(d,p) values (open purple diamonds) with BSSE corrections, BIRD results from ref 11 adjusted to 0 K (solid blue circles), and HPMS free energies from ref 12 adjusted to 0 K (solid green circles). The x = 10 and 11 structure notations refer to (6,4)_4D,2DD_4AA C_2 and (6,5)_4D,2DD_AA,$2AAD_2$,$2AA_2$, respectively.

improved by 1−4 kJ/mol when BSSE corrections are included (Table S4). The M06 level of theory with and without empirical dispersion corrections has higher MAD values as this level of theory typically overestimates the BDEs across the cluster sizes. Interestingly, Table S4 shows the addition of dispersion forces to both B3LYP and M06 degrades the agreement with experiment by 2−3 kJ/mol. Examining the overall trends in Figure 9, the experimental BDEs for primary water loss decrease as the complex size increases, an almost linear trend for x = 5−9 and then flattens for x = 9−11. In comparison, the secondary and theoretical BDEs exhibit a similar decrease for x = 4−7, remain relatively constant from x = 7−9, and then the theoretical values decrease again for x = 10 and 11. Notably, the largest difference in BDEs for both experiment and theory is between x = 6 and 7, consistent with a change from the primary hydration shell to a second solvent shell.

Comparison of Experimental and Theoretical Bond Enthalpies for Excited Structures. Table 4 also includes experimental and calculated 0 K hydration bond enthalpies for the excited structures produced for $x \leq 6$. For x = 6(ES), the most reasonable agreement between experimental and theoretical bond enthalpies is for the (4,2)_3D_AA,A isomer (Table S2, Figure S1). Here B3LYP predicted values are within 2 kJ/mol of the measured bond enthalpy, whereas the M06 and MP2(full) levels are lower by ∼21 kJ/mol. The best assignment for x = 5(ES) is (4,1)_AA C_2 (Table S2, Figure S1), as theoretical values for this isomer are within 0.5−7 kJ/mol of the experimental result. As for the ground structures, BSSE corrections generally improve the agreement, although MP2(full) without BSSE agree better with the experimental value for x = 6(ES) by 10 kJ/mol. Notably, these assignments appear sufficiently good that the MADs between experiment and theory improve by ∼2 kJ/mol when the ES isomers are included.

As discussed above, there are no primary experimental values for x < 4 as these smaller complexes could not be formed in the ESI source. Also, the primary x = 4 and secondary x = 3 values are determined from analysis of the data using molecular parameters for an assumed ES isomer. Table 4 provides calculated theoretical hydration enthalpies of multiple high energy isomers for x = 4 and x = 3 for comparison to the modeled experimental values. For x = 4, Table 4 shows that the primary hydration enthalpy obtained lies between 100−111 kJ/mol depending on the reactant isomer used to model the data. Accordingly, we find the (4,0) planar and (3,1)_A (shown in Figure S1,Table S2) excited isomers compare reasonably well with these thresholds, with the (3,1)_A ES agreeing nicely with the MP2(full) calculation. We also find that the resulting secondary bond enthalpy for x = 3 (148 ± 8 kJ/mol) is significantly lower than those calculated for the (3,0) GS (222−234 kJ/mol) by 75−87 kJ/mol (Table 4), but deviates from those calculated for the higher energy (2,1)_A isomer by only 11−26 kJ/mol. Because multiple high-energy isomers were possibly present experimentally, the isomer assignments for x = 3 and 4 are clearly more speculative.

Comparison of Present and Literature Values. $Ni^{2+}(H_2O)_x$ hydration enthalpies have been previously reported by other experimental techniques for x = 6−13, as well as one theoretical study. Figure 9 and Table 4 compare our experimental and theoretical bond enthalpies at 0 K for $Ni^{2+}(H_2O)_x$ with reported experimental literature results. Williams and co-workers[16] have previously reported BIRD $Ni^{2+}(H_2O)_x$ 298 K hydration enthalpies for x = 6−8, and their reported values in Table 4 have been adjusted to 0 K using information in Table 3. Our experimental results agree within combined uncertainties with the BIRD results for x = 6−8. Notably, the x = 6 BIRD value agrees better with our primary BDE compared with the secondary BDE. Kebarle and co-workers[17,18] previously measured $Ni^{2+}(H_2O)_x$ hydration free energies at 298 K for x = 8−13 using HPMS. They then estimated hydration enthalpies at 298 K by assuming a uniform change in entropy of 96 J/mol K. Here we utilize our theoretical entropy changes listed in Table 3 (71−51 J/mol K) to correct the HPMS ΔG_{298} values to obtain more accurate 298 and 0 K hydration enthalpies. Compared to corrected HPMS results, there is excellent agreement among all three experimental bond enthalpies for x = 8. For x = 9−11, HPMS results are 24−28 kJ/mol higher than the primary GIBMS values, outside of experimental uncertainties. Interestingly, the HPMS values agree nicely with the secondary BDEs determined here. Although we firmly believe that the primary values are the best reference, one cannot rule out the possibility that the primary BDE values for these large weakly bound complexes may correspond to ions hotter than the assumed 300 K. Whereas the secondary BDEs are relative measurements, this excitation energy influences both thresholds equally such that a more accurate 0 K value is extracted.

Castro and co-workers[20] have previously performed DFT calculations on the $Ni^{2+}(H_2O)_x$ system for x = 1−24, and their results are also included in Table 4. Their calculations were at the BPW91 level of theory with 6-311+G(d,p) and 6-31G(d,p)

DOI: 10.1021/acs.jpca.7b00635
J. Phys. Chem. A 2017, 121, 3629−3646

Table 5. Comparison of 0 K Transition State Energies and Hydration Enthalpies (kJ/mol)

x	reactant	product	experiment	B3LYP[a]	B3LYP-GD3BJ[a]	B3P86[a]	M06[a]	M06-GD3[a]	MP2(full)[a]
4	(3,1)_A	(3,0)	100 ± 8[b]	132	137	138	131	132	124
	(3,1)_A	TS[2 + 1]		55	60	59	46	46	75
		$NiOH^+(H_2O)_2 + H^+H_2O$		−111	−106	−106	−109	−109	−125
5	(5,0)	(4,0)	128 ± 5[b]	134	146	139	153	156	148
		TS[2 + 2]	170 ± 6[c]	82	99	85	105	107	145
		$NiOH^+(H_2O)_2 + H^+(H_2O)_2$		−80	−61	−79	−60	−56	−2
6	(6,0)	(5,0)	113 ± 7[b]	111	124	115	135	138	129
		TS[3 + 2]	141 ± 7[c]	100	120	101	137	141	150
		$NiOH^+(H_2O)_3 + H^+(H_2O)_2$		−56	−34	−58	−23	−17	4
		TS[2 + 3]		103	129	107	151	156	183
		$NiOH^+(H_2O)_{2\ k}$		−54	−26	−51	−8	−2	39

[a]Single point energies corrected for zero point energy calculated at the indicated level of theory using 6-311+G(2d,2p) basis set with geometries and vibrational frequencies calculated at the B3LYP/6-311+G(d,p) level. [b]Values taken from Table 2 using the primary dissociation channel model. [c]Values taken from Table 2 calculated by competitive analysis model with primary water loss channel.

basis sets. They found that the formation of the inner hydration shell consisted of six water molecules binding directly to the nickel ion, except for $Ni^{2+}(H_2O)_4$, where a (3,1)_A isomer was calculated to be about 50 kJ/mol more stable than their calculated square planar (4,0) D_4 cluster. They apparently did not locate the seesaw (4,0) conformation found to be the GS in this study (46−70 kJ/mol more stable at 298 K than (3,1)_A, and 38−108 kJ/mol more stable than (4,0) D_4, Table 1). Except for the x = 4 and 5 values (where the (3,1)_A isomer was the assumed reactant and product, respectively), their BPW91 dissociation enthalpies agree well with our DFT calculated values, whereas the MP2(full) values are almost consistently lower than BPW91, in particular, the MADs for x = 2, 3, 6−11 are less than 10 kJ/mol. If we correct their values for x = 4 and 5 by our calculated excitation energy of ∼43 kJ/mol, the MAD for x = 1−11 becomes 11 kJ/mol compared to our B3LYP calculations. Comparing our experimental values for primary water loss to their BPW91 calculated values, we find good agreement particularly for x = 6 and 7 values (within 10 kJ/mol). Overall, the MADs for primary and secondary water loss compared to the BPW91 values are 24 and 16 kJ/mol, respectively. If the x = 4 and 5 values are corrected by our calculated excitation energies, the MADs improve to 14 and 10 kJ/mol, respectively.

Charge Separation: Energetic Barriers. Table 5 presents the predicted barrier heights for the charge separation (CS) of $Ni^{2+}(H_2O)_x$, where x = 4−6, corresponding to reactions 7−10. The structures of each of the rate-limiting transition states are shown in Figure S5 of the Supporting Information, and, in each case, correspond to heterolytic cleavage of an O−H bond leading to the incipient products. The dominant CS channel of $Ni^{2+}(H_2O)_6$ is $NiOH^+(H_2O)_3 + H^+(H_2O)_2$, which occurs through the TS[3 + 2] transition state (where the numbers in brackets refer to the number of water ligands in the products). Theory finds that this barrier height is 100−150 kJ/mol. Here, the experimental value of 141 ± 7 kJ/mol agrees best with M06 and MP2 results. The alternative CS channel forming $NiOH^+(H_2O)_2 + H^+(H_2O)_3$ occurs through TS[2 + 3], predicted to be slightly higher with barrier heights of 103−183 kJ/mol (3−33 kJ/mol above TS[3 + 2]). Notably, the reverse Coulomb barriers for each of these channels are nearly equivalent to each other, ∼157 kJ/mol for DFT levels of theory and ∼145 kJ/mol for MP2(full), consistent with the largely electrostatic origins of the Coulomb barrier.

For x = 5, the predicted TS[2 + 2] barriers range from 82−145 kJ/mol, compared to an experimental value of 170 ± 6 kJ/mol, with the MP2 result agreeing the best. Interestingly, the TS[2 + 2] predicted barrier height is smaller than that for TS[2 + 3] and comparable to TS[3 + 2] at the MP2 level. The reverse Coulomb barrier is again comparable to those for x = 5. For x = 4, the experimental reactant is believed to be the (3,1)_A isomer such that barriers are tabulated relative to this species. The predicted barrier heights for TS[2 + 1] are relatively consistent for all levels of theory at 46−75 kJ/mol. Here, the Coulomb barrier is about the same as the larger systems for the various DFT calculations, near 160 kJ/mol, but larger at the MP2(full) level, 200 kJ/mol. In previous studies of the hydrated Fe^{2+}, Zn^{2+}, and Cd^{2+} systems, the reverse Coulomb barriers generally decreased as x increased, more consistent with the MP2(full) results here.[9,13,15]

Comparison of Water Loss and Charge Separation Energetics: x = 5−6. Experimental and theoretically predicted energies for water loss dissociation pathways are compared to those for the barrier heights of the charge separation pathway TSs in Table 5. For the x = 6 complex, B3 DFT levels of theory predict the TS[3 + 2] barrier height to be lower in energy than the single water loss BDE by 4−14 kJ/mol, with the higher energy TS[2 + 3] lying 8 kJ/mol below to 5 kJ/mol above water loss. In contrast, the M06 and MP2(full) levels calculate that water loss is the lowest energy pathway by 2−21 kJ/mol compared to TS[3 + 2] and by 16−54 kJ/mol compared to TS[2 + 3]. These latter predictions are consistent with our experimental observations, Figure 4b, where the apparent threshold of the $NiOH^+(H_2O)_3$ product in reaction 7 is ∼1 eV higher in energy compared to the water loss product. Modeling of these processes to include the effects of competition between these two channels shows that the threshold for charge separation is only 28 ± 7 kJ/mol higher than that for water loss (Table 5), in reasonable agreement with the MP2(full) difference of 21 kJ/mol.

For x = 5, DFT levels of theory predict the barrier height of TS[2 + 2] to be lower in energy than the water loss BDE by 47−54 kJ/mol, whereas the MP2(full) level predicts a much higher barrier height for reaction 8, such that there is only a 3 kJ/mol energetic preference for CS over water loss dissociation pathway. As discussed above, the experimental results of Figure 5b suggest that reaction 8 is enthalpically disfavored over reaction 1, in better agreement with the MP2(full) predictions. Here, modeling of the data suggests that the threshold for

DOI: 10.1021/acs.jpca.7b00635
J. Phys. Chem. A 2017, 121, 3629−3646

charge separation is 42 ± 6 kJ/mol higher than that for water loss.

In an effort to address the experimental observation that excited isomers of x = 4−6 complexes do not readily undergo the charge separation reactions, we thoroughly explored the complete potential energy surfaces for decomposition of $Ni^{2+}(H_2O)_5$. Reaction coordinate pathways for $Ni^{2+}(H_2O)_5$ GS decomposing by both water loss and charge separation to $NiOH^+(H_2O)_2 + H^+(H_2O)_2$ (reaction 8) are shown in Figures S6 and S7, where these utilize singly (A) and doubly (AA) coordinated outer shell water ligands, respectively. The latter pathway proceeds through the excited (4,1)_AA isomer (ES), but is higher in energy than the former pathway. Ultimately, both GS and ES reactants must pass over the same rate-limiting TSs for charge separation and for water loss, such that the only difference comes from the different density of states of the two reactants (denominator in eq 5). Because the (4,1)_AA ES must have a lower density of states compared to the (5,0) GS, the rate of decomposition of the ES should be higher than that of the GS such that we might have expected the ES to decompose via both pathways more readily, in contrast to our observations, Figure 5a. One possible explanation is a dynamical one that hypothesizes that the second shell water ligand of (4,1)_AA (ES) provides a larger collision cross section compared to the more compact (5,0) structure. Collisions at larger impact parameters with the ES will preferentially excite this ligand leading to direct water loss, whereas smaller impact parameters leading to more general vibrational excitation are needed for the system to explore the tight TSs leading to charge separation.

The experimental cross sections show that charge separation occurs at x = 4−6. From the previous definition of critical size, the maximum x at which CS and water loss become competitive, we would assign x_{crit} = 6. Modeling of these processes show that the CS processes are energetically disfavored over water loss for x = 5 and 6, whereas Figure 5b suggests the opposite is true for x = 4, such that the energetic definition of critical size would assign x_{crit} = 4. This assignment is in agreement with theory where the barrier height for TS[2 + 1] is predicted to be lower than water loss by all levels of theory including MP2 (Table 5) and corresponds with the conclusions of the HPMS studies by Kebarle and co-workers.[18] A value of x_{crit} = 4 would also explain why we could never generate ground state complexes of $Ni^{2+}(H_2O)_x$ smaller than x = 5, as fragmentation of the larger complexes would preferentially lead to charge separation products rather than water loss.

CONCLUSION

The kinetic energy-dependent cross sections for collision-induced dissociation of $Ni^{2+}(H_2O)_x$ complexes where x = 4−11 are determined using guided ion beam tandem mass spectrometry. The dominant CID pathway in all systems observed is the loss of a single water molecule from the reactant ion followed by sequential losses of additional water ligands. We observe through experiment and theory that the bond dissociation energies progressively increase as each water molecule is removed from a hydrated nickel dication complex. Charge separation processes are also observed as higher energy product pathways, but are not competitive with primary or secondary water loss, with evidence suggesting that the critical size for competition between these two processes is probably at x_{crit} = 4. These studies also made liberal use of in-source fragmentation electrodes, which proved advantageous as we could tune the conditions of the reactant ions to control the population of higher or lower energy reactant ion isomers present. Utilizing this fragmentation method, the CID data under different source conditions allowed for extrapolation to both ground and excited isomer cross sections, such that modeling yielded reaction thresholds for both isomers.

Our experimental results for the $Ni^{2+}(H_2O)_x$ (x = 6−8) systems agree with other experimental techniques.[16−18] For larger complexes (x = 9−11), our primary BDEs fall below HPMS results, potentially because thermalization of the larger complexes may not be complete. Over this range, both our results and the HPMS results vary within a few kJ/mol as x increases, suggesting these water ligands bind to the inner hydration shell in a similar fashion. Our theoretical calculations of geometries and energetics for the $Ni^{2+}(H_2O)_x$ (x = 1−11) find unambiguously that six water molecules bind directly to the nickel ion, leading to a coordination number of 6, which agrees with conclusions of previous theoretical work[20] and is consistent with the present experimental findings. As the number of water ligands increases past the coordination number, the second solvent shell waters prefer to hydrogen bond to pairs of the inner shell water molecules as double acceptors in similar structural motifs. In comparison with our experiment, the present theoretical results indicate that accurate calculations of the binding energies are best represented by B3LYP/6-311+G(2d,2p)//B3LYP/6-311+G(d,p) and MP2(full)/6-311+G(2d,2p)//B3LYP/6-311+G(d,p) calculations including counterpoise corrections. Additionally, modeling of the charge separation pathways indicates that MP2(full) theory more accurately predicts the experimentally observed CID pathways and relative energetics of the $Ni^{2+}(H_2O)_x$ systems compared to DFT methods employed in this study.

ASSOCIATED CONTENT

Supporting Information

The Supporting Information is available free of charge on the ACS Publications website at DOI: 10.1021/acs.jpca.7b00635.

Overview of theoretical results and additional geometries (PDF)

AUTHOR INFORMATION

ORCID

P. B. Armentrout: 0000-0003-2953-6039

Notes

The authors declare no competing financial interest.

ACKNOWLEDGMENTS

This work is supported by the National Science Foundation, Grant CHE-1359769. In addition, we thank the Center for High Performance Computing (CHPC) at the University of Utah for the generous allocation of computing time.

REFERENCES

(1) Sigel, A. S. H.; Sigel, R. K. O. *Nickel and Its Surprising Impact in Nature*, 2 ed.; John Wiley & Sons, Ltd.: Chichester, U.K., 2008.

(2) EPA. Clean Water Act. In *Appendix A to Part 423 - 126 Priority Pollutants*; Agency, U. S. E. P., 2014; Vol. *29*.

(3) Coogan, T. P.; Latta, D. M.; Snow, E. T.; Costa, M.; Lawrence, A. Toxicity and Carcinogenicity of Nickel Compounds. *Crit. Rev. Toxicol.* **1989**, *19*, 341−384.

DOI: 10.1021/acs.jpca.7b00635
J. Phys. Chem. A 2017, 121, 3629−3646

(4) Carl, D. R.; Armentrout, P. B. Threshold Collision-Induced Dissociation of Hydrated Magnesium: Experimental and Theoretical Investigation of the Binding Energies for $Mg^{2+}(H_2O)_x$ complexes (x = 2 − 10). *ChemPhysChem* **2013**, *14*, 681−697.
(5) Carl, D. R.; Moision, R. M.; Armentrout, P. B. Binding Energies for the Inner Hydration Shells of Ca^{2+}: An Experimental and Theoretical Investigation of $Ca^{2+}(H_2O)_x$ Complexes (x = 5 − 9). *Int. J. Mass Spectrom.* **2007**, *265*, 308−325.
(6) Carl, D. R.; Armentrout, P. B. Experimental Investigation of The Complete Inner Shell Hydration Energies of Ca^{2+}: Threshold Collision-Induced Dissociation of $Ca^{2+}(H_2O)_x$ Complexes (x = 2 − 8). *J. Phys. Chem. A* **2012**, *116*, 3802−3815.
(7) Carl, D. R.; Chatterjee, B. K.; Armentrout, P. B. Threshold Collision-Induced Dissociation of $Sr^{2+}(H_2O)_x$ Complexes (x = 1 − 6): An Experimental and Theoretical Investigation of the Complete Inner Shell Hydration Energies of Sr^{2+}. *J. Chem. Phys.* **2010**, *132*, 1−12.
(8) Wheeler, O. W.; Carl, D. R.; Hofstetter, T. E.; Armentrout, P. B. Hydration Enthalpies of $Ba^{2+}(H_2O)_x$, x = 1−8: A Threshold Collision-Induced Dissociation and Computational Investigation. *J. Phys. Chem. A* **2015**, *119*, 3800−15.
(9) Hofstetter, T. E.; Armentrout, P. B. Threshold Collision-Induced Dissociation and Theoretical Studies of Hydrated Fe(II): Binding Energies and Coulombic Barrier Heights. *J. Phys. Chem. A* **2013**, *117*, 1110−1123.
(10) Armentrout, P. B.; Sweeney, A. F. Hydrated Copper Ion Chemistry: Guided Ion Beam and Computational Investigation of $Cu^{2+}(H_2O)_n$ (n = 7−10) Complexes. *Eur. Mass Spectrom.* **2015**, *21*, 497−516.
(11) Sweeney, A. F.; Armentrout, P. B. Guided Ion Beam Studies of the Collision-Induced Dissociation of $CuOH^+(H_2O)_n$ (n = 1- 4): Comprehensive Thermodynamic Data for Copper Ion Hydration. *J. Phys. Chem. A* **2014**, *118*, 10210−10222.
(12) Cooper, T. E.; Carl, D. R.; Armentrout, P. B. Hydration Energies of Zinc (II): Threshold Collision-Induced Dissociation Experiments and Theoretical Studies. *J. Phys. Chem. A* **2009**, *113*, 13727−13741.
(13) Cooper, T. E.; Armentrout, P. B. An Experimental and Theoretical Investigation of the Charge Separation Energies of Hydrated Zinc (II): Redefinition of the Critical Size. *J. Phys. Chem. A* **2009**, *113*, 13742−13751.
(14) Cooper, T. E.; Armentrout, P. B. Threshold Collision-induced Dissociation of Hydrated Cadmium (II): Experimental and Theoretical Investigation of the Binding Energies for $Cd^{2+}(H_2O)_n$ Complexes (n = 4 − 11). *Chem. Phys. Lett.* **2010**, *486*, 1−6.
(15) Cooper, T. E.; Armentrout, P. B. Sequential Bond Energies and Barrier Heights for the Water Loss and Charge Separation Dissociation Pathways of $Cd^{2+}(H_2O)_n$, n = 3−11. *J. Chem. Phys.* **2011**, *134*, 114308.
(16) Rodriguez-Cruz, S. E.; Jockusch, R. A.; Williams, E. R. Hydration Energies of Divalent Metal Ions, $Ca^{2+}(H_2O)_n$ (n = 5 - 7) and $Ni^{2+}(H_2O)_n$ (n = 6 - 8), Obtained by Blackbody Infrared Radiative Dissociation. *J. Am. Chem. Soc.* **1998**, *120*, 5842−5843.
(17) Blades, A. T.; Jayaweera, P.; Ikonomou, M. G.; Kebarle, P. Studies of Alkaline-Earth and Transition-Metal M^{+2} Gas-Phase Ion Chemistry. *J. Chem. Phys.* **1990**, *92*, 5900−5906.
(18) Blades, A. T.; Jayaweera, P.; Ikonomou, M. G.; Kebarle, P. Ion−Molecule Clusters Involving Doubly Charged Metal-Ions (M^{2+}). *Int. J. Mass Spectrom. Ion Processes* **1990**, *102*, 251−267.
(19) O'Brien, J. T.; Williams, E. R. Coordination Numbers of Hydrated Divalent Transition Metal Ions Investigated with IRPD Spectroscopy. *J. Phys. Chem. A* **2011**, *115*, 14612−9.
(20) Bustamante, M.; Valencia, I.; Castro, M. Theoretical Study of $[Ni(H_2O)_n]^{2+}(H_2O)_m$ (n < /= 6, m < /= 18). *J. Phys. Chem. A* **2011**, *115*, 4115−34.
(21) Shvartsburg, A. A.; Siu, K. W. M. Is There a Minimum Size for Aqueous Doubly Charged Metal Cations? *J. Am. Chem. Soc.* **2001**, *123*, 10071−10075.
(22) Jayaweera, P.; Blades, A. T.; Ikonomou, M. G.; Kebarle, P. Production and Study in the Gas-Phase of Multiply Charged Solvated or Coordinated Metal-Ions. *J. Am. Chem. Soc.* **1990**, *112*, 2452−2454.
(23) Muntean, F.; Armentrout, P. B. Guided Ion Beam Study of Collision-Induced Dissociation Dynamics: Integral and Differental Cross Sections. *J. Chem. Phys.* **2001**, *115*, 1213−1228.
(24) Ervin, K. M.; Armentrout, P. B. Translational Energy Dependence of $Ar^+ + XY \rightarrow ArX^+ + Y$ (XY = H_2, D_2, HD) from Thermal to 30 eV c.m. *J. Chem. Phys.* **1985**, *83*, 166−189.
(25) Moision, R. M.; Armentrout, P. B. An Electrospray Source for Thermochemical Investigation with the Guided Ion Beam Mass Spectrometer. *J. Am. Soc. Mass Spectrom.* **2007**, *18*, 1124−1134.
(26) Shaffer, S. A.; Prior, D. C.; Anderson, G. A.; Udseth, H. R.; Smith, R. D. An Ion Funnel Interface for Improved Ion Focusing and Sensitivity Using Electrospray Ionization Mass Spectrometry. *Anal. Chem.* **1998**, *70*, 4111−4119.
(27) Kim, T.; Tang, K.; Udseth, H. R.; Smith, R. D. A Multicapillary Inlet Jet Disruption Electrodynamic Ion Funnel Interface for Improved Sensitivity Using Atmospheric Pressure Ion Sources. *Anal. Chem.* **2001**, *73*, 4162−4170.
(28) Carl, D. R.; Moision, R. M.; Armentrout, P. B. In-Source Fragmentation Technique for the Production of Thermalized Ions. *J. Am. Soc. Mass Spectrom.* **2009**, *20*, 2312−2317.
(29) Cooper, T. E.; O'Brien, J. T.; Williams, E. R.; Armentrout, P. B. Zn^{2+} Has a Primary Hydration Sphere of Five: IR Action Spectroscopy and Theoretical Studies of Hydrated Zn^{2+} Complexes. *J. Phys. Chem. A* **2010**, *114*, 12646−12655.
(30) Ye, S. J.; Armentrout, P. B. Absolute Thermodynamic Measurements of Alkali Metal Cation Interactions with a Simple Dipeptide and Tripeptide. *J. Phys. Chem. A* **2008**, *112*, 3587−3596.
(31) Gerlich, D. Inhomogeneous rf Fields: A Versatile Tool for the Study of Processes with Slow Ions. *Adv. Chem. Phys.* **1992**, *82*, 1−176.
(32) Aristov, N.; Armentrout, P. B. Collision-Induced Dissociation of Vanadium Monoxide Ion. *J. Phys. Chem.* **1986**, *90*, 5135−5140.
(33) Dalleska, N. F.; Honma, K.; Sunderlin, L. S.; Armentrout, P. B. Solvation of Transition Metal Ions by Water. Sequential Binding Energies of $M^+(H_2O)_x$ (x = 1 - 4) for M = Ti - Cu Determined by Collision-Induced Dissociation. *J. Am. Chem. Soc.* **1994**, *116*, 3519−3528.
(34) Daly, N. R. Scintillation Type Mass Spectrometer Ion Detector. *Rev. Sci. Instrum.* **1960**, *31*, 264−267.
(35) Hales, D. A.; Lian, L.; Armentrout, P. B. Collision-Induced Dissociation of Nb_n^+ (n = 2 - 11): Bond Energies and Dissociation Pathways. *Int. J. Mass Spectrom. Ion Processes* **1990**, *102*, 269−301.
(36) Schultz, R. H.; Crellin, K. C.; Armentrout, P. B. Sequential Bond Energies of $Fe(CO)_x^+$ (x = 1 - 5): Systematic Effects on Collision-Induced Dissociation Measurements. *J. Am. Chem. Soc.* **1991**, *113*, 8590−8601.
(37) Beyer, T. S.; Swinehart, D. F. Number of Multiply-Restricted Partitions. *Commun. ACM* **1973**, *16*, 379.
(38) Stein, S. E.; Rabinovitch, B. S. On the Use of Exact State Counting Methods in RRKM Rate Calculations. *Chem. Phys. Lett.* **1977**, *49*, 183−188.
(39) Stein, S. E.; Rabinovitch, B. S. Accurate Evaluation of Internal Energy Level Sums and Densities Including Anharmonic Oscillators and Hindered Rotors. *J. Chem. Phys.* **1973**, *58*, 2438−2445.
(40) Gilbert, R. G.; Smith, S. C. *Theory of Unimolecular and Recombination Reactions*; Blackwell Scientific: London, 1990.
(41) Holbrook, K. A.; Pilling, M. J.; Robertson, S. H. *Unimolecular Reactions*, 2nd ed.; Wiley: New York, 1996.
(42) Truhlar, D. G.; Garrett, B. C.; Klippenstein, S. J. Current Status of Transition-State Theory. *J. Phys. Chem.* **1996**, *100*, 12771−12800.
(43) Rodgers, M. T.; Ervin, K. M.; Armentrout, P. B. Statistical Modeling of Collision-Induced Dissociation Thresholds. *J. Chem. Phys.* **1997**, *106*, 4499−4508.
(44) Rodgers, M. T.; Armentrout, P. B. Statistical Modeling of Competitive Threshold Collision-Induced Dissociation. *J. Chem. Phys.* **1998**, *109*, 1787−1800.

DOI: 10.1021/acs.jpca.7b00635
J. Phys. Chem. A 2017, 121, 3629−3646

(45) Armentrout, P. B.; Simons, J. Understanding Heterolytic Bond Cleavage. *J. Am. Chem. Soc.* **1992**, *114*, 8627−8633.
(46) Armentrout, P. B. Statistical Modeling of Sequential Collision-induced Dissociation. *J. Chem. Phys.* **2007**, *126*, 234302.
(47) Dalleska, N. F.; Honma, K.; Armentrout, P. B. Stepwise Solvation Enthalpies of Protonated Water Clusters: Collision Induced Dissociation as an Alternative to Equilibrium Studies. *J. Am. Chem. Soc.* **1993**, *115*, 12125−12131.
(48) Moision, R. M.; Armentrout, P. B. An Experimental and Theoretical Dissection of Sodium Cation/Glycine Interactions. *J. Phys. Chem. A* **2002**, *106*, 10350−10362.
(49) Frisch, M. J.; Trucks, G. W.; Schlegel, H. B.; Scuseria, G. E.; Robb, M. A.; Cheeseman, J. R.; Scalmani, G.; Barone, V.; Mennucci, B.; Petersson, G. A.; Nakatsuji, H.; Caricato, M.; Li, X.; Hratchian, H. P.; Izmaylov, A. F.; Bloino, J.; Zheng, G.; Sonnenberg, J. L.; Hada, M.; Ehara, M.; Toyota, K.; Fukuda, R.; Hasegawa, J.; Ishida, M.; Nakajima, T.; Honda, Y.; Kitao, O.; Nakai, H.; Vreven, T.; Montgomery, J. A.; Peralta, J. E.; Ogliaro, F.; Bearpark, M.; Heyd, J. J.; Brothers, E.; Kudin, K. N.; Staroverov, V. N.; Kobayashi, R.; Normand, J.; Raghavachari, K.; Rendell, A.; Burant, J. C.; Millam, J. M.; Iyengar, S. S.; Tomasi, J.; Cossi, M.; Rega, N.; Millam, J. M.; Klene, M.; Knox, J. E.; Cross, J. B.; Bakken, V.; Adamo, C.; Jaramillo, J.; Gomperts, R.; Stratmann, R. E.; Yazyev, O.; Austin, A. J.; Cammi, R.; Pomelli, C.; Ochterski, J. W.; Martin, R. L.; Morokuma, K.; Zakrzewski, V. G.; Voth, G. A.; Salvador, P.; Dannenberg, J. J.; Dapprich, S.; Daniels, A. D.; Farkas, O.; Foresman, J. B.; Ortiz, J. V.; Cioslowski, J.; Fox, D. J. *Gaussian 09*, Revision A.02; Gaussian Inc.: Pittsburgh, PA, 2009.
(50) Becke, A. D. Density-Functional Thermochemistry. III. The Role of Exact Exchange. *J. Chem. Phys.* **1993**, *98*, 5648−5652.
(51) Ditchfield, R.; Hehre, W. J.; Pople, J. A. Self-Consistent Molecular-Orbital Methods. IX. An Extended Gaussian-Type Basis for Molecular-Orbital Studies of Organic Molecules. *J. Chem. Phys.* **1971**, *54*, 724−728.
(52) Grimme, S.; Ehrlich, S.; Goerigk, L. Effect of the Damping Function in Dispersion Corrected Density Functional Theory. *J. Comput. Chem.* **2011**, *32*, 1456−65.
(53) Bauschlicher, C. W.; Partridge, H. A Modification of the Gaussian-2 Approach Using Density Functional Theory. *J. Chem. Phys.* **1995**, *103*, 1788−91.
(54) Perdew, J. P. Density-functional Approximation for the Correlation Energy of the Inhomogeneous Electron Gas. *Phys. Rev. B: Condens. Matter Mater. Phys.* **1986**, *33*, 8822−8824.
(55) Zhao, Y.; Truhlar, D. G. The M06 Suite of Density Functionals for Main Group Thermochemistry, Thermochemical Kinetics, Noncovalent Interactions, Excited States, and Transition Elements: Two New Functionals and Systematic Testing of Four M06-Class Functionals and 12 Other Functionals. *Theor. Chem. Acc.* **2008**, *120*, 215−241.
(56) Möller, C.; Plesset, M. S. Note on an Approximation Treatment for Many-Electron Systems. *Phys. Rev.* **1934**, *46*, 618−622.
(57) Boys, S. F.; Bernardi, R. The Calculation of Small Molecular Interactions by the Differences of Separate Total Energies. Some Procedures with Reduced Errors. *Mol. Phys.* **1970**, *19*, 553−566.
(58) van Duijneveldt, F. B.; van Duijneveldt-van de Rijdt, J. G. C. M.; van Lenthe, J. H. State of the Art in Counterpoise Theory. *Chem. Rev.* **1994**, *94*, 1873−1885.

DOI: 10.1021/acs.jpca.7b00635
J. Phys. Chem. A 2017, 121, 3629−3646

CHAPTER 4

BINDING ENERGIES OF HYDRATED COBALT(II) BY COLLISION-INDUCED DISSOCIATION AND THEORETICAL STUDIES: EVIDENCE FOR A NEW CRITICAL SIZE

4.1 Abstract

The experimental sequential bond energies for loss of water from $Co^{2+}(H_2O)_x$ complexes, $x = 5 – 11$, are determined by threshold collision-induced dissociation (TCID) using a guided ion beam tandem mass spectrometer with a thermal electrospray ionization source. Kinetic energy dependent TCID cross sections are analyzed to yield 0 K thresholds for sequential loss of neutral water molecules. The thresholds are converted from 0 to 298 K values to give hydration enthalpies and free energies. Theoretical geometry optimizations and single point energy calculations at several levels of theory are performed for the reactant and product ion complexes. Theoretical bond energies for ground structures are used for direct comparison with experimental values to obtain structural information on these complexes. In addition, the dissociative charge separation process, $Co^{2+}(H_2O)_x \rightarrow CoOH^+(H_2O)_m + H^+(H_2O)_{x-m-1}$, is observed at $x = 4$, 6 and 7 in competition with primary water loss products. Energies for the charge separation rate-limiting transition states are calculated and compared to experimental threshold

measurements. Results suggest that the critical size for charge separation is $x_{crit} = 6$, in contrast to lower values in previous literature reports.

4.2 Introduction

Transition metals play important roles in many chemical and biological systems. Although metals can be essential for life, they can also become toxic in high concentrations from excessive intake. Humans mainly obtain transition metals from the environment through breathing air, drinking water, and eating food that contains such metals. As such, metal ion interactions with these media have become the subject of extensive research in order to understand the fundamentals of these intermolecular interactions. For the past several years, the Armentrout group has studied the thermochemistry of the hydration of many transition metal dications, $M^{2+}(H_2O)_x$ where M = Fe,[1] Ni,[2] Cu,[3] Zn,[4-5] and Cd,[6-7] and $MOH^+(H_2O)_x$ where M = Co[8] and Cu[9] in the gas-phase using threshold collision-induced dissociation (TCID) complemented by theoretical calculations. Such thermochemistry has also been explored by several other research groups using different techniques including blackbody infrared radiative dissociation,[10-11] collision induced dissociation,[12-14] and ion equilibria.[15-17]

The present study extends our TCID studies to complete the late 3d transition metal dication hydration energies by examining the sequential dissociation of $Co^{2+}(H_2O)_x$ complexes, where $x = 5 – 11$. Understanding the hydration of Co^{2+} is vital as cobalt is an essential element for life, e.g., the core of vitamin B12,[18] yet can be toxic if consumed in excess of 1 mg/kg.[19] In agreement with our previous $M^{2+}(H_2O)_x$ studies, the dominant

process observed upon activation of the cobalt complexes studied is reaction 4.1, loss of a single water ligand,

$$M^{2+}(H_2O)_x \rightarrow M^{2+}(H_2O)_{x-1} + H_2O \quad (4.1)$$

followed by sequential loss of additional water molecules. In addition, $M^{2+}(H_2O)_x$ complexes of particular sizes that depend on the metal identity are found to undergo dissociative charge separation processes, reactions 4.2.

$$M^{2+}(H_2O)_x \rightarrow MOH^{+}(H_2O)_m + H^{+}(H_2O)_{x-m-1} \quad (4.2)$$

Some interest in reaction 4.2 has focused on determining the minimum size at which water loss is favored over charge separation. This critical size, x_{crit}, has been defined as "the maximum number of ligands at which dissociative charge transfer is competitive with simple ligand loss."[14] For hydrated cobalt dications, Kebarle and coworkers reported that the largest complex size for which dissociative charge separation occurred was a lower limit of 4,[12,16-17] whereas Shvartzburg and Siu suggested $x_{crit} = 5$.[14] By more precisely defining the critical size as "the largest value of x at which the charge separation is energetically favored over the loss of one water ligand,"[5] previous studies in our laboratory have determined the energy-dependent x_{crit} for late 3d transition metals: 4 for Fe^{2+},[1] 4 for Ni^{2+},[2] 8 for Cu^{2+},[3] and 7 for Zn^{2+}.[5] As will be shown below, the present study determines x_{crit} for $Co^{2+}(H_2O)_x$ using the energy-dependent definition as $x_{crit} = 6$.

As detailed below, TCID experiments with complementary theoretical calculations are used in the present work to establish hydration energies and the threshold energies for charge separation, which allows identification of the critical size and coordination number (CN) of hydrated Co^{2+}. In contrast to our previous hydrated 3d

transition metal dication studies,[1-7] the present work shows evidence for $Co^{2+}(H_2O)_x$ complexes in which H_2O molecules start to occupy the second shell even though the first shell is not completely closed. Such detailed understanding of the hydration structure, aqueous reactivity, and periodic trends of transition metals can provide insight into the roles and transport of these metals in biological systems.

4.3 Experimental and Computational Methods

4.3.1 Experimental procedures. Cross sections for the CID of hydrated cobalt dication complexes are measured using a guided ion beam tandem mass spectrometer (GIBMS), which has been described in detail previously.[20-21] The hydrated cobalt dications, $Co^{2+}(H_2O)_x$, are created from a 10^{-4} M solution of $CoCl_2$ in pure water using an electrospray ionization (ESI) source.[22] The solution is pumped through a stainless steel needle at a low flow rate of 0.08 – 0.10 L/h and an applied voltage of 2.0 – 2.2 kV. Ions then enter the vacuum system through an inlet cap and drift through a capillary heated to 80 °C to promote desolvation of large droplets. The ions that emerge from the capillary are collected and focused into an 88 plate radiofrequency (rf) ion funnel (IF),[23] with a DC gradient typically 8 – 12 V. Ions are injected from the IF into an rf-only hexapole ion guide (6P) that traps the ions in the radial direction with an rf amplitude of 250 V peak-to-peak. An in-source fragmentation technique utilizing negatively biased dc electrodes in between the hexapole rods, as described in detail elsewehere,[24] was used to effectively enhance the signal intensity of smaller $M^{2+}(H_2O)_x$ complexes by fragmenting larger complexes. However, increasing the voltage beyond the peak intensity for the $x = 5$ complex resulted primarily in dissociation to form charge separation products rather than

water loss. This phenomenon was also seen previously for $Ni^{2+}(H_2O)_x$,[2] $Cu^{2+}(H_2O)_x$,[3] and $Zn^{2+}(H_2O)_x$ complexes.[4] It has been postulated this is partly a result of the relatively high second ionization energies (IEs) for these late 3d transition metals, 17.1 – 20.3 eV.[25] As a result, we were unable to create $Co^{2+}(H_2O)_x$ complexes where $x \leq 4$ with appreciable intensity for further study. Once past the electrodes, the ions undergo $>10^4$ collisions with ambient gas as they drift through the hexapole ion guide. Previous studies have shown that under the proper conditions, the ions emerging from the hexapole are thermalized to room temperature.[2,6,24,26-30] To further investigate the thermalization of the ions, a 5.1 cm long nitrogen gas cell that surrounds the hexapole (15.2 cm total length) starting 2.5 cm from the inlet was added to the ESI/IF/6P source. Various pressures of nitrogen gas were added to the cell to alter the thermalization conditions, but no changes in the cross sections for $Co^{2+}(H_2O)_x$, where $x = 5$ and 6, were observed.

The ions generated and thermalized in the source were extracted from the hexapole ion guide and focused into a magnetic sector momentum analyzer for mass selection of the reactant ion. These reactant ions were then decelerated to a known kinetic energy and injected into an rf octopole ion guide[31] where the ions were trapped radially and passed through a collision gas cell containing Xe at varying pressures (0.05 – 0.20 mTorr). The pressures are low enough that single collision conditions dominate. Xenon was used as the collision gas to induce dissociation because it is heavy, monoatomic, polarizable, and chemically unreactive, all of which increase the efficiency of the transfer of kinetic energy to internal modes.[32-34] After collision, product ions and remaining reactant ions drifted to the end of the octopole where they were extracted, mass analyzed using a quadrupole mass filter, and detected using a Daly detector.[35]

4.3.2 Data analysis. Ion intensities were converted to absolute cross sections using a Beer-Lambert law analogue, as described in detail elsewhere, with an uncertainty of ± 20% (10% uncertainties each in pressure measurement and collision cell length).[21] The laboratory ion potential, V_{lab}, was converted to the relative kinetic energy in the center-of-mass (CM) frame by $E_{CM} = E_{lab} \times m/(m + M)$, where $E_{lab} = 2V_{lab}$ because the ions are doubly charged, m is the mass of the neutral collision gas, and M is the mass of the reactant ion. The absolute zero of energy and the kinetic energy distribution of the ion beam were determined using a retarding potential technique, in which the derivative of the normalized ion intensity was fit to a Gaussian distribution (~0.12 eV FWHM).[21] All energies below are reported in CM frame, unless noted otherwise.

To produce accurate thermochemical data from the modeling of the CID process, several effects must be considered: multiple collisions, lifetime effects, and energy distributions. To ensure rigorous single collision conditions, cross sections were obtained at multiple Xe pressures, about 0.20, 0.10, and 0.05 mTorr, and linearly extrapolated to zero pressure cross sections.[36-37] The zero-pressure extrapolated cross sections for loss of a single ligand were modeled using the empirical threshold model shown in eq 4.3:

$$\sigma_j(E) = \sigma_0 \sum g_i\left(E + E_i - E_{0,j}\right)^n / E \qquad (4.3)$$

where σ_0 is an energy independent scaling factor, E is the relative translational energy of the reactants, $E_{0,j}$ is the reaction threshold for channel j at 0 K, and n is an adjustable fitting parameter that describes the efficiency of the energy transfer upon collision.[20] The summation is over the ro-vibrational states of the reactants with excitation energies, E_i, and populations, g_i, where $\Sigma g_i = 1$. The number of ro-vibrational states was directly

counted by the Beyer−Swinehart−Stein−Rabinovich algorithm to evaluate the internal energy distribution for the reactants.[38-41] A Maxwell-Boltzmann distribution at 300 K was used to compute the relative populations, g_i. The number of accessible ro-vibrational states increases as the size of the reactant ions increases, such that those with energy in excess of the dissociation threshold may not have time to dissociate on the time scale of the experiment, $\tau \approx 5 \times 10^{-4}$ s.[20] This can lead to a kinetic shift in the energy threshold, which can be accounted for by incorporating Rice−Ramsperger−Kassel−Marcus (RRKM) statistical theory[41-43] for unimolecular dissociation into eq 4.3, as shown in eq 4.4.[44]

$$\sigma_j(E) = \left(\frac{n\sigma_{0,j}}{E}\right) \sum g_i \int_{E_{0,j}-E_i}^{E} \left[\frac{k_j(E^*)}{k_{tot}(E^*)}\right] (E-\varepsilon)^{n-1} P_{D1} d(\varepsilon) \qquad (4.4)$$

In eq 4.4, ε is the energy transferred into internal degrees of freedom of the reactant ion during collision, such that the energized molecule (EM) has an internal energy of $E^* = \varepsilon + E_i$, and $k_{tot}(E^*)$ is the total unimolecular dissociation rate coefficient. The rate coefficient was used to calculate a probability of dissociation, $P_{D1} = 1 - \exp[-k_{tot}(E^*)\tau]$. The RRKM unimolecular dissociation rate coefficient is defined by eq 4.5,

$$k_{tot}(E^*) = \sum k_j(E^*) = \sum d_j N_j^{\dagger}\left(E^* - E_{0,j}\right)/h\rho(E^*) \qquad (4.5)$$

where $k_j(E^*)$ is the rate coefficient for a single dissociation channel j, d_j is the reaction degeneracy calculated from the ratio of rotational symmetry numbers[41] of the reactants and products of channel j, $N_j^{\dagger}(E^* - E_{0,j})$ is the sum of the ro-vibrational states of the transition state (TS) at an energy ($E^* - E_{0,j}$) above the threshold for channel j, and $\rho(E^*)$ is the density of ro-vibrational states for the EM at the energy available, E^*. When the rate

of dissociation is much faster than the average experimental time scale, eq 4.4 reduces to eq 4.3. Eq 4.4 also accounts for the competition between multiple dissociation pathways using the $k_j(E^*)/k_{tot}(E^*)$ ratio.[44-45]

Cross sections for the first and second water losses were modeled by combining eq 4.4, the cross section of the primary dissociation product, with the probability for further dissociation given by eq 4.6,

$$P_{D2} = 1 - e^{-k_2(E_2^*)\tau} \tag{4.6}$$

where E_2^* is the internal energy of the product ion undergoing sequential dissociation. This energy is determined by energy conservation, $E_2^* = E^* - E_{0,j} - T_1 - E_L$, where T_1 is the translational energy of the primary products and E_L is the internal energy of the neutral product. As discussed elsewhere, the distributions in these energies are assigned on the basis of statistical considerations.[46] For the remainder of this paper, representation of this sequential dissociation model that combines eqs 4.4 and 4.6 will be notated as eq 4 × 6. The BDE for the $Co^{2+}(H_2O)_{x-1}$ complex is the difference between the thresholds of these two product cross sections.

Calculation of the RRKM unimolecular rate coefficients requires the ro-vibrational states of the EM and TS. The molecular parameters for the EM were taken from quantum chemical calculations of the reactant ion. Water loss from a metal cation species, reaction 4.1, is a heterolytic bond cleavage with all the charge remaining on the cobalt containing fragment complex. As such these TSs were assumed to be loose with no reverse activation barrier[47] and were treated in the phase space limit (PSL), such that it used molecular parameters taken from quantum chemical calculations of the products.[44] Because the charge separation processes 4.2 produce two singly charged species, there

must be an associated Coulomb barrier along the reaction coordinate for this dissociation channel such that the charge separation TSs are tight. The rate-limiting TSs for charge separation are labeled according to the products formed in reaction 4.2, i.e., TS[m + (x – m – 1)] where m is the number of waters attached to the $CoOH^+$ product and (x – m – 1) is the number of waters attached to the H^+ product. Molecular parameters for these TSs were taken directly from the calculations described below.

The CID cross sections of eq 4.4 and eq 4 × 6 were convoluted over the relative kinetic energy distributions of the $Co^{2+}(H_2O)_x$ and Xe reactants for comparison with the experimental cross sections.[21] A nonlinear least-squares fitting procedure was used to optimize the fitting parameters in each model. The uncertainties associated with the fitting parameters, $\sigma_{0,j}$, n, and $E_{0,j}$, were determined from modeling multiple data sets (at least eight zero pressure extrapolated cross sections for each system) and additional modeling of the cross sections by scaling the vibrational frequencies by ±10%, varying the best fit n value by ±0.1, scaling the experimental time-of-flight up and down by a factor of 2, and including the absolute uncertainty of the energy scale, 0.05 eV (Lab). Because all sources of energy are accounted for in these analyses, the measured thresholds, $E_{0,j}$, equal the BDE at 0 K for the $Co^{2+}(H_2O)_x$ complex dissociating as in reaction 4.1[48] or the height of the charge separation barrier of reaction 4.2.

4.3.3 Computational details. Geometry optimizations for multiple isomers of the $Co^{2+}(H_2O)_x$ system were performed at the B3LYP/6-31G(d) level of theory[49-50] for CN = 4, 5, and 6 at each x. The optimizations were refined at a B3LYP/6-311+G(d,p) level, which was used for the final geometry optimizations and to provide vibrational frequencies and rotational constants for the data analysis. Geometry optimizations

utilizing empirical dispersion corrections were also determined at the B3LYP-GD3BJ/6-311+G(d,p) level.[51] Single point energy calculations using the B3LYP/6-311+G(d,p) optimized geometries were performed at B3LYP, B3P86,[52] and MP2(full)[53] (where full indicates correlation of all electrons) levels of theory using a 6-311+G(2d,2p) basis set and also at the B3LYP-GD3BJ/6-311+G(2d,2p)//B3LYP-GD3BJ/6-311+G(d,p) level. For brevity, these levels of theory will simply be referred to as B3LYP, B3P86, MP2, and B3LYP-GD3BJ throughout the rest of the paper.

Vibrational frequencies were scaled by 0.989[54] before being used in the modeling process and to calculate zero point energies to yield 0 K values as well as thermal corrections to 298 K. Basis set superposition errors (BSSE) were calculated for dissociation of the lowest energy structures at each level of theory in the full counterpoise (cp) limit.[55-56]

4.4 Results

4.4.1 Collision-induced dissociation cross-sections of $Co^{2+}(H_2O)_x$.

Experimental cross-sections for the collision-induced dissociation with Xe were acquired for $Co^{2+}(H_2O)_x$, $x = 5 – 11$, and are shown in Figure 4.1. In all cases, the loss of a single water molecule, reaction 4.1, is the dominant pathway, followed by the sequential loss of additional water molecules as the kinetic energy increases. In all cases, the total cross sections reach a plateau with a magnitude that increases with *x*, consistent with sequential dissociation processes. As seen in Figure 4.1(a) and (b), for $x = 11$ and 10, respectively, cross sections for losses of up to six water ligands each were characterized. In addition, products corresponding to charge separation (CS) processes, reaction 4.2, were observed

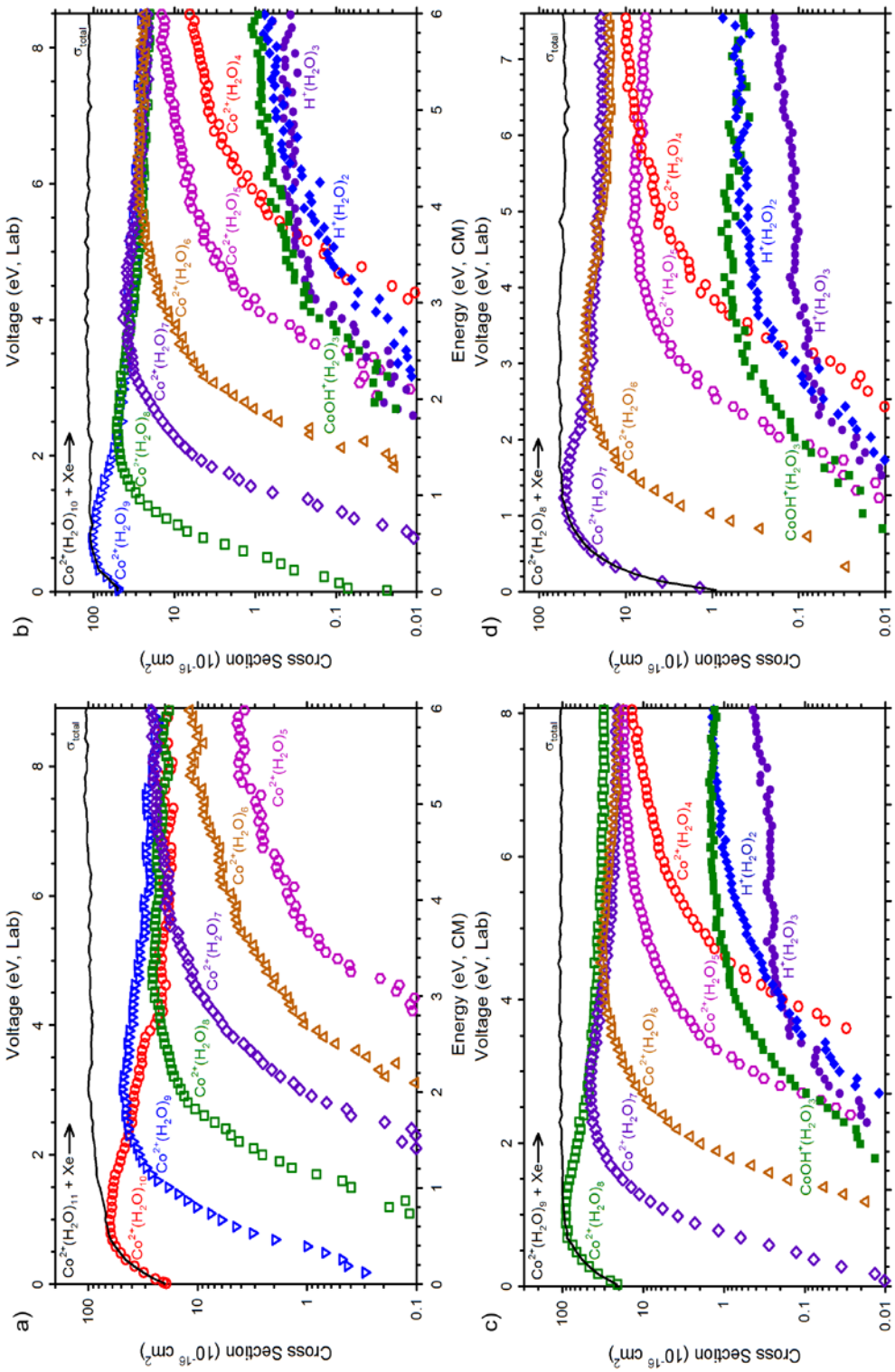

Figure 4.1. Cross sections for collision-induced dissociation of $Co^{2+}(H_2O)_x$ where $x = 5 – 11$ (parts a – g) with Xe (~ 0.2 mTorr) as a function of kinetic energy in the center-of-mass frame (bottom x-axis) and applied voltage in the laboratory frame (top x-axis). Water loss products are represented by open symbols and charge separation products by closed symbols.

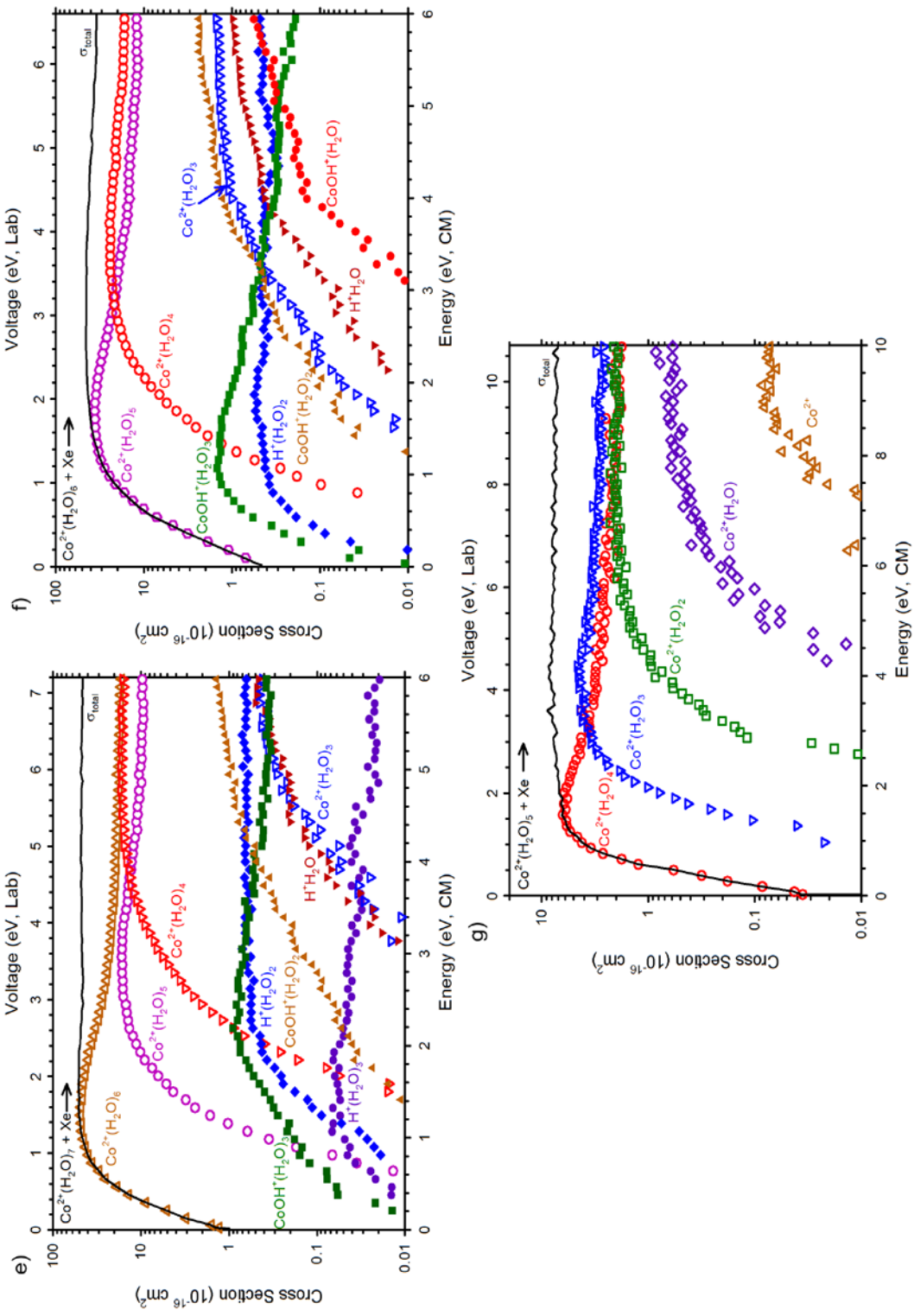

Figure 4.1. (continued).

for $x = 10$. It can be seen that the $CoOH^+(H_2O)_3$ and $H^+(H_2O)_3$ products rise from similar thresholds, meaning that these species must come from dissociation of the $Co^{2+}(H_2O)_7$ product in reaction 4.7.

$$Co^{2+}(H_2O)_7 \rightarrow CoOH^+(H_2O)_3 + H^+(H_2O)_3 \quad (4.7)$$

The apparent threshold for this CS reaction clearly exceeds that for loss of a water molecule from the $x = 7$ complex to form $Co^{2+}(H_2O)_6$, which explains why the CS cross section is so much smaller and rises less sharply than the cross section for water loss. It is also useful to recognize that the CS processes are entropically disfavored as they must pass over a rate-limiting TS corresponding to bringing the two incipient singly charged product ions together over a Coulombic barrier, whereas water loss processes always involve loose TSs. The cross section for $H^+(H_2O)_2$ rises with a similar magnitude as the $CoOH^+(H_2O)_3$ at a somewhat higher threshold than $H^+(H_2O)_3$. The apparent threshold of the $H^+(H_2O)_2$ product is much lower than that expected for sequential loss of water from $H^+(H_2O)_3$, where the BDE for $H^+(H_2O)_2$-H_2O is 0.86 ± 0.06 eV.[48] Thus, the $H^+(H_2O)_2$ must come from the dissociation of the $Co^{2+}(H_2O)_6$ product in reaction 4.8.

$$Co^{2+}(H_2O)_6 \rightarrow CoOH^+(H_2O)_3 + H^+(H_2O)_2 \quad (4.8)$$

The apparent thresholds for reaction 4.8 and that for loss of a water molecule to form $Co^{2+}(H_2O)_5$ are competitive with the apparent CS threshold ~0.3 eV higher.

For CID of $x = 9$ and 8, sequential loss of water ligands down to $Co^{2+}(H_2O)_4$ and the CS products found in reactions 4.7 and 4.8 were again characterized. It is now apparent that the magnitude of the $H^+(H_2O)_3$ cross section is smaller than those for $CoOH^+(H_2O)_3$ and $H^+(H_2O)_2$. Onsets of these CS reactions relative to H_2O loss products

remain similar to those described for the $x = 10$ complex. Figure 4.1(e) shows the CID of $Co^{2+}(H_2O)_7$ follows the same product pathways as $Co^{2+}(H_2O)_8$, exhibiting the loss of four water ligands, although the cross section for $Co^{2+}(H_2O)_3$ is quite small. The CS products are also similar to those for $x = 8 – 10$, but now $CoOH^+(H_2O)_2$ and H^+H_2O are also observed at higher energies, starting near 1.5 and 3.0 eV, respectively. Indeed, the threshold for $CoOH^+(H_2O)_2$ relative to that for $CoOH^+(H_2O)_3$ in Figure 4.1(e) is comparable to the BDE for $CoOH^+(H_2O)_2$-H_2O measured previously as 1.12 ± 0.07 eV.[8] As such, the $CoOH^+(H_2O)_2$ product at its threshold is a result of sequential loss of water from $CoOH^+(H_2O)_3$ and its cross section exhibits evidence of contributions from the $CoOH^+(H_2O)_3$ precursors formed in both reactions 4.7 and 4.8. At higher energies (above about 3 eV), the $CoOH^+(H_2O)_2$ cross section increases, paralleling the onset in the H^+H_2O cross section. This observation suggests that CS reaction 4.9 is occurring.

$$Co^{2+}(H_2O)_4 \rightarrow CoOH^+(H_2O)_2 + H^+H_2O \qquad (4.9)$$

If so, it can be seen that the apparent threshold for the H^+H_2O product from CS reaction 4.9 is similar in both threshold energy and magnitude to that for formation of $Co^{2+}(H_2O)_3$, Figure 4.1(e), suggesting these are competitive dissociation pathways of the $Co^{2+}(H_2O)_4$ product. The CS reaction 4.9 has previously been identified in the photodissociation of $Co^{2+}(H_2O)_4$ by Metz and coworkers.[57] They found that simple water loss was at least an order of magnitude less probable, which differs from the very similar probabilities of the two pathways observed here. This difference may simply be attributable to the differing activation methods. In addition, Kebarle and coworkers[12,16-17] used high pressure mass spectrometry (HPMS) to observe $CoOH^+(H_2O)_2$, $CoOH^+(H_2O)$, and H^+H_2O, assigning

these observations to reaction 4.9, although there is nothing in this work that allows them to definitively link the products observed as coming from the same reaction.

The presence of reaction 4.8 is confirmed by the results for $Co^{2+}(H_2O)_6$, Figure 4.1(f), which can no longer dissociate by reaction 4.7. Now the $H^+(H_2O)_3$ product is no longer observed and the cross sections for $CoOH^+(H_2O)_3$ and H^+H_2O have similar energy dependences. Further, the sum of the $CoOH^+(H_2O)_3$ and $CoOH^+(H_2O)_2$ cross sections matches that of the sum of $H^+(H_2O)_2$ and H^+H_2O in shape, consistent with sequential loss of water ligands from the former to produce the latter at their thresholds. Relative thresholds are also consistent with this conclusion. The magnitudes of these two sums differ by approximately 50%. We have previously demonstrated that this can occur because the products of charge separation reactions have appreciable kinetic energy that is released once they pass over the Coulombic barrier.[5] Momentum conservation dictates that the lighter products have a higher kinetic energy, such that they are less efficiently collected and detected. Reaction 4.9 is also more easily observed in Figure 4.1(f) as a large increase in the $CoOH^+(H_2O)_2$ and H^+H_2O cross sections compared to those for $CoOH^+(H_2O)_3$ and $H^+(H_2O)_2$ (very evident on a linear cross section scale). Again, it can be seen that these cross sections follow a similar energy dependence and magnitude as formation of $Co^{2+}(H_2O)_3$.

Unexpectedly, the dissociation of $Co^{2+}(H_2O)_5$, Figure 4.1(g), exhibits only loss of water ligands and no CS reactions were observed from $x = 5$ or from smaller complexes (e.g., reaction 4.9). The failure to observe a CS reaction from $Co^{2+}(H_2O)_5$ is consistent with no evidence for such a reaction in the larger complexes. In contrast, on the basis of the results described above for dissociation of the $x = 7$ and 6 complexes, one might have

expected to observe $CoOH^+(H_2O)_2$ and H^+H_2O products of reaction 4.9 with cross section magnitudes similar to that of the $Co^{2+}(H_2O)_3$ product. These products were specifically looked for but never seen with appreciable intensity above the signal-to-noise level (~0.01 $Å^2$). At this point in time, we have no ready explanation for the failure to observe reaction 4.9 in Figure 4.1(g) although this result is discussed further below.

4.4.2 Overview of theoretical results. Relative energies at 0 and 298 K of $Co^{2+}(H_2O)_x$ (x = 4 – 11) complexes calculated at different levels of theory are given in Table 4.1, with geometries of ground structures (GSs) shown in Figure 4.2. For all complexes, the quartet spin state of the $3d^7$ configuration on cobalt was found to be much more favorable energetically (by over 1.0 eV) compared to a doublet or sextet spin state.

We use an (x,y,z) nomenclature to describe the number of water molecules in the first (x), second (y), and third (z) solvent shells of each unique structure. To describe the hydrogen bonding of waters in the cluster, isomers are further denoted using an A/D nomenclature where a water molecule can be a single (A) or double (AA) hydrogen bond acceptor and/or single (D) or double (DD) hydrogen bond donor. To indicate waters that bridge between two different solvent shells, a subscript "2" is denoted on both the donor and acceptor (which is more easily visualized by example, see Table 4.1 and Figure 4.2). To further distinguish between structures with similar bonding schemes but differing geometric parameters, additions to the nomenclature may include point group symmetries; the subscripts "a" or "b" to indicate if the bond connects to an axial or base ligand, respectively; series of oxygen – cobalt dication –oxygen angles denoted as subscript "g" (gauche) for angles between 45° and 135° and "t" (trans) for angles >135°.

Table 4.1. Theoretical Relative Enthalpy (ΔH_0) and Free Energies (ΔG_{298})[a] (kJ/mol) for Hydrated Cobalt Complexes [a]

	complex (x,y,z)[b]	B3LYP	B3LYP-GD3BJ[c]	B3P86	MP2(full)
$Co^{2+}(H_2O)_4$	(4,0)	**0.0 (0.0)**	**0.0 (0.0)**	**0.0 (0.0)**	**0.0 (0.0)**
	(3,1)_A	52.8 (52.7)	56.6 (56.5)	50.8 (50.6)	80.5 (80.4)
$Co^{2+}(H_2O)_5$	(4,1)_AA	**0.0 (0.0)**	**0.0 (0.0)**	**0.0 (0.0)**	**0.0 (0.0)**
	(4,1)_A	2.0 (6.2)	5.1 (9.3)	1.8 (6.1)	6.4 (10.7)
	(5,0)	17.0 (26.4)	13.5 (22.8)	16.4 (25.8)	7.8 (17.1)
$Co^{2+}(H_2O)_6$	(4,2)_4D_2AA	**0.0 (0.0)**	3.0 **(0.0)**	**0.0 (0.0)**	19.5 (12.7)
	(4,2)_3D_AA_A	5.3 (8.8)	11.2 (11.6)	5.1 (8.6)	29.6 (26.2)
	(4,2)_2D,DD_2AA	11.1 (10.0)	13.7 (9.6)	11.6 (10.6)	31.8 (24.0)
	(5,1)_A_aA_b	7.1 (10.1)	6.9 (6.8)	7.5 (10.5)	39.2 (35.4)
	(5,1)_A_bA_b	16.5 (17.9)	16.2 (14.5)	15.6 (16.9)	27.3 (21.9)
	(6,0) T_h	6.3 (10.5)	16.6 (17.8)	7.2 (11.4)	17.5 (14.9)
	(6,0) D_{2h}	4.9 (11.7)	**0.0** (3.7)	5.8 (12.5)	**0.0 (0.0)**
$Co^{2+}(H_2O)_7$	(4,3)_3D,DD_2AA,A	**0.0 (0.0)**	4.5 **(0.0)**	**0.0 (0.0)**	20.3 (17.4)
	(4,3)_2D,2DD_3AA	8.3 (5.2)	9.0 (4.1)	9.1 (6.0)	20.3 (20.7.)
	(4,3)_4D_AA_2A	1.0 (2.0)	8.0 (7.4)	0.5 (1.6)	26.7 (20.7)
	(5,2)_2D,DD_2AA	9.2 (8.4)	7.2 (4.6)	8.0 (7.2)	11.6 (9.0)
	(5,2)_4D_2AA	5.2 (3.7)	3.3 (2.7)	3.6 (2.0)	9.3 (4.9)
	(6,1)_AA	6.8 (9.7)	**0.0** (1.1)	7.0 (9.9)	**0.0 (0.0)**
$Co^{2+}(H_2O)_8$	(4,4)_2D,2DD_2A,2AA	5.7 (8.6)	15.0 (18.0)	6.6 (9.6)	20.8 (20.6)
	(4,4)_2D,2DD_2AA,AD_2,AA_2	19.0 (18.2)	23.5 (22.8)	20.4 (19.6)	32.1 (28.2)
	(4,4)_3D,DD_A,AA,AD_2,AA_2	12.9 (14.9)	21.2 (23.2)	13.9 (15.9)	28.9 (27.6)
	(4,4)_4DD_4AA	10.0 (7.2)	12.6 (9.8)	12.2 (9.4)	20.3 (14.4)
	(5,3)_2D,2DD_3A_bA_b	**0.0 (0.0)**	4.3 **(0.0)**	**0.0 (0.0)**	16.1 (12.9)
	(5,3)_2D,2DD_2A_bA_b,A_aA_b	6.8 (5.6)	6.7 (5.5)	5.4 (4.2)	8.4 (4.0)

Table 4.1. continued

	complex $(x,y,z)^b$	B3LYP	B3LYP-GD3BJ[c]	B3P86	MP2(full)
$Co^{2+}(H_2O)_8$	(5,3)_4D,DD_3AA	9.3 (8.6)	9.2 (8.4)	8.2 (7.5)	10.2 (6.2)
	(6,2)_2D,DD_2AA	21.7 (24.9)	16.7 (19.9)	21.4 (24.7)	7.6 (7.7)
	(6,2)_4D_2AA$_g$	9.9 (13.1)	4.9 (8.1)	10.4 (13.6)	15.9 (15.9)
	(6,2)_4D_2AA$_t$	13.8 (17.0)	**0.0** (2.0)	13.9 (17.0)	**0.0 (0.0)**
$Co^{2+}(H_2O)_9$	(4,4,1)_2D,2DD_2AA,2AD_AA	16.1 (18.4)	28.1 (27.1)	18.2 (20.5)	45.7 (44.8)
	(4,4,1)_2D,2DD_A,2AD_2AA	14.2 (18.1)	28.6 (29.3)	15.8 (19.7)	47.5 (48.1)
	(4,5)_2D,2DD_AA,2A,AD$_2$,AA$_2$	8.9 (14.4)	24.1 (26.3)	11.1 (16.6)	41.1 (43.3)
	(4,5)_D,3DD_2AA,3A	2.4 (8.9)	18.7 (21.9)	4.5 (10.9)	34.0 (37.2)
	(4,5)_D,3DD_2AA,A,AD$_2$,AA$_2$	11.7 (15.1)	23.4 (23.5)	14.2 (17.6)	45.4 (45.4)
	(5,4)_2D,3DD_4AA	**0.0 (0.0)**	4.5 (1.3)	**0.0 (0.0)**	16.7 (13.4)
	(5,4)_3D,2DD_A,3AA	6.4 (9.2)	12.9 (12.5)	6.3 (9.1)	24.5 (24.1)
	(5,4)_4D,DD_2AA,AD$_2$,AA$_2$	14.1 (15.9)	20.0 (18.5)	13.9 (15.7)	33.6 (32.1)
	(5,4)_4DD_4AA	1.2 (1.7)	4.9 (2.1)	0.7 (1.2)	16.1 (13.4)
	(6,3)_2D,2DD_3AA	6.5 (11.1)	5.3 (6.6)	7.7 (12.2)	6.3 (7.6)
	(6,3)_4D,DD_3AA	2.6 (6.6)	1.8 (2.6)	3.9 (7.9)	1.9 (2.7)
	(6,3)_6D_3AA	0.6 (3.9)	**0.0 (0.0)**	1.7 (5.0)	**0.0 (0.0)**
$Co^{2+}(H_2O)_{10}$	(4,4,2)_4D,4AD_2AA	20.7 (22.5)	36.8 (37.2)	22.1 (23.9)	55.9 (56.3)
	(4,4,2)_4DD,2AA_2AAD,2A	17.2 (16.2)	29.1 (26.6)	18.4 (17.4)	48.1 (45.6)
	(4,5,1)_2D,2DD_2AA,A,2AD_AA	11.5 (13.1)	25.7 (25.9)	14.1 (15.8)	41.3 (41.5)
	(4,5,1)_D,3DD_2A,AA,AAD,AD_AA	19.9 (22.0)	34.0 (34.6)	21.6 (23.7)	50.6 (51.2)
	(4,6)_4DD,2AA_4A	0.2 (6.7)	18.8 (23.8)	3.1 (9.6)	31.3 (36.4)
	(5,4,1)_4DD,4AA_A	7.3 (6.4)	13.2 (10.8)	6.0 (5.1)	24.0 (21.6)
	(5,5)_D,4DD_3AA,AAD_AA	9.5 (6.7)	10.3 (6.1)	9.3 (6.5)	20.4 (16.2)
	(5,5)_D,4DD_4AA,A	**0.0 (0.0)**	5.9 (4.5)	**0.0 (0.0)**	15.8 (14.4)

Table 4.1. continued

	complex (x,y,z)[b]	B3LYP	B3LYP-GD3BJ[c]	B3P86	MP2(full)
$Co^{2+}(H_2O)_{10}$	(6,4)_4DD,4AA	17.4 (19.8)	14.8 (15.7)	18.7 (21.0)	14.1 (15.0)
	(6,4)_5D,DD_2AA,AAD_2,AA_2	5.7 (6.3)	2.3 (1.4)	30.1 (30.7)	1.2 (0.3)
$Co^{2+}(H_2O)_{11}$	(4,4,3)_4DD,AA_3AAD,3A	19.6 (16.6)	35.3 (35.2)	17.3 (16.8)	55.4 (55.4)
	(4,6,1)_4DD,4A_AA,AAD_A	6.1 (9.8)	28.4 (34.9)	5.4 (11.5)	42.6 (49.1)
	(5,4,2)_4DD,2AA_2AAD,2A	10.5 (7.0)	20.0 (19.4)	5.4 (4.4)	32.4 (31.8)
	(5,5,1)_D,4DD_A,3AA,AAD_A	3.8 (1.3)	13.4 (13.8)	**0.0 (0.0)**	24.6 (25.0)
	(5,6)_5DD_4AA,2A	**0.0 (0.0)**	9.3 (12.2)	0.6 (3.1)	34.4 (37.3)
	(6,5)_4D,2DD_AA,$2AAD_2$,$2AA_2$	8.5 (3.1)	3.6 (1.1)	6.1 (3.1)	23.7 (21.2)
	(6,5)_D,4DD_4AA,A	22.2 (21.7)	22.4 (24.9)	20.5 (22.6)	22.6 (25.1)
	(6,5)_3D,3DD_3AA,AAD_2_AA_2	6.2 (1.9)	3.4 (2.0)	3.9 (2.1)	30.6 (29.3)
	(6,5)_2D,4DD_5AA	3.5 (0.5)	**0.0 (0.0)**	1.3 (0.9)	**0.0 (0.0)**
	(6,4,1)_4D,2DD_3AA,AAD_A	17.6 (15.9)	19.1 (20.3)	13.7 (14.5)	21.1 (22.3)

[a]ΔG_{298} values are given in parentheses. Values are single-point energies calculated at the level shown using a 6-311+G(2d,2p) basis set from geometries optimized at the B3LYP/6-311+G(d,p) level except as noted. Zero point energy corrections are included. [b]To differentiate otherwise similar structures, several additions to the nomenclature were made: 1) the point group symmetry may be added; 2) subscripts "a" and "b" refer to apex and base sites in an inner shell of five waters; 3) O – M^{2+} – O angles denoted as subscript "g" (gauche) for angles between 45° and 135°, and "t" (trans) for angles >135°; 4) waters that can be assigned to two shells and always indicate a cyclic structure are denoted with a subscript "2". [c]Geometries optimized at B3LYP-GD3BJ/6-311+G(d,p) level.

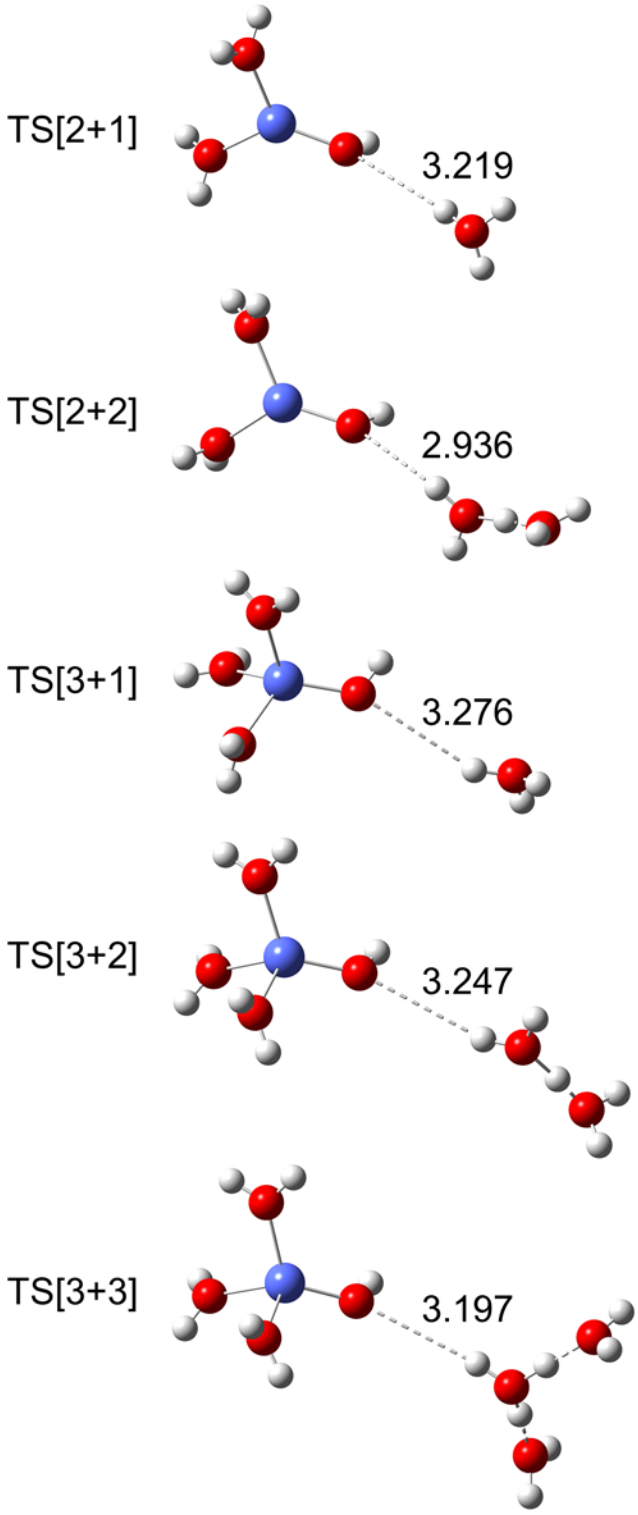

Figure 4.2. Possible rate-limiting charge separation transition states for reactions 4.7 – 4.9 and those for x = 5. Structures were optimized at the B3LYP/6-311+G(d,p) level of theory. Brackets denote TS[x+y] naming scheme where x indicates the number of waters directly bound to the $CoOH^+$ center and y indicates the number of waters bound to the leaving H^+. Bond lengths for the O-H^+ bond being broken (dashed line) are provide in Angstroms (Å).

4.4.3 Theoretical geometries for $Co^{2+}(H_2O)_x$ ground structures. As seen in Table 4.1, there is discrepancy among the different levels of theory as to the coordination number (CN), the number of ligands that directly bind to the metal and form the first solvent shell, for $Co^{2+}(H_2O)_x$. The progression of the GS solvent shell growth at the different CNs are displayed in Figure 4.2. The B3LYP and B3P86 levels predict that CN = 4 for $x = 4 – 7$, and then CN= 5 for $x \geq 8$ at 0 and 298 K. MP2 predicts four-coordinate GSs for $x = 4$ and 5 and then CN = 6 for $x \geq 6$ at 0 and 298 K. Temperature becomes a factor for B3LYP-GD3BJ. For $x = 4 – 8$, the B3LYP-GD3BJ 298 K GSs are the same as B3LYP and B3P86, whereas the 0 K GSs agree with MP2 GSs. At $x = 9 – 11$, the B3LYP-GD3BJ GSs are CN = 6 at both 0 and 298 K GS, agreeing with MP2.

All levels of theory predict GSs with four waters directly binding to Co^{2+} for $x = 4$ and 5 (Table 4.1). The (4,0) $Co^{2+}(H_2O)_4$ GS isomer exhibits a distorted tetrahedral geometry with ∠O-Co-O of 105° and 112° and four Co-O bond lengths of 2.012 Å. The nonsymmetrical orientation of the water ligands results from their participation in long-range hydrogen bonding interactions (~3.6 Å between H and O). The $x = 5$ GS, (4,1)_AA, is the (4,0) isomer with addition of the fifth water ligand promoted to a second solvent shell by accepting a single hydrogen bond from two inner shell waters. Table 4.1 shows the (5,0) isomer is 17 – 26 kJ/mol higher in 298 K energy than the (4,1) GS. These four-coordinate structures are similar to those predicted and identified spectroscopically for $CoOH^+(H_2O)_x$,[8,58] where the $CoOH^+(H_2O)_3$ GS complex had three water ligands and the hydroxide bound directly to the cobalt ion. The fourth water ligand in $CoOH^+(H_2O)_4$ was also promoted into the second solvent shell where it accepted a single hydrogen bond from an inner shell water and donated a hydrogen bond to the inner shell hydroxide. It

can be realized that in both the Co^{2+} and $CoOH^{+}$ complexes the metal ion has a $3d^7$ electron configuration such that a tetrahedral geometry is favored, as this gives an orbital occupation of $(e)^4(t_2)^3$ for a quartet spin state.

At $Co^{2+}(H_2O)_6$, levels of theory diverge for predicting the lowest energy isomer. The B3LYP, B3P86, and B3LYP-GD3BJ (298 K) levels of theory continue to predict a four-water inner solvent shell GS with the (4,2)_4D_2AA isomer. This isomer has the sixth water ligand accepting hydrogen bonds from two inner shell water ligands of the (4,1)_AA complex, such that the two second solvent shell water molecules are opposite each other. MP2 and B3LYP-GD3BJ (0 K) predict the lowest energy $x = 6$ isomer to be the six-coordinate (6,0) complex, where all six water molecules directly interact with the metal center in a pseudo-octahedral geometry with Co – O bond lengths of 2.126 Å (4) and 2.128 Å (2). In the (6,0) complex, the orientations of the ligands are again determined by long (3.0 – 3.1 Å) interligand hydrogen bonding occurring between the hydrogen atom of one ligand and the oxygen atom of a neighboring water unit (Figure 4.2) such that the symmetry is D_{2h}. The Co – O bond lengths determined here are ~0.016 Å shorter than predicted by Akesson et al.[59] using MCSCF methods for their (6,0) complex with T_h symmetry (where all Co-O bond lengths are equal and the hydrogen bonding dictates the high symmetry), predicted to be 11 – 18 kJ/mol higher in relative 298 K energy than GS here. Note that the six-coordinate geometry has an orbital occupation of $(t_{2g})^5(e_g)^2$ for a quartet spin state, such that a Jahn-Teller distortion from the octahedral T_h symmetry is expected.

Theory also predicts both four- and six-coordinate ground structures at $x = 7$, Figure 4.2. B3LYP, B3P86, and B3LYP-GD3BJ (298 K) levels predict the lowest energy

isomer of $Co^{2+}(H_2O)_7$ to have a four water inner shell structure, (4,3)_3D,DD_2AA,A which is similar to the (4,2)_4D_2AA isomer where the third outer shell water accepts a single hydrogen bond from an inner shell water. The six water inner shell isomer, (6,1)_AA, is predicted by MP2(full) and B3LYP-GD3BJ (0 K) levels to be the lowest energy isomer. In this isomer, the seventh water is in the second solvent shell, doubly bound via two hydrogen bonds from neighboring inner-shell water ligands.

At $Co^{2+}(H_2O)_8$, theory stops predicting a four-coordinate ground structure. Here, the B3LYP, B3P86 and B3LYP-GD3BJ (298 K) levels predict the lowest energy isomer to have a five water inner solvent shell, (5,3)_2D,2DD_3A_bA_b. Figure 4.2 shows this isomer has a distorted square pyramidal inner shell geometry with the three outer shell ligands adjacent to each other in the plane of the pyramid base. For MP2 and B3LYP-GD3BJ (0 K) levels, the (6,2)_4D_2AA_t isomer is predicted to be the GS. As shown in Figure 4.2, this structure has two second-shell water ligands doubly hydrogen bonded to the inner solvent shell opposite each other (t = trans).

The five-coordinate GS predicted by B3LYP and B3P86 levels for $x = 9$ is (5,4)_2D,3DD_4AA. This structure is similar in geometry to the $x = 8$ (5,3) GS but the eighth water accepts hydrogen bonds from two inner solvent waters, one in the axial position and one in the base. If all four second shell waters bind symmetrically to inner shell base waters, (5,4)_4DD_4AA, this isomer lies 0 - 2 kJ/mol higher in 298 K relative energy. The six-coordinate GS predicted by MP2 and B3LYP-GD3BJ (0 and 298 K) is a (6,3)_6D_3AA geometry with each of the six inner solvent shell waters donating only a single hydrogen bond to an outer solvent shell water. In this complex, the second solvent shell water ligands bind in equivalent locations, Figure 4.2.

The two predicted lowest energy $Co^{2+}(H_2O)_{10}$ complexes are shown in Figure 4.2. B3LYP and B3P86 levels predict the (5,5)_D,4DD_4AA,A geometry to be the GS. In this structure, four second solvent shell waters form two hydrogen bonds with the base of the square pyramidal inner solvent shell and the fifth second shell water accepts a single hydrogen bond from the axial inner solvent shell water. The (6,4)_4D,2DD_4AA isomer is predicted to be the MP2 and B3LYP-GD3BJ GS. This isomer has the outer shell waters oriented in such a way that two of the outer solvent shell water ligands are adjacent to each other with one inner solvent water shared between the two in the *xy* plane, while the other two outer water ligands are adjacent to each other with one inner solvent water shared between the two in the *xz* plane.

Figure 4.2 shows the three possible GSs for the $Co^{2+}(H_2O)_{11}$ complex, two five-coordinate and one six-coordinate, depending on the level of theory. B3LYP predicts the (5,6)_5DD_4AA,2A isomer as the GS, similar in structure to the $x = 10$ (5,5) GS with the addition of another water ligand accepting a single hydrogen bond from the inner shell water ligand in the axial position. The B3P86 level of theory predicted a GS of (5,5,1)_D,4DD_A,3AA,AAD_A, which is also similar to the $x = 10$ (5,5) GS, with the eleventh water in a third solvent shell singly bound to a second solvent shell water in the base of the square pyramid. MP2 and B3LYP-GD3BJ continue to predict a six-coordinate GS with the (6,5)_2D,4DD_5AA structure where the five second shell waters are all adjacent to each other in different planes with four double donating (DD) inner shell waters shared between them.

In agreement with the MP2 and B3LYP-GD3BJ results predicting CN = 6, Gilson and Krauss[60] used CAS-MCSCF and MCQDPT calculations to interpret the absorption

spectrum of aqueous Co^{2+} and found that the dominant species in solution is six-coordinate with some evidence of five-coordinate species. Metz and coworkers[57] reported that their photodissociation spectrum of $Co^{2+}(H_2O)_6$ was only consistent with the (6,0) structure, which suggests that the relative energies predicted by MP2 are more accurate than the other methods explored here. This conclusion is consistent with previous infrared multiple photon dissociation (IRMPD) spectroscopy experiments of $Zn^{2+}(H_2O)_x$, $x = 6 - 12$,[29] where the MP2(full)/6-311+G(2d,2p)//B3LYP/6-311+G(d,p) level of theory gave good agreement with experiment whereas B3LYP and B3P86 levels did not.

4.4.4 Theoretical geometries for charge separation transition states. The transition states for the charge separation reactions 4.7 – 4.9 involve the heterolytic cleavage of an O-H bond leading to the incipient products, $CoOH^+(H_2O)_m$ and $H^+(H_2O)_{x-m-1}$. Molecular parameters for these rate-limiting TSs are needed for thermochemical analysis. Optimized geometries of these tight TSs are shown in Figure 4.3 and include possible pathways for CS reactions of $Co^{2+}(H_2O)_5$ as well (both TS[3+1] and T[2+2]). The $(O – H^+)$ distances between the hydroxide oxygen and leaving proton in these TSs is generally near 3.2 Å, although TS[2+2] has an $O–H^+$ distance of only 2.94 Å. Such variations in these TS geometries have been observed previously for the analogous complexes of Fe^{2+} and Ni^{2+}.[1-2]

4.4.5 Thermochemical results. Primary and secondary dissociation product cross sections for all $Co^{2+}(H_2O)_x$ complexes observed were modeled in several ways, with average optimum modeling parameters obtained listed in Table 4.2. All complexes are believed to be thermally equilibrated in the source, such that the modeling assumes the reactant isomers are the 298 K GS with an internal energy distribution of 298 K. The

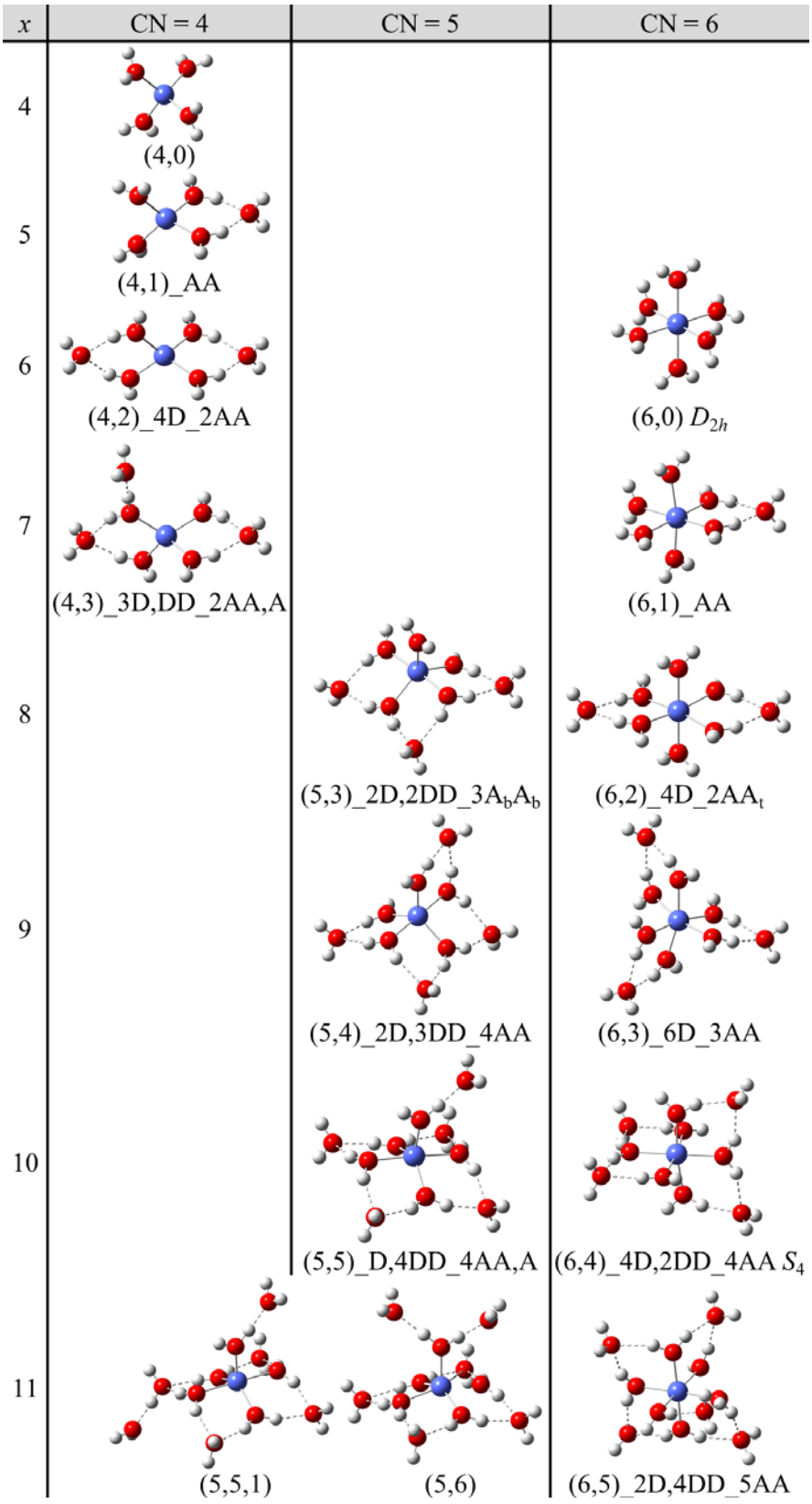

Figure 4.3. Geometries for the predicted ground structures of $Co^{2+}(H_2O)_x$ complexes, x = 4 – 11, as optimized at the B3LYP/6-311+G(d,p) level of theory.

Table 4.2. Optimized Parameters from Analysis of Cross Sections for Collision-Induced Dissociation of $Co^{2+}(H_2O)_x$ [a]

x	Reactant	Product	σ_0 [b]	n [b]	E_0 [b] (eV) (PSL)	E_0 [c] (eV) (No RRKM)	$\Delta S^{\dagger}_{1000}$ [b] ($^{J}/_{mol\ K}$)
5	(4,1)	(4,0)[d]	7 (2)	0.8 (0.1)	1.02 (0.07)	1.12 (0.09)	50 (21)
		(3,0)[e]	10 (3)		2.76 (0.10)		38 (14)
6	(4,2)	(4,1)[d]	58 (3)	0.8 (0.1)	1.10 (0.08)	1.21 (0.10)	75 (31)
	(6,0)	(4,1)[d]	59 (4)	0.8 (0.1)	1.11 (0.07)	1.26 (0.11)	52 (32)
		TS[3+2][f]	4 (3)		0.97 (0.06)	1.56 (0.08)	58 (10)
		(4,0)[g]	65 (4)		2.22 (0.09)		58 (5)
7	(4,3)	(4,1)[d]	79 (7)	1.0 (0.1)	0.77 (0.07)	0.95 (0.09)	13 (18)
	(6,1)	(6,0)[d]	73 (5)	1.0 (0.2)	0.80 (0.08)	0.99 (0.11)	62 (22)
		TS[3+3][f]	1 (1)		0.82 (0.10)	1.43 (0.15)	43 (15)
		(4,1)[g]	74 (10)		1.93 (0.09)		24 (4)
8	(5,3)	(4,3)[d]	62 (7)	1.0 (0.1)	0.68 (0.07)	0.90 (0.10)	55 (14)
8	(6,2)	(6,1)[d]	62 (7)	1.0 (0.1)	0.70 (0.06)	0.94 (0.10)	61 (43)
		(6,0)[e]	60 (4)		1.56 (0.08)		50 (5)
9	(5,4)	(5,3)[d]	88 (3)	1.0 (0.1)	0.58 (0.08)	0.92 (0.10)	55 (5)
	(6,3)	(6,2)[d]	88 (3)	1.0 (0.2)	0.60 (0.07)	0.82 (0.10)	67 (5)
		(6,1)[e]	84 (8)		1.36 (0.09)		51 (12)
10	(5,5)	(5,4)[d]	99 (7)	0.9 (0.1)	0.45 (0.08)	1.00 (0.14)	7 (10)
	(6,4)	(6,3)[d]	100 (6)	0.9 (0.1)	0.48 (0.07)	0.98 (0.15)	30 (15)
		(6,2)[e]	102 (9)		1.08 (0.09)		65 (14)
11	(5,5,1)	(5,5)[d]	74 (9)	1.2 (0.3)	0.40 (0.08)	0.99 (0.14)	32 (10)
	(5,6)	(5,5)[d]	75 (8)	1.2 (0.3)	0.40 (0.08)	0.98 (0.15)	2 (8)
	(6,5)	(6,4)[d]	75 (9)	1.2 (0.3)	0.42 (0.07)	1.01 (0.15)	64 (22)
		(6,3)[e]	77 (16)		1.05 (0.10)		34 (14)

[a]Uncertainties in parentheses. [b]Parameters for modeling with lifetime effects (PSL) considered. [c]Parameters for modeling where lifetime effects are not included. [d]Single channel modeling of total cross section using eq 4.4. [e]Sequential modeling of primary and secondary cross sections using eqs 4 × 6. [f]Competitive analysis modeling of primary water loss and charge separation cross sections using eq 4.4. [g]Competitive sequential analysis modeling of primary water and charge separation losses and secondary water loss cross sections using eqs 4.4 and 4 × 6.

product isomer is assigned as the 0 K GS because previous studies have found that our threshold analyses are dominated by the lowest energy 0 K enthalpy species.[1,4] Threshold E_0 values were determined for the primary dissociation of each complex from modeling with (eq 4.4) and without (eq 4.3) including RRKM theory, which takes lifetime effects into account. The primary threshold values without lifetime effects are higher because of a kinetic shift, which increases as the complexes get larger (from 0.1 eV for x = 5 to 0.6 eV for x = 11) because of the increased dissociation lifetime. Table 4.2 also includes values of the entropies of activation, $\Delta S^{\dagger}_{1000}$, which represent the measure of looseness of the transition states. All of these values are positive, consistent with a loose PSL TS.

The predicted GSs differ for the $x = 6 - 11$ complexes depending on the level of theory, and in several cases, there are low-energy isomers at 298 K energies such that multiple isomers could be present in the source. In these cases, the data were modeled using each of these possible isomers individually, Table 4.2. Changes in the reaction thresholds are a consequence of differences in the kinetic shifts of the model. This becomes more evident for reactant complexes with more outer shell waters and more single hydrogen bound waters (A) with low torsional frequencies that lead to a higher density of states, lowering the rate of dissociation, thereby increasing the kinetic shift and lowering the 0 K reaction threshold.[4] Consequently, we observed very minimal changes in the reaction thresholds when the data were modeled using different CN assumptions, with differences of only 0.01 – 0.03 eV for x = 6 – 11, where isomers with higher densities of states (CN = 4 and 5) have lower thresholds than CN = 6. In general, as the complex size increases from $Co^{2+}(H_2O)_6$ to $Co^{2+}(H_2O)_{11}$, reaction thresholds for loss of a single water molecule decrease. The largest decrease in consecutive E_0 values is 0.31 –

0.33 eV for the $x = 6$ to $x = 7$ complexes. This large change is potentially consistent with the onset of the second solvent shell and evidence for the (6,0) → (6,1) isomers (MP2 and B3LYP-GD3BJ) as opposed to the (4,2) → (4,3) (B3LYP and B3P86).

Uncharacteristically, the measured BDEs increase by 0.09 eV for $x = 5$ to 6. We attribute this increase to a change from (4,1) with a weakly bound second solvent shell water ligand to (6,0), where all ligands bind directly to the cobalt ion. Again, this increase is consistent with geometries predicted by MP2 and B3LYP, but not for B3LYP, B3P86, and B3LYP-GD3BJ, which suggest geometries of (4,1) and (4,2). Because MP2 theory predicts several aspects of this thermochemistry more correctly, additional thermochemical analysis below is based on the GS structures predicted by the MP2 energetics.

4.4.6 Thermochemical results for competitive water loss versus charge separation. For the $Co^{2+}(H_2O)_6$ and $Co^{2+}(H_2O)_7$ complexes, water loss and charge separation processes are competitive primary dissociation pathways (Figure 4.1 parts e and f, respectively). These dissociative pathways are modeled simultaneously using eq 4.4 with optimum modeling parameters also included in Table 4.2. The primary water loss thresholds are essentially unaffected by including competition with the CS products. Competitive analysis of the $x = 6$ CID cross sections (assuming a (6,0) reactant) measures a dissociation threshold for H_2O loss of 1.11 ± 0.07 eV and a threshold for TS[3+2] of 0.97 ± 0.06 eV. The CS dissociation pathway is energetically favored by 0.14 ± 0.04 eV over the water loss channel and they have similar entropies of activation. These results help explain why the relative magnitudes of the two pathways differ by only about an order of magnitude, Figure 4.1(f). For competitive analysis of the $x = 7$ dissociation cross

sections (assuming a (6,1)_AA reactant), H_2O loss is measured as 0.80 ± 0.08 eV and the threshold for TS[3+3] is 0.82 ± 0.10 eV, with a difference of only 0.02 ± 0.03 eV. Loss of H_2O is energetically and entropically more favorable at $x = 7$ with its lower threshold for dissociation and larger $\Delta S^{\dagger}_{1000}$ value. As a consequence, here the water loss channel is favored by about two orders of magnitude compared to the competing CS reaction pathway, Figure 4.1(e).

4.4.7 Thermochemical results for sequential dissociation. Thermochemical results for the secondary water loss thresholds using the sequential model for analysis are also reported in Table 4.2. The sequential secondary water losses were modeled by simultaneously analyzing the primary and secondary dissociation product cross sections using eqs 4.4 and 4 × 6, where the difference between the primary and secondary thresholds is used to calculate an independent measurement for the bond dissociation energy for $Co^{2+}(H_2O)_{x-1}$ dissociating to $Co^{2+}(H_2O)_{x-2} + H_2O$. This difference in thresholds can be measured with more precision than the absolute values for each threshold because many systematic sources of uncertainty cancel; however, their accuracy can suffer from the additional assumptions needed in the modeling. Figure 4.4 shows the sequential analysis of primary and secondary cross sections for $x = 8$ as well as the model of the total cross section. Figure 4.4 shows the sequential analysis reproduces both product cross sections and their total well over extended magnitude and energy ranges (~ 2.5 eV). Direct comparison of the models for the total cross sections versus the sequential models of the primary cross sections show that the analogous σ_0, n, and E_0 values are nearly identical with the threshold values within 0.06 eV in all cases. Thus, threshold energies

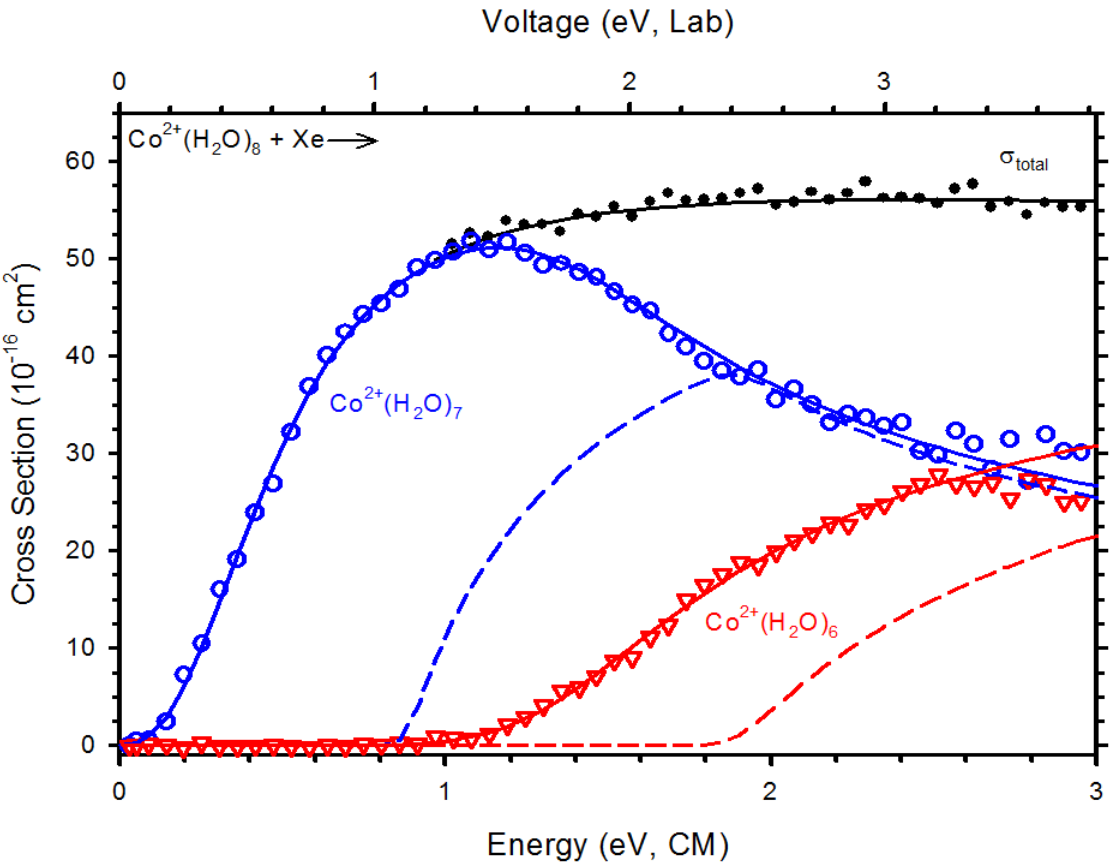

Figure 4.4. Zero-pressure extrapolated cross sections for the CID of $Co^{2+}(H_2O)_8$. Solid lines show the best fits to the primary (open circles) and secondary (open triangles) water loss cross sections using eq 4 × 6 for the sequential model convoluted over the neutral and ion kinetic and internal energy distributions. Dashed lines show the models in the absence of experimental kinetic energy broadening for reactants with an internal energy of 0 K. Optimized parameters for these fits are found in Table 4.2.

for the primary water loss channels are basically unaffected by consideration of the secondary loss channel.

The sequential dissociation at $x = 6$ is modeled as a $(6,0) \rightarrow (4,1) + H_2O \rightarrow (4,0) + 2\ H_2O$ process; however, the primary dissociation to form the (4,1) product is complicated by competition with the CS process, reaction 4.8. Analyzing this sequential process including competition, Figure 4.5, we measure thresholds of 1.08 ± 0.07 eV and 2.22 ± 0.09 eV for the first and second water losses, respectively. The difference between thresholds, 1.13 eV ± 0.08 eV, gives the sequential BDE for $Co^{2+}(H_2O)_4$-H_2O, which is within combined experimental uncertainty of the threshold for single water loss from $Co^{2+}(H_2O)_5$, 1.02 ± 0.07 eV. Similarly, sequential modeling of the $x = 7$ reactant of the CS reaction 4.7 gives a sequential BDE of 1.13 ± 0.06 eV, which is in excellent agreement with the primary dissociation threshold of 1.11 ± 0.08 eV determined for $x = 6$.

4.4.8 Comparison of experimental and theoretical bond enthalpies. Primary and secondary experimental 0 K hydration enthalpies for the loss of water from $Co^{2+}(H_2O)_x$ ($x = 5 – 11$) complexes are compared in Table 4.3. As discussed above, there is evidence that our most accurate interpretations of the data are from the relative energies and GSs predicted at the MP2 level of theory. Therefore only the BDEs from the MP2 predicted GSs are given in Table 4.3 (although alternative interpretations give very similar values, within 3 kJ/mol). Secondary bond enthalpies (obtained from differences between the primary and secondary thresholds) are systematically higher than the values obtained from the corresponding primary thresholds, but agree fairly well. Specifically, the secondary BDE for $x = 5$ agrees within 10 kJ/mol of the primary value, the $x = 6 – 9$

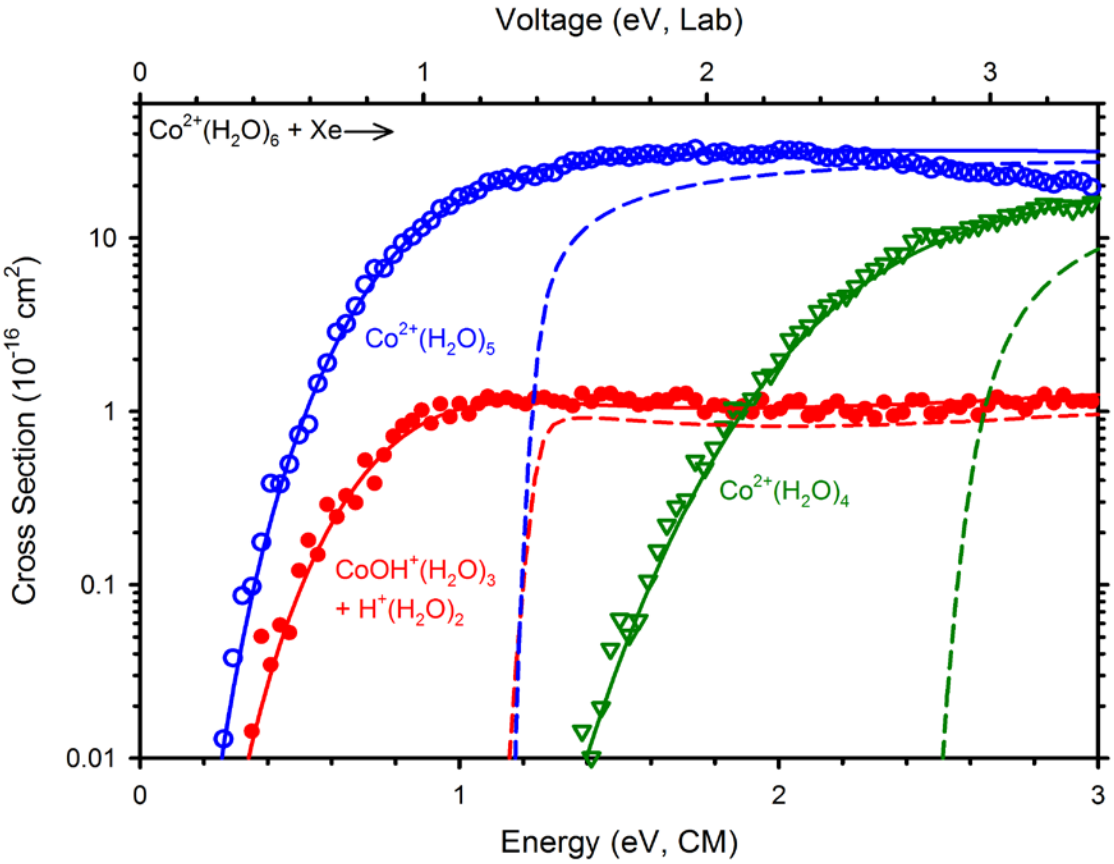

Figure 4.5. Zero-pressure extrapolated cross sections for the CID of $Co^{2+}(H_2O)_6$. Solid lines show the best fits to the primary water loss (open circles), the competing charge separation products (closed circles), and secondary water loss (open triangles) using eq 4.4 and eq 4 × 6 for the competitive sequential model convoluted over the neutral and ion kinetic and internal energy distributions. The dashed lines show the models in the absence of experimental kinetic energy broadening for reactants with an internal energy of 0 K. Optimized parameters for these fits are found in Table 4.2.

Table 4.3. Comparison of Experimental[a] and Theoretical 0 K Hydration Enthalpies (kJ/mol) for $Co^{2+}(H_2O)_x$

x	Reactant	Product	Primary	Secondary	B3LYP[b]	B3LYP-GD3BJ[c]	B3P86[b]	MP2(full)[b]
1	(1,0)	Co^{2+}			408.4 (442.8)	415.2 (418.4)	410.0 (443.0)	498.8 (402.3)
2	(2,0)	(1,0)			326.6 (329.9)	331.7 (335.0)	330.2 (333.6)	310.1 (320.4)
3	(3,0)	(2,0)			228.8 (232.0)	234.9 (238.0)	233.3 (236.5)	211.6 (221.5)
4	(4,0)	(3,0)		167.6 ±7.7	174.4 (177.4)	183.0 (186.0)	178.0 (181.1)	190.9 (200.6)
5	(4,1)	(4,0)	100.0 ±6.4	109.5 ±8.0	101.0 (104.2)	109.1 (112.2)	105.1 (108.3)	98.8 (108.1)
6	(6,0)	(4,1)	107.3 ±7.3	108.7 ±6.0	91.4 (94.8)	107.0 (110.3)	94.0 (97.4)	111.4 (124.1)
7	(6,1)	(6,0)	77.3 ±7.5	84.1 ±6.4	77.4 (80.1)	85.1 (87.8)	80.7 (83.5)	76.1 (84.3)
8	(6,2)	(6,1)	67.7 ±5.8	74.1 ±7.5	72.7 (75.5)	80.1 (82.8)	65.6 (78.8)	82.1 (92.0)
9	(6,3)	(6,2)	57.7 ±6.6	64.3 ±8.8	72.7 (75.5)	80.1 (85.9)	78.2 (81.1)	77.4 (85.7)
10	(6,4)	(6,3)	45.9 ±7.0	60.0 ±8.7	59.2 (61.9)	67.2 (69.9)	61.5 (64.2)	60.0 (66.9)
11	(6,5)	(6,4)	40.2 ±7.1		56.4 (58.9)	65.9 (68.4)	58.9 (61.4)	59.5 (66.4)
MAD[d]			6.8[e]	7.9	9.5 (11.4)	14.1 (17.3)	11.2 (14.0)	8.8 (17.0)
MAD[f]				7.6[e]	7.1 (6.8)	6.8 (9.5)	8.1 (7.5)	8.8 (12.0)

[a]Values from Table 4.2. [b]Theoretical values with (and without) cp correction. Single point energies calculated at the indicated level of theory using 6-311+G(2d,2p) basis set using B3LYP/6-311+G(d,p) geometries and zero point energy corrected. [c]Single point energies calculated at the indicated level of theory using 6-311+G(2d,2p) basis set using B3LYP-GD3BJ/6-311+G(d,p) geometries and zero point energy corrected. [d]Mean absolute deviations from primary experimental BDEs. [e]Mean experimental uncertainty. [f]Mean absolute deviations from secondary experimental BDEs.

secondary BDEs are similar to the primary values (less than 7 kJ/mol difference), and the largest complex studied, $x = 10$, has primary and secondary BDEs that differ by a larger amount of 14 kJ/mol.

Table 4.3 also includes theoretical 0 K hydration bond enthalpies for the loss of water from $Co^{2+}(H_2O)_x$ ($x = 1 – 11$) complexes with and without cp corrections. Our experimental values agree well with calculated 0 K hydration enthalpies at all levels of theory considered here, with MADs of 9 – 14 kJ/mol for primary BDEs and 7 – 9 kJ/mol for secondary BDEs, Table 4.3. When cp corrections are not included, agreement is worsened by 2 – 8 kJ/mol for primary BDEs. Interestingly, Table 4.3 shows the addition of dispersion forces to B3LYP degrades the agreement with experiment by ~5 kJ/mol. Figure 4.6 graphically compares the primary and secondary experimental $Co^{2+}(H_2O)_x$ BDEs for $x = 4 – 11$ with theoretical values. BDEs decrease very sharply from x = 4 to 5, attributed above to putting the fifth ligand in the second solvent shell. The increase in BDEs from $x = 5$ and 6 results from putting all ligands back into the first solvent shell of the (6,0) complex. This leads to a relatively large decrease from $x = 6$ to 7, which again involves addition to the second solvent shell. The almost linear trend for $x = 7 – 10$ emphasizes no changes in coordination number over this range of complex sizes. Figure 4.6 shows that MP2 predicts a slightly larger decrease in BDEs from $x = 6$ to 7 compared to that experimentally observed and a significantly larger decrease compared to the DFT levels, which do not predict a solvent shell growth here. MP2 results also predict a small increase in BDEs from $x = 7$ and 8, whereas experiment and DFT results show decreases. This difference is attributed to MP2 being more sensitive to long range hydrogen bonding. Here attachment of the second shell ligand in the (6,1)_AA complex perturbs

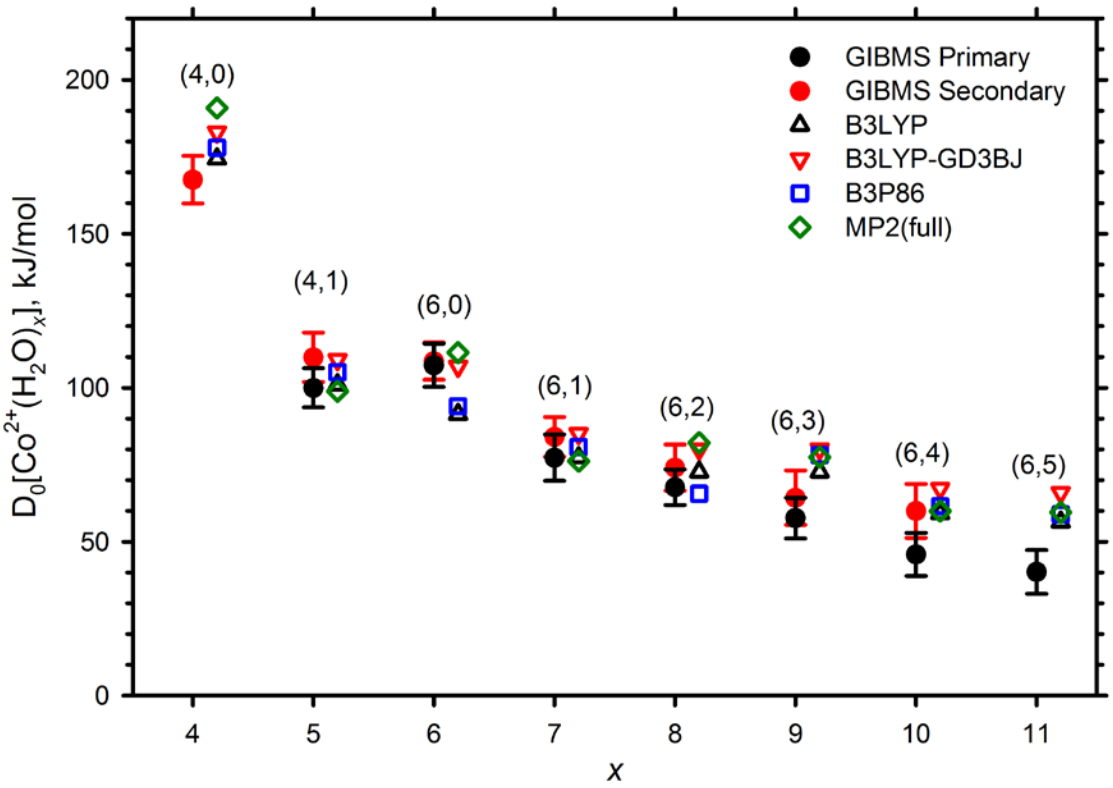

Figure 4.6. Comparison of experimental primary (black solid circles) and secondary (red solid circles) 0 K bond energies with theoretical B3LYP (open black up triangles), B3LYP-GD3BJ (open red down triangles), B3P86 (open blue squares) and MP2 values (open green diamonds), and with cp corrections.

the network of these interactions established in (6,0), Figure 4.2. Addition of the eighth water takes advantage of the already perturbed network such that the (6,2) GS has a larger BDE.

4.4.9 Comparison to Fe^{2+} and Ni^{2+} hydration enthalpies. Figure 4.7 plots the experimental 0 K bond enthalpies for $Co^{2+}(H_2O)_x$ ($3d^7$) with those previously determined for $Fe^{2+}(H_2O)_x$ ($3d^6$)[1] and $Ni^{2+}(H_2O)_x$ ($3d^8$),[2] to highlight the trends for each value of x where x = 4 - 11. Figure 4.7 illustrates that the BDEs for larger complexes ($x \geq 7$) are essentially equivalent, within experimental uncertainty of each other. This trend is not unexpected as all three metals are predicted to have similar octahedral inner-shell GSs for $x \geq 6$ with similar second solvent shell growth. Thus, the BDEs for all three metals at the large x values are governed by loss of a water accepting hydrogen bonds from one or two inner shell waters. An interesting diversion from this similarity of BDEs occurs at x = 5 and 6, where the BDE for Co^{2+} is lower than that of Fe^{2+}, which is lower than that of Ni^{2+}, whereas values for x = 6 increase steadily from Fe^{2+} to Co^{2+} to Ni^{2+}. The latter changes can be assigned to the expected trend for (6,0) complexes as the metal dication gets smaller (because of the increasing nuclear charge as one moves across the periodic table), 0.78 to 0.75 to 0.69 Å for Fe^{2+} to Co^{2+} to Ni^{2+}, respectively.[61] The very different trend for x = 5 can be attributed to the differing coordination numbers of the different metals, as iron and nickel have all five water ligands directly bound to the metal ion in (5,0) GSs and follow the same increasing BDE trend exhibited for x = 6. In contrast, for cobalt, the fifth water is more weakly bound in the second solvent shell in a (4,1) GS.

At x = 4, all geometries are predicted to be (4,0), but the BDEs do not follow the nuclear charge trend seen for x = 6 because the geometries are actually distinct. For Ni^{2+}

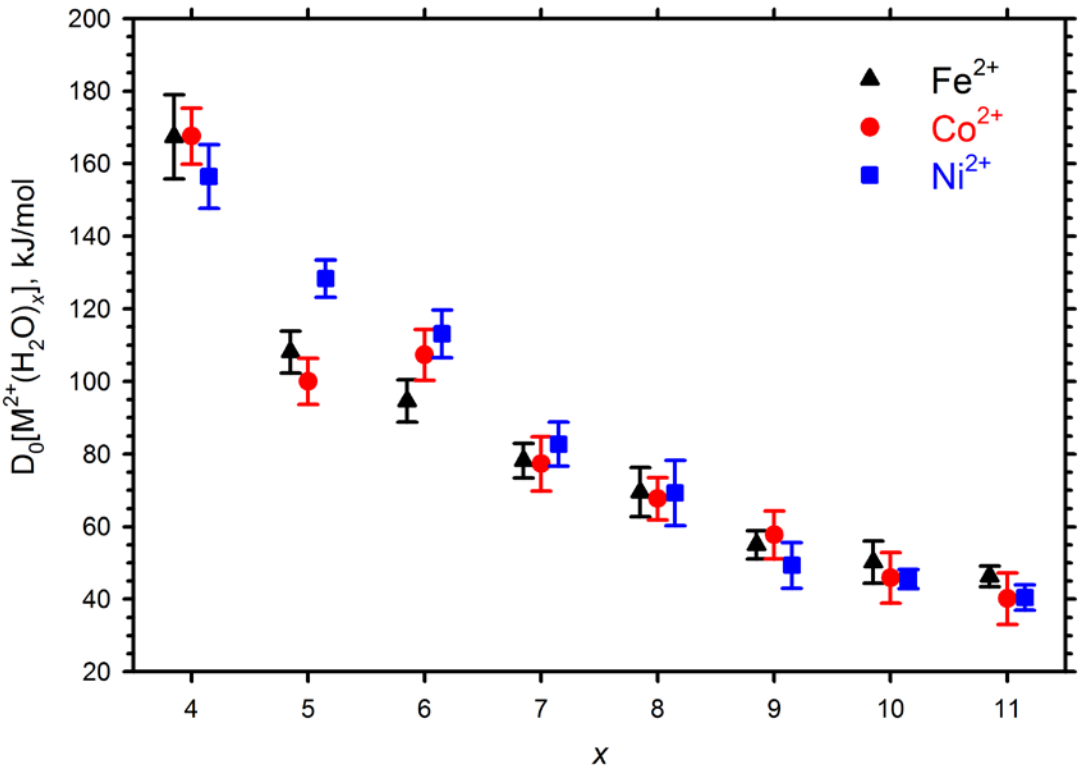

Figure 4.7. Comparison of experimental primary 0 K bond energies for $Fe^{2+}(H_2O)_x$ (black triangles, reference 1), $Co^{2+}(H_2O)_x$ (red circles, present work), and $Ni^{2+}(H_2O)_x$ (blue squares, reference 2). All $x = 4$ values are secondary 0 K BDE values.

($3d^8$), calculations showed triplet state (4,0) GS had a see-saw geometry with singly occupied molecular orbitals (SOMOs) in octahedral-like e_g MOs.[2] For Co^{2+} ($3d^7$), the quartet state (4,0) GS SOMOs are the three tetrahedral t_2 MOs, in agreement with that found for the (3,1) GS of $CoOH^+(H_2O)_4$.[8] Thus, the Co^{2+} (4,0) GS has a distorted tetrahedral molecular geometry with ∠O-Co-O of 105° and 112°. This scheme is similar for Fe^{2+} ($3d^6$), where the quintet state (4,0) GS also exhibits distorted tetrahedral geometry, but distorts to a lesser degree than Co^{2+} with ∠O-Co-O of 108° and 110°. The distortion and increased ligand-ligand repulsion for Co^{2+} and to a greater extent for Ni^{2+} explain the decreasing BDE trend at $x = 4$.

4.4.10 Conversion of 0 K hydration energies to 298 K. In all cases, the threshold energies obtained including lifetime effects are assigned as the 0 K bond energies. A rigid rotor/harmonic oscillator (RR/HO) approximation using the vibrational frequencies (scaled by 0.989) and rotational constants calculated at the B3LYP/6-311+G(d,p) level of theory was used to calculate ΔH_{298}-ΔH_0 and $T\Delta S_{298}$ values for dissociation. These factors were used to convert the 0 K bond energies into 298 K bond enthalpies (ΔH_{298}) and to determine free energies (ΔG_{298}) of dissociation. These values are listed for $Co^{2+}(H_2O)_x$, $x = 4 – 11$ in Table 4.4. The uncertainties in these conversions were obtained by scaling the vibrational frequencies up and down by 10%. It should be noted that some of the low vibrational frequencies correspond to torsional motions of the water ligands and thus the RR/HO approximations may not be accurate. The 298 K hydration enthalpies (ΔH_{298}) track the trends from the 0 K hydration enthalpies (ΔH_0) discussed above. The free energies of dissociation (ΔG_{298}) decrease with increasing number of water ligands for all complexes observed. Note that the $x = 11$ free energy of

Table 4.4. Conversion of 0 K Thresholds to 298 K Enthalpies and Free Energies (kJ/mol) for $Co^{2+}(H_2O)_x$[a]

x	Reactant	Product	ΔH_0[b]	ΔH_{298}-ΔH_0[c]	ΔH_{298}	$T\Delta S_{298}$[c]	ΔG_{298}
4	(4,0)	(3,0)	167.6 (7.7)	-3.7 (0.9)	163.9 (7.7)	24.6 (2.3)	139.3 (8.6)
5	(4,1)	(4,0)	98.9 (6.4)	4.5 (0.4)	103.4 (6.4)	39.3 (1.0)	64.1 (6.7)
6	(6,0)	(4,1)	107.3 (7.3)	-0.8 (0.7)	106.4 (7.3)	43.7 (1.1)	62.8 (8.6)
		TS[3+2]	93.9 (5.6)	3.5 (0.5)	97.4 (5.6)	20.8 (0.4)	76.6 (5.6)
7	(6,1)	(6,0)	77.3 (7.5)	3.6 (0.4)	80.9 (7.5)	36.8 (1.0)	44.1 (8.0)
		TS[3+3]	79.0 (9.3)	4.8 (0.5)	83.7 (9.4)	28.4 (0.3)	55.4 (9.7)
8	(6,2)	(6,1)	67.7 (5.8)	3.6 (0.4)	71.3 (5.8)	40.3 (1.0)	30.9 (6.2)
9	(6,3)	(6,2)	57.7 (8.3)	4.5 (0.5)	62.3 (8.3)	44.1 (1.0)	18.2 (9.0)
10	(6,4)	(6,3)	45.9 (7.9)	2.2 (0.4)	48.1 (7.9)	33.9 (1.2)	14.1 (8.5)
11	(6,5)	(6,4)	40.2 (10.8)	3.4 (0.4)	43.6 (10.8)	43.5 (1.1)	0.04 (10.9)

[a]Uncertainties in parentheses. [b]Values from Table 4.2. [c]Values are calculated from the vibrational frequencies and rotational constants calculated at the B3LYP/6-311+G(d,p) level of theory. Uncertainties are found by scaling the vibrational frequencies up and down by 10%.

dissociation is only 0.04 ± 0.9 kJ/mol, which indicates that at room temperature its dissociation is nearly spontaneous. This explains why our source does not make larger clusters (with weaker hydration energies) efficiently.

4.4.11 Charge separation: Energetic barriers. Table 4.5 presents the predicted barrier heights for the charge separation processes of $Co^{2+}(H_2O)_x$, where $x = 4 – 7$, including reactions 4.7 – 4.9, and also compares the experimental and theoretical barrier heights of the charge separation pathways to the experimental and predicted energies for water loss dissociation pathways. The structures of each of the likely rate-limiting TSs are shown in Figure 4.3, and in each case correspond to heterolytic cleavage of an O-H bond. The dominant CS channel of $Co^{2+}(H_2O)_7$ is $CoOH^+(H_2O)_3 + H^+(H_2O)_3$, reaction 4.7, which occurs through TS[3+3]. Theory finds that this barrier height is 60 – 94 kJ/mol, such that the B3LYP-GD3BJ value agrees best with the experimental value of 79 ± 9 kJ/mol. DFT levels of theory predict the TS[3+3] barrier to be lower in energy than the single water loss BDE by 4 – 23 kJ/mol; however, the MP2 level calculates water loss to be lower in energy than the TS[3+3] pathway by 28 kJ/mol. Modeling the competitive channels determines the threshold for charge separation is indeed higher than that for water loss but by only 2 ± 3 kJ/mol (Table 4.5). This energetic difference is closest to that predicted by B3LYP-GD3BJ. However, the MP2(full) level best represents the enthalpic preference for water loss over CS as determined experimentally here. The predicted reverse Coulomb barriers for $CoOH^+(H_2O)_3 + H^+(H_2O)_3$ to TS[3+3] are nearly equivalent, 146 – 150 kJ/mol for the DFT levels of theory and slightly lower for MP2 at 139 kJ/mol. Note that the overall CS reaction 4.8 is strongly exothermic.

Table 4.5. Comparison of 0 K Transition State Energies and Hydration Enthalpies (kJ/mol)

x	Reactant	Product	Experiment	B3LYP[a]	B3LYP-GD3BJ[b]	B3P86[a]	MP2(full)[a]
4	(4,0)	(3,0)	168 ± 8[c]	177.4	186.0	181.1	200.6
		TS[2+1]		126.0	134.6	127.2	156.9
		$CoOH^+(H_2O)_2$ + H^+H_2O		-37.3	-27.8	-35.8	7.7
5	(4,1)	(4,0)	100 ± 6[c]	104.2	112.2	108.3	108.1
		TS[(3,2)-(3,1,1)]		109.0	116.6	110.2	117.8
		TS[2+2]		77.2	89.3	77.5	117.3
		$CoOH^+(H_2O)_2$ + $H^+(H_2O)_2$		-79.6	-65.9	-79.7	-47.6
		TS[3+1]		123.6	132.1	125.6	142.3
		$CoOH^+(H_2O)_3$ + H^+H_2O		-30.2	-21.2	-29.8	-4.1
6	(6,0)	(4,1)	107 ± 7[c]	94.8	110.3	97.4	124.1
		TS[3+2]	94 ± 6[d]	66.5	86.2	65.9	117.0
		$CoOH^+(H_2O)_3$ + $H^+(H_2O)_2$		-81.9	-61.2	-84.7	-23.5
7	(6,1)	(6,0)	77 ± 8[c]	80.1	87.8	83.5	65.6
		TS[3+3]	79 ± 9[d]	59.8	83.3	60.5	93.5
		$CoOH^+(H_2O)_3$ + $H^+(H_2O)_3$		-87.9	-63.1	-89.0	-45.9

[a]Single point energies corrected for zero point energy calculated at the indicated level of theory using 6-311+G(2d,2p) basis set with geometries and vibrational frequencies calculated at the B3LYP/6-311+G(d,p) level. [b]Single point energies corrected for zero point energy calculated 6-311+G(2d,2p) basis set with geometries and vibrational frequencies calculated at the B3LYP-GD3BJ/6-311+G(d,p) level. [c]Values taken from Table 4.2, using the primary dissociation channel model for $x = 5 – 7$ and the sequential model for $x = 4$. [d]Values taken from Table 4.2 calculated by competitive analysis model (eq 4.4).

For $x = 6$, the dominant CS channel of $CoOH^+(H_2O)_3 + H^+(H_2O)_2$ occurs through TS[3+2] with predicted barrier height of 66 – 117 kJ/mol. Again, the experimental value of 94 ± 6 kJ/mol agrees best with B3LYP-GD3BJ results, which also predicts the threshold for reaction 4.1 well. All levels of theory predict the barrier height of TS[3+2] to be lower in energy than the water loss BDE by 24 – 32 kJ/mol for DFT levels and 7 kJ/mol for MP2. Modeling of the data suggests that the threshold for charge separation is 13 ± 4 kJ/mol lower in energy than that for water loss, most closely agreeing with the enthalpic predictions of the B3LYP-GD3BJ and MP2 levels. The predicted values for the reverse Coulomb barrier are nearly identical to those for $x = 7$, with values only ~ 1 kJ/mol higher. Again, the overall CS reaction is exothermic.

For $x = 5$, the predicted barrier heights for TS[2+2] range from 77 – 117 kJ/mol and 124 -142 kJ/mol for TS[3+1]. DFT levels of theory predict the TS[2+2] barrier to be lower in energy than the single water loss BDE by 23 – 31 kJ/mol; however, the MP2 level calculates TS[2+1] to be higher in energy by 9 kJ/mol. All levels of theory predict the TS[3+1] barrier height to be higher in energy than water loss by 17 - 34 kJ/mol. These results and the MP2 results for TS[2+2] are consistent with no primary dissociative CS pathways being observed directly from the CID of $x = 5$. To investigate this further, a complete reaction coordinate for the decomposition of $Co^{2+}(H_2O)_5$ by water loss or charge separation to $CoOH^+(H_2O)_2 + H^+(H_2O)_2$ was investigated theoretically and is shown in Figure 4.8. Here we find that the rate-limiting transition state for this process is not TS[2+2], but TS[(3,2)-(3,1,1)] in which a second solvent shell water must be promoted to the third solvent shell. TS[(3,2)-(3,1,1)] is found to be higher in energy than water loss for all levels of theory (Table 4.5). Hence, all levels of theory agree that both

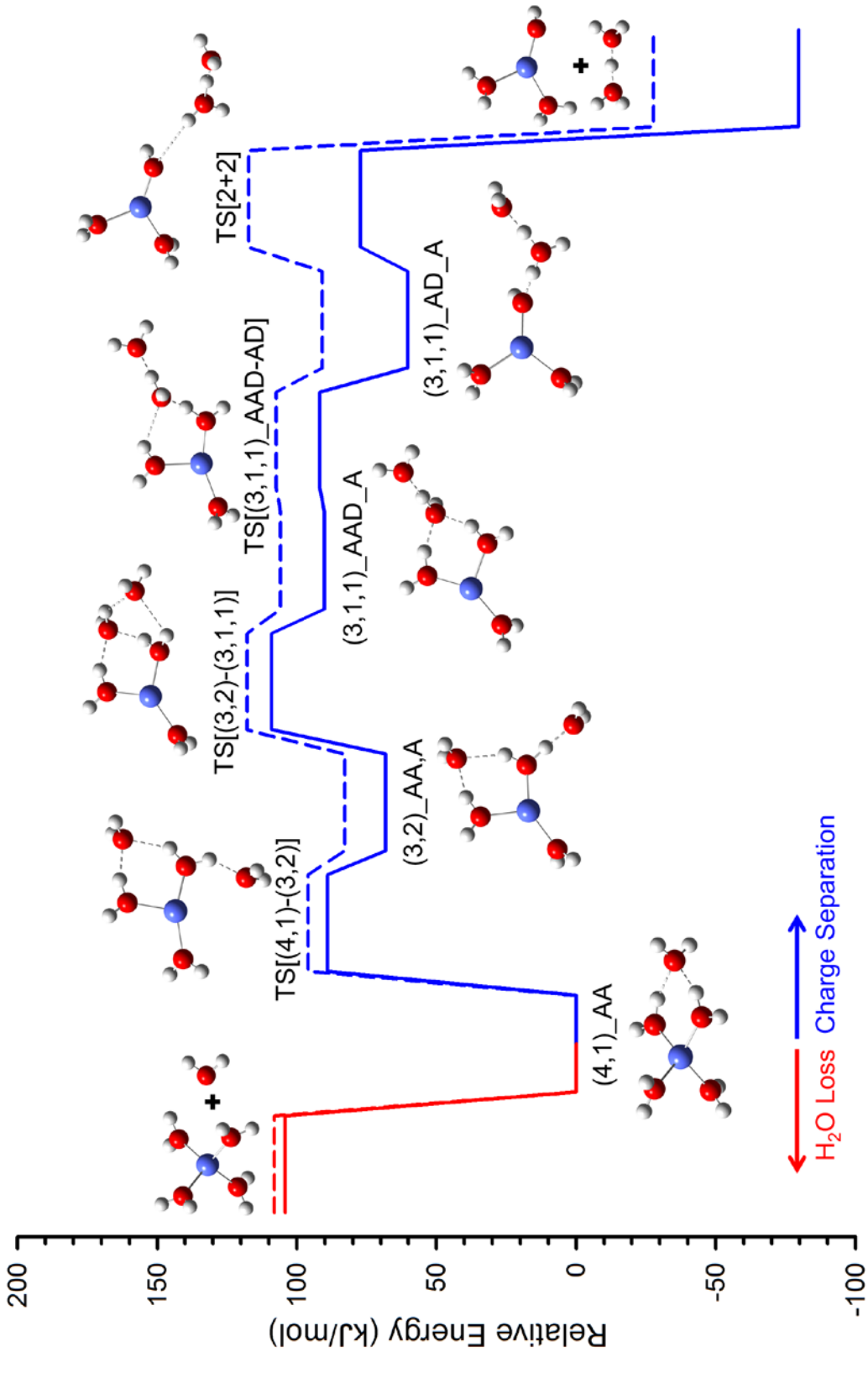

Figure 4.8. Reaction coordinates for water loss and charge separation pathways of $Co^{2+}(H_2O)_5$ from the (4,1)_AA GS. Single point energies are calculated at the B3LYP (solid line) and MP2 (dashed line) levels of theory with the 6-311+G(d,p) basis set and include zero point energies.

charge separation processes available for the $x = 5$ complex are enthalpically disfavored compared with water loss in reaction 4.1.

The predicted barrier heights for the $x = 4$ rate-limiting TS[2+1] range from 126 to 157 kJ/mol, with a reverse barrier height predicted to be ~ 163 kJ/mol for DFT levels and 149 kJ/mol for MP2. The complete potential energy surface is shown in Figure 4.9 and confirms that TS[2+1] is rate limiting. This particular system ($x = 4$) has been examined theoretically before by Beyer and Metz, who obtained a TS[2+1] barrier height of 145 kJ/mol and a reverse barrier of 166 kJ/mol.[62] Compared to water loss, all levels of theory predict that the barrier height for TS[2+1] is 44 – 54 kJ/mol lower in energy than water loss. As x increases, the reverse Coulomb barriers increase for all levels of theory here, consistent with observations from previous studies of hydrated Fe^{2+}, Ni^{2+}, Zn^{2+}, and Cd^{2+} systems. [1-2,5,7]

The theoretical conclusion that TS[2+1] lies below the energy for formation of $Co^{2+}(H_2O)_3 + H_2O$ is consistent with the observation of reaction 4.9 by Metz and coworkers[57] as well as observation of this process in the dissociation of the $Co^{2+}(H_2O)_6$ complex here. The question remains why no signs of this reaction were observed for dissociation of $Co^{2+}(H_2O)_5$, Figure 4.1(g). Notably, this complex could only be generated in the source in sufficient abundance for CID study by use of the in-source electrodes, with maximum ion signal at -17.0 V on the electrodes. It seems possible that these conditions perturb the behavior of the $Co^{2+}(H_2O)_5$ complex formed, but this conclusion is not consistent with the reasonable thermochemistry that analysis of these data provided above. Further, as noted in the experimental section, additional experiments designed to

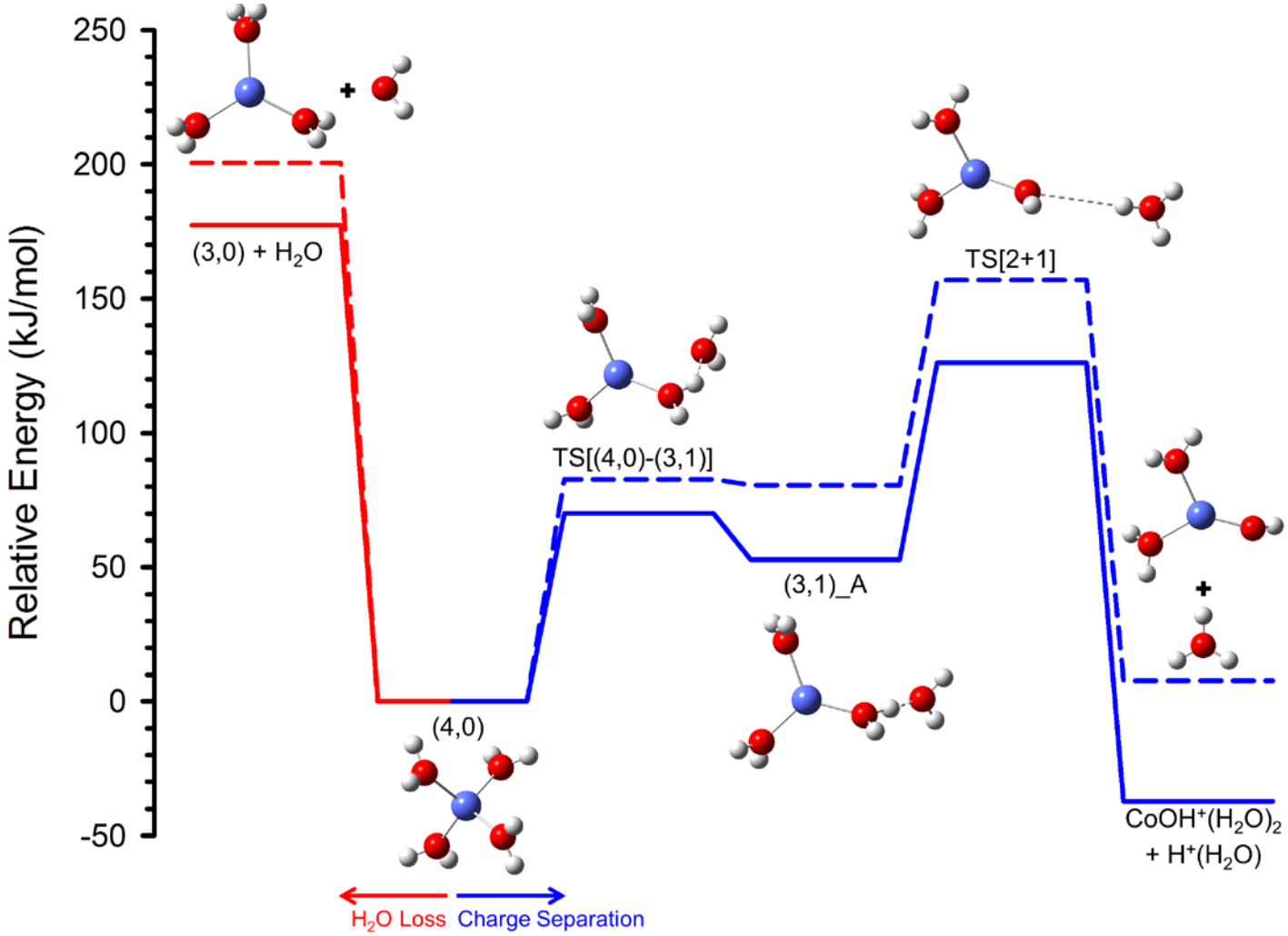

Figure 4.9. Reaction coordinates for water loss and charge separation pathways of $Co^{2+}(H_2O)_4$ from the (4,0) GS. Single point energies are calculated at the B3LYP (solid line) and MP2 (dashed line) levels of theory with the 6-311+G(d,p) basis set and include zero point energies.

test complete thermalization by adding nitrogen gas in a collision cell in the source region led to no changes in the observed behavior of either $x = 5$ or 6 complexes.

Discussed above and seen in Figure 4.1, the experimental cross sections show that charge separation occurs for $Co^{2+}(H_2O)_x$ complexes of $x = 4$, 6, and 7. From earlier definitions of critical size, we would assign the maximum x at which CS and water loss become competitive to be $x_{crit} = 7$. In contrast, modeling the competitive processes for $x = 7$ shows that the CS process is energetically disfavored over water loss. The largest value of x at which the charge separation is energetically favored over the loss of one water ligand for $Co^{2+}(H_2O)_x$ is $x_{crit} = 6$, as determined by modeling the competitive pathways of TS[3+2] and water loss. This assignment also agrees with theory where the barrier height for TS[3+2] is predicted to be lower than water loss by all levels of theory investigated here (Table 4.5). This x_{crit} value for Co^{2+} is greater than found by Kebarle and coworkers, $x_{crit} = 4$,[12,16-17] and Shvartzburg and Siu, $x_{crit} = 5$, although in both of these reports, their observations do not permit both partners in the charge separation pathways to be linked together, thereby prohibiting a definitive assignment.[14] A value of $x_{crit} = 6$ would also explain the difficulty of generating smaller complex sizes, and potentially contribute to the lack of evidence of expected CS pathways at $x = 5$. A similar lack of CS pathways phenomenon was observed for $Ni^{2+}(H_2O)_4$,[2] in which larger complex sizes of x showed evidence for a CS pathway from $x = 4$, yet none were observed when this ion was selected as the reactant for CID. This observation was explained by a dynamical hypothesis that the second shell water ligand of (4,1)_AA provides a larger collision cross section compared to a more compact structure, i.e. (5,0). Collisions at larger impact parameters with an outer shell water ligand will preferentially excite this ligand leading

to direct water loss, whereas smaller impact parameters leading to more general vibrational excitation are needed for the system to explore the tight TSs leading to charge separation.

4.5 Conclusion

Complementing our previous transition metal dication hydration studies,[1-7] the kinetic energy dependent cross sections for collision-induced dissociation of $Co^{2+}(H_2O)_x$ complexes were determined using guided ion beam tandem mass spectrometry for $x = 5 - 11$. The dominant CID pathway for all values of x studied is the loss of a single water molecule from the reactant ion. The data were analyzed to yield primary and secondary bond dissociation energies (BDEs) for the loss of one or two ligands from the reactant complexes. There is excellent agreement between the primary and secondary BDEs along with good agreement with theoretical hydration enthalpies for all levels examined here. Our best experimental results are believed to correspond to the measurement of primary dissociation thresholds as they have fewer uncertainties regarding the distribution of energy available to the dissociating species.

There are four distinct trends in the experimental and theoretical BDEs for the $Co^{2+}(H_2O)_x$ systems. The BDEs decrease rapidly from $x = 4$ to 5 as all waters are directly bound to the metal center in $x = 4$, whereas a second solvent shell is formed with a double accepting (AA) water in $x = 5$. The slight increase in BDEs from $x = 5$ to 6 indicates a change of coordination numbers (from 4 to 6) as all waters become bound directly to the metal center again at $x = 6$. Another large decrease indicating second solvent shell formation is observed from $x = 6$ to 7. For larger complexes, $x = 7 – 11$, the waters lost

are all AA in the second shell, such that their BDEs decrease slowly. MP2 theory is believed to account for the trends in these BDEs more accurately than DFT levels.

Charge separation (CS) processes are also observed as higher energy product pathways compared to water loss and become competitive primary dissociative pathways for x = 4, 6, and 7. The molecular parameters for the tight TSs associated with charge separation are calculated and used to analyze the product cross sections for the CID of $Co^{2+}(H_2O)_6$ and $Co^{2+}(H_2O)_7$ by including the competition between water loss and charge separation reactions to obtain accurate bond energies and CS barriers. Oddly, the charge separation reaction 4.9 is not observed in our CID of x = 5, an observation for which there is no ready explanation. Experimental thresholds, in agreement with theory, determine that the $Co^{2+}(H_2O)_x$ critical size (according to the energetic definition) for competition between the CS and water loss pathways is x_{crit} = 6.

4.6 References

(1) Hofstetter, T. E.; Armentrout, P. B., Threshold Collision-Induced Dissociation and Theoretical Studies of Hydrated Fe(II): Binding Energies and Coulombic Barrier Heights. *J. Phys. Chem. A* **2013,** *117,* 1110-1123.

(2) Coates, R. A.; Armentrout, P. B., Thermochemical Investigations of Hydrated Nickel Dication Complexes by Threshold Collision-Induced Dissociation and Theory. *J. Phys. Chem. A* **2017,** *121,* 3629-3646.

(3) Sweeney, A. F.; Armentrout, P. B., Hydrated Copper Ion Chemistry: Guided Ion Beam and Computational Investigation of $Cu^{2+}(H_2O)_n$ (n = 7-10) Complexes. *Eur. J. Mass Spectrom. (Chichester, Eng)* **2015,** *21,* 497-516.

(4) Cooper, T. E.; Carl, D. R.; Armentrout, P. B., Hydration Energies of Zinc (II): Threshold Collision-Induced Dissociation Experiments and Theoretical Studies. *J. Phys. Chem. A* **2009,** *113,* 13727–13741.

(5) Cooper, T. E.; Armentrout, P. B., An Experimental and Theoretical Investigation of the Charge Separation Energies of Hydrated Zinc (II): Redefinition of the Critical Size. *J. Phys. Chem. A* **2009,** *113,* 13742–13751.

(6) Cooper, T. E.; Armentrout, P. B., Threshold Collision-induced Dissociation of Hydrated Cadmium (II): Experimental and Theoretical Investigation of the Binding Energies for $Cd^{2+}(H_2O)_n$ Complexes (n = 4 – 11). *Chem. Phys. Lett.* **2010,** *486*, 1-6.

(7) Cooper, T. E.; Armentrout, P. B., Sequential Bond Energies and Barrier Heights for the Water Loss and Charge Separation Dissociation Pathways of $Cd^{2+}(H_2O)_n$, n = 3-11. *J. Chem. Phys.* **2011,** *134*, 114308.

(8) Coates, R. A.; Armentrout, P. B., Binding Energies of Hydrated Cobalt Hydroxide Ion Complexes: A Guided Ion Beam and Theoretical Investigation. *J. Chem. Phys.* **2017,** *147*, 064305.

(9) Sweeney, A. F.; Armentrout, P. B., Guided Ion Beam Studies of the Collision-Induced Dissociation of $CuOH^+(H_2O)_n$ (n = 1-4): Comprehensive Thermodynamic Data For Copper Ion Hydration. *J. Phys. Chem. A* **2014,** *118*, 10210-10222.

(10) Rodriguez-Cruz, S. E.; Jockusch, R. A.; Williams, E. R., Hydration Energies of Divalent Metal Ions, $Ca^{2+}(H_2O)_n$ (n = 5-7) and $Ni^{2+}(H_2O)_n$ (n = 6-8), Obtained by Blackbody Infrared Radiative Dissociation. *J. Am. Chem. Soc.* **1998,** *120*, 5842-5843.

(11) O'Brien, J. T.; Williams, E. R., Coordination Numbers of Hydrated Divalent Transition Metal Ions Investigated With IRPD Spectroscopy. *J. Phys. Chem. A* **2011,** *115*, 14612-9.

(12) Jayaweera, P.; Blades, A. T.; Ikonomou, M. G.; Kebarle, P., Production and Study in the Gas-Phase of Multiply Charged Solvated or Coordinated Metal-Ions. *J. Am. Chem. Soc.* **1990,** *112*, 2452-2454.

(13) Cheng, Z. L.; Siu, K. W. M.; Guevremont, R.; Berman, S. S., Electrospray Mass Spectrometry: A Study on Some Aqueous Solutions of Metal Salts. *J. Am. Soc. Mass Spectrom.* **1992,** *3*, 281-288.

(14) Shvartsburg, A. A.; Siu, K. W. M., Is There a Minimum Size for Aqueous Doubly Charged Metal Cations? *J. Am. Chem. Soc.* **2001,** *123*, 10071-10075.

(15) Peschke, M.; Blades, A. T.; Kebarle, P., Binding Energies for Doubly-charged Ions M^{2+} = Mg^{2+}, Ca^{2+} and Zn^{2+} with the Ligands L = H_2O, Acetone and N-methylacetamide in Complexes ML_n^{2+} for n = 1 - 7 from Gas Phase Equilibra Determinations and Theoretical Calculations. *J. Am. Chem. Soc.* **2000,** *122*, 10440-10449.

(16) Blades, A. T.; Jayaweera, P.; Ikonomou, M. G.; Kebarle, P., Ion-Molecule Clusters Involving Doubly Charged Metal-Ions (M^{2+}). *Int. J. Mass Spectrom. Ion Processes* **1990,** *102*, 251-267.

(17) Blades, A. T.; Jayaweera, P.; Ikonomou, M. G.; Kebarle, P., Studies of Alkaline-Earth and Transition-Metal M^{++} Gas-Phase Ion Chemistry. *J. Chem. Phys.* **1990,** *92*, 5900-5906.

(18) Barceloux, D. G., Cobalt. *J. Toxicol. Clin. Toxicol.* **1999,** *37*, 201-206.

(19) Prashanth, L.; Kattapagari, K. K.; Chitturi, R. T.; Baddam, V. R. R.; Prasad, L. K., A Review on Role of Essential Trace Elements in Health and Disease. *J. Dr. NTR Univ. Health Sci.* **2015,** *4*, 75-85.

(20) Muntean, F.; Armentrout, P. B., Guided Ion Beam Study of Collision-Induced Dissociation Dynamics: Integral and Differental Cross Sections. *J. Chem. Phys.* **2001,** *115*, 1213-1228.

(21) Ervin, K. M.; Armentrout, P. B., Translational Energy Dependence of $Ar^+ + XY \rightarrow ArX^+ + Y$ (XY = H_2, D_2, HD) from Thermal to 30 eV c.m. *J. Chem. Phys.* **1985,** *83*, 166-189.

(22) Moision, R. M.; Armentrout, P. B., An Electrospray Source for Thermochemical Investigation with the Guided Ion Beam Mass Spectrometer. *J. Am. Soc. Mass Spectrom.* **2007,** *18*, 1124-1134.

(23) Shaffer, S. A.; Prior, D. C.; Anderson, G. A.; Udseth, H. R.; Smith, R. D., An Ion Funnel Interface for Improved Ion Focusing and Sensitivity Using Electrospray Ionization Mass Spectrometry. *Anal. Chem.* **1998,** *70*, 4111-4119.

(24) Carl, D. R.; Moision, R. M.; Armentrout, P. B., In-source Fragmentation Technique for the Production of Thermalized Ions. *J. Am. Soc. Mass Spectrom.* **2009,** *20*, 2312-2317.

(25) Moore, C. E., *Atomic Energy Levels, NSRDS-NBS 35*. Washington, D. C., 1971; Vol. III, p 1.

(26) Carl, D. R.; Chatterjee, B. K.; Armentrout, P. B., Threshold Collision-induced Dissociation of $Sr^{2+}(H_2O)_x$ complexes (x = 1 – 6): An Experimental and Theoretical Investigation of the Complete Inner Shell Hydration Energies of Sr^{2+}. *J. Chem. Phys.* **2010,** *132*, 1-12.

(27) Ye, S. J.; Armentrout, P. B., Absolute Thermodynamic Measurements of Alkali Metal Cation Interactions with a Simple Dipeptide and Tripeptide. *J. Phys. Chem. A* **2008,** *112*, 3587-3596.

(28) Carpenter, J. E.; McNary, C. P.; Furin, A.; Sweeney, A. F.; Armentrout, P. B., How Hot are Your Ions Really? A Threshold Collision-Induced Dissociation Study of Substituted Benzylpyridinium "Thermometer" Ions. *J. Am. Soc. Mass Spectrom.* **2017**.

(29) Cooper, T. E.; O'Brien, J. T.; Williams, E. R.; Armentrout, P. B., Zn^{2+} Has a Primary Hydration Sphere of Five: IR Action Spectroscopy and Theoretical Studies of Hydrated Zn^{2+} Complexes. *J. Phys. Chem. A* **2010,** *114*, 12646–12655.

(30) Wheeler, O. W.; Carl, D. R.; Hofstetter, T. E.; Armentrout, P. B., Hydration Enthalpies of $Ba^{2+}(H_2O)_x$, x = 1-8: A Threshold Collision-Induced Dissociation and Computational Investigation. *J. Phys. Chem. A* **2015,** *119*, 3800-15.

(31) Gerlich, D., Inhomogeneous rf Fields: A Versatile Tool for the Study of Processes with Slow Ions. *Adv. Chem. Phys.* **1992,** *82*, 1-176.

(32) Aristov, N.; Armentrout, P. B., Collision-Induced Dissociation of Vanadium Monoxide Ion. *J. Phys. Chem.* **1986,** *90*, 5135-5140.

(33) Dalleska, N. F.; Honma, K.; Sunderlin, L. S.; Armentrout, P. B., Solvation of Transition Metal Ions by Water. Sequential Binding Energies of $M^+(H_2O)_x$ (x = 1-4) for M = Ti - Cu Determined by Collision-Induced Dissociation. *J. Am. Chem. Soc.* **1994,** *116*, 3519-3528.

(34) Hales, D. A.; Armentrout, P. B., Effect of Internal Excitation on the Collision-Induced Dissociation and Reactivity of Co_2^+. *J. Cluster Science* **1990,** *1*, 127-142.

(35) Daly, N. R., Scintillation Type Mass Spectrometer Ion Detector. *Rev. Sci. Instrum.* **1960,** *31*, 264-267.

(36) Hales, D. A.; Lian, L.; Armentrout, P. B., Collision-Induced Dissociation of Nb_n^+ (n = 2 - 11): Bond Energies and Dissociation Pathways. *Int. J. Mass Spectrom. Ion Processes* **1990,** *102*, 269-301.

(37) Schultz, R. H.; Crellin, K. C.; Armentrout, P. B., Sequential Bond Energies of $Fe(CO)_x^+$ (x = 1 - 5): Systematic Effects on Collision-Induced Dissociation Measurements. *J. Am. Chem. Soc.* **1991,** *113*, 8590-8601.

(38) Beyer, T.; Swinehart, D. F., Number of Multiply-Restricted Partitions. *Commun. Acm.* **1973,** *16*, 379-379.

(39) Stein, S. E.; Rabinovich, B. S., On the Use of Exact State Counting Methods in RRKM Rate Calculations. *Chem. Phys. Lett.* **1977,** *49*, 183-188.

(40) Stein, S. E.; Rabinovitch, B. S., Accurate Evaluation of Internal Energy Level Sums and Densities Including Anharmonic Oscillators and Hindered Rotors. *J. Chem. Phys.* **1973,** *58*, 2438-2445.

(41) Gilbert, R. G.; Smith, S. C., *Theory of Unimolecular and Recombination Reactions*. Blackwell Scientific: London, 1990.

(42) Holbrook, K. A.; Pilling, M. J.; Robertson, S. H., *Unimolecular Reactions*. 2nd ed.; Wiley: New York, 1996.

(43) Truhlar, D. G.; Garrett, B. C.; Klippenstein, S. J., Current Status of Transition-State Theory. *J. Phys. Chem.* **1996,** *100*, 12771-12800.

(44) Rodgers, M. T.; Ervin, K. M.; Armentrout, P. B., Statistical Modeling of Collision-Induced Dissociation Thresholds. *J. Chem. Phys.* **1997,** *106*, 4499-4508.

(45) Rodgers, M. T.; Armentrout, P. B., Statistical Modeling of Competitive Threshold Collision-Induced Dissociation. *J. Chem. Phys.* **1998,** *109*, 1787-1800.

(46) Armentrout, P. B., Statistical Modeling of Sequential Collision-induced Dissociation. *J. Chem. Phys.* **2007,** *126*, 234302.

(47) Armentrout, P. B.; Simons, J., Understanding Heterolytic Bond Cleavage. *J. Am. Chem. Soc.* **1992,** *114*, 8627-8633.

(48) Dalleska, N. F.; Honma, K.; Armentrout, P. B., Stepwise Solvation Enthalpies of Protonated Water Clusters: Collision Induced Dissociation as an Alternative to Equilibrium Studies. *J. Am. Chem. Soc.* **1993,** *115*, 12125-12131.

(49) Becke, A. D., Density-Functional Thermochemistry. III. The Role of Exact Exchange. *J. Chem. Phys.* **1993,** *98*, 5648-5652.

(50) Ditchfield, R.; Hehre, W. J.; Pople, J. A., Self-Consistent Molecular-Orbital Methods. IX. An Extended Gaussian-Type Basis for Molecular-Orbital Studies of Organic Molecules. *J. Chem. Phys.* **1971,** *54*, 724-728.

(51) Grimme, S.; Ehrlich, S.; Goerigk, L., Effect of the Damping Function in Dispersion Corrected Density Functional Theory. *J. Comput. Chem.* **2011,** *32*, 1456-1465.

(52) Perdew, J. P., Density-functional Approximation for the Correlation Energy of the Inhomogeneous Electron Gas. *Phys. Rev. B* **1986,** *33*, 8822-8824.

(53) Möller, C.; Plesset, M. S., Note on an Approximation Treatment for Many-Electron Systems. *Phys. Rev.* **1934,** *46*, 618-622.

(54) Bauschlicher, C. W.; Partridge, H., A Modification of the Gaussian-2 Approach Using Density-Functional Theory. *J. Chem. Phys.* **1995,** *103*, 1788-1791.

(55) Boys, S. F.; Bernardi, R., The Calculation of Small Molecular Interactions by the Differences of Separate Total Energies. Some Procedures with Reduced Errors. *Mol. Phys.* **1970,** *19*, 553-566.

(56) van Duijneveldt, F. B.; van Duijneveldt-van de Rijdt, J. G. C. M.; van Lenthe, J. H., State of the Art in Counterpoise Theory. *Chem. Rev.* **1994,** *94*, 1873-1885.

(57) Faherty, K. P.; Thompson, C. J.; Aguirre, F.; Michne, J.; Metz, R. B., Electronic Spectroscopy and Photodissociation Dynamics of Hydrated Co^{2+} Clusters: $Co^{2+}(H_2O)_n$ (n = 4-7). *J. Phys. Chem. A* **2001,** *105*, 10054-10059.

(58) Marsh, B. M.; Voss, J. M.; Zhou, J.; Garand, E., Coordination Structure and Charge Transfer in Microsolvated Transition Metal Hydroxide Clusters $[MOH]^+(H_2O)_{1-4}$. *Phys. Chem. Chem. Phys.* **2015,** *17*, 23195-23206.

(59) Åkesson, R.; Pettersson, L. G. M.; Sandstrom, M.; Siegbahn, P. E. M.; Wahlgren, U., Theoretical ab Initio SCF Study of Binding Energies and Ligand-Field Effects for the Hexahydrated Divalent Ions of the First-Row Transition Metals. *J. Phys. Chem.* **1992,** *96*, 10773-10779.

(60) Gilson, H. S. R.; Krauss, M., Reinterpretation of the Spectra of Hydrated Co^{++}: An ab Initio Study. *J. Phys. Chem. A* **1998,** *102*, 6525-6532.

(61) Shannon, R. D., Revised Effective Ionic-Radii and Systematic Studies of Interatomic Distances in Halides and Chalcogenides. *Acta Cryst.* **1976,** *32*, 751-767.

(62) Beyer, M. K.; Metz, R. B., Salt-Bridge Transition State for the Charge Separation $Co(H_2O)_4^{2+} \rightarrow CoOH(H_2O)^{2+} + H_3O^+$. *J. Phys. Chem. A* **2003,** *107*, 1760-1762.

CHAPTER 5

BINDING ENERGIES OF HYDRATED COBALT HYDROXIDE ION COMPLEXES: A GUIDED ION BEAM AND THEORETICAL INVESTIGATION

Reprinted with permission from Rebecca A. Coates and P. B. Armentrout, Binding Energies of Hydrated Cobalt Hydroxide Ion Complexes: A Guided Ion Beam and Theoretical Investigation, *The Journal of Chemical Physics*, **2017** *147*, 064305. DOI: 10.1063/1.4991557.

THE JOURNAL OF CHEMICAL PHYSICS **147**, 064305 (2017)

Binding energies of hydrated cobalt hydroxide ion complexes: A guided ion beam and theoretical investigation

Rebecca A. Coates and P. B. Armentrout[a)]
Department of Chemistry, University of Utah, 315 S. 1400 E. Rm 2020, Salt Lake City, Utah 84112, USA

(Received 21 June 2017; accepted 26 July 2017; published online 11 August 2017)

The sequential bond energies of $CoOH^+(H_2O)_x$ complexes, where $x = 1$–4, are measured by threshold collision-induced dissociation using a guided ion beam tandem mass spectrometer. The primary dissociation pathway for all reactants consists of loss of a single water molecule. This is followed by the sequential loss of additional water molecules at higher collision energies for the $x = 2$–4 complexes, whereas the $x = 1$ reactant loses the OH ligand competitively with the H_2O ligand. The kinetic energy dependent cross sections for dissociation of $CoOH^+(H_2O)_x$ complexes are modeled to obtain 0 and 298 K binding energies. Our experimental results agree well with theoretically determined bond dissociation energies (BDEs) at the B3LYP, B3LYP-GD3BJ, B3P86, and MP2(full) levels of theory with a 6-311+G(2d,2p) basis set using geometries and vibrational frequencies determined at the B3LYP/6-311+G(d,p) level. Thermochemical information for the loss of OH from $CoOH^+(H_2O)_x$ where $x = 0$–4 is also derived by combining the present experimental HO–$Co^+(H_2O)$ and water loss BDEs from $CoOH^+(H_2O)_x$ with those for $Co^+(H_2O)_y$ from the literature. These BDEs are also compared to theory with mixed results. *Published by AIP Publishing.* [http://dx.doi.org/10.1063/1.4991557]

INTRODUCTION

Cobalt is a naturally occurring element that has both beneficial and harmful effects on human health. Cobalt is vital for humans because it forms part of the active site in vitamin B12.[1] It has been shown that the metal stimulates erythropoiesis, the production of red blood cells.[2] However, the amount of cobalt we need is very small as the body typically contains less than 1 mg/kg of body weight.[3] Thus, large doses of cobalt are toxic and can be carcinogenic.[1] Sources of environmental cobalt are both natural and anthropogenic. Industrial plants and mines may leak cobalt and other toxic metals into the environment. Once mobile, cobalt particles enter the atmosphere, sediment, and water supply. Most of the population is exposed to cobalt through food and drinking water. Cobalt cannot be destroyed as it makes its way through the environment but may easily become ligated especially in its ionic form.[4] Because of cobalt's mobility and toxic consequences, an important interaction to fully understand is that involving the hydration of cobalt ions in their normal oxidation state.

One way to study hydrated metal ions is in a controlled fashion in the gas-phase. Previously, our group has investigated such systems using threshold collision-induced dissociation (TCID) in tandem with theoretical calculations to investigate the hydration of singly and doubly charged transition metal cations: $M^+(H_2O)_y$ where $M^+ =$ Ti to Cu;[5] and $M^{2+}(H_2O)_y$ where M = Fe,[6] Ni,[7] Cu,[8] Zn,[9,10] and Cd.[11,12] In these $M^{2+}(H_2O)_y$ studies, the dominant processes observed are loss of a single water ligand, reaction (1),

$$M^{2+}(H_2O)_y \rightarrow M^{2+}(H_2O)_{y-1} + H_2O, \quad (1)$$

followed by sequential loss of additional water molecules when $y > 1$. In addition, particular sized complexes (depending on the metal identity) are found to undergo dissociative charge separation processes, reaction (2),

$$M^{2+}(H_2O)_y \rightarrow MOH^+(H_2O)_x + H^+(H_2O)_{y-x-1}. \quad (2)$$

Some interest in the latter reaction has focused on determining the minimum size at which water loss is favored over this charge separation process. For instance, Kebarle and coworkers reported that the largest complex size for which dissociative charge separation occurred (y_{crit}) for Co^{2+} was a lower limit of 4,[13–15] whereas Shvartzburg and Siu found $y_{crit} = 5$.[16]

Reaction (2) can occur during the formation of $M^{2+}(H_2O)_y$ complexes such that independent experimental studies of the binding energies and structures of hydrated metal hydroxides, $MOH^+(H_2O)_x$, are feasible. Formally, transition metal hydroxide cations can be viewed as either M^{2+} bound to OH^- or as M^+ bound to neutral OH. To probe the magnitude of this charge transfer, Garand and co-workers used vibrational spectroscopy of $MOH^+(H_2O)$ complexes where M = Mn, Fe, Co, Ni, Cu, Zn.[17] They found that the interaction between the hydroxide ligand and the metal center was relatively covalent in character for the $CoOH^+(H_2O)$ complex. In a complementary study, Garand and co-workers used density functional theory calculations and vibrational spectroscopy to determine the solvation shell motifs of $MOH^+(H_2O)_{1\text{-}4}$ for the same six metals.[18] They found that cobalt hydroxide cations form a second solvent shell upon the addition of the fourth water, determining $CoOH^+$ to have a coordination number (CN) of four ligands (three water molecules and hydroxide). The CN is the maximum number of ligands that bind directly to the metal center in the first ligand shell.

a)Author to whom correspondence should be addressed: armentrout@chem.utah.edu

Recently in our laboratory, a comprehensive investigation of the thermochemistry for hydrated copper hydroxide, $CuOH^+(H_2O)_x$ ($x = 1–4$), complexes was investigated by TCID and *ab initio* calculations.[19] In this investigation, it was found that the $CuOH^+(H_2O)$ complex loses both neutral H_2O and OH competitively to form $CuOH^+$ and $Cu^+(H_2O)$, respectively. In addition, by combining this thermochemistry for $CuOH^+(H_2O)_x$ with $Cu^+(H_2O)_y$ bond dissociation energies (BDEs) determined by Dalleska *et al.*,[5] BDEs for the loss of hydroxide from the $CuOH^+(H_2O)_x$ complexes were determined for $x = 0–4$. The present study obtains analogous thermodynamic data for water and hydroxide binding energies for another solvated 3d transition metal hydroxide cation, as we investigate $CoOH^+(H_2O)_x$ for $x = 1–4$. Using TCID in conjunction with theoretical calculations, the present study provides an in-depth look at the structures and binding interactions that form the inner and second hydration shells of the cobalt and cobalt hydroxide cations.

EXPERIMENTAL AND COMPUTATIONAL METHODS

Experimental procedures

Cross sections for the collision-induced dissociation (CID) of hydrated cobalt hydroxide monocation complexes were measured using a guided ion beam tandem mass spectrometer (GIBMS), which has been described previously in detail.[20,21] The hydrated cobalt hydroxide ions, $CoOH^+(H_2O)_x$, were generated by electrospray ionization (ESI)[22] techniques from a 10^{-4} M $CoCl_2$ dilute water solution with a low flow rate of 0.08–0.10 l/h and a voltage of ~2 kV applied to the electrospray needle. Once in the gas phase, the ions entered the vacuum system through a stainless-steel inlet cap followed by a heated capillary (80 °C) to promote desolvation of large droplets. The ions were collected and focused by an 88-plate radio frequency (rf) ion funnel with a dc gradient field,[23] and then injected into an rf hexapole ion guide where the ions were trapped in the radial direction with an rf amplitude of 250 V peak-to-peak. The ions underwent cooling by $>10^4$ collisions with ambient gas as they drifted through the hexapole ion guide. An in-source fragmentation technique using electrodes in the hexapole region[24] was used to preferentially enhance the signal intensity of the smaller $CoOH^+(H_2O)_x$ complexes by fragmenting the larger x complexes.

Previous studies have shown that under the proper conditions, the ions emerging from the hexapole are thermalized to room temperature even when the fragmentation electrodes are used.[7,11,24–28] The ions generated and thermalized in the source were extracted from the hexapole ion guide and focused into a magnetic sector momentum analyzer, where the desired reactant ion was mass selected. The reactant ions were then decelerated to a known kinetic energy and injected into an rf octopole ion guide,[29] where they were trapped radially and passed through a collision cell containing xenon at varying pressures (0.05–0.20 mTorr). The Xe pressures were low enough that single collision conditions dominate. Xenon was used as the collision gas to induce dissociation because it is heavy, monoatomic, polarizable, and chemically unreactive.[5,30] After collision, product ions and unreacted reactant ions drifted to the end of the octopole where they were extracted, mass selected using a quadrupole mass filter, and detected using a Daly detector.[31]

Thermochemical analysis

Ion intensities measured were converted to absolute reaction cross sections with an uncertainty of ±20% as described previously.[20] The laboratory ion potential, V_{lab}, was converted to the relative kinetic energy in the center-of-mass (CM) frame by

$$E_{CM} = qV_{lab} \times m/(m + M), \tag{3}$$

where m is the mass of the neutral collision gas, M is the mass of the reactant ion, and q is the charge of the ion. The absolute zero of energy and the kinetic energy distribution of the ion beam were determined using a retarding potential technique.[20] The derivative of the normalized ion intensity was fit to a Gaussian distribution (~0.12 eV FWHM) to determine the absolute energy zero and ion kinetic energy distribution. All energies below are reported in the CM frame, unless noted otherwise.

To produce accurate thermochemical data from the modeling of the CID process, several effects must be considered: multiple collisions, lifetime effects, and energy distributions. To ensure rigorous single collision conditions, cross sections were obtained at multiple Xe pressures, about 0.05, 0.10, and 0.20 mTorr, and linearly extrapolated to zero-pressure cross sections.[32,33] The zero-pressure extrapolated cross sections for the dissociation of a reactant $CoOH^+(H_2O)_x$ complex are modeled using the empirical threshold model shown in the following equation:

$$\sigma_j(E) = \sigma_{0,j} \sum g_i (E + E_i - E_{0,j})^n / E, \tag{4}$$

where $\sigma_{0,j}$ is an energy independent scaling factor for product channel j, E is the relative translational energy of the reactants, $E_{0,j}$ is the reaction threshold at 0 K for channel j, and n is an adjustable fitting parameter that describes the efficiency of the energy transfer upon collision.[21] The summation is over the ro-vibrational states of the reactants with excitation energies, E_i, and populations, g_i, where $\Sigma g_i = 1$. The number of ro-vibrational states was directly counted by the Beyer–Swinehart–Stein–Rabinovich algorithm to evaluate the internal energy distribution for the reactants.[34–37] A Maxwell-Boltzmann distribution at 300 K was used to compute the relative populations.

As the $CoOH^+(H_2O)_x$ ions become larger, those with energy more than the dissociation threshold may not have time to dissociate on the time scale of the experiment, $\tau \approx 5 \times 10^{-4}$ s. This can lead to a kinetic shift in the energy threshold obtained from our modeling, which can be accounted for by incorporating Rice–Ramsperger–Kassel–Marcus (RRKM) statistical theory[37–39] for unimolecular dissociation into Eq. (4), as shown in the following equation:

$$\sigma(E) = \left(\frac{n\sigma_{0,j}}{E}\right) \sum g_i \int_{E_{0,j}-E_i}^{E} \left[\frac{k_j(E^*)}{k_{tot}(E^*)}\right] (E - \varepsilon)^{n-1} P_{D1} d(\varepsilon). \tag{5}$$

Here ε is the energy transferred into internal degrees of freedom of the reactant ion at a relative translational energy, E, such that the internal energy of the energized molecule after collision is $E^* = \varepsilon + E_i$, and $k_{tot}(E^*)$ is the total unimolecular dissociation rate coefficient. The rate coefficient is used to calculate a probability of dissociation, $P_{D1} = 1 - \exp[-k_{tot}(E^*)\tau]$.[40,41] The RRKM unimolecular dissociation rate coefficient is defined by the following equation:

$$k_{tot}(E^*) = \sum k_j(E^*) = \sum d_j N_j^{\dagger}(E^* - E_{0,j})/h\rho(E^*), \quad (6)$$

where $k_j(E^*)$ is the rate coefficient for channel j, d_j is the reaction degeneracy calculated from the ratio of rotational symmetry numbers[37] of the reactants and products of channel j, $N^{\dagger}_j(E^* - E_{0,j})$ is the sum of the ro-vibrational states of the transition state (TS) at an energy $(E^* - E_{0,j})$ above the threshold for channel j, and $\rho(E^*)$ is the density of ro-vibrational states for the energized molecule (EM). When the rate coefficient is much faster than the average experimental time scale, Eq. (5) reduces to Eq. (4). Calculation of the RRKM unimolecular rate coefficients in Eq. (6) requires the ro-vibrational states of the EM and TS. The molecular parameters for the EM were taken from quantum chemical calculations of the reactant ion. For water loss, the TS was assumed to be loose with no reverse activation barrier, as the bond cleavage is heterolytic with all the charge remaining on the cobalt containing fragment complex.[42] Thus, the TS is product-like and treated in the phase space limit (PSL), such that it uses molecular parameters taken from quantum chemical calculations of the products.[40]

For $CoOH^+(H_2O)_x$ complexes where $x = 2$–4, a sequential dissociation model was employed to simultaneously analyze cross sections for the first and second water losses.[43] Thresholds for sequential dissociation of two water ligands were modeled with a statistical approach that has been shown to provide reasonable threshold energies for singly and doubly charged systems.[5–9,12,19,40,43] The BDE for the $CoOH^+(H_2O)_{x-2}$–H_2O complex is the difference between the thresholds of these two product cross sections. The model for sequential dissociation combines Eq. (5), the cross section of the primary dissociation product, with the probability for further dissociation in the following equation:

$$P_{D2} = 1 - e^{-k_2(E_2^*)\tau}, \quad (7)$$

where E_2^* is the internal energy of the product ion undergoing sequential dissociation. This energy was determined by energy conservation, $E_2^* = E^* - E_{0,j} - T_1 - E_L$, where T_1 is the translational energy of the primary products and E_L is the internal energy of the primary neutral product. For the remainder of this paper, representation of this sequential dissociation model that combines Eqs. (5) and (7) will be notated as Eq. (5) × (7).

The cross sections of Eq. (5) and (5) × (7) for both primary and secondary processes were convoluted over the relative kinetic energy distributions of the $CoOH^+(H_2O)_x$ ($x = 1$–4) and Xe reactants for comparison with the experimental cross sections.[20] A nonlinear least-squares fitting procedure was used to optimize the fitting parameters ($\sigma_{0,j}$, n, and $E_{0,j}$) in each model. The 0 K BDE of the metal–ligand complex is equivalent to the $E_{0,j}$ threshold energies obtained or the difference in the threshold energies for sequential dissociation. The uncertainties associated with these fitting parameters were determined from modeling eight independent zero-pressure extrapolated cross sections and additional modeling in which the vibrational frequencies were scaled by ±10%, the best fit n value was varied by ±0.1, the experimental time-of-flight was scaled up and down by a factor of 2, and the 0.05 eV (lab) absolute uncertainty of the energy scale was included.

Computational details

Geometry optimizations for $CoOH^+(H_2O)_x$ and $Co^+(H_2O)_y$ complexes were calculated utilizing the Gaussian09 suite of programs[44] at the B3LYP/6–31G(d) level of theory[45,46] using the "loose" keyword to utilize a large step size of 0.01 a.u. and a rms force constant of 0.0017 a.u. to ensure a rapid geometry convergence. These structures were refined by geometry optimization at a B3LYP/6-311+G(d,p) level, which was used for the final geometry optimizations as well as providing vibrational frequencies and rotational constants. Vibrational frequencies were scaled by 0.989[47] before being used in the modeling process and to calculate zero point energy (ZPE) and thermal corrections. Basis set superposition error (BSSE) corrections were calculated in the full counterpoise (cp) limit.[48,49] Single point energy calculations using the B3LYP/6-311+G(d,p) optimized geometries were performed at B3LYP, Coulomb attenuating method (cam) B3LYP,[50] B3P86,[51] M06,[52] M06-GD3, and MP2(full)[53] (where full indicates correlation of all electrons) levels of theory using a 6-311+G(2d,2p) basis set. Calculations utilizing empirical dispersion corrections at the B3LYP-GD3BJ/6-311+G(2d,2p)//B3LYP-GD3BJ/6-311+G(d,p) level were also performed.[54] The relative energetics calculated from these single point energy calculations include ZPE corrections to yield 0 K values as well as thermal corrections to the source temperature at 298 K.

RESULTS

Overview of theoretical results

Important structural parameters of the B3LYP/6-311+G(d,p) predicted ground structures of $CoOH^+(H_2O)_x$ (x = 0–4) complexes are provided in Table S1 of the supplementary material. For all complexes, the quartet spin state (corresponding to Co^{2+}, which has a $3d^7$ atomic configuration) was found to be energetically favorable compared to a doublet spin state. Structures and relative energies at 0 and 298 K at all levels of theory for all investigated isomers of $CoOH^+(H_2O)_x$ are given in Fig. S1 and Table S2 of the supplementary material, respectively. All levels of theory unambiguously predict the same ground structures (GSs) for each complex size, shown in Fig. 1 for x = 0–4. We use an (x,y) nomenclature to describe the number of water molecules in the first ligand shell (x), where $x + 1$ = CN, and second ligand shell (y) of each unique structure. To describe the hydrogen bonding of waters in the cluster, isomers are further denoted using an A/D nomenclature where a water molecule can be a single (A) or double (AA) hydrogen bond acceptor and/or single (D) or double (DD) hydrogen bond donor. Binding to the OH ligand rather than a water ligand is specified by an "OH" subscript. To

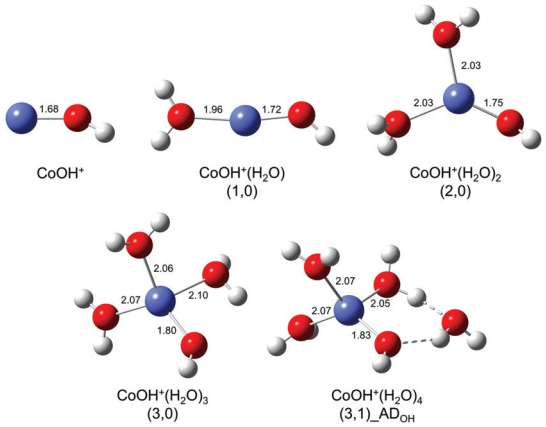

FIG. 1. Ground isomers of $CoOH^+(H_2O)_x$ complexes where x = 0–4 optimized at the B3LYP/6-311+G(d,p) level of theory. Co–O bond lengths are provided in Å.

further help distinguish between structures with similar bonding schemes but differing geometric parameters, additions to the nomenclature may include point group symmetries and series of O–Co–O angles denoted as subscript "c" (cis) for angles <45°, "g" (gauche) for angles between 45° and 135°, and "t" (trans) for angles >135°.

Theoretical geometries of ground structures: $CoOH^+(H_2O)_x$

Table I reports relative energetics at 0 and 298 K for distinct low energy isomers of $CoOH^+(H_2O)_x$ where x = 2–4. Values for B3LYP-GD3BJ (very similar to B3LYP results) and M06-GD3 (very similar to M06 results) can be found in Table S2 of the supplementary material. All levels of theory predict that up to three waters bind directly to cobalt for structures with the lowest relative energies. At the B3LYP level, the $CoOH^+$ structure has a Co–O–H bond angle of 150° with a Co–OH bond length of 1.68 Å, Fig. 1. The GS for $CoOH^+(H_2O)$ has a slightly bent geometry with a ∠OCoO bond angle of 171° and all hydrogens in the same plane. This permits the out-of-plane lone pair electrons on both oxygens to interact with a half-filled π-like orbital on Co. In this complex, the Co–OH bond length is 1.72 Å, and the Co–OH_2 bond length is 1.96 Å.

The calculated GS for $CoOH^+(H_2O)_2$ is the (2,0) structure, Fig. 1, where cobalt is three-coordinate with all ligands bound to the metal center at all levels of theory. This GS exhibits a near trigonal planar geometry with ∠OCoO of 101° between the two waters and ∠OCoO angles of 127° and 131° between the waters and the hydroxide, and a 174° ∠OCoOO dihedral angle. In this GS isomer, the water molecules and hydroxide tilt to participate in long-range hydrogen bonding (3.4–4.1 Å) with one another and the Co–OH and Co–OH_2 bond lengths increase from those in the x = 1 GS to 1.75 and 2.03 Å, respectively.

Table I shows that at x = 3, all levels of theory predict a (3,0) geometry for the GS, Fig. 1. This GS is 4-coordinate with three water molecules and one hydroxide bound directly to the metal center in a distorted tetrahedral geometry with respect to the oxygen atoms. Examination of the molecular orbitals for this isomer shows that the singly occupied molecular orbitals (SOMOs) are the $3d_{xy}$, $3d_{xz}$, and $3d_{yz}$ orbitals that point towards the ligands, consistent with ligand field theory for a tetrahedral complex. The orientation of the ligands

TABLE I. Theoretical relative enthalpies (ΔH_0) and free energies (ΔG_{298}) (kJ/mol) for hydrated cobalt complexes.[a]

x		B3LYP	B3P86	M06	MP2(full)	cam-B3LYP
$CoOH^+(H_2O)_2$	(2,0)	**0.0 (0.0)**	**0.0 (0.0)**	**0.0 (0.0)**	**0.0 (0.0)**	**0.0 (0.0)**
	(1,1)_A	74.6 (74.2)	74.8 (74.4)	42.5 (42.1)	85.1 (84.7)	49.0 (48.7)
	(1,1)_A_{OH}	107.1 (107.9)	108.2 (109.1)	75.4 (76.2)	126.9 (127.7)	112.8 (113.6)
$CoOH^+(H_2O)_3$	(3,0)	**0.0 (0.0)**	**0.0 (0.0)**	**0.0 (0.0)**	**0.0 (0.0)**	**0.0 (0.0)**
	(2,1)_A	29.2 (30.2)	31.7 (32.7)	18.4 (19.4)	48.5 (49.5)	34.9 (36.0)
	(2,1)_A_{OH}	62.8 (64.7)	67.0 (68.6)	50.1 (52.1)	88.1 (90.0)	71.7 (73.7)
$CoOH^+(H_2O)_4$	(3,1)_AD_{OH}	**0.0 (0.0)**	**0.0 (0.0)**	**0.0 (0.0)**	**0.0 (0.0)**	**0.0 (0.0)**
	(3,1)_AA	4.4 (5.0)	7.4 (8.0)	0.9 (1.5)	7.9 (8.6)	6.0 (6.7)
	(4,0)	20.7 (22.5)	22.1 (23.9)	12.2 (14.0)	12.4 (14.2)	19.9 (21.7)
$Co^+(H_2O)_2$	(2,0) D_{2h}	**0.0 (0.0)**	**0.0 (0.0)**	**0.0 (0.0)**	**0.0 (0.0)**	**0.0 (0.0)**
	(2,0) D_{2d}	9.0 (9.7)	10.0 (10.8)	10.0 (10.8)	0.1 (0.8)	16.8 (17.5)
$Co^+(H_2O)_3$	(3,0)	**0.0 (0.0)**	**0.0 (0.0)**	**0.0 (0.0)**	**0.0 (0.0)**	**0.0 (0.0)**
	(2,1)_A	1.8 (0.8)	3.8 (2.7)	13.8 (12.8)	12.9 (11.8)	5.9 (4.8)
$Co^+(H_2O)_4$	(2,2)_$2A_t$	**0.0 (0.0)**	**0.0 (0.0)**	19.8 (17.1)	48.6 (45.9)	0.6 **(0.0)**
	(2,2)_$2A_c$	0.1 (0.6)	0.1 (0.6)	20.2 (17.9)	49.6 (47.2)	4.2 (4.0)
	(3,1)_A_t	3.5 (5.9)	1.6 (4.0)	11.4 (11.1)	53.3 (52.9)	20.9 (22.7)
	(3,1)_A_g	12.9 (16.3)	11.4 (14.7)	20.2 (20.9)	63.9 (64.9)	23.0 (25.8)
	(3,1)_AA	11.9 (13.0)	10.3 (11.4)	15.9 (14.3)	13.0 (11.3)	17.7 (18.2)
	(4,0)	6.4 (11.8)	4.9 (10.3)	**0.0 (0.0)**	**0.0 (0.0)**	**0.0** (4.8)

[a]ΔG_{298} values are given in parentheses. Values are single-point energies calculated at the level shown using a 6-311+G(2d,2p) basis set from geometries optimized at the B3LYP/6-311+G(d,p) level. Zero point energy corrections are included. Bold values represent the predicted ground structures (GSs).

is dictated by long hydrogen bonding interactions, where an adjacent water molecule donates a 2.37 Å hydrogen bond to the hydroxide. Again, we see metal–ligand bond lengthening as the complex size increases for Co–OH (1.80 Å) and Co–OH_2 (2.06 Å, 2.07 Å, 2.10 Å).

The lowest energy isomer for $CoOH^+(H_2O)_4$ is similar to the 4-coordinate x = 3 GS with addition of the fourth water molecule in the second solvent shell, where it accepts a single hydrogen bond from an inner shell water and donates a hydrogen bond to the hydroxide, (3,1)_AD_{OH} (Fig. 1). The Co–OH bond length is 1.83 Å, with Co–OH_2 bond lengths of 2.05, 2.07, and 2.07 Å. Overall, all levels of theory predict three waters and a hydroxide directly bound to the cobalt dication for the first solvent shell for $CoOH^+(H_2O)_x$, x = 3–4, suggesting Co(II) has a CN = 4. An expanded description of additional geometries for high and low energy isomers of $CoOH^+(H_2O)_x$, x = 1–4, can also be found in the supplementary material.

Garand and co-workers performed a theoretical study using the cam-B3LYP/def2-TZVP level to assign coordination structures to $CoOH^+(H_2O)_x$, x = 1–4, complexes by comparing computed linear infrared (IR) spectra with experimental IR vibrational predissociation spectra.[18] In agreement with the present work, they determined that a maximum of three waters directly coordinate to the metal in $CoOH^+$. Additionally, their assigned structures are equivalent to the structures we have determined to be GSs in the present study for all complex sizes (Fig. 1). CAS-MCSCF/DZP calculations performed by Gilson and Krauss examined the geometries of $CoOH^+(H_2O)_x$ complexes for x = 3–5.[55] They found the lowest energy isomer of x = 4 to be (4,0) trigonal bipyramidal but do not seem to have investigated the possibility of a second solvent shell as was found to be the GS in this study and by Garand and co-workers.[18] In agreement with these studies, they found a similar four-coordinate x = 3 structure also exhibiting water–hydroxide hydrogen bonding. Gilson and Krauss also performed a detailed investigation of the $CoOH^+(H_2O)_x$ spin states and found the quartet to be favored, in agreement with our theoretical investigations as well as $Co(OH)_x^+$ calculations performed by Bauschlicher and coworkers.[56] In the quantum chemical investigation for the transition state of the charge separation of $Co^{2+}(H_2O)_4$ into $CoOH^+(H_2O)_2$ and H_3O^+, Beyer and Metz used B3LYP/6-311++G(d,p) calculations and found that $CoOH^+(H_2O)_2$ had a geometry[57] in agreement with our (2,0) GS, having analogous bond lengths and angles (Table S1 of the supplementary material).

Theoretical geometries of ground structures: $Co^+(H_2O)_y$

Relative energetics at 0 and 298 K for distinct low energy $Co^+(H_2O)_y$ isomers of y = 2–4 complexes are also included in Table I. For all hydrated monocation complexes, the triplet spin state of Co^+ (with a $3d^8$ atomic configuration) was found to be energetically favorable. The ground structures for y = 1–4 are shown in Fig. 2, and geometric parameters are included in Table S1 of the supplementary material. The $Co^+(H_2O)$ structure has a ∠CoOH bond angle of 126° and a Co–O bond length of 1.95 Å, 0.27 Å longer compared to that of $CoOH^+$. All levels of theory predict the linear (2,0) structure with D_{2h} molecular symmetry to be the lowest energy isomer for y = 2 with a Co–O bond length of 1.95 Å. (This planar geometry is driven by donation of electron density on the out-of-plane oxygen lone pair electrons into a singly occupied $3d_\pi$ orbital on Co^+.) The y = 3 GS is a T-shaped (3,0) isomer with two 1.99 and one 2.20 Å Co–O bond lengths. Similar to the $CoOH^+(H_2O)_2$ GS, this (3,0) geometry has long-range hydrogen bonding (2.8 and 3.3 Å) between the water ligands, which slightly distorts the symmetry leading to ∠OCoO bond angles of 89°, 102°, and 170°. For the $Co^+(H_2O)_4$ complex, two possible GSs are predicted depending on the level of theory, Fig. 2. B3LYP, B3LYP-GD3BJ (298 K), B3P86, and cam-B3LYP (298 K) predict (2,2)_$2A_t$ to be the lowest energy isomer. This two-coordinate structure is similar to the linear (2,0) GS, where the two inner shell waters each donate a single hydrogen bond (1.63 Å) to an outer shell water, in a trans-configuration with respect to the oxygens. The M06, M06-GD3, and MP2(full) levels of theory predict this (2,2) isomer to be 17–46 kJ/mol higher in energy at 298 K than the square-planar (4,0) geometry GS (Table I). B3LYP-GD3BJ and cam-B3LYP predict that (4,0) is the 0 K GS. The triplet (4,0) isomer aligns the water ligands along the x and y axes, with the SOMOs in $3d_{z^2}$ and $3d_{x^2-y^2}$ orbitals (Fig. S2 of the supplementary material), consistent with ligand field theory for a square planar complex. The (4,0) isomer has distorted D_{4h} symmetry with Co–O bond lengths of 2.09 (2) and 2.25 (2) Å, 0.18–0.33 Å longer than the (2,2) GS. The symmetry of the (4,0) isomer is distorted by the orientation of the water ligands as they participate in long-range hydrogen bonds with each other (two 2.6 and two 3.4 Å). With the exception of the ambiguity for the y = 4 GSs, theory predicts that Co^+ also has a coordination number of four ligands in the first solvent shell, similar to the results for $CoOH^+(H_2O)_x$ complexes.

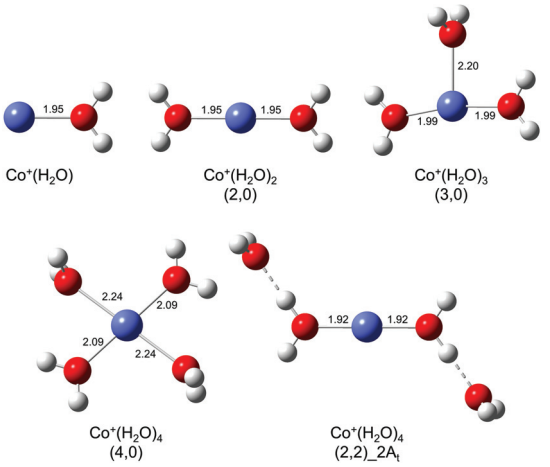

FIG. 2. Ground isomers of $Co^+(H_2O)_y$ complexes where y = 1–4 optimized at the B3LYP/6-311+G(d,p) level of theory. Co–O bond lengths are provided in Å.

Molecular orbital analysis for geometry assignments by Dalleska *et al.* concluded that $Co^+(H_2O)_4$ should be the square planar (4,0) GS,[5] in agreement with the M06 and MP2(full) results of the present study. Furukawa *et al.* performed

calculations using the B3LYP functional and basis sets of 6-311+G(2df) for cobalt and 6-31+G(d) for oxygen and hydrogen to assign structures of the $Co^+(H_2O)_y$, $y = 4$–6, complexes by comparing computed linear IR spectra with IR photodissociation spectra in the OH-stretch region, 2900–3800 cm^{-1}.[58] In agreement with our $y = 3$ assignment, they determined a T-shaped (3,0) GS exhibiting long-range hydrogen bonding between water ligands. They also found a similar (4,0) square planar isomer as the present study, but predicted it to be 7 kJ/mol higher in energy than their assigned GS (3,1)_AA isomer, similar to our B3LYP and B3P86 results where the calculated difference is about 6 kJ/mol. However, they did not mention locating any (2,2) isomer, which is found to be the B3LYP and B3P86 GS in the present study (Table I). Furukawa also measured the IR photodissociation spectrum for $Co^+(H_2O)_4$, observing broad bands at about 3140, 3310, and 3660 cm^{-1}, where the former two must correspond to hydrogen bonded interactions and the latter to free OH stretches. Compared to their calculated theoretical linear IR spectra, they concluded that the experimental spectrum was best reproduced by (3,1) theoretical spectra.[58] A reevaluation of this conclusion in light of the (2,2) isomers was conducted here. We find that the broad band at 3660 cm^{-1} is consistent with all the isomers, such that the presence or absence of the (4,0) isomer cannot be confirmed or denied. The 3140 cm^{-1} band can be reproduced by either the (2,2)_A or (3,1)_A_g isomer, in which the second shell water binds in a gauche configuration to one of the axial inner shell waters. In agreement with Furukawa *et al.*, the (3,1)_A_t isomer [which they call (3+1$_s$)], in which the second shell water binds to the more weakly bound side inner shell water ligand, can be assigned to the band at 3310 cm^{-1}. This band is not found in the (2,2) nor (4,0) spectra. Thus, their experimental results are consistent with our B3LYP and B3P86 calculations, but none of the other levels of theory. It is also notable that upon tagging with N_2, the experimental spectrum obtained is readily assigned to (3,1)_AA. Furukawa *et al.* suggest that this is because of the lower temperature; however, this isomer is never the 0 K GS at any level of theory, suggesting that the tag is perturbing the relative energies of the different isomers. CID and photofragmentation experiments of $Co^+(H_2O)_y$ complexes performed by Poisson *et al.* also were interpreted as providing evidence of populated isomers having second solvent shells, CN = 2 (dominant and presumed to be kinetically trapped) and 3 for $y = 3$ and only CN = 3 for $y = 4$.[59] The latter result is not consistent with any levels of theory explored here unless their complex is actually CN = 2.

Experimental results

TCID cross sections for $CoOH^+(H_2O)_x$ complexes with Xe were obtained for $x = 1$–4 and are shown in Fig. 3. In all cases, the primary dissociation pathway is the loss of a single water molecule and is followed by the sequential dissociation of additional water molecules at higher energies until $CoOH^+$ is reached for $x = 2$–4. In all cases, the total cross section rises sharply with energy thresholds that gradually decrease as x increases. Note that in Fig. 3(a) the probability for $CoOH^+(H_2O)_4$ dissociating into $CoOH^+(H_2O)_3$ exists even at 0 eV collision energy, indicating that the BDE of $x = 4$ is comparable to the internal energy of the complex. This explains why we were unable to experimentally observe any complexes of $x > 4$ with appreciable intensity as any additional waters are expected to be even more weakly bound. At higher energies, the total cross sections for all complexes plateau indicating the sequential nature of the water loss products. The magnitude of these cross sections increases as the complex size increases and are similar to those found for $CuOH^+(H_2O)_x$.[19] For $x = 1$, Fig. 3(d), competitive primary dissociation pathways were observed as the loss of a single water molecule to form $CoOH^+$ [reaction (8)] and the loss of a hydroxyl radical to form $Co^+(H_2O)$ [reaction (9)],

$$CoOH^+(H_2O) + Xe \rightarrow CoOH^+ + H_2O + Xe, \quad (8)$$

$$\rightarrow Co^+(H_2O) + OH + Xe. \quad (9)$$

Clearly, reaction (8) is strongly favored. At sufficiently high energies, a small cross section was observed for the monocation, Co^+, which must be formed in a secondary process from either of the primary products.

Zero-pressure extrapolated CID cross sections for the $x = 1$–4 reactants were modeled to ascertain dissociation thresholds at each complex size. For all complexes, the total cross sections for water dissociation, reaction (1), were modeled using Eq. (4) (without lifetime effects) and Eq. (5) (with lifetime effects). For the $x = 2$–4 systems, cross sections for the primary and sequential dissociation products were simultaneously analyzed using Eq. (5) and Eq. (5) × (7) to obtain 0 K BDEs. For $x = 1$, competitive analysis using Eq. (5) was used to model the H_2O and OH loss cross sections of reactions (8) and (9) to acquire accurate 0 K thresholds. As noted above, all complexes are believed to be thermally equilibrated in the source, such that the model assumes the reactant isomers are the 298 K GS with an internal energy distribution of 298 K. The product isomer is assigned as the 0 K GS because previous studies have found that our threshold analyses are dominated by the lowest energy 0 K enthalpy species.[6,9] As mentioned above, all levels of theory for this study unambiguously predicted the same GSs at 298 K and 0 K for each complex size of $CoOH^+(H_2O)_x$.

The optimum modeling parameters are listed in Table II for primary and sequential dissociation products being simultaneously analyzed using Eq. (5) and Eq. (5) × (7). Figure 4 shows these models compared to zero-pressure extrapolated cross sections. The sequential analysis reproduces the product cross sections well over extended energy and magnitude ranges. Differences in threshold energies for the primary products obtained with (PSL) and without lifetime effects are the kinetic shifts, which Table II shows are relatively small (0.02–0.04 eV). When modeling the hydroxide loss from $CoOH^+(H_2O)$ [reaction (9)], competition with the dominant primary loss of water is illustrated by the significant shift of 0.76 eV. Direct comparison of the models for the total cross sections versus the sequential models of the primary cross sections shows that the σ_0, n, and E_0 values are nearly identical. Threshold energies for the primary water loss channels are basically unaffected by consideration of the secondary loss channel, within 0.04 eV in all cases (Table II). The entropies of

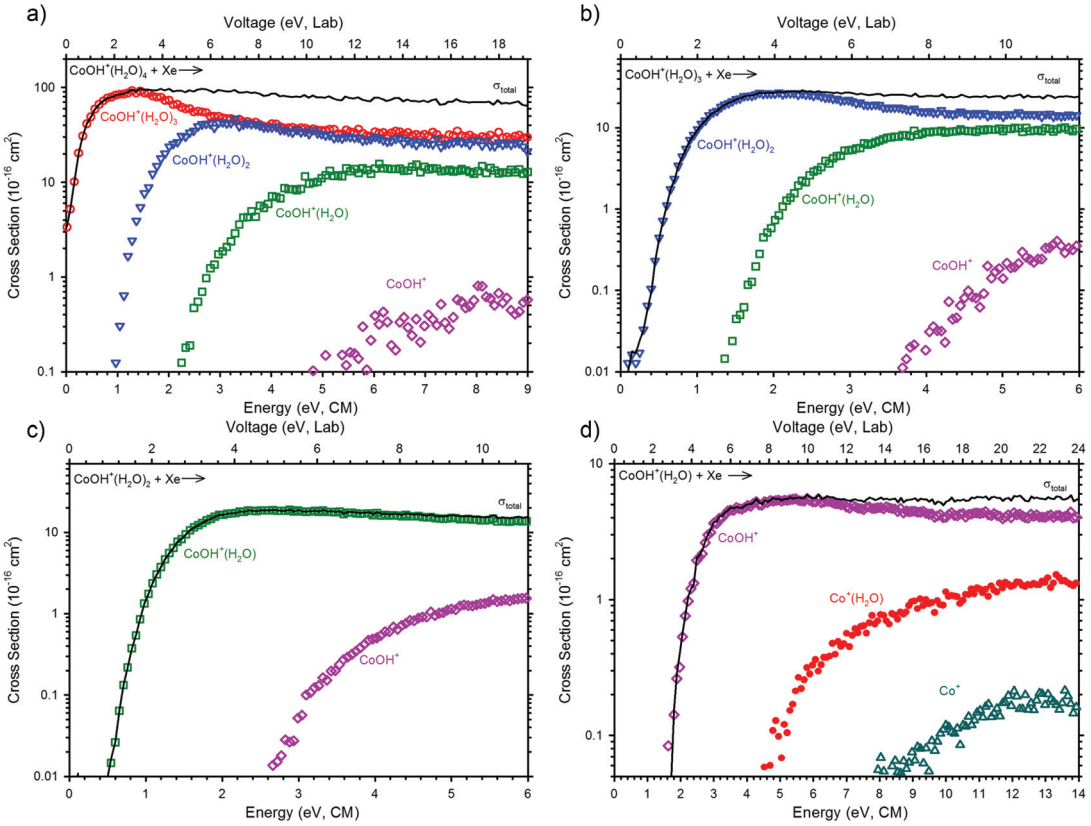

FIG. 3. Cross sections for collision-induced dissociation of $CoOH^+(H_2O)_x$ where $x = 1$–4 [parts (a)–(d)] with Xe (~0.2 mTorr) as a function of kinetic energy in the center-of-mass frame (bottom x-axis) and applied voltage in the laboratory frame (top x-axis). Water loss products are represented by open symbols, and hydroxide loss products are represented by closed symbols [part (d)].

activation, $\Delta S^{\dagger}_{1000}$, which represent the measure of looseness of the transition state, are positive and increase with increasing complex size, Table II.

The difference between the primary and secondary thresholds is used to calculate an independent measurement for the bond dissociation energy for $CoOH^+(H_2O)_{x-1}$ dissociating to

TABLE II. Optimized parameters of Eqs. (4) and (5) from analysis of total, primary, and secondary cross sections for collision-induced dissociation of $CoOH^+(H_2O)_x$.[a]

Reactant	Product ion	σ_0[b] (Å^2)	n[b]	E_0[b] (PSL) (eV)	E_0[c] (eV)	$\Delta S^{\dagger}_{1000}$[b] (J/mol K)
$CoOH^+(H_2O)$[d]	$CoOH^+$	9 (1)	0.8 (0.1)	2.37 (0.08)	2.41 (0.12)[e]	25 (5)
	$Co^+(H_2O)$	9 (1)		3.66 (0.10)	4.42 (0.19)[e]	33 (7)
$CoOH^+(H_2O)_2$[f]	$CoOH^+(H_2O)$	33 (4)	1.1 (0.1)	1.30 (0.09)	1.34 (0.11)	26 (13)
$CoOH^+(H_2O)_2$[g]	$CoOH^+(H_2O)$	34 (7)	1.1 (0.1)	1.34 (0.19)		23 (5)
	$CoOH^+$	12 (3)		3.62 (0.15)		32 (5)
$CoOH^+(H_2O)_3$[f]	$CoOH^+(H_2O)_2$	44 (2)	1.0 (0.1)	1.12 (0.07)	1.15 (0.09)	45 (19)
$CoOH^+(H_2O)_3$[g]	$CoOH^+(H_2O)_2$	44 (4)	1.0 (0.1)	1.10 (0.10)		51 (5)
	$CoOH^+(H_2O)$	33 (5)		2.54 (0.06)		22 (17)
$CoOH^+(H_2O)_4$[f]	$CoOH^+(H_2O)_3$	119 (7)	1.0 (0.1)	0.65 (0.08)	0.67 (0.11)	54 (5)
$CoOH^+(H_2O)_4$[g]	$CoOH^+(H_2O)_3$	119 (9)	1.0 (0.1)	0.65 (0.06)		54 (3)
	$CoOH^+(H_2O)_2$	112 (4)		1.81 (0.05)		43 (3)

[a]Uncertainties in parentheses.
[b]Parameters for modeling with lifetime effects considered, Eq. (5).
[c]Parameters for modeling where lifetime effects are not included, Eq. (4).
[d]Competitive analysis modeling of primary water and hydroxide loss cross sections using Eq. (5).
[e]Modeling of individual channels without competition.
[f]Single channel modeling of the total cross section using Eq. (5).
[g]Sequential modeling of primary and secondary cross sections using Eqs. (5) and (5) × (7).

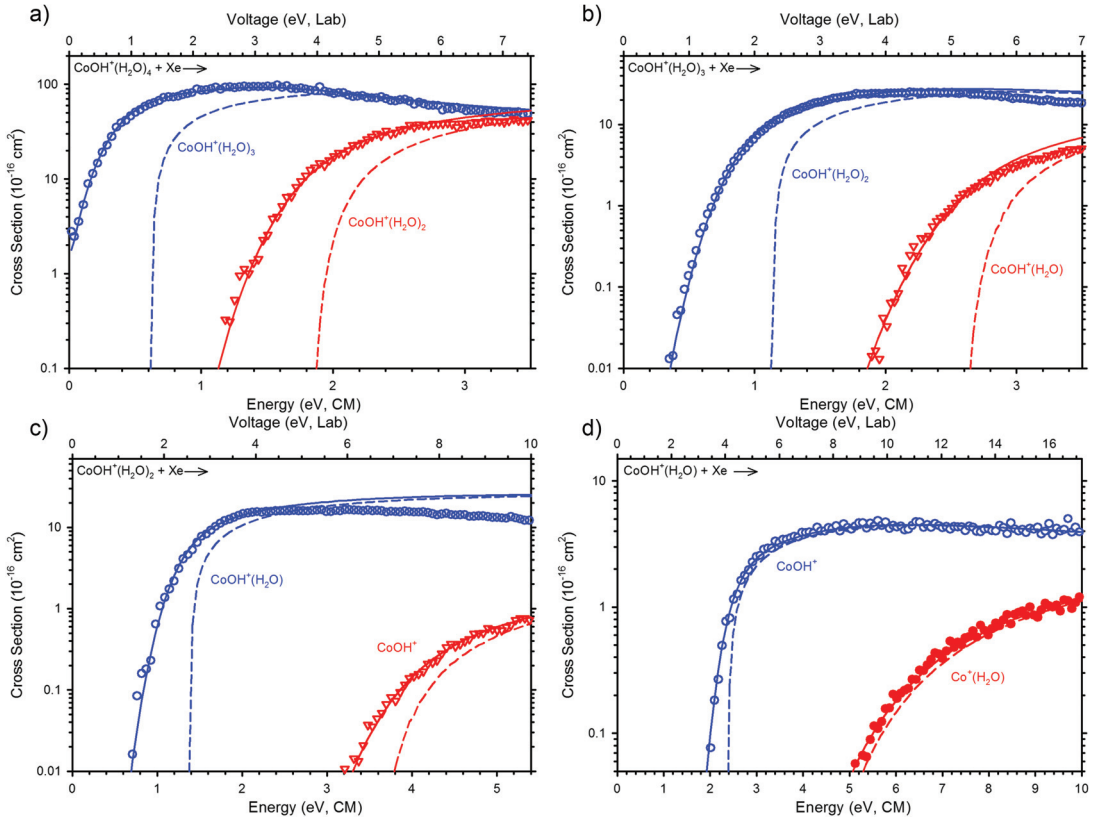

FIG. 4. Zero-pressure extrapolated cross sections for the CID of $CoOH^+(H_2O)_x$ $x = 1$–4. Solid lines show the best fits to the primary (open circles), and secondary (open triangles) water loss cross sections using Eq. (5) × (7) convoluted over the neutral and ion kinetic and internal energy distributions. The dashed lines show the model cross sections in the absence of experimental kinetic energy broadening for reactants with an internal energy of 0 K. Optimized parameters for these fits are found in Table II. Part (d) shows best fits for competitive water loss (open circles) and hydroxide loss (solid circles) using Eq. (5).

$CoOH^+(H_2O)_{x-2}$ + H_2O. This difference can be measured with more precision than the absolute values for each threshold because many systematic sources of uncertainty cancel; however, their accuracy can suffer from the additional assumptions needed in the modeling. For the $x = 4$ complex, Fig. 4(a), analysis with the sequential model, Eq. (5) × (7), finds the thresholds for loss of one and two water molecules as 0.65 ± 0.06 eV and 1.81 ± 0.05 eV, respectively. The difference of 1.16 eV ± 0.06 eV between these thresholds equals the $CoOH^+(H_2O)_2$–(H_2O) bond energy, which agrees well with the 1.12 ± 0.07 eV threshold for the $CoOH^+(H_2O)_3$ primary dissociation channel. Sequential modeling of the $x = 3$ reactant, Fig. 4(b), gives thresholds of 1.10 ± 0.10 and 2.54 ± 0.06 eV for the first and second water losses, respectively. The difference between thresholds, 1.44 eV ± 0.07 eV, is within combined experimental uncertainty of the threshold for single water loss from $CoOH^+(H_2O)_2$, 1.30 ± 0.09 eV. Comparing sequential modeling of $CoOH^+(H_2O)_2$, Fig. 4(c), to the primary water loss threshold analysis of $CoOH^+(H_2O)$, we find good agreement between 2.28 eV ± 0.10 eV and 2.37 ± 0.08 eV, respectively. Competitive analysis of the $CoOH^+(H_2O)$ dissociation cross sections, Fig. 4(d), reveals a dissociation threshold for H_2O loss of 2.37 ± 0.08 eV and a threshold for OH loss of 3.66 ± 0.10 eV, with a difference measured as 1.29 ± 0.10 eV. Loss of H_2O is energetically more favorable at $x = 1$ with its lower threshold for dissociation; however, it can be seen in Table II that the OH loss is entropically more favorable with its larger $\Delta S^{\dagger}_{1000}$ value. At first, this observation is unexpected because the $Co^+(H_2O)$ ($^3B_2$) + OH ($^2\Pi$) product channel has one less rotational degree of freedom than the $CoOH^+$ ($^4A''$) + H_2O ($^1A_1$) channel; however, it can be noted that the electronic degeneracy of the former channel is 12, whereas that for the latter channel is only 4.

Comparison of experimental and theoretical bond enthalpies: $CoOH^+(H_2O)_x$

Primary and secondary experimental 0 K bond dissociation enthalpies for the loss of water from $CoOH^+(H_2O)_x$ ($x = 1$–4) complexes are compared in Table III. As mentioned above, there is good agreement between the primary and secondary (obtained from differences between the primary and secondary thresholds) bond enthalpies, with a mean absolute deviation (MAD) of 8.6 kJ/mol, comparable to the experimental uncertainties. It should be noted

TABLE III. Comparison of experimental[a] and theoretical[b] 0 K bond enthalpies (kJ/mol) for $CoOH^+(H_2O)_{x-1}-H_2O$.

x	Primary	Secondary	B3LYP	B3P86	M06	MP2(full)	cam-B3LYP/def2-TZVP[c]
1	228.4 ± 7.9	219.6 ± 16.5	245.1 (248.1)	249.2 (252.6)	183.8 (188.6)	258.2 (265.4)	223.0 (226.3)
2	125.7 ± 8.7	138.5 ± 7.7	114.7 (118.0)	118.0 (121.4)	146.7 (151.5)	121.3 (128.5)	129.9 (133.2[d])
3	107.6 ± 7.0	111.8 ± 5.5	105.1 (108.1)	99.1 (102.3)	86.0 (89.4)	109.2 (119.9)	109.8 (112.9[d])
4	63.1 ± 7.7		63.0 (65.9)	68.2 (71.2)	66.1 (69.7)	66.3 (76.5)	77.4 (80.5[d])
MAD[e]	7.8[f]	8.6	7.6 (7.7)	10.5 (10.5)	22.6 (22.6)	9.7 (16.3)	6.5 (8.1)
MAD[g]		9.9[f]	18.7 (17.7)	20.9 (19.9)	23.3 (22.1)	19.5 (21.3)	4.7 (4.4)

[a]Values from Table II.
[b]Theoretical values with (and without) cp corrections. Single point energies calculated at the indicated level of theory using the 6-311+G(2d,2p) basis set using B3LYP/6-311+G(d,p) geometries and zero point energy corrected.
[c]Geometries optimized at the cam-B3LYP/def2-TZVP level of theory consistent with calculations of Garand and co-workers.[18]
[d]Values reproduced from Ref. 18.
[e]Mean absolute deviations from primary experimental BDEs.
[f]Mean experimental uncertainty.
[g]Mean absolute deviations from secondary experimental BDEs.

that in general the primary bond enthalpies from the total cross section models provide the best experimental information as fewer assumptions associated with the modeling are needed.

Table III lists theoretical BDEs calculated at the B3LYP, B3P86, M06, and MP2(full) levels of theory using a 6-311+G(2d,2p) basis set and structures and zero point energy corrections calculated at the B3LYP/6-311+G(d,p) level with and without counterpoise (cp) corrections. (Table S3 of the supplementary material lists values for M06-GD3 and cam-B3LYP levels as well.) Additional values were calculated at the B3LYP-GD3BJ/6-311+G(2d,2p)//B3LYP-GD3BJ/6-311+G(d,p) level (Table S3) and cam-B3LYP/def2-TZVP level (Table III). These latter calculations match the level used by Garand and co-workers and were performed to augment their results with cp corrections, a value for the $x = 1$ complex, and for the loss of OH from $CoOH^+(H_2O)_x$. Counterpoise corrections for each complex size were relatively small for DFT levels (≤5 kJ/mol), whereas corrections for MP2(full) were larger, 7–11 kJ/mol. Overall, cp corrections make very little difference in MADs from experimental values for all levels of theory, except cp corrections for MP2(full) level improve MADs by 7 kJ/mol for primary but only by 2 kJ/mol for secondary BDEs. All further comparisons between experimental and theoretical BDEs will be made with the cp corrected values.

The MAD values in Table III and Table S3 of the supplementary material show that our primary water loss experimental values agree well with calculated 0 K hydration enthalpies for B3LYP, B3LYP-GD3BJ, B3P86, MP2(full), and cam-B3LYP/def2-TZVP with MADs of 7.6, 10.1, 10.5, 9.7, and 6.5 kJ/mol, respectively. The M06, M06-GD3, and cam-B3LYP levels do not agree as well with a MAD of ~23 kJ/mol. Figure 5 shows the comparison of theoretical BDEs with experiment for loss of water from $CoOH^+(H_2O)_x$ where $x = 1$–4. For $x = 1$, the cam-B3LYP/def2-TZVP value agrees with experiment, M06 levels underestimate the BDE, while the other levels overestimate this BDE. For $x = 2$ and 3, the BDEs at the B3LYP, B3P86, MP2(full), and cam-B3LYP/def2-TZVP levels of theory maintain reasonable agreement among each other and with experiment. For $x = 4$, most levels of theory yield a BDE in very good agreement with experiment, whereas the cam-B3LYP/def2-TZVP value overestimates the BDE by 14.3 kJ/mol, outside of the experimental uncertainty, Table III. Table III and Fig. 5 also include the secondary water loss BDEs for comparison with theory. In general, MADs from secondary BDEs are larger than those from the primary BDEs by 0.7–11.1 kJ/mol for all levels of theory except cam-B3LYP/def2-TZVP, where agreement is improved by 1.8 kJ/mol.

Comparison of experimental and theoretical bond enthalpies: $Co^+(H_2O)_y$

The BDEs of the hydrated transition metal monocations were previously studied in this group, where $y = 1$–4 for $Co^+(H_2O)_y$.[5] Table IV and Fig. 6 provide these 0 K hydration BDEs along with selected theoretical results with and

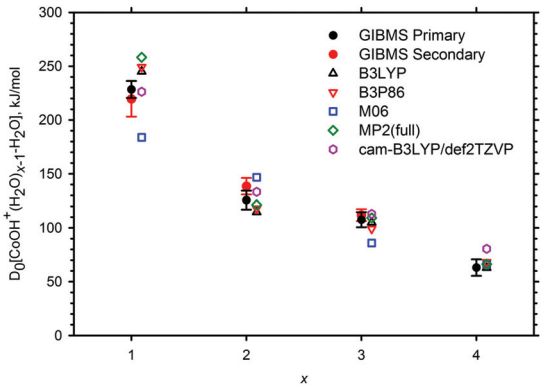

FIG. 5. Comparison of 0 K BDEs for neutral H_2O loss from $CoOH^+(H_2O)_x$ as a function of complex size (x): experimental primary (black solid circles) and secondary (red solid circles) values with theoretical values calculated at the B3LYP/6-311+G(2d,2p)//B3LYP/6-311+G(d,p) (open black up triangles), B3P86/6-311+G(2d,2p)//B3LYP/6-311+G(d,p) (open red down triangles), M06/6-311+G(2d,2p)//B3LYP/6-311+G(d,p) (open blue squares), MP2(full)/6-311+G(2d,2p)//B3LYP/6-311+G(d,p) values (open green diamonds), and cam-B3LYP/def2-TZVP//cam-B3LYP/def2-TZVP (open pink hexagons) levels with cp corrections.

TABLE IV. Comparison of experimental and theoretical[a] 0 K bond enthalpies.

x/*y*	Expt.	B3LYP[b]	B3P86[b]	M06[b]	MP2(full)[b]	cam-B3LYP/def2-TZVP[c]
			$Co^+(H_2O)_{y-1}–(H_2O)$			
1	161.1 ± 5.8[d]	159.6 (162.6)	162.0 (165.0)	160.5 (164.0)	156.1 (166.1)	172.2 (182.1)
2	162.1 ± 6.8[d]	157.5 (160.5)	160.6 (163.6)	163.2 (166.7)	152.5 (162.4)	175.3 (185.2)
3	64.6 ± 4.8[d]	63.2 (66.2)	67.8 (70.9)	75.5 (79.0)	57.3 (67.3)	84.9 (94.9)
(4,0)	57.9 ± 5.8[d]	49.4 (52.7)	51.3 (54.7)	63.0 (67.8)	52.0 (59.2)	58.1 (65.3)
MAD[e]	5.8[f]	4.0 (2.5)	3.0 (3.7)	4.4 (7.9)	6.9 (2.3)	11.2 (20.4)
			$HO–Co^+(H_2O)_x$			
0	285.8 ± 13.8[g] 300 ± 4[h]	234.7 (238.0)	245.6 (249.0)	280.9 (285.7)	159.4 (166.5)	305.7 (308.8)
1	353.1 ± 9.8[i]	329.3 (332.5)	341.9 (345.4)	314.2 (319.0)	257.4 (264.6)	358.6 (361.6)
2	316.7 ± 14.7[g]	285.1 (288.4)	298.1 (301.5)	297.3 (302.1)	376.2 (383.4)	304.9 (307.9)
3	359.7 ± 17.0[g]	319.4 (322.5)	333.0 (336.2)	312.3 (315.8)	268.6 (279.3)	326.1 (329.2)
4	365.0 ± 19.5[g]	338.4 (341.4)	355.3 (358.3)	319.6 (323.2)	292.0 (302.2)	347.0 (350.0)
MAD[e]	13.2[f]	37.5 (34.3)	24.1 (20.8)	34.0 (29.7)	92.0 (86.4)	14.9 (14.3)
Overall MAD[j]	6.7[f]	12.3 (11.1)	9.4 (8.7)	15.3 (15.1)	27.2 (26.3)	8.2 (10.7)

[a]Theoretical values with (and without) cp corrections.
[b]Single point energies calculated at the indicated level of theory using the 6-311+G(2d,2p) basis set using B3LYP/6-311+G(d,p) geometries and zero point energy corrected.
[c]Geometries optimized at the cam-B3LYP/def2-TZVP level of theory.
[d] Values from the work of Dalleska *et al.*[5]
[e]Mean absolute deviations from experimental BDEs. $HO–Co^+(H_2O)_x$ MAD values are calculated with $x = 0$ value from the work of Chen *et al.*[60]
[f]Mean experimental uncertainty.
[g]Derived values from thermodynamic cycle (Fig. 7).
[h]Value from the work of Chen *et al.*[60]
[i]Table II.
[j]Includes all values in this table and Table III.

without cp corrections performed in the present study (and Table S4 of the supplementary material for all levels of theory). Comparison of the experimental and present theoretical values show that B3LYP, B3P86, and M06 levels of theory yield the best results, with MADs less than the mean experimental uncertainty (5.8 kJ/mol), and MP2(full) results are only slightly worse (MAD = 6.9 kJ/mol). In contrast, the cam-B3LYP/def2-TZVP theoretical results overestimate the $y = 1–3$ $Co^+(H_2O)_y$ experimental BDEs leading to a MAD of 11.2 kJ/mol.

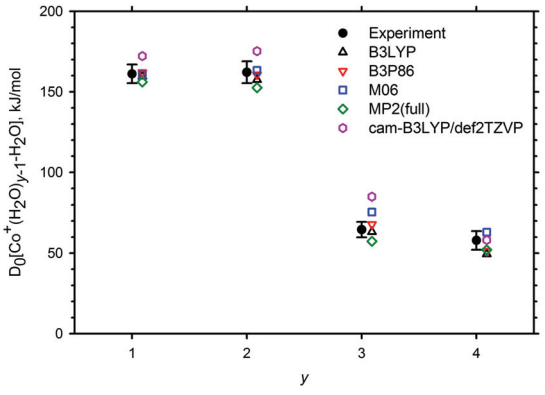

FIG. 6. Comparison of 0 K BDEs for neutral H_2O loss from $Co^+(H_2O)_y$ as a function of complex size (*y*): experimental values (black solid circles) and theoretical values for B3LYP/6-311+G(2d,2p)//B3LYP/6-311+G(d,p) (open black up triangles), B3P86/6-311+G(2d,2p)//B3LYP/6-311+G(d,p) (open red down triangles), M06/6-311+G(2d,2p)//B3LYP/6-311+G(d,p) (open blue squares), MP2(full)/6-311+G(2d,2p)//B3LYP/6-311+G(d,p) values (open green diamonds), and cam-B3LYP/def2-TZVP//cam-B3LYP/def2-TZVP (open pink hexagons) with cp corrections.

Table S4 of the supplementary material includes the theoretical BDEs for the two $Co^+(H_2O)_4$ predicted GSs, (4,0) and (2,2), for comparison with experiment. The B3LYP, B3LYP-GD3BJ, B3P86, and cam-B3LYP/def2-TZVP levels all predict that the (4,0) structure is low-lying such that calculated BDEs for either structure agree with experiment within the uncertainty [with differences of 0.1–8.5 kJ/mol for (4,0) and 1.9–2.1 kJ/mol for (2,2)]. In contrast, the M06 and MP2(full) levels calculate a (4,0) GS with (2,2) lying much higher in energy. Here, the BDEs for the (4,0) structure are in good agreement with experiment, within 6.6 kJ/mol, and BDEs for the (2,2) structure are much too small. In previous work, we have found that the MP2(full) level properly predicts the ground state structures of $Zn^{2+}(H_2O)_x$ and $CuOH^+(H_2O)_x$ complexes,[9,19] such that it seems more likely that (4,0) is the experimental ground structure; however, this conclusion appears at odds with the spectroscopic evidence from Furukawa *et al.*[58] discussed above.

Derived thermochemical values for dehydroxylation

Using the experimental BDEs for $CoOH^+(H_2O)$ dehydroxylation, $CoOH^+(H_2O)_x$ dehydration, and $Co^+(H_2O)_y$ dehydration, Hess's law can be used to derive values for the loss of the OH ligand from $CoOH^+(H_2O)_x$, where $x = 0$, and 2–4, Fig. 7. The derived BDE for loss of OH from $CoOH^+$ is 285.8 ± 13.8 kJ/mol, which is in good agreement with the

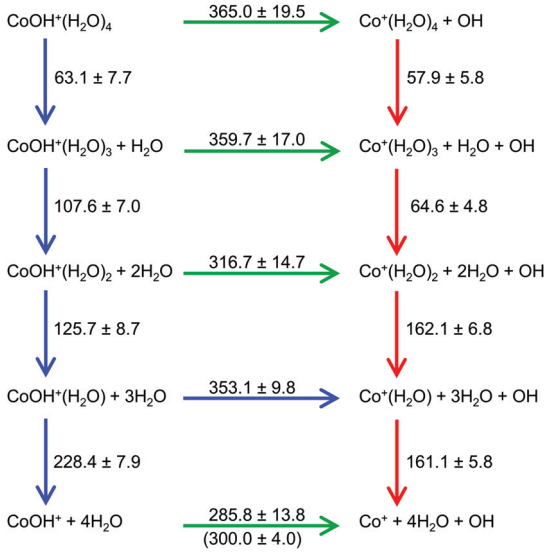

FIG. 7. Comparison of present experimental results (blue arrows, left side) with those of Dalleska *et al.* (red arrows, right side, Ref. 5). Derived BDEs for the loss of OH lie in between (green arrows), with the experimental value from Chen *et al.* in parenthesis (Ref. 60).

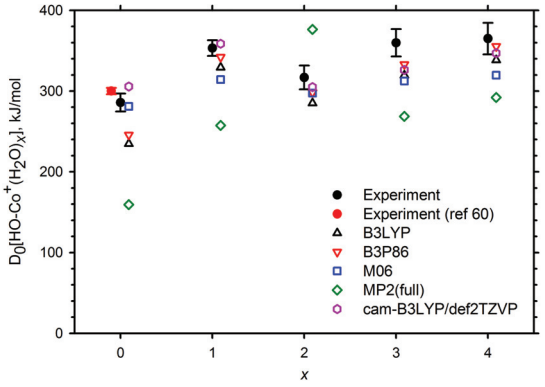

FIG. 8. Comparison of 0 K BDEs for neutral OH loss from $CoOH^+(H_2O)_x$ as a function of complex size (x): experimental values (black solid circles), literature values (red solid circle, Ref. 60) and theoretical values for B3LYP/6-311+G(2d,2p)//B3LYP/6-311+G(d,p) (open black up triangles), B3P86/6-311+G(2d,2p)//B3LYP/6-311+G(d,p) (open red down triangles), M06/6-311+G(2d,2p)//B3LYP/6-311+G(d,p) (open blue squares), MP2(full)/6-311+G(2d,2p)//B3LYP/6-311+G(d,p) values (open green diamonds), and cam-B3LYP/def2-TZVP//cam-B3LYP/def2-TZVP (open pink hexagons) with cp corrections.

0 K BDE value of 300 ± 4 kJ/mol,[60] obtained from previous studies in our laboratory of the endothermic reaction $Co^+ + H_2O \rightarrow CoOH^+ + H$. This helps confirm the accuracy of the present measurements for this reaction. As is clear from the dissociation behavior observed in Fig. 3(d), the BDE for Co^+–OH is much stronger than that for Co^+–OH_2. Indeed, the analysis indicates that the former is ~80% larger than the latter. In an examination of the periodic trends in the BDEs of first-row transition metal hydroxide cations, it has been found that these MOH^+ BDEs are 120 ± 21 kJ/mol stronger than those for the analogous metal-methyl cations for the late transition metals (Mn, Fe, Co).[61] This has been attributed to the ability of the lone pairs of electrons on oxygen to donate into half-filled 3dπ orbitals on the metal center, leading to a bond order for these dative π bonds of one-half. For the $^4A''$ state of $CoOH^+$, there are two such acceptor orbitals, effectively allowing the formation of two half-dative π bonds, in addition to the covalent sigma bond (the only bond for MCH_3^+). As the bonding in $Co^+(H_2O)$ is primarily the donation of the oxygen electrons into an empty 4s-3d (sd) hybrid orbital, only a single dative sigma bond is formed here, consistent with the observation of the strong increase in bonding observed for $CoOH^+$.

The HO–$Co^+(H_2O)_x$ BDEs for $x = 0$–4 are also compared to theoretical BDEs determined at the same levels used above with (and without) cp corrections in Table IV and Fig. 8. Figure 8 indicates that all levels of theory except MP2(full) qualitatively predict the trends in these BDEs, including the decrease at $x = 2$. (The MP2(full) level also did not accurately predict the dehydroxylation BDEs for the copper system.[19]) Table IV shows that theory has more difficulty accurately predicting the HO–$Co^+(H_2O)_x$ BDEs compared to those for dehydration, with much larger MADs, 24–38 kJ/mol, substantially greater than the average experimental uncertainty, 13.2 kJ/mol. The exception is the cam-B3LYP/def2-TZVP results, which have a MAD of only 15 kJ/mol.

Table IV also includes overall MADs from $CoOH^+(H_2O)_{x-1}$–(H_2O), $Co^+(H_2O)_{y-1}$–(H_2O), and HO–$Co^+(H_2O)_x$ BDEs for all levels of theory. Compared with the overall experimental uncertainty (6.7 kJ/mol), the B3LYP, B3LYP-GD3BJ, B3P86, and cam-B3LYP/def2-TZVP levels of theory have comparable overall MADs of 8–12 kJ/mol, whereas the M06, M06-GD3, MP2(full), and cam-B3LYP levels have higher overall MADs of 15–31 kJ/mol.

Trends in bond enthalpies

Co^{2+} and Co^+ have $3d^7$ and $3d^8$ configurations, respectively. The $CoOH^+(H_2O)_x$ complexes have a preference for CN = 4 with a tetrahedral geometry. As this is the preferred ligand field coordination for Co^{2+} ($3d^7$), this shows that the hydroxide acts as a strong electron withdrawer effectively inducing more Co^{2+} character. Indeed, examination of the molecular orbitals for $CoOH^+$ finds the holes (SOMOs) to be in the $3d_{xy}$ (δ), $3d_{yz}$ (π), and $3d_{xz}$ (π) orbitals (where the z axis lies along the Co–O bond, Fig. S3 of the supplementary material), which become the t_{2g} orbitals in the near tetrahedral $CoOH^+(H_2O)_3$. The $Co^+(H_2O)_y$ complexes also show a preference for CN = 4 but with a square planar geometry, described above. Here the SOMOs are the $3d_{z^2}$ and $3d_{x^2-y^2}$ orbitals for the $Co^+(H_2O)_4$ system (where the ligands lie along the x and y axes, Fig. S2 of the supplementary material).

Comparison of the experimentally determined dehydration energies for $CoOH^+(H_2O)_x$ and $Co^+(H_2O)_y$ (where $x/y = 1$–4) values can be seen in Fig. 7. The BDEs for $Co^+(H_2O)_y$ are nearly identical for $y = 1$ and 2, followed by a large decrease (98 kJ/mol), and then the values for $y = 3$ and 4 are again similar. This sequence has been explained in terms of sd orbital hybridization.[5,62] Here, the first water ligand induces sd hybridization, which empties the sd orbital along the Co–O

bond axis and puts electron density in an sd orbital perpendicular to this axis. A second water can also donate into the empty sd orbital at 180° relative to the first water ligand, resulting in a comparable BDE because the energetic cost of promotion has already been paid by the first ligand. If the third water adds directly to the metal, it must approach the sd orbital containing the electron density, leading to a much weaker bond (consistent with the T-shaped geometry shown in Fig. 2 and the longer bond length for the side water ligand). The fourth water is similarly behaved, and sd hybridization explains why the (4,0) complex has two short and two long Co–O bonds. Depending on the strength of the hydrogen bonding, the weaker third and fourth bonds to the metal allow the (2,2) complex to be competitive with (4,0) at some levels of theory.

A similar general trend is observed in the $CoOH^+(H_2O)_x$ system, Fig. 5. As for $Co^+(H_2O)_y$, there is a similar large decrease in BDE (103 kJ/mol) between complexes having CN = 2 and 3 (x = 1 and 2 for the hydroxides). Again, there is a leveling for CN = 3 and 4 (decrease of only 18 kJ/mol), which is consistent with sd hybridization. The larger decrease between x = 3 and 4 (44 kJ/mol) is a result of having the fourth ligand in the second solvent shell as the ligand–ligand hydrogen bonding is weaker than the dative metal–ligand bonds. For complexes having the same CN, the loss of water from $CoOH^+(H_2O)_{CN-1}$ requires more energy than from $Co^+(H_2O)_{CN}$, with fairly uniform differences of 66, 61, and 50 kJ/mol for CN = 2, 3, and 4, respectively. This enhancement can be attributed to the $Co^{2+}OH^-$ character of the $CoOH^+$ species.

For the $HO–Co^+(H_2O)_x$ BDEs, there is an interesting decrease at x = 2, Fig. 8. A similar observation was made for the analogous $HO–Cu^+(H_2O)_x$ BDEs. We attribute this lower BDE to the fact that the system is going from a CN = 3 complex to a favorable CN = 2 complex. As noted above, sd hybridization leads to weaker BDEs for the CN = 3 complexes, compared with CN = 2. All other dehydroxylations occur between complexes having comparable strong (CN = 1 → 0 and 2 → 1) or weak (CN = 4 → 3 and 4 → 4) binding, leading to similar $HO–Co^+(H_2O)_x$ BDEs. Although all $Co^+–OH$ BDEs for x = 0–4 are fairly large, >300 kJ/mol, the addition of waters to $CoOH^+$ increases this BDE by additional 31–79 kJ/mol. We attribute these increases to the ionic $Co^{2+}OH^-$ character, which is stabilized by addition of water ligands to the metal cation.

These results can also be compared to the analogous values for $CuOH^+(H_2O)_x$ complexes.[19] The $Cu^+–OH$ BDE is only 151.5 ± 8.0 kJ/mol, 148.5 kJ/mol smaller than that for $CoOH^+$ because the additional two electrons on Cu^+ fully occupy the 3dπ orbitals, such that the $CuOH^+$ bond is not augmented by dative π bonding. Interestingly, upon addition of water molecules, the $HO–Co^+(H_2O)_x$ dehydroxylation values are on average 191 ± 10 kJ/mol higher than the previously derived values for $HO–Cu^+(H_2O)_x$.[19] The additional 40 kJ/mol enhancement suggests that there is more $M^{2+}OH^-$ character for the cobalt species than the copper system.

Conversion of 0 K hydration energies to 298 K

In all cases, the primary threshold energies obtained including lifetime effects are assigned as the 0 K bond energies. A rigid rotor/harmonic oscillator (RR/HO) approximation using the vibrational frequencies (scaled by 0.989) and rotational constants calculated at the B3LYP/6-311+G(d,p) level of theory was used to calculate $\Delta H_{298} - \Delta H_0$ and $T\Delta S_{298}$ values for dissociation. These conversion factors were used to convert the 0 K bond energies into 298 K bond enthalpies (ΔH_{298}) and to determine free energies (ΔG_{298}) of dissociation. These values are listed in Table V. The uncertainties in these conversions were obtained by scaling the vibrational frequencies up and down by 10%. It should be noted that some of the low vibrational frequencies correspond to torsional motions of the water ligands and thus the RR/HO approximation may not be accurate for these degrees of freedom.

TABLE V. Conversion of 0 K thresholds to 298 K enthalpies and free energies (kJ/mol).[a]

x/y	ΔH_0[b]	ΔH_{298}-ΔH_0[c]	ΔH_{298}	$T\Delta S_{298}$[c]	ΔG_{298}
		$CoOH^+(H_2O)_{x-1}–(H_2O)$			
1	228.4 (7.9)	3.4 (0.5)	231.8 (7.9)	36.7 (1.1)	195.1 (8.0)
2	125.7 (8.7)	2.7 (1.1)	128.4 (8.8)	34.9 (2.7)	93.5 (9.2)
3	107.6 (7.0)	2.9 (1.6)	110.6 (7.2)	41.0 (3.9)	69.5 (8.2)
4	63.1 (7.7)	4.9 (1.4)	68.1 (7.8)	43.9 (3.2)	24.1 (8.5)
		$Co^+(H_2O)_{y-1}–(H_2O)$			
1	161.1 (5.8)[d]	2.7 (0.3)	163.8 (5.8)	22.3 (0.5)	141.5 (5.8)
2	162.1 (6.8)[d]	2.4 (0.5)	164.5 (6.8)	38.2 (1.2)	126.3 (6.9)
3	64.6 (4.8)[d]	1.4 (0.5)	66.6 (4.8)	33.5 (1.3)	32.5 (5.0)
4	57.9 (5.8)[d]	1.7 (0.5)	59.6 (5.8)	38.4 (1.3)	21.2 (6.0)
		$HO–Co^+(H_2O)_x$			
0	300.0 (4.0)[e]	3.9 (0.2)	303.9 (4.0)	27.2 (0.3)	276.7 (4.0)
1	353.1 (9.8)	3.4 (0.3)	356.5 (9.8)	37.3 (0.9)	319.6 (9.8)
2	316.7 (14.7)	2.9 (0.4)	319.6 (14.7)	33.8 (0.9)	285.8 (14.7)
3	359.7 (17.0)	4.4 (0.4)	364.1 (17.0)	38.6 (0.8)	325.6 (17.0)
4	365.0 (19.5)	7.1 (0.3)	372.0 (19.5)	45.5 (0.4)	262.6 (19.5)

[a]Uncertainties in parentheses.
[b]Values from Tables III and IV.
[c]Values are calculated from the vibrational frequencies and rotational constants calculated at the B3LYP/6-311+G(d,p) level of theory. Uncertainties are found by scaling the vibrational frequencies up and down by 10%.
[d]Reference 5.
[e]Reference 60.

For the $CoOH^+(H_2O)_{x-1}–(H_2O)$, $Co^+(H_2O)_{y-1}–(H_2O)$, and $HO–Co^+(H_2O)_x$ systems, the ΔH_{298} and ΔG_{298} values track the 0 K hydration enthalpies (ΔH_0) as the values decrease with an increasing number of water ligands. The only exception is for $Co^+(H_2O)_{y-1}–(H_2O)$ at y = 1 and 2 where the entropy difference means that $\Delta G_{298}(1)$ is greater than $\Delta G_{298}(2)$ by ~15 kJ/mol.

CONCLUSION

The kinetic energy dependent cross sections for collision-induced dissociation of $CoOH^+(H_2O)_x$ complexes with Xe where x = 1–4 are determined using guided ion beam tandem mass spectrometry. The dominant CID pathway in all systems observed is the loss of a single water molecule from the reactant ion followed by sequential losses of additional water ligands when possible. At x = 1, the loss of the hydroxide ligand is also observed at much higher energies than the loss of water. Statistical analysis of the TCID data is used to obtain 0 K BDEs, and these energies are converted to 298 K using a rigid rotor/harmonic oscillator approximation. The water loss BDEs

decrease monotonically from $x = 1$–4. In addition, BDEs for the loss of hydroxide are derived by combining the directly measured $x = 1$ hydroxide BDE with dehydration BDEs for $CoOH^+(H_2O)_x$ and $Co^+(H_2O)_y$ results taken from the literature.[5] The derived BDE for $CoOH^+$ matches a previously determined value[60] within experimental uncertainty.

In agreement with previous work, the present theoretical results indicate that cobalt has a coordination number of four for the first inner solvent shell. BDEs are best reproduced by cam-B3LYP/def2-TZVP calculations including counterpoise corrections with the lowest overall MADs, with B3LYP/6-311+G(2d,2p), B3LYP-GD3BJ/6-311+G(2d,2p), and B3P86/6-311+G(2d,2p) results being only slightly worse. MP2(full)/6-311+G(2d,2p) calculations have a large overall MAD primarily because of discrepancies with the homolytic bond cleavage for the $HO–Co^+(H_2O)_x$ BDEs. Otherwise, this level of theory has good agreement with experiment for calculating the heterolytic water loss BDEs for both $CoOH^+$ and Co^+.

SUPPLEMENTARY MATERIAL

See supplementary material for additional tables including structural parameters for optimized geometries of $CoOH^+(H_2O)_x$ ($x = 0$–4) and $Co^+(H_2O)_y$ ($y = 1$–4) predicted ground structures; a table of relative 0 K enthalpies and 298 K energies for all conformers of $CoOH^+(H_2O)_x$ ($x = 0$–4) and $Co^+(H_2O)_y$ ($y = 1$–4) at seven levels of theory; and two tables comparing experimental 0 K bond enthalpies for $CoOH^+(H_2O)_{x-1}–(H_2O)$, $Co^+(H_2O)_{y-1}–(H_2O)$, and $HO–Co^+(H_2O)_x$ with seven levels of theory with and without counterpoise corrections. Also included is a detailed discussion of high and low energy isomer geometries and figures of all isomers of $CoOH^+(H_2O)_x$ ($x = 0$–4) and two figures of the singly occupied molecular orbitals (SOMOs) for $Co^+(H_2O)_4$ and $CoOH^+$.

ACKNOWLEDGMENTS

This work is supported by the National Science Foundation, Grant No. CHE-1359769. In addition, we thank the Center for High Performance Computing (CHPC) at the University of Utah for the generous allocation of computing time.

[1] D. G. Barceloux, J. Toxicol., Clin. Toxicol. **37**, 201 (1999).
[2] P. Maxwell and K. Salnikow, Cancer Biol. Ther. **3**, 29 (2004).
[3] L. Prashanth, K. K. Kattapagari, R. T. Chitturi, V. R. R. Baddam, and L. K. Prasad, J. Dr. NTR Univ. Health Sci. **4**, 75 (2015).
[4] Agency for Toxic Substances and Disease Registry, *Public Health Statement Cobalt* (Center for Disease Control Department of Health and Human Services, 2004), p. 29.
[5] N. F. Dalleska, K. Honma, L. S. Sunderlin, and P. B. Armentrout, J. Am. Chem. Soc. **116**, 3519 (1994).
[6] T. E. Hofstetter and P. B. Armentrout, J. Phys. Chem. A **117**, 1110 (2013).
[7] R. A. Coates and P. B. Armentrout, J. Phys. Chem. A **121**, 3629 (2017).
[8] P. B. Armentrout and A. F. Sweeney, Eur. J. Mass Spectrom. **21**, 497 (2015).
[9] T. E. Cooper, D. R. Carl, and P. B. Armentrout, J. Phys. Chem. A **113**, 13727 (2009).
[10] T. E. Cooper and P. B. Armentrout, J. Phys. Chem. A **113**, 13742 (2009).
[11] T. E. Cooper and P. B. Armentrout, Chem. Phys. Lett. **486**, 1 (2010).
[12] T. E. Cooper and P. B. Armentrout, J. Chem. Phys. **134**, 114308 (2011).
[13] P. Jayaweera, A. T. Blades, M. G. Ikonomou, and P. Kebarle, J. Am. Chem. Soc. **112**, 2452 (1990).
[14] A. T. Blades, P. Jayaweera, M. G. Ikonomou, and P. Kebarle, J. Chem. Phys. **92**, 5900 (1990).
[15] A. T. Blades, P. Jayaweera, M. G. Ikonomou, and P. Kebarle, Int. J. Mass Spectrom. Ion Processes **102**, 251 (1990).
[16] A. A. Shvartsburg and K. W. M. Siu, J. Am. Chem. Soc. **123**, 10071 (2001).
[17] B. M. Marsh, J. Zhou, and E. Garand, Phys. Chem. Chem. Phys. **17**, 25786 (2015).
[18] B. M. Marsh, J. M. Voss, J. Zhou, and E. Garand, Phys. Chem. Chem. Phys. **17**, 23195 (2015).
[19] A. F. Sweeney and P. B. Armentrout, J. Phys. Chem. A **118**, 10210 (2014).
[20] K. M. Ervin and P. B. Armentrout, J. Chem. Phys. **83**, 166 (1985).
[21] F. Muntean and P. B. Armentrout, J. Chem. Phys. **115**, 1213 (2001).
[22] R. M. Moision and P. B. Armentrout, J. Am. Soc. Mass Spectrom. **18**, 1124 (2007).
[23] T. Kim, K. Tang, H. R. Udseth, and R. D. Smith, Anal. Chem. **73**, 4162 (2001).
[24] D. R. Carl, R. M. Moision, and P. B. Armentrout, J. Am. Soc. Mass Spectrom. **20**, 2312 (2009).
[25] D. R. Carl, B. K. Chatterjee, and P. B. Armentrout, J. Chem. Phys. **132**, 044303 (2010).
[26] T. E. Cooper, J. T. O'Brien, E. R. Williams, and P. B. Armentrout, J. Phys. Chem. A **114**, 12646 (2010).
[27] O. W. Wheeler, D. R. Carl, T. E. Hofstetter, and P. B. Armentrout, J. Phys. Chem. A **119**, 3800 (2015).
[28] J. E. Carpenter, C. P. McNary, A. Furin, A. F. Sweeney, and P. B. Armentrout, "How hot are your ions really? A threshold collision-induced dissociation study of substituted benzylpyridinium "thermometer" ions," J. Am. Soc. Mass Spectrom. (published online 2017).
[29] D. Gerlich, Adv. Chem. Phys. **82**, 1 (1992).
[30] N. Aristov and P. B. Armentrout, J. Phys. Chem. **90**, 5135 (1986).
[31] N. R. Daly, Rev. Sci. Instrum. **31**, 264 (1960).
[32] D. A. Hales, L. Lian, and P. B. Armentrout, Int. J. Mass Spectrom. Ion Processes **102**, 269 (1990).
[33] R. H. Schultz, K. C. Crellin, and P. B. Armentrout, J. Am. Chem. Soc. **113**, 8590 (1991).
[34] T. S. Beyer and D. F. Swinehart, Commun. ACM **16**, 379 (1973).
[35] S. E. Stein and B. S. Rabinovich, Chem. Phys. Lett. **49**, 183 (1977).
[36] S. E. Stein and B. S. Rabinovitch, J. Chem. Phys. **58**, 2438 (1973).
[37] R. G. Gilbert and S. C. Smith, *Theory of Unimolecular and Recombination Reactions* (Blackwell Scientific, Oxford, 1990).
[38] K. A. Holbrook, M. J. Pilling, and S. H. Robertson, *Unimolecular Reactions*, 2nd ed. (Wiley, New York, 1996).
[39] D. G. Truhlar, B. C. Garrett, and S. J. Klippenstein, J. Phys. Chem. **100**, 12771 (1996).
[40] M. T. Rodgers, K. M. Ervin, and P. B. Armentrout, J. Chem. Phys. **106**, 4499 (1997).
[41] P. B. Armentrout, K. M. Ervin, and M. T. Rodgers, J. Phys. Chem. A **112**, 10071 (2008).
[42] P. B. Armentrout and J. Simons, J. Am. Chem. Soc. **114**, 8627 (1992).
[43] P. B. Armentrout, J. Chem. Phys. **126**, 234302 (2007).
[44] M. J. Frisch *et al.*, GAUSSIAN 09, Revision D01, Gaussian, Inc., Pittsburgh, PA, 2009.
[45] A. D. Becke, J. Chem. Phys. **98**, 5648 (1993).
[46] R. Ditchfield, W. J. Hehre, and J. A. Pople, J. Chem. Phys. **54**, 724 (1971).
[47] C. W. Bauschlicher and H. Partridge, J. Chem. Phys. **103**, 1788 (1995).
[48] S. F. Boys and R. Bernardi, Mol. Phys. **19**, 553 (1970).
[49] F. B. van Duijneveldt, J. G. C. M. van Duijneveldt-van de Rijdt, and J. H. van Lenthe, Chem. Rev. **94**, 1873 (1994).
[50] T. Yanai, D. P. Tew, and N. C. Handy, Chem. Phys. Lett. **393**, 51 (2004).
[51] J. P. Perdew, Phys. Rev. B **33**, 8822 (1986).
[52] Y. Zhao and D. G. Truhlar, Theor. Chem. Acc. **120**, 215 (2008).
[53] C. Møller and M. S. Plesset, Phys. Rev. **46**, 618 (1934).
[54] S. Grimme, S. Ehrlich, and L. Goerigk, J. Comput. Chem. **32**, 1456 (2011).
[55] H. S. R. Gilson and M. Krauss, J. Phys. Chem. A **102**, 6525 (1998).
[56] A. Ricca and C. W. J. Bauschlicher, J. Phys. Chem. A **101**, 8949 (1997).
[57] M. K. Beyer and R. B. Metz, J. Phys. Chem. A **107**, 1760 (2003).
[58] K. Furukawa, K. Ohashi, N. Koga, T. Imamura, K. Judai, N. Nishi, and H. Sekiya, Chem. Phys. Lett. **508**, 202 (2011).
[59] L. Poisson, L. Dukan, O. Sublemontier, F. Lepetit, F. Réau, P. Pradel, J. M. Mestdagh, and J. P. Visticot, Int. J. Mass Spectrom. **220**, 111 (2002).
[60] Y.-M. Chen, D. E. Clemmer, and P. B. Armentrout, J. Am. Chem. Soc. **116**, 7815 (1994).
[61] P. B. Armentrout, and B. L. Kickel, in *Organometallic Ion Chemistry*, edited by B. S. Freiser (Kluwer, Dordrecht, 1996), p. 1.
[62] M. Rosi and C. W. Bauschlicher, Jr., J. Chem. Phys. **90**, 7264 (1989).

CHAPTER 6

STRUCTURAL CHARACTERIZATION OF GAS-PHASE CYSTEINE AND CYSTEINE METHYL ESTER COMPLEXES OF ZINC AND CADMIUM DICATIONS BY INFRARED MULTIPLE PHOTON DISSOCIATION SPECTROSCOPY

Reprinted with permission from Rebecca A. Coates, Christopher P. McNary, Georgia C. Boles, Giel Berden, Jos Oomens and P. B. Armentrout, Structural Characterization of Gas-Phase Cysteine and Cysteine Methyl Ester Complexes of Zinc and Cadmium Dications by Infrared Multiple Photon Dissociation Spectroscopy, *Physical Chemistry Chemical Physics*, **2015** *17*, 25799-25808. DOI: 10.1039/c5cp01500f.

PCCP

PAPER

Cite this: *Phys. Chem. Chem. Phys.*, 2015, **17**, 25799

Structural characterization of gas-phase cysteine and cysteine methyl ester complexes with zinc and cadmium dications by infrared multiple photon dissociation spectroscopy†

Rebecca A. Coates,[a] Christopher P. McNary,[a] Georgia C. Boles,[a] Giel Berden,[b] Jos Oomens[bc] and P. B. Armentrout*[a]

Received 13th March 2015,
Accepted 8th April 2015

DOI: 10.1039/c5cp01500f

www.rsc.org/pccp

Structural characterization of gas-phase ions of cysteine (Cys) and cysteine methyl ester (CysOMe) complexed to zinc and cadmium is investigated by infrared multiple photon dissociation (IRMPD) action spectroscopy using a free electron laser in combination with density functional theory calculations. IRMPD spectra are measured for $[Zn(Cys\text{-}H)]^+$, $[Cd(Cys\text{-}H)]^+$, $[Zn(CysOMe\text{-}H)]^+$, $[Cd(CysOMe\text{-}H)]^+$ and $CdCl^+(CysOMe)$ and are accompanied by quantum mechanical calculations of the predicted linear absorption spectra at the B3LYP/6-311+G(d,p) (Zn^{2+} complexes) and B3LYP/def2TZVP levels (Cd^{2+} complexes). On the basis of these experiments and calculations, the conformation that best reproduces the IRMPD spectra for the complexes of the deprotonated amino acids, $[M(Cys\text{-}H)]^+$ and $[M(CysOMe\text{-}H)]^+$, is a charge-solvated (CS) tridentate structure where the metal dication binds to the amine and carbonyl groups of the amino acid backbone and the deprotonated sulfur atom of the side chain, [N,CO,S$^-$]. The intact amino acid complex, $CdCl^+(CysOMe)$ binds in the equivalent motif [N,CO,S]. These binding motifs are in agreement with the predicted ground structures of these complexes at the B3LYP, B3LYP-GD3BJ (with empirical dispersion corrections), B3P86, and MP2(full) levels.

Introduction

A large number of proteins have been found to exhibit metal-dependent transcription regulation activities and contain cysteine-rich sequence motifs capable of coordinating Zn^{2+} ions.[1] Included in these are zinc finger proteins, metalloproteins that utilize zinc ions for structural integrity.[2] These zinc finger proteins are characterized by divalent Zn^{2+} centers directly coordinated to amino acid residues, most commonly binding as $Zn(Cys)_{4-n}(His)_n$, where n = 0–2.[3] Zinc finger proteins are active in transcription factors as well as in DNA-repair of enzymes. Competition from toxic metal ions that replace the essential zinc ion center has been observed[4,5] and has a profound effect on the protein's structure and function, essentially deactivating it.

Toxic metals that have high affinities for thiol groups make cysteine containing zinc finger proteins particularly susceptible to Zn^{2+} replacement. This includes cadmium, its group 12 congener, even in low concentrations.[6] The mechanisms of cadmium toxicity is not well understood, although cadmium is known to target thiol groups in proteins.[7] The mechanism for zinc finger protein inactivation by toxic metal replacement is presumed to involve structural changes of the coordinating amino acid residues. Investigating these complexes in isolation at the fundamental level may be beneficial to unveiling structural evidence for how these metals coordinate with the relevant amino acid residues. Theoretical investigations by Russo *et al.* of the interactions of cysteine with Cu^{2+}, Zn^{2+}, Cd^{2+}, and Hg^{2+} found that zinc and cadmium both form stable complexes by coordination of the metal to cysteine in a tridentate binding pattern involving the amino nitrogen, carbonyl oxygen, and side-chain sulfur.[8] Similarly, quantum chemical studies by Mori *et al.*[9] examined the interactions of Hg^{2+}, Cd^{2+}, and Zn^{2+} with deprotonated cysteine either microsolvated by one or two water molecules or using a polarized continuum model. For one water ligand, they found a similar tridentate motif, where deprotonation occurs at the thiol. When placed in solution, the Zn complex retains the tridentate binding motif, whereas the Cd complex prefers the bidentate conformation. For two waters (gas-phase or in solution),

[a] *Department of Chemistry, University of Utah, Salt Lake City, UT 84112, USA. E-mail: armentrout@chem.utah.edu*
[b] *Radboud University, Institute for Molecules and Materials, FELIX Laboratory, Toernooiveld 7, NL-6525ED Nijmegen, The Netherlands*
[c] *van't Hoff Institute for Molecular Sciences, University of Amsterdam, Amsterdam, The Netherlands*

† Electronic supplementary information (ESI) available: Relative 0 K enthalpies and 298 K free energies for all conformers of all complexes studied here calculated at the B3LYP, B3LYP-GD3BJ, B3P86, and MP2(full) levels of theory with 6-311+G(2d,2p) and def2TZVPP basis sets are given in Table S1. This material is available free of charge *via* the Internet see DOI: 10.1039/c5cp01500f

a bidentate chelation by the amino nitrogen and deprotonated sulfur is preferred for both Zn and Cd. In the context of hydration, we have previously studied the hydration energies of both Zn^{2+} and Cd^{2+},[10,11] finding that Zn^{2+} binds more strongly than Cd^{2+} by $\sim$8 kJ mol^{-1} for six through eight water ligands, but less strongly by $\sim$5 kJ mol^{-1} for the ninth and tenth water ligands. It should be realized that the solvated environment may be relevant to the delivery of these metal ions to the zinc finger sites, but in the protein, the metal ion remains unsolvated by water.

In previous experimental work, Bohme and coworkers examined the collision-induced dissociation of Zn^{2+} bound to 12-residue peptides containing either two cysteines and two histidines (CCHH and CHCH) or four cysteines (CCCC).[12] They concluded that zinc binds to both residues but prefers binding to histidine. No specific details of the binding site for these residues could be provided. Previously, our group has examined complexes of the single amino acid histidine (His) with Zn^{2+} and Cd^{2+} using infrared multiple photon dissociation (IRMPD) action spectroscopy.[13] In these cases, the simple M^{2+}(His) complexes were not generated directly by electrospray ionization. Thus the interactions of the metal ions with histidine were mimicked by examining the $CdCl^+$(His) and $[M(His-H)]^+$ systems. Structures for these systems were determined definitively using IRMPD spectroscopy and quantum chemical calculations, finding that the metal ions bind to His in a tridentate conformation by attaching to a carboxylate oxygen, the backbone amino group (N), and the imidazole side-chain nitrogen (N_π). Deprotonation in the $[M(His-H)]^+$ complexes was found unequivocally to be at the carboxylic acid for both metals. The present study approaches the metal–cysteine (Cys) binding interaction similarly with a systematic structural investigation using IRMPD action spectroscopy and quantum chemical calculations. Conformations are identified by comparing the experimental IRMPD action spectra to IR spectra derived from quantum chemical calculations at the B3LYP/6-311+G(d,p) (Zn^{2+} complexes) and B3LYP/def2TZVP levels (Cd^{2+} complexes) levels of theory of the low-lying structures of the complexes. In order to definitively ascertain whether structures of these complexes involve deprotonation of the carboxylic acid site, as seen in the His study, metal binding to cysteine methyl ester (CysOMe) is also examined.

Experimental and theoretical methods

Mass spectrometry and IRMPD spectroscopy

Experiments were performed at the FELIX Facility, Radboud University, The Netherlands, using the Free Electron Laser for Infrared eXperiments (FELIX)[14] beam line. A 4.7 T Fourier transform ion cyclotron resonance (FT-ICR) mass spectrometer, described elsewhere,[15–17] was used to record the IRMPD spectra. The metal–cysteine complex ions were generated using a Micromass Z-spray electrospray ionization source. Solutions of 1.0 mM Cys with 1.0 mM zinc nitrate or cadmium chloride in 50 : 50 MeOH : H_2O solution were used with a flow rate of 3–10 μL min^{-1}. Ions generated from the ESI were accumulated in a hexapole trap for 5–7 s before being pulse extracted through a quadrupole bender and injected into the ICR cell *via* a radiofrequency (rf) octopole ion guide. Ion capturing was affected by electrostatic switching of the dc bias of the octopole to avoid collisional heating of the ions.[15] Once trapped in the ICR cell, the ions are cooled to room temperature and the ion of interest is mass isolated using a stored waveform inverse Fourier transform (SWIFT) excitation pulse[18,19] and irradiated with FELIX for 3–5 s at a 5 or 10 Hz macropulse repetition rate. At each wavelength, the parent and fragment ion intensities are used to determine the fractional yield, $Y = \Sigma I_F/(I_P + \Sigma I_F)$, where I_P and I_F are the integrated intensities of the parent and fragment ion mass peaks, respectively. The IRMPD spectra are generated by plotting the yield as a function of the wavenumber of the IR radiation.

The ESI source generated $[M(Cys-H)ACN]^+$, $[M(CysOMe-H)ACN]^+$ and $CdCl^+$(CysOMe) directly for M = Zn and Cd where ACN = acetonitrile (originally, the ACN was present adventitiously from previous experiments, although in some cases, additional ACN was added to the electrospray solution to enhance intensities of these complexes). The $[M(Cys-H)]^+$ and $[M(CysOMe-H)]^+$ species interrogated here were generated by irradiation of their corresponding ACN adduct ions with a 40 W continuous-wave CO_2 laser for 0.2 s and then allowing the resulting ions to cool for an additional 0.1 s before isolation in the FT-ICR and irradiation with the FELIX light.

Computational details

Possible geometries for Zn^{2+}(Cys) complexes were taken from previously published geometries of Li^+(Cys) complexes.[20] Structures were optimized using density functional theory (DFT) and the Gaussian09 suite of programs[21] at the B3LYP/6-31G(d) level of theory[22,23] using the ''loose'' keyword to utilize a large step size of 0.01 au and rms force constant of 0.0017 to ensure a rapid geometry convergence. These structures were refined by geometry optimization at a B3LYP/6-311+G(d,p) level. From these optimized structures, the Cys residue was deprotonated at likely sites (S, O, or N) yielding $[Zn(Cys-H)]^+$ structures that were refined again in the loose optimization step. Remaining unique converged structures were then chosen for further geometry optimization and vibrational frequency calculations at the B3LYP/6-311+G(d,p) level of theory. Geometry optimizations utilizing empirical dispersion corrections were also determined at the B3LYP-GD3BJ/6-311+G(d,p) level.[24] The $[Cd(Cys-H)]^+$ complexes went through the same geometry optimization procedure except the def2TZVP basis set was used, where def2TZVP is a size-consistent basis set for all atoms and includes triple-ζ + polarization functions with a small core (28 electron) effective core potential (ECP) on Cd.[25,26] The def2TZVP basis set and affiliated ECP were obtained from the EMSL basis set exchange.[27] Single-point energy calculations were carried out at the B3LYP, B3LYP-GD3BJ, B3P86,[28] and MP2(full)[29] (where full indicates correlation of all electrons) levels using the 6-311+G(2d,2p) (def2TZVPP) basis sets for Zn (Cd) complexes. Zero point energy (ZPE) corrections scaled by 0.989 were determined in order to provide 0 K relative energies and thermal corrections to free energies at 298 K. For comparison to IRMPD experimental spectra, calculated frequencies were scaled by 0.975, as this factor

leads to good agreement between calculated and experimentally well-resolved peaks and is consistent with previous IRMPD studies of metal–amino acid complexes.[13,30–34] Calculated vibrational frequencies are broadened using a 15 cm^{-1} full width at half maximum Gaussian line shape for comparison with experimental spectra.

Results and discussion

Theoretical results

Overview. As described above, low-energy structures of the $[M(Cys\text{-}H)]^+$, $[M(CysOMe\text{-}H)]^+$, and $CdCl^+(CysOMe)$ complexes were optimized at the B3LYP/6-311+G(d,p) level of theory. Table 1 provides relative 298 K Gibbs free energies for the low-energy conformers of $[M(Cys\text{-}H)]^+$. Relative energies at 0 K with respect to the ground structure (GS) calculated at three different levels of theory are given in Table S1 of the ESI,† for low-energy conformations of $[M(Cys\text{-}H)]^+$, $[M(CysOMe\text{-}H)]^+$, and $CdCl^+(CysOMe)$ complexes. Several higher energy isomers of these complexes, although not explicitly discussed here because of their high energies, were also calculated and are included in Table S1 (ESI†). Select low-lying conformations of $[Zn(Cys\text{-}H)]^+$ are shown in Fig. 1. Similar binding modes are found for $[Zn(CysOMe\text{-}H)]^+$, Cd^{2+} complexes with deprotonated Cys and CysOMe, and $CdCl^+(CysOMe)$. The nomenclature used to identify the different structural isomers is based on that described previously for other IRMPD studies of metal–amino acid complexes.[35–37] Briefly, conformations are identified by their metal binding site in brackets, followed by a description of the amino acid orientation by a series of dihedral angles. The angles are denoted as "*c*" (*cis*) for angles $<50^\circ$, "*g*" (*gauche*) for angles between 50° and 135° along with an indication of its sign (+ or −) when needed, and "*t*" (*trans*) for angles $>135^\circ$. For charge-solvated (CS) structures, these dihedral angles start with the carboxylic acid hydrogen atom (or methyl carbon atom for CysOMe) and proceed along the molecule to the terminal hydrogen of the amino acid side group; ∠HOCC, ∠OCCC, ∠CCCS, and ∠CCSH. The former or latter angles are missing if the carboxylic acid or sulfur has been dehydrogenated, respectively. The deprotonation site is designated by a negative ion symbol on the appropriate atom. In the case of salt-bridge (SB) structures, the proton originally on the carboxylic acid terminus is attached instead to the nitrogen. For these complexes, the first dihedral angle starts at this bridging proton and moves along the molecule as above. In the case of the $[M(Cys\text{-}H)]^+$ complexes, both the sulfur and carboxylic acid proton sites can participate in deprotonation and salt-bridge formation.

Theoretical results for $[M(Cys\text{-}H)]^+$. For both metals, the GS is a tridentate $[N,CO,S^-]tgg$ geometry, with deprotonation at the side-chain sulfur, for all levels of theory (Table 1). This is similar to the results of Mori *et al.* who find this $[N,CO,S^-]tgg$ structure as the ground state conformer for $[(H_2O)M(Cys\text{-}H)]^+$ where M = Zn^{2+} (gas phase and in solution) and Cd^{2+} (gas phase).[9] As seen in Fig. 1 for $[Zn(Cys\text{-}H)]^+$ $[N,CO,S^-]tgg$, the metal is bound to the amino nitrogen, carbonyl oxygen, and sulfur with bond distances of 2.139, 2.141, and 2.215 Å, respectively. For the $[Cd(Cys\text{-}H)]^+$ GS structure, the bond distances to the metal are elongated by 0.258 Å for N–M, 0.285 Å for CO–M, and 0.190 Å for S–M. The longer bond distances are largely accounted for by the 0.21 Å larger ionic radius of Cd^{2+} compared to Zn^{2+}.[38] The $[N,CO,S^-]cgg$ conformer is 26 kJ mol^{-1} higher in 298 K free energy at all levels of theory for both metals because the intramolecular OH•OC hydrogen bond is lost. DFT predicts the bidentate species, $[N,S^-]tgt$ and $[CO,S^-]cgg$, are lower in energy than the tridentate $[N,OH,S^-]tgg$ (where the

Table 1 B3LYP,[a] B3P86, and MP2(full) relative free energies (kJ mol^{-1}) at 298 K of low-lying conformers of $[M(Cys\text{-}H)]^+$ and $[M(CysOMe\text{-}H)]^+$ [b]

Complex	Structure	Zn	Cd
$[M(Cys\text{-}H)]^+$	$[N,CO,S^-]tgg$	0.0 (0.0), 0.0, 0.0	0.0 (0.0), 0.0, 0.0
	$[N,CO,S^-]cgg$	26.6 (26.2), 26.2, 25.4	25.3 (25.1), 24.8, 26.0
	$[CO,S^-]cgg$	31.4 (36.4), 35.1, 48.7	30.0 (36.3), 32.0, 46.3
	$[N,S^-]tgt$	37.1 (41.4), 44.0, 44.3	26.6 (32.0), 31.6, 36.5
	$[CO^-,S^-]cgg$[c]	40.0 (40.9), 44.5, 46.0	45.6 (47.0), 47.0, 50.7
	$[N,OH,S^-]tgg$	41.4 (39.6), 45.4, 38.4	34.6 (33.4), 38.9, 34.9
	$[CO,S^-]ctg$	53.6 (57.4), 58.0, 71.8	43.0 (47.4), 45.8, 59.4
	$[N,CO^-,S]gggg$	62.1 (59.1), 62.3, 59.6	81.6 (78.6), 81.9, 83.8
	$[N,S^-]cgt$	70.3 (73.6), 76.6, 78.0	59.2 (63.5), 63.4, 69.0
	$[N^-,CO,S]tggg$	103.6 (104.3), 104.6, 105.9	105.8 (106.7), 107.9, 113.9
	$[S^-]tgg$	155.3 (162.2), 175.8, 191.4	85.3 (94.2), 99.8, 106.9
$[M(CysOMe\text{-}H)]^+$	$[N,CO,S^-]tgg$	0.0 (0.0), 0.0, 0.0	0.0 (0.0), 0.0, 0.0
	$[N,CO,S^-]cgg$	35.9 (33.1), 34.8, 35.8	37.5 (34.6), 36.4, 37.9
	$[N,S^-]tgt$	41.2 (45.5), 47.6, 50.8	30.6 (35.7), 35.1, 40.9
	$[N,OMe,S^-]tgg$	44.8 (40.0), 47.4, 38.3	38.8 (34.6), 41.6, 35.3
	$[CO,S^-]tgg$	60.7 (66.4), 69.2, 79.3	55.4 (61.8), 62.0, 74.7
	$[CO,S^-]ctg$	79.7 (80.4), 86.2, 96.3	75.1 (76.7), 79.8, 93.3
	$[N,S^-]cgt$	87.4 (87.8), 92.6, 95.9	75.6 (76.8), 78.7, 84.6
	$[N^-,CO,S]tgggg$	103.2 (103.5), 104.2, 106.8	105.0 (104.9), 107.1, 113.3

[a] Values including empirical dispersion corrections are given in parentheses. [b] Calculations performed at B3LYP, B3P86, and MP2(full) levels of theory using a 6-311+G(2d,2p) basis set for Zn-containing complexes and def2TZVPP for Cd-containing complexes. Geometries and vibrational frequencies calculated at B3LYP/6-311+G(d,p) level for Zn-containing complexes and B3LYP/def2TZVP for Cd-containing complexes. Energies include ZPE corrections scaled by 0.989. [c] Salt-bridge between NH_3^+, CO_2^-, and S^- groups.

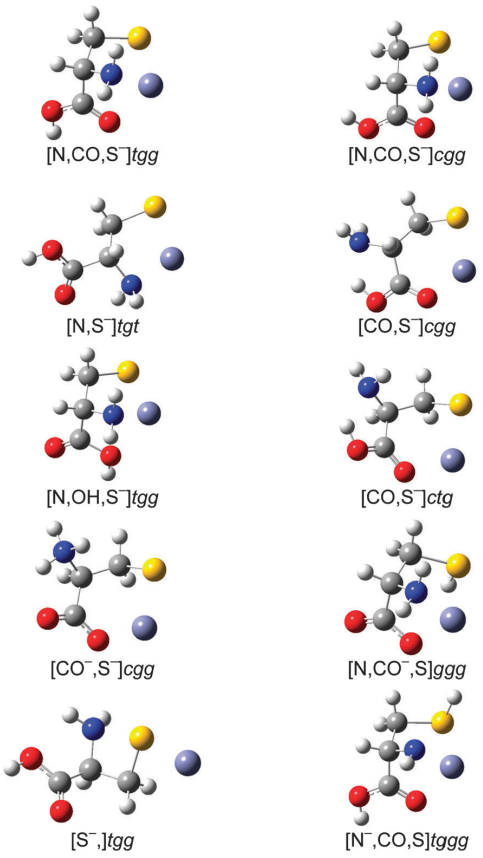

Fig. 1 Structures of select low-lying [Zn(Cys-H)]$^+$ complexes calculated at the B3LYP/6-311+G(d,p) level of theory. Grey = C, red = O, blue = N, yellow = S, white = H, light purple = Zn.

hydroxyl group is bound to the metal rather than the carbonyl), whereas MP2(full) inverts this order and places [N,OH,S$^-$]*tgg* as the lowest energy and [CO,S$^-$]*cgg* as the highest energy of these three conformers. All levels of theory predict that both metals have similar relative energetics for the [CO,S$^-$]*cgg* species (Cd being more stable by 1–3 kJ mol^{-1}). The [N,OH,S$^-$]*tgg* species have Cd complexes more stable by 3–7 kJ mol^{-1}, and the [N,S$^-$]*tgt* conformer (as well as its *cgt* variant) is more stable by about 10 kJ mol^{-1} for Cd than for Zn. These differences are probably related to the five-membered rings in the latter complexes (Fig. 1), which are stabilized for Cd^{2+} because the longer N–M and S–M bond distances relieve torsional strain in these rings.

Deprotonation is also possible at the carboxylic acid or amine groups. For [M(Cys-H)]$^+$, the lowest energy conformer with deprotonation at the carboxylic acid is the salt-bridge [CO$^-$,S$^-$]*cgg* lying 40–46 kJ mol^{-1} above the GS for Zn^{2+} and 46–51 kJ mol^{-1} for Cd^{2+}. This is lower than [N,OH,S$^-$]*tgg* and [CO,S$^-$]*ctg* for Zn^{2+} but not for Cd^{2+}. The tridentate [N,CO$^-$,S]*ggg* lies another 13–22 kJ mol^{-1} higher for Zn^{2+} and 26–35 kJ mol^{-1} higher for Cd^{2+}. Deprotonation at N is much less favorable with [N$^-$,CO,S]*tggg* calculated to be 104–114 kJ mol^{-1} higher in 298 K free energy for both metals.

In general, the two DFT levels of theory predict the same trends in relative energy with the exception of [N,CO$^-$,S]*ggg*, Table 1; whereas B3LYP-GD3BJ and MP2(full) levels greatly favor tridentate conformations compared to the bidentate species. There is reasonable agreement among all levels of theory (deviations less than 10 kJ mol^{-1}) for the relative free energies of most conformers, Table 1. The two [CO,S$^-$] conformers show larger deviations with MP2(full) results lying 16–18 kJ mol^{-1} above the B3LYP values (with B3P86 and B3LYP-GD3BJ being slightly higher). The biggest differences occur for the extended [S$^-$]*tgg* structure, with deviations of 22–36 kJ mol^{-1}. Here also, changing the metal drastically alters the relative energies with Zn^{2+} being much higher in relative energy. Here the stability appears to be related to the strength of the S–N bond (forming a four-membered ring, Fig. 1). For the Cd complex, this intermolecular S–N bond distance is 0.151 Å shorter than that calculated for the Zn^{2+} complex (2.295 Å), suggesting more covalent character in the former.

Theoretical results for [M(CysOMe-H)]$^+$. Theory predicts similar low energy structures for the substituted amino acid complexes, [M(CysOMe-H)]$^+$, as compared to [M(Cys-H)]$^+$. Relative 298 K free energies for [M(CysOMe-H)]$^+$ can be found in Table 1 (with 0 K values in Table S1 of the ESI†). As for Cys, the predicted lowest energy structure for the metal binding to CysOMe is the tridentate coordination, [N,CO,S$^-$]*tgg*, with deprotonation at the thiol. In these GSs, the exchange of the carboxylic acid hydrogen for a methyl shortens the O–M bond distances by 0.028 Å for the Zn^{2+} complex and 0.027 Å for Cd^{2+}. Clearly, methylation eliminates structures associated with deprotonation of the carboxylic acid and also pushes the [N,CO,S$^-$]*cgg* structure to higher energy (now 36 kJ mol^{-1} above the *tgg* ground structure). Presumably, this occurs because of unfavorable interactions between the methyl group and the amino acid backbone. Indeed, most structures for the [M(CysOMe-H)]$^+$ complexes have relative energies that are higher than those for the [M(Cys-H)]$^+$ analogues. This is most apparent in the [CO,S$^-$] conformers with the deprotonated CysOMe laying 23–34 kJ mol^{-1} higher in relative energy compared to their Cys analogs. Exceptions to this general trend are the [N,OMe,S$^-$]*tgg* and [N$^-$,CO,S]*tggg* structures, where the relative energies compared to their [M(Cys-H)]$^+$ counterparts are essentially equivalent for CysOMe (lower by $<$1 kJ mol^{-1}) at the MP2(full) level.

Theoretical results for CdCl$^+$(CysOMe). For the intact CysOMe binding with $CdCl^+$, the predicted GS is again tridentate [N,CO,S]*tggg*$_+$, which is the direct analogue of the GS for deprotonated Cys and CysOMe (Tables 1 and 2). The [N,CO,S]*tggg*$_-$ conformer is only $\sim$2 kJ mol^{-1} higher in 298 K free energy at all levels of theory and differs in structure from the GS only in the orientation of the SH hydrogen. These structures are similar to the GSs found in previous work for H^+(Cys),[39] M^+(Cys) where M = Li and Na,[20] as well as predictions by Russo *et al.* of M^{2+}(Cys) where M = Cu, Zn, Cd and Hg.[8] Previous theoretical work in the Armentrout group has found that the CS structures

Table 2 Relative free energies (kJ mol^{-1}) at 298 K of low-lying CdCl$^+$(CysOMe) conformers[a]

Structure	B3LYP[b]	B3P86	MP2(full)
[N,CO,S]*tggg*$_+$	0.0 (0.0)	0.0	0.0
[N,CO,S]*tggg*$_-$	2.0 (2.6)	2.1	2.6
[S$^-$]*tcg*[c]	20.8 (22.3)	21.4	24.8
[N,CO]*tgtg*$_-$	22.6 (31.8)	27.4	33.6
[N,CO]*tggg*	23.0 (31.5)	27.6	33.0
[N,CO]*tcgg*	25.7 (34.7)	30.4	36.3
[N,S]*tgtg*	27.8 (34.6)	30.3	38.0
[N,CO]*tgtg*$_+$	28.2 (37.6)	33.1	39.7
[CO,S$^-$]*ttg*[c]	28.5 (32.6)	29.2	33.4
[N,OMe,S]*tggg*$_+$	29.7 (34.3)	30.7	23.5
[N,OMe,S]*tggg*$_-$	34.1 (29.6)	35.4	28.6
[N,CO,S]*cggg*	40.6 (37.9)	39.7	41.0
[CO,S]*ttgt*	58.3 (67.9)	64.2	80.0
[CO,S$^-$]*cgg*[c]	69.7 (70.3)	68.2	75.7
[CO,S]*ctgt*	87.6 (93.9)	92.7	109.3

[a] Calculations performed at the stated level of theory using a 6-311+G(2d,2p) basis set for Zn-containing complexes and def2TZVPP for Cd-containing complexes. Geometries and vibrational frequencies calculated at B3LYP/6-311+G(d,p) level for Zn-containing complexes and B3LYP/def2TZVP for Cd-containing complexes. Energies include ZPE corrections scaled by 0.989. [b] Values including empirical dispersion corrections are given in parentheses. [c] Salt-bridge between NH_3^+, CO_2^-, and S^- groups.

for protonated and metal cationized Cys are highly favored over salt-bridge structures.[20,36,39] It is worth noting that the lowest energy salt-bridge structure for CdCl$^+$(CysOMe) is [S$^-$]tcg. This conformer is considerably lower in relative energy at 21–25 kJ mol^{-1} than the similar structure for the [Cd(Cys-H)]$^+$ system at 85–107 kJ mol^{-1}. Similar to the [Cd(CysOMe-H)]$^+$ complex, the tridentate [N,CO,S]*cggg* structure is higher in relative energy by ~40 kJ mol^{-1}.

IRMPD action spectroscopy

Fig. 2 shows the photodissociation spectra of [Zn(Cys-H)]$^+$ and [Cd(Cys-H)]$^+$ were examined from 550 to 1800 cm^{-1}; whereas [Zn(CysOMe-H)]$^+$, [Cd(CysOMe-H)]$^+$, and CdCl$^+$(CysOMe) were examined from 950 to 1800 cm^{-1}. The lower energy wavelength range was not examined for the latter species because theory suggested there would be little diagnostic information in this region. Dominant dissociation pathways are as follows. Photodissociation of [Zn(Cys-H)]$^+$ resulted in the loss of (H_2O + CO). Likewise [Zn(CysOMe-H)]$^+$ dissociates by loss of (CH_3OH + CO). [Cd(Cys-H)]$^+$ and [Cd(CysOMe-H)]$^+$ also dissociate similarly to each other by loss of neutral Cd resulting in formation of the radical cations (Cys-H)$^+$ and (CysOMe-H)$^+$, respectively. For CdCl$^+$(CysOMe), the photodissociation pathway corresponded to the loss of NH_3. The IRMPD action spectra shown correspond to the fractional yield of the product ions as a function of free electron laser wavenumber.

Comparison of the IRMPD spectra in Fig. 2 shows the similarities between the spectra of Zn and Cd containing species for both amino acid analogues. The experimental bands are identified on the basis of previous work[36,40] as well as comparisons to theoretical spectra. The vertical lines drawn through the spectra at 630, 1020, 1160, 1580, and 1660 cm^{-1} mark the major bands in the [Zn(Cys-H)]$^+$ spectrum. Additional lines at

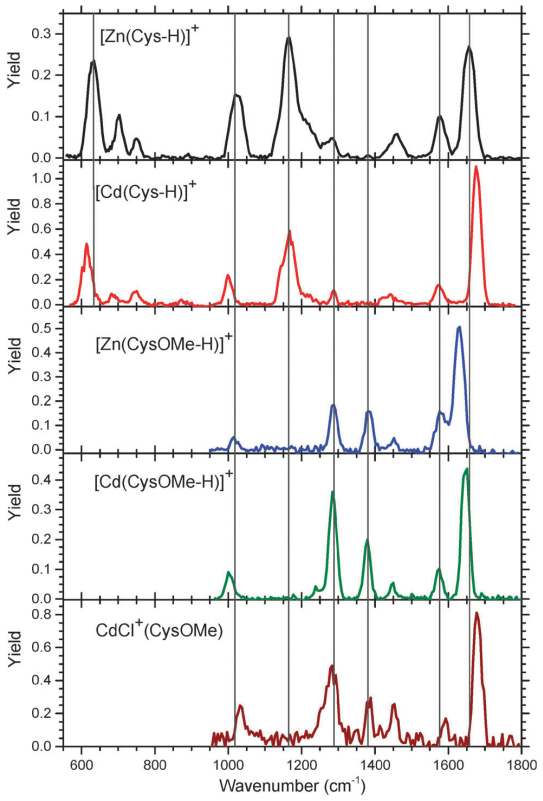

Fig. 2 IRMPD spectra of [Zn(Cys-H)]$^+$, [Cd(Cys-H)]$^+$, [Zn(CysOMe-H)]$^+$, [Cd(CysOMe-H)]$^+$ and CdCl$^+$(CysOMe) complexes. Solid lines at 630, 1020, 1160, 1280, 1380, 1580 and 1660 cm^{-1} are drawn to approximate COH wagging, NH_2 wagging, COH bending, HNCH bend, CH_3 umbrella, NH_2 bending and C=O stretch of [Zn(Cys-H)]$^+$, respectively.

1280 and 1380 cm^{-1} mark bands found in the methyl ester spectra. With [Zn(Cys-H)]$^+$ as the standard, the major band at 1660 cm^{-1}, the C=O stretch, shifts to the blue for [Cd(Cys-H)]$^+$ and CdCl$^+$(CysOMe), but shifts to the red for [M(CysOMe-H)]$^+$. In all cases, these C=O stretches occur in a lower frequency range than previously observed for alkali metal cationized Cys, 1718 cm^{-1} for Li$^+$(Cys) to 1745 cm^{-1} for Cs$^+$(Cys).[36] Clearly, interaction with the doubly charged metal (or nearly doubly charged for CdCl$^+$) weakens the CO bond more than the singly charged metal cations. The band at 1580 cm^{-1}, the NH_2 bend, shifts little in most spectra, but shifts to the blue for CdCl$^+$(CysOMe). This spectrum also shows a blue shift for the 1020 cm^{-1} band, associated with NH_2 wagging.

The 610 and 1160 cm^{-1} bands are attributed to COH wagging and COH bending, respectively. Thus, these bands are not expected to be observed in the cysteine methyl ester complexes as the methyl caps the carboxylic acid terminus of the amino acid, as found for the latter band. Conversely, the presence of these bands in the [M(Cys-H)]$^+$ spectra shows that deprotonation of Cys has not occurred at the carboxylic acid.

The other pronounced difference between the amino acid derivatives is the appearance of the 1380 cm^{-1} band in the three CysOMe spectra, which is primarily associated with the methyl umbrella motion. The band at 1280 cm^{-1} corresponds to an HNCH bend, but also has contributions from methyl umbrella motions. The latter explains why the intensity of this band is enhanced in the spectra involving CysOMe.

Comparison to theory: [M(Cys-H)]$^+$. Fig. 3 shows the experimental [Zn(Cys-H)]$^+$ IRMPD action spectrum compared to calculated linear IR absorption spectra for selected low energy structures, with corresponding relative 298 K free energies at B3LYP, B3P86, and MP2(full) levels. Although the relative intensities of linear absorption spectra offer good qualitative comparison to the experimental intensities, IRMPD intensities are not always reproduced by the single photon linear absorption spectra. Nonetheless, the major and minor bands predicted by the [N,CO,S$^-$]*tgg* GS conformer correspond well with the observed spectrum, in terms of both band positions and relative intensities. A notable exception is the NH_2 bend observed at 1580 cm^{-1}, but predicted to occur at 1606 cm^{-1}. This vibrational mode is known to have strong anharmonic character in amino acids, an effect that is often manifested as a shift in IRMPD spectra.[41–43] None of the other conformers shown in Fig. 3 have predicted spectra that match the experimental spectrum.

The band observed at 1656 cm^{-1} corresponds to the carbonyl stretch, which explains its large intensity. The interaction with the metal cation results in a large shift to the red of the C=O stretch band with respect to free Cys, calculated at 1799 cm^{-1}.[20] The C=O stretch predicted by the ground [N,CO,S$^-$]*tgg* conformer at 1658 cm^{-1} agrees well with the experimental band. The location of the C=O stretch in the calculated spectra of the higher energy deprotonated sulfur structures are within 60 cm^{-1} of the observed band, with the exception of [N,S$^-$] (+113 cm^{-1}). Nevertheless, the [N,CO,S$^-$]*tgg* ground structure best replicates the C=O stretch frequency. The alternative carboxylic acid hydrogen orientation conformer, [N,CO,S$^-$]*cgg*, lacks hydrogen bonding within the carboxylic acid, which affects spectral characteristics within the lower frequency range such that the spectrum for this conformer disagrees with experiment. The salt-bridge [CO$^-$,S$^-$]*cgg* conformer with a C=O stretch at 1716 cm^{-1} does not match experiment, which also does not exhibit the intense band at 1419 cm^{-1} associated with the NH_3 umbrella motion characteristic of this SB conformer. Although the two bidentate species, [CO,S$^-$]*cgg* and [N,S$^-$]*tgt*, are also

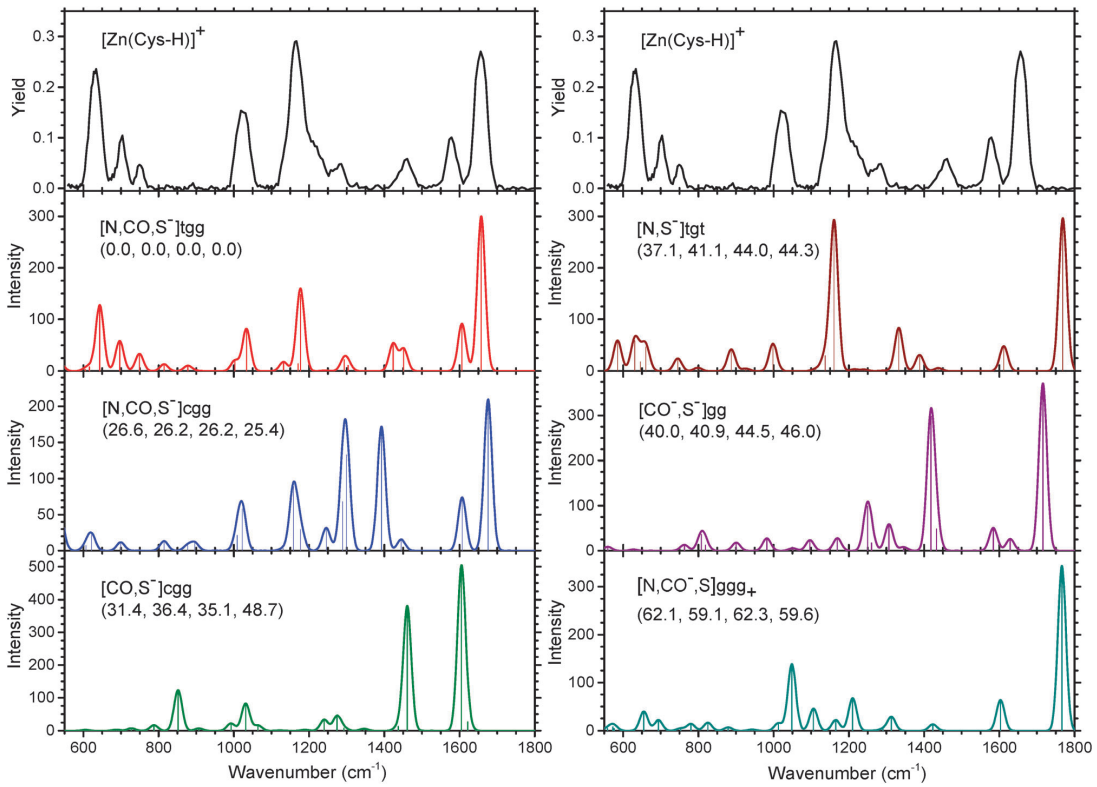

Fig. 3 Comparison of the experimental IRMPD spectrum of [Zn(Cys-H)]$^+$ with IR spectra of select low-energy conformers predicted at B3LYP/6-311+G(d,p) level. Relative 298 K free energies from Table 1 are given in parentheses calculated at the B3LYP, B3LYP-GD3BJ, B3P86 and MP2(full) levels with 6-311+G(2d,2p) basis set.

deprotonated at the sulfur, their calculated C═O stretch frequencies do not replicate this band observed in the experimental IR action spectrum.

The bands observed at 1167 and 1016 cm^{-1} are also diagnostic bands for the [N,CO,S^-] structures. These bands are primarily associated with bending of the COH group and the NH_2 wagging motion, respectively. The predicted IR spectra for these conformers adequately reproduce the position and relative intensity of these bands, whereas no other conformation does so at both of these frequencies. In the case of [N,CO,S^-]*cgg*, this calculated spectrum disagrees with the observed action spectrum by the presence of strong bands calculated at 1296 and 1392 cm^{-1}. Less intense peaks observed at 1461, 750, 703, and 633 cm^{-1} are well represented by the spectrum calculated for the ground conformer. The band at 1461 cm^{-1} corresponds to HCH bends in the amino acid side chain, whereas those observed at 750, 703, and 633 cm^{-1} correspond to wagging motions of the carboxylic acid hydrogen atom. The [N,S^-] conformer also has bands predicted near the observed 1167 and 1016 cm^{-1} bands, but their relative intensities do not agree well nor do the calculated spectra predict the other diagnostic bands observed in the experimental IR action spectrum. Overall, the experimental IRMPD action spectrum can be adequately explained by the calculated spectrum of the ground [N,CO,S^-]*tgg* conformer. The only inadequacies in this comparison are the inconsistent relative intensities of the double peak predicted at 1450 cm^{-1} and the absence of the side band observed near 1210 cm^{-1}. The differences in intensities may result from comparing a multiple photon experimental spectrum with the predicted one-photon spectrum. The missing side band could be an overtone of the band at 620 cm^{-1}.

IRMPD action spectra for $[Cd(Cys\text{-}H)]^+$ and $[Zn(Cys\text{-}H)]^+$ are very similar (Fig. 2), exhibiting all of the same characteristic spectral features. The predicted spectrum for the ground conformer of $[Cd(Cys\text{-}H)]^+$, [N,CO,S^-]*tgg*, shows good agreement with the observed IRMPD spectrum, as seen in Fig. 4. The intense band observed at 1675 cm^{-1} agrees very well with the predicted C═O for the lowest energy conformer at 1679 cm^{-1}. In addition, the major bands observed at 1166, 1001, and 613 cm^{-1} are also reproduced in the predicted spectrum for [N,CO,S^-]*tgg*. Another diagnostic band that is reproduced well by the ground conformer is the side band observed at 1143 cm^{-1}, a feature that is not predicted for any other conformer. Consistent with the $[Zn(Cys\text{-}H)]^+$ spectrum, there is again a deviation in the position of the observed 1575 cm^{-1} NH_2 bending band compared to 1605 cm^{-1} calculated for the $[Cd(Cys\text{-}H)]^+$ GS.

Compared with $[Zn(Cys\text{-}H)]^+$, the C═O stretch is calculated to shift to the blue by 20 cm^{-1} and is observed to shift by 27 cm^{-1} upon substitution of Cd for Zn. Likewise, theory and experiment agree that peaks associated with NH_2 and carboxylic acid wagging motions should shift to the blue by 30 and 20 cm^{-1}, respectively, upon Cd substitution.

Comparison to theory: $[M(CysOMe\text{-}H)]^+$. There is good agreement comparing the experimental spectrum of $[Zn(CysOMe\text{-}H)]^+$ to the predicted ground structure, [N,CO,S^-]*tgg* (Fig. 5a). Relative intensities and peak positions discussed above are also reproduced well, with the only exception being the NH_2 bending motion observed at 1580 cm^{-1} because of its anharmonic character discussed above. This GS is similar to the GS for the $[M(Cys\text{-}H)]^+$ species. The $[M(CysOMe\text{-}H)]^+$ spectra are similar to that of the $[M(Cys\text{-}H)]^+$ complexes as seen in Fig. 2, with the addition of the diagnostic bands characteristic of the methyl addition. Specifically, these are the band associated with the methyl umbrella motion at 1380 cm^{-1} and the enhancement of the HNCH bend band at 1280 cm^{-1} because this also has contributions from methyl umbrella motions. The predicted spectra for the various tridentate [N,CO,S^-] complexes are nearly indistinguishable. Only the relative energetics and slight red shift of the C═O stretch band in the *cgg* structure ensure the better agreement for the GS *tgg* spectrum. The bidentate complex, [N,S^-]*tgt*, does not reproduce the experimental spectrum well with a significant C═O blue shift and bands not characteristic of the observed experimental spectrum.

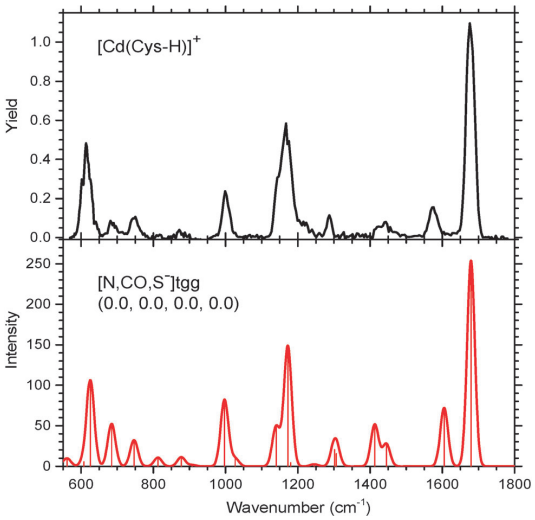

Fig. 4 Comparison of the experimental IRMPD spectrum of $[Cd(Cys\text{-}H)]^+$ with IR spectra of ground structure conformer predicted at B3LYP/def2TZVP level. Relative 298 K free energies from Table 1 are given in parentheses calculated at the B3LYP, B3LYP-GD3BJ, B3P86 and MP2(full) levels with def2TZVPP basis set.

The $[Cd(CysOMe\text{-}H)]^+$ IRMPD action spectrum is similar to that of its Zn equivalent in both peak shape and position (Fig. 5b). The prominent exceptions are the enlarged gap between the C═O stretch at 1650 cm^{-1} and the NH_2 bend at 1575 cm^{-1}, and the relative intensities of the 1280 and 1380 cm^{-1} peaks. The gap and relative intensities observed experimentally are well reproduced by the predicted GS spectra of the [N,CO,S^-]*tgg* complexes. An interesting difference between the Cd and Zn containing complexes is that the 1240 cm^{-1} shoulder predicted in the GS for both species is only observed in the $[Cd(CysOMe\text{-}H)]^+$ IRMPD action spectrum. As for the Zn analogue, the [N,CO,S^-]*tgg* calculated spectrum reproduces all

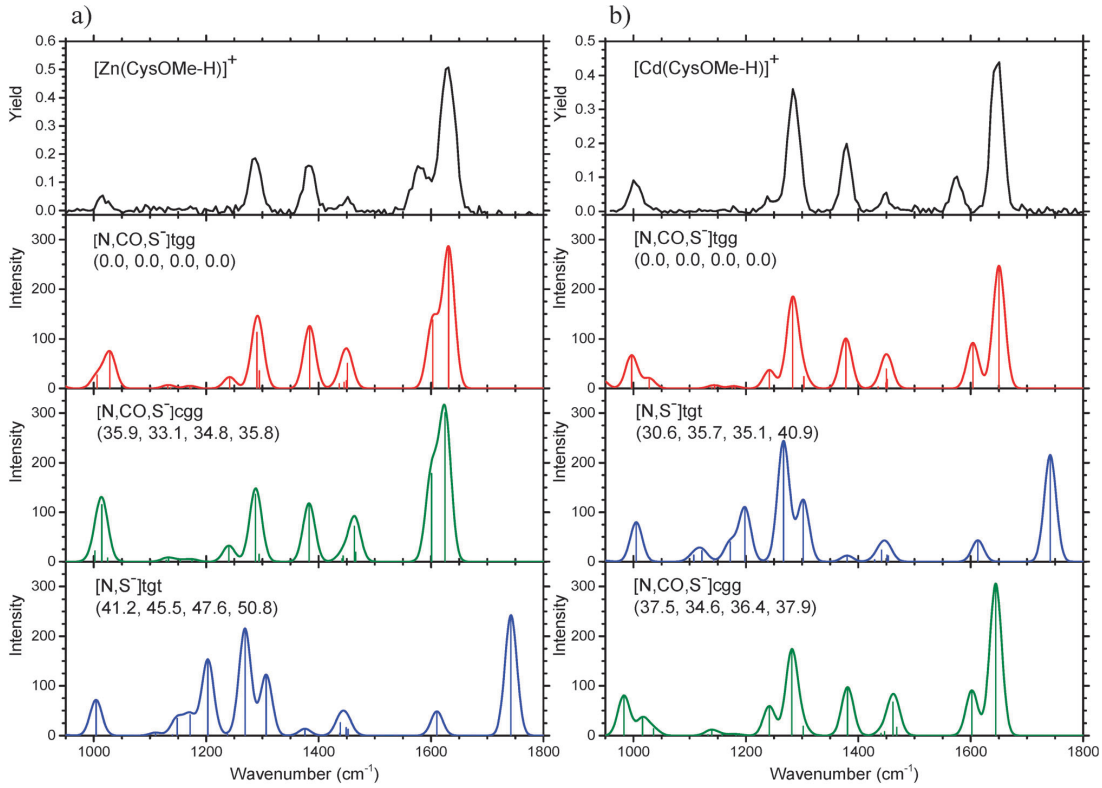

Fig. 5 Comparison of the experimental IRMPD spectrum of (a) $[Zn(CysOMe-H)]^+$ and (b) $[Cd(CysOMe-H)]^+$ with calculated IR spectra of select low-energy conformers predicted at B3LYP/6-311+G(d,p) and B3LYP/def2TZVP levels. Relative 298 K free energies from Table 1 are given in parentheses calculated at the B3LYP, B3LYP-GD3BJ, B3P86, and MP2(full) levels with 6-311+G(2d,2p) and def2TZVPP basis sets.

of the bands observed in the experimental spectrum for $[Cd(CysOMe-H)]^+$ better than those for any higher energy complex.

Comparison to theory: $CdCl^+$(CysOMe). Fig. 6 shows the experimental IRMPD action spectrum along with calculated linear IR absorption spectra for selected low-energy structures of $CdCl^+$(CysOMe). In analogy with the $[M(Cys-H)]^+$ and $[M(CysOMe-H)]^+$ complexes, the predicted ground tridentate [N,CO,S]*tggg*$_+$ structure for the intact CysOMe binding to the metal chloride cation is in good agreement with experiment in both peak position and relative intensities. The C═O stretch observed at 1677 cm^{-1} is reproduced well by the predicted band at 1680 cm^{-1}. The only noticeable variation is the predicted NH_2 bend, which is higher in wavenumber by 25 cm^{-1} compared to the observed spectrum, again because of the anharmonicity of this motion. The alternative [N,CO,S$^-$]*tggg*$_-$ structure has a predicted spectrum nearly identical to that of the *tggg*$_+$ GS, which is reasonable as the only difference between the two is the direction that the SH hydrogen points. Because this species is very low in energy, it is probably populated in our ion source. At 298 K, its equilibrium population is calculated as 26–31%.

Comparison of the observed spectrum with that predicted for the lowest energy salt-bridge complex, [S$^-$]tcg, confirms there are no SB spectral characteristics in the $CdCl^+$(CysOMe) system. Again, the most diagnostic band is the C═O stretch, which is predicted to lie much higher in wavenumber than observed. Likewise the strong band predicted at 1430 cm^{-1} is not found experimentally. Although the bidentate [N,CO]*tg*$_-$*tg*$_-$ conformer has peaks in the 1370 and 1450 cm^{-1} range comparable to the observed spectrum, the C═O band is shifted to lower wavenumber and peaks observed in the lower frequency region do not agree with experiment. In addition, the calculated spectrum for the other bidentate binding mode, [N,S]*tgtg* (not shown), does not reproduce experiment well with a significantly blue shifted C═O stretch and a predicted band at 1213 cm^{-1} that is not observed.

The $CdCl^+$(CysOMe) spectrum is similar to that of $[Cd(CysOMe-H)]^+$ (Fig. 2) with respect to peak intensities and even relative intensities of the diagnostic bands. Notable differences are the blue shifts in bands at 999 to 1032 cm^{-1}, 1575 to 1592 cm^{-1}, and 1650 to 1677 cm^{-1}. These shifts are most likely a result of the presence of the spectator Cl^- ion bound to Cd^{2+}, lengthening the coordinating distance of the metal from the CysOMe binding sites. This difference for the metal to OC is calculated to be 0.02 Å. Changes in the S–M bond distances are

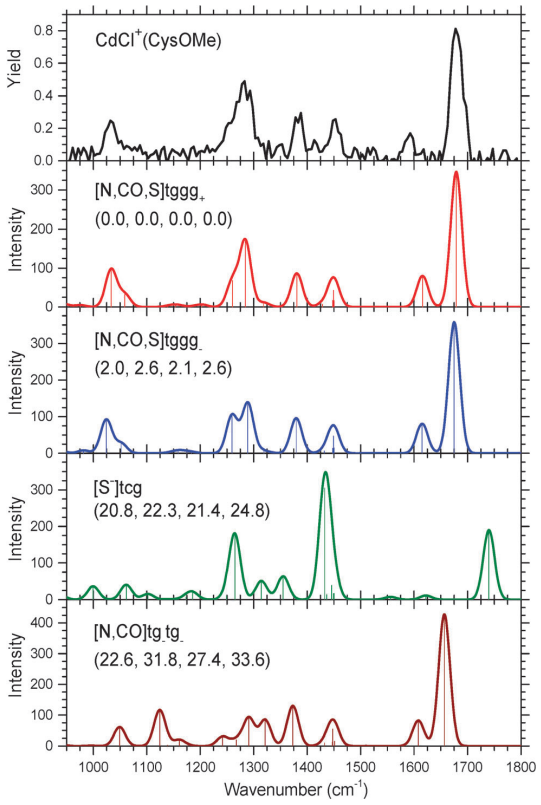

Fig. 6 Comparison of the experimental IRMPD action spectrum of $CdCl^+$(CysOMe) with IR spectra of selected low energy conformers predicted at B3LYP/def2TZVP level. Relative 298 K free energies from Table 2 are given in parentheses calculated at the B3LYP, B3LYP-GD3BJ, B3P86 and MP2(full) levels with def2TZVPP basis set.

much more pronounced with that for the $CdCl^+$ complex longer by 0.36 Å, clearly because the sulfur group is no longer negatively charged. Interestingly, the peak positions of the C═O stretches for $CdCl^+$(CysOMe) and $[Cd(Cys\text{-}H)]^+$ are observed to be very close, consistent with nearly identical Cd to OC binding distances. Compared with the Zn complexes, the C═O stretches for Cd containing species are systematically higher in wavenumber as a result of the larger ionic radius, which elongates the O–M bond lengths, weakens the bond strengths, and decreases the perturbations on the C═O stretch.

Conclusions

IRMPD action spectra in tandem with quantum chemical calculations were used to investigate the role of metal dependence in the structural binding to cysteine and cysteine methyl ester. Action spectra were collected for complexes of Zn^{2+} and Cd^{2+} with deprotonated cysteine and deprotonated cysteine methyl ester, in addition to $CdCl^+$ with intact cysteine methyl ester. Comparison of these experimental spectra with calculated IR spectra at the B3LYP/6-311+G(d,p) and B3LYP/def2TZVP levels of theory allow the conformations likely to be present in the experiment to be identified. The deprotonated species are unambiguously identified as charge solvated, tridentate complexes that bind the metal dications to the amine and carbonyl groups of the amino acid backbone and the deprotonated thiol of the side chain. This assignment is in agreement with the predicted ground structures, $[N,CO,S^-]tgg$, of these complexes. The assignment of the deprotonation at the thiol site is evident from the positions of the intense C═O stretch bands and the presence of the free OH motion of the intense COH bend band observed in the cysteine systems. The excellent agreement between the Cys and CysOMe observed spectra corroborates thiol deprotonation for the cysteine systems. The comparison of experiment and theory finds $CdCl^+$(CysOMe) to bind in an analogous fashion, $[N,CO,S]tggg_+$. Thus, the presence of the Cl^- spectator ion has little effect on the observed spectra or predicted low energy conformer.

The action spectra are very similar for both Zn^{2+} and Cd^{2+} complexed with the amino acids. Minor differences in the positions and relative intensities were observed, most notably at the position of the C═O stretch and NH_2 wagging bands. These differences are also predicted and observed in the IR spectra for the ground complexes and all spectral characteristics were well reproduced by the calculated ground structures. Examination of the GS structures indicates that zinc binds more tightly than cadmium to Cys and CysOMe. This is evident from the differences in the metal to binding site bond distances, which are >0.2 Å larger for Cd^{2+}. This difference is consistent with the difference in ionic radii, 0.78 Å for Zn^{2+} and 0.99 Å for Cd^{2+}.[38] Upon investigating the role of metal binding to cysteine, significant structural changes in motifs for binding in the metal–cysteine complex do not occur when zinc ion is replaced with the toxic cadmium ion. This similarity presumably allows for facile substitution of Zn by Cd. At this fundamental level, the change in binding site spacing of the M^{2+} to a single Cys residue may lead to the toxic effects of zinc finger deactivation by cadmium. The weaker binding upon zinc replacement by cadmium may lead to misfolding of these metal dependent proteins. In addition, it needs to be considered that zinc finger proteins have a Zn^{2+} metal bound to four amino acid residue ligands, and the additional ligands may be necessary to understand how metal replacement influences structural changes. Nevertheless, the present study provides important insight to begin understanding the involvement of metal dependence within metalloproteins and acts as a valuable first step for future work that tries to mimic physiologically relevant binding sites with additional amino acids.

Acknowledgements

Financial support for this work was provided by the National Science Foundation, Grants CHE-1359769 and PIRE-0730072. The skillful assistance of the FELIX staff is appreciatively acknowledged. Also, we gratefully thank the Center for High

Performance Computing at the University of Utah for their generous allocation of computing time.

Notes and references

1 J. M. Berg and Y. Shi, *Science*, 1996, **271**, 1081–1085.
2 A. D. Frankel, J. M. Berg and C. O. Pabo, *Proc. Natl. Acad. Sci. U. S. A.*, 1987, **84**, 4841–4845.
3 N. P. Pavletich and C. O. Pabo, *Science*, 1991, **252**, 809–817.
4 F. W. Sunderman, Jr. and A. M. Barber, *Ann. Clin. Lab. Sci.*, 1988, **18**, 267–288.
5 P. F. Predki and B. Sarkar, *J. Biol. Chem.*, 1992, **267**, 5842–5846.
6 M. Asmuss, L. H. F. Mullenders, A. Eker and A. Hartwig, *Carcinogenesis*, 2000, **21**, 2097–2104.
7 M. Huang, D. Krepkiy, W. W. Hu and D. H. Petering, *J. Inorg. Biochem.*, 2004, **98**, 775–785.
8 M. Belcastro, T. Marino, N. Russo and M. Toscano, *J. Mass Spectrom.*, 2005, **40**, 300–306.
9 S. Mori, T. Endoh, Y. Yaguchi, Y. Shimizu, T. Kishi and T. K. Yanai, *Theor. Chem. Acc.*, 2011, **130**, 279–297.
10 T. E. Cooper, J. T. O'Brien, E. R. Williams and P. B. Armentrout, *J. Phys. Chem. A*, 2010, **114**, 12646–12655.
11 T. E. Cooper and P. B. Armentrout, *Chem. Phys. Lett.*, 2010, **486**, 1–6.
12 L. Banu, V. Blagojevic and D. K. Bohme, *J. Am. Soc. Mass Spectrom.*, 2013, **24**, 1534–1542.
13 T. E. Hofstetter, C. Howder, G. Berden, J. Oomens and P. B. Armentrout, *J. Phys. Chem. B*, 2011, **115**, 12648–12661.
14 D. Oepts, A. F. G. van der Meer and P. W. van Amersfoort, *Infrared Phys. Technol.*, 1995, **36**, 297–308.
15 N. C. Polfer, J. Oomens, D. T. Moore, G. von Helden, G. Meijer and R. C. Dunbar, *J. Am. Chem. Soc.*, 2006, **128**, 517–525.
16 J. J. Valle, J. R. Eyler, J. Oomens, D. T. Moore, A. F. G. van der Meer, G. von Heldon, G. Meijer, C. L. Hendrickson, A. G. Marshall and G. T. Blakney, *Rev. Sci. Instrum.*, 2005, **76**, 023103.
17 N. C. Polfer and J. Oomens, *Phys. Chem. Chem. Phys.*, 2007, **9**, 3804–3817.
18 A. G. Marshall, T. C. L. Wang and T. L. Ricca, *J. Am. Chem. Soc.*, 1985, **107**, 7893–7897.
19 S. H. Guan and A. G. Marshall, *Int. J. Mass Spectrom. Ion Processes*, 1996, **158**, 5–37.
20 P. B. Armentrout, E. I. Armentrout, A. A. Clark, T. E. Cooper, E. M. S. Stennett and D. R. Carl, *J. Phys. Chem. B*, 2010, **114**, 3927–3937.
21 M. J. Frisch, G. W. Trucks, H. B. Schlegel, G. E. Scuseria, M. A. Robb, J. R. Cheeseman, G. Scalmani, V. Barone, B. Mennucci, G. A. Petersson, H. Nakatsuji, M. Caricato, X. Li, H. P. Hratchian, A. F. Izmaylov, J. Bloino, G. Zheng, J. L. Sonnenberg, M. Hada, M. Ehara, K. Toyota, R. Fukuda, J. Hasegawa, M. Ishida, T. Nakajima, Y. Honda, O. Kitao, H. Nakai, T. Vreven, J. A. Montgomery, J. E. Peralta, F. Ogliaro, M. Bearpark, J. J. Heyd, E. Brothers, K. N. Kudin, V. N. Staroverov, R. Kobayashi, J. Normand, K. Raghavachari, A. Rendell, J. C. Burant, J. M. Millam, S. S. Iyengar, J. Tomasi, M. Cossi, N. Rega, J. M. Millam, M. Klene, J. E. Knox, J. B. Cross, V. Bakken, C. Adamo, J. Jaramillo, R. Gomperts, R. E. Stratmann, O. Yazyev, A. J. Austin, R. Cammi, C. Pomelli, J. W. Ochterski, R. L. Martin, K. Morokuma, V. G. Zakrzewski, G. A. Voth, P. Salvador, J. J. Dannenberg, S. Dapprich, A. D. Daniels, O. Farkas, J. B. Foresman, J. V. Ortiz, J. Cioslowski and D. J. Fox, *Gaussian 09, Revision A.02*, Gaussian Inc., Pittsburgh, PA, 2009.
22 A. D. Becke, *J. Chem. Phys.*, 1993, **98**, 5648–5652.
23 R. Ditchfield, W. J. Hehre and J. A. Pople, *J. Chem. Phys.*, 1971, **54**, 724–728.
24 S. Grimme, S. Ehrlich and L. Goerigk, *J. Comput. Chem.*, 2011, **32**, 1456–1465.
25 F. Weigend and R. Ahlrichs, *Phys. Chem. Chem. Phys.*, 2005, **7**, 3297–3305.
26 D. Andrae, U. Haeussermann, M. Dolg, H. Stoll and H. Preuss, *Theor. Chim. Acta*, 1990, **77**, 123–141.
27 K. L. Schuchardt, B. T. Didier, T. Elsethagen, L. Sun, V. Gurumoorthi, J. Chase, J. Li and T. L. Windus, *J. Chem. Inf. Model.*, 2007, **47**, 1045–1052.
28 J. P. Perdew, *Phys. Rev. B: Condens. Matter Mater. Phys.*, 1986, **33**, 8822–8824.
29 C. Möller and M. S. Plesset, *Phys. Rev.*, 1934, **46**, 618–622.
30 M. Citir, C. S. Hinton, J. Oomens, J. D. Steill and P. B. Armentrout, *J. Phys. Chem. A*, 2012, **116**, 1532–1541.
31 R. C. Dunbar, J. Steill, N. C. Polfer and J. Oomens, *J. Phys. Chem. B*, 2009, **113**, 10552–10554.
32 J. S. Prell, J. T. O'Brien, J. D. Steill, J. Oomens and E. R. Williams, *J. Am. Chem. Soc.*, 2009, **131**, 11442.
33 J. T. O'Brien, J. S. Prell, J. D. Steill, J. Oomens and E. R. Williams, *J. Phys. Chem. A*, 2008, **112**, 10823–10830.
34 R. C. Dunbar, N. C. Polfer and J. Oomens, *J. Am. Chem. Soc.*, 2007, **129**, 14562–14563.
35 A. L. Heaton, V. N. Bowman, J. Oomens, J. D. Steill and P. B. Armentrout, *J. Phys. Chem. A*, 2009, **113**, 5519–5530.
36 M. Citir, E. M. S. Stennett, J. Oomens, J. D. Steill, M. T. Rodgers and P. B. Armentrout, *Int. J. Mass Spectrom.*, 2010, **297**, 9–17.
37 D. R. Carl, T. E. Cooper, J. Oomens, J. D. Steill and P. B. Armentrout, *Phys. Chem. Chem. Phys.*, 2010, **12**, 3384–3398.
38 R. G. Wilson and G. R. Brewer, *Ion Beams with Applications to Ion Implantation*, Wiley, New York, 1973.
39 P. B. Armentrout and E. M. S. Stennett, *J. Am. Soc. Mass Spectrom.*, 2014, **25**, 512–523.
40 H. Susi, D. M. Byler and W. V. Gerasimowicz, *J. Mol. Struct.*, 1983, **102**, 63–79.
41 P. B. Armentrout, M. T. Rodgers, J. Oomens and J. D. Steill, *J. Phys. Chem. A*, 2008, **112**, 2248–2257.
42 M. T. Rodgers, P. B. Armentrout, J. Oomens and J. D. Steill, *J. Phys. Chem. A*, 2008, **112**, 2258–2267.
43 J. Oomens, D. T. Moore, G. Meijer and G. von Helden, *Phys. Chem. Chem. Phys.*, 2004, **6**, 710–718.

PCCP

CORRECTION

View Article Online
View Journal | View Issue

Cite this: *Phys. Chem. Chem. Phys.*, 2017, **19**, 18777

Correction: Structural characterization of gas-phase cysteine and cysteine methyl ester complexes with zinc and cadmium dications by infrared multiple photon dissociation spectroscopy

Rebecca A. Coates,[a] Christopher P. McNary,[a] Georgia C. Boles,[a] Giel Berden,[b] Jos Oomens[bc] and P. B. Armentrout *[a]

DOI: 10.1039/c7cp90144e

rsc.li/pccp

Correction for 'Structural characterization of gas-phase cysteine and cysteine methyl ester complexes with zinc and cadmium dications by infrared multiple photon dissociation spectroscopy' by Rebecca A. Coates *et al.*, *Phys. Chem. Chem. Phys.*, 2015, **17**, 25799–25808.

Although the overall conclusions of the original article remain unaffected (no experimental or theoretical IR spectra are changed, nor is any calculated thermochemistry at 0 K), the thermal corrections to the Gibbs free energy at 298 K were mistakenly overestimated. Corrected 298 K values for Tables 1 and 2 from the original manuscript are given below. Notably, only very subtle changes are found such that the relative order of all 298 K theoretically determined low-energy species remains the same for the $[Zn(Cys\text{-}H)]^+$, $[Cd(Cys\text{-}H)]^+$, $[Zn(CysOMe\text{-}H)]^+$, $[Cd(CysOMe\text{-}H)]^+$ and $CdCl^+(CysOMe)$ systems. Therefore, we have not corrected the relative energies used throughout the text.

Table 1 B3LYP,[a] B3P86, and MP2(full) relative free energies (kJ mol^{-1}) at 298 K of low-lying conformers of $[M(Cys\text{-}H)]^+$ and $[M(CysOMe\text{-}H)]^+$[b]

Complex	Structure	Zn	Cd
$[M(Cys\text{-}H)]^+$	$[N,CO,S^-]tgg$	0.0 (0.0), 0.0, 0.0	0.0 (0.0), 0.0, 0.0
	$[N,CO,S^-]cgg$	24.4 (24.0), 24.0, 23.2	25.1 (24.9), 24.7, 25.9
	$[CO,S^-]cgg$	27.8 (32.8), 31.5, 45.0	23.1 (28.5), 28.1, 33.0
	$[N,S^-]tgt$	30.8 (35.1), 37.7, 38.0	27.7 (34.0), 29.8, 44.0
	$[CO^-,S^-]cgg$[c]	36.0 (36.9), 40.5, 42.0	30.5 (29.4), 34.9, 30.9
	$[N,OH,S^-]tgg$	38.2 (36.3), 42.1, 35.2	41.7 (46.0), 44.4, 58.0
	$[CO,S^-]ctg$	50.2 (54.0), 54.6, 68.5	44.8 (46.2), 46.1, 49.9
	$[N,CO^-,S]ggg$	60.6 (57.7), 60.9, 58.2	55.9 (60.2), 60.0, 65.7
	$[N,S^-]cgt$	63.9 (67.2), 70.2, 71.5	77.0 (86.0), 91.5, 98.7
	$[N^-,CO,S]tggg$	100.5 (101.2), 101.5, 102.8	104.5 (108.8), 106.6, 112.6
	$[S^-]tgg$	143.8 (150.7), 164.3, 179.9	86.3 (95.2), 100.7, 107.9
$[M(CysOMe\text{-}H)]^+$	$[N,CO,S^-]tgg$	0.0 (0.0), 0.0, 0.0	0.0 (0.0), 0.0, 0.0
	$[N,CO,S^-]cgg$	36.2 (33.4), 35.2, 36.2	37.2 (34.6), 36.0, 37.6
	$[N,OMe,S^-]tgg$	43.7 (38.9), 46.3, 37.2	36.7 (32.8), 39.5, 33.2
	$[N,S^-]tgt$	36.9 (41.2), 43.4, 46.5	27.0 (32.4), 31.5, 37.2
	$[CO,S^-]tgg$	55.5 (61.2), 64.0, 74.1	50.7 (57.4), 57.3, 70.0
	$[CO,S^-]ctg$	76.9 (77.6), 83.5, 93.6	72.3 (74.2), 77.0, 90.6
	$[N,S^-]cgt$	84.3 (84.7), 89.5, 92.8	73.1 (74.5), 76.3, 82.1
	$[N^-,CO,S]tggg$	102.3 (102.6), 103.3, 105.9	104.4 (104.6), 106.4, 112.7

[a] Values including empirical dispersion corrections are given in parentheses. [b] Calculations performed at the B3LYP, B3P86, and MP2(full) levels of theory using a 6-311+G(2d,2p) basis set for Zn-containing complexes and def2TZVPP for Cd-containing complexes. Geometries and vibrational frequencies calculated at the B3LYP/6-311+G(d,p) level for Zn-containing complexes and B3LYP/def2TZVP for Cd-containing complexes. [c] Salt bridge between $NH3^+$, CO_2^-, and S^- groups.

[a] *Department of Chemistry, University of Utah, Salt Lake City, UT 84112, USA. E-mail: armentrout@chem.utah.edu*
[b] *Radboud University, Institute for Molecules and Materials, FELIX Laboratory, Toernooiveld 7, NL-6525ED Nijmegen, The Netherlands*
[c] *van't Hoff Institute for Molecular Sciences, University of Amsterdam, Amsterdam, The Netherlands*

Table 2 Relative free energies (kJ mol^{-1}) at 298 K of low-lying CdCl^{+}(CysOMe) conformers[a]

Structure	B3LYP[b]	B3P86	MP2(full)
[N,CO,S]*tggg*$_{+}$	0.0 (0.0)	0.0	0.0
[N,CO,S]*tggg*$_{-}$	1.1 (1.7)	1.2	1.7
[S^{-}]*tcg*[c]	17.6 (19.0)	18.2	21.5
[N,CO]*tgtg*$_{-}$	20.1 (29.3)	24.9	31.1
[N,CO]*tggg*	20.7 (29.2)	25.3	30.7
[N,CO]*tcgg*	21.2 (30.2)	25.9	31.8
[N,S]*tgtg*	23.4 (30.3)	26.0	33.7
[N,CO]*tgtg*$_{+}$	23.4 (32.8)	28.3	35.0
[CO,S^{-}]*ttg*[c]	26.0 (30.1)	26.7	31.0
[N,OMe,S]*tggg*$_{+}$	27.7 (22.2)	28.6	21.5
[N,OMe,S]*tggg*$_{-}$	32.2 (27.7)	33.4	26.7
[N,CO,S]*cggg*	38.8 (36.1)	37.9	39.2
[CO,S]*ttgt*	51.0 (58.8)	56.8	72.6
[CO,S^{-}]*cgg*[c]	66.2 (66.8)	64.7	72.2
[CO,S]*ctgt*	82.5 (88.9)	87.6	104.2

[a] Calculations performed at the stated level of theory using a def2TZVPP basis set. Geometries and vibrational frequencies calculated at the B3LYP/def2TZVP level of theory. [b] Values including empirical dispersion corrections are given in parentheses. [c] Salt bridge between $NH3^{+}$, CO_2^{-}, and S^{-} groups.

The Royal Society of Chemistry apologises for these errors and any consequent inconvenience to authors and readers.

CHAPTER 7

Zn^{2+} AND Cd^{2+} CATIONIZED SERINE COMPLEXES: INFRARED MULTIPLE PHOTON DISSOCIATION SPECTROSCOPY AND DENSITY FUNCTIONAL THEORY INVESTIGATIONS

Reprinted with permission from Rebecca A. Coates, Georgia C. Boles, Christopher P. McNary, Giel Berden, Jos Oomens and P. B. Armentrout, Zn^{2+} and Cd^{2+} Cationized Serine Complexes: Infrared Multiple Photon Dissociation Spectroscopy and Density Functional Theory Investigation, *Physical Chemistry Chemical Physics,* **2016** *18*, 22434-22445. DOI: 10.1039/c6cp03805k.

PCCP

PAPER

Cite this: *Phys. Chem. Chem. Phys.*, 2016, **18**, 22434

Zn^{2+} and Cd^{2+} cationized serine complexes: infrared multiple photon dissociation spectroscopy and density functional theory investigations†

Rebecca A. Coates,[a] Georgia C. Boles,[a] Christopher P. McNary,[a] Giel Berden,[b] Jos Oomens[bc] and P. B. Armentrout*[a]

Received 1st June 2016,
Accepted 18th July 2016

DOI: 10.1039/c6cp03805k

www.rsc.org/pccp

The gas-phase structures of zinc and cadmium dications bound to serine (Ser) are investigated by infrared multiple photon dissociation (IRMPD) action spectroscopy using the free electron laser FELIX, in combination with *ab initio* calculations. To identify the structures of the experimentally observed species, $[Zn(Ser\text{-}H)CH_3CN]^+$ and $CdCl^+(Ser)$, the measured action spectra are compared to linear absorption spectra calculated at the B3LYP/6-311+G(d,p) level for Zn^{2+} containing complexes and B3LYP/def2-TZVP levels for Cd^{2+} containing complexes. Good agreement between the observed IRMPD spectra and the predicted spectra allows identification of the isomers present. The intact amino acid interacting with cadmium chloride adopts a tridentate chelation involving the amino acid backbone amine and carbonyl groups as well as the hydroxyl group of the side-chain, [N,CO,OH]. The presence of two low-energy conformers is observed for the deprotonated serine–zinc complex, with the same tridentate coordination as for the cadmium complex but proton loss occurs at both the hydroxyl side-chain, $[N,CO,O^-]$, and the carboxylic acid of the amino acid backbone, $[N,CO^-,OH]$. These results are profitably compared with the analogous results previously obtained for comparable complexes with cysteine.

Introduction

Recently, the interactions of cysteine (Cys)[1] and histidine (His)[2] with transition metal dications, Zn^{2+} and Cd^{2+}, have been studied using infrared multiple photon dissociation (IRMPD) action spectroscopy. These studies were motivated by the biological relevance of zinc ions coordinating to these specific amino acids, as is observed in metalloproteins, and by the susceptibility of such zinc binding sites to toxic metal (Cd) replacement.[3,4] A large number of these metal-dependent proteins, such as zinc fingers, have been found to contain cysteine-rich sequence motifs capable of coordinating Zn^{2+} ions, utilizing the metal ion for structural integrity.[5] These zinc finger proteins are characterized by divalent Zn^{2+} centers directly coordinated to four amino acid residues, most commonly binding Cys and His.[3] Our work is designed to help interpret why Zn^{2+} preferentially binds to Cys and His, and how replacing these residues with other amino acids might influence the protein. We recently examined such interactions for glutamine (Gln),[6] and in the current work, we expand our metalated amino acid examinations to include serine (Ser), which differs from Cys only by the replacement of oxygen for the sulfur in the side-chain. Preferential binding of Zn^{2+} to Cys over Ser has been observed in metalloproteins, as is the case in the prokaryotic zinc finger domain of the Ros protein.[7] In that study, Baglivo *et al.* found that when Cys is replaced by Ser in the coordination sphere of the zinc finger domain, Cys_2His_2 to Ser_2His_2, the protein can still fold into a functional protein, but the zinc ion is lost. Moreover, they found that even single amino acid mutations of Cys to Ser in the first coordinating position of the zinc finger would transform the domain from zinc-binding to non-zinc-binding. Thus, the presence of Cys in this domain is essential for binding the zinc ion to the protein.[7] A pairwise examination at the fundamental level of metal binding with the amino acid Ser compared to Cys could provide valuable information about this strong metal-dependent binding of proteins.

In addition to the IRMPD action spectroscopy studies of the transition metal dications Zn^{2+} and Cd^{2+} with Cys,[1] His,[2] and Gln,[6] complexes of alkali-metal cations, Li^+, Na^+, K^+, Rb^+, and Cs^+ with single amino acid Ser,[8] Cys,[9] His,[10] and Asn[11] have been examined. The alkali-metal ions interacted to form $M^+(Ser)$ and $M^+(Cys)$ directly from the electrospray ionization (ESI) source; however, for group 12 metals, the ESI source does

[a] *Department of Chemistry, University of Utah, Salt Lake City, UT 84112, USA. E-mail: armentrout@chem.utah.edu*
[b] *Radboud University, Institute for Molecules and Materials, FELIX Laboratory, Toernooiveld 7c, NL-6525ED Nijmegen, The Netherlands*
[c] *van't Hoff Institute for Molecular Sciences, University of Amsterdam, Science Park 904, NL-1098XH Amsterdam, The Netherlands*

† Electronic supplementary information (ESI) available. See DOI: 10.1039/c6cp03805k

not generate M^{2+}(Cys) complexes directly. Thus interactions of the metal dications with deprotonated cysteine, $[M(Cys-H)]^+$, were examined.[1] Structures for all these systems were determined definitively using IRMPD spectroscopy and quantum chemical calculations, finding that the transition metal dications bind to deprotonated Cys in a charge-solvated tridentate structure where the metal binds to the amine and carbonyl groups of the amino acid backbone and the deprotonated thiol of the side chain, $[N,CO,S^-]$. Alkali metal cations were found to bind to intact Ser and Cys amino acids also in a tridentate motif with coordination to the amine and carbonyl groups of the backbone and to the hydroxyl or thiol side-chain, [N,CO,OH] and [N,CO,SH]. The present study approaches the transition metal dications binding to Ser similarly with a systematic structural investigation using IRMPD action spectroscopy and quantum chemical calculations. Conformations are identified by comparing the experimental IRMPD action spectra to IR spectra derived from quantum chemical calculations at the B3LYP/6-311+G(d,p) (Zn^{2+} complexes) and B3LYP/def2-TZVP (Cd^{2+} complexes) levels of theory of the low-lying structures of the complexes. The use of IRMPD action spectroscopy in tandem with theoretical investigation allows examination of how the conformations of experimentally generated metal ion–amino acid complexes change as a function of the amino acid side-chain. Such results provide insight regarding the preferential binding of zinc to specific amino acids in zinc finger proteins and the propensity for replacement by cadmium.

Experimental and theoretical methods

Mass spectrometry and IRMPD spectroscopy

Experiments were performed at the FELIX Laboratory, Radboud University, The Netherlands, using the Free Electron Laser for Infrared eXperiments (FELIX)[12] beam line. Experiments have been described previously,[1,2,8] but a brief description follows. A 4.7 T Fourier transform ion cyclotron resonance (FT-ICR) mass spectrometer[13–15] was used to record the IRMPD spectra. The metal–serine complex ions were generated using a Micromass Z-spray electrospray ionization source. Solutions of 1.0 mM Ser with 1.0 mM zinc nitrate or cadmium chloride in a 50 : 50 MeOH : H_2O solution were used with a flow rate of 3–10 μL min^{-1}. Ions generated by the ESI source were accumulated in a hexapole trap for 5–7 s before being pulse extracted through a quadrupole bender and injected into the ICR cell *via* a radio-frequency (rf) octopole ion guide. Ion capturing was affected by the electrostatic switching of the dc bias of the octopole to avoid collisional heating of the ions.[13] Once trapped in the ICR cell, the ions were allowed to cool radiatively to room temperature for up to 0.4 s.[16] The ion of interest was mass isolated using a stored waveform inverse Fourier transform (SWIFT) excitation pulse[17,18] and irradiated with FELIX for 3–5 s at a 5 or 10 Hz macropulse repetition rate (energy up to 45 mJ per pulse and the bandwidth is 0.5% of the central frequency).

At each wavelength, the parent and fragment ion intensities were used to determine the fractional yield as $\sum I_F/(I_P + \sum I_F)$, where I_P and I_F are the integrated intensities of the parent and fragment ion mass peaks (including all isotopes as detailed below), respectively. The IRMPD spectra were generated by plotting the yield as a function of the wavenumber of IR radiation after correcting for laser power. Infrared spectra obtained using IRMPD methods are comparable to those recorded using linear absorption techniques, in part because the spectra result from incoherent, rather than coherent, multiple photon excitation. Previous modeling studies have demonstrated the near-linear absorption character of IRMPD studies.[19,20] For some bands (here the high frequency range for $CdCl^+$(Ser)), the laser energy drops quickly, which results in a yield higher than one after correcting for the laser power. The application of a linear laser power correction is well described in the literature,[21] and is appropriate because the power dependence is basically linear until saturation begins, again because of the incoherent rather than the coherent nature of the multiple photon excitation process. A yield greater than unity is an indication that the band would have been saturated if the laser power was higher.

The ESI source directly generated $[Zn(Ser-H)ACN]^+$ and $CdCl^+$(Ser) complexes, where ACN = acetonitrile. (Originally, the ACN was present adventitiously from previous experiments, although in some experiments, additional ACN was added to the electrospray solution to enhance intensities of this complex.) Unlike the previous study of Zn and Cd interacting with cysteine, species of the metals interacting solely with deprotonated Ser, $[M(Ser-H)]^+$, could not be generated. Even irradiating the $[Zn(Ser-H)ACN]^+$ species with a 40 W continuous-wave CO_2 laser did not result in the loss of ACN, although this had been a successful strategy for obtaining the $[M(Cys-H)]^+$ and $[M(CysOMe-H)]^+$ species.[1]

Computational details

Possible geometries for Zn^{2+}(Ser) complexes were taken from the previously examined geometries of Li^+(Ser) complexes,[22] which were determined using a simulated annealing procedure that combines annealing cycles and *ab initio* calculations.[23] Structures were optimized using density functional theory (DFT) and the Gaussian09 suite of programs[24] at the B3LYP/6-31G(d) level of theory[25,26] using the ''loose'' keyword to utilize a large step size of 0.01 au and a rms force constant of 0.0017 to ensure a rapid geometry convergence. These structures were refined by geometry optimization at the B3LYP/6-311+G(d,p) level. From these optimized structures, the Ser residue was deprotonated at the likely sites (OH, COOH, or NH_2) yielding $[Zn(Ser-H)]^+$ structures that were refined again in the loose optimization step. The converged structures were then chosen for further refinement with the acetonitrile (ACN) ligand added, optimized at the loose level. Unique $[Zn(Ser-H)ACN]^+$ conformers underwent final geometry optimization and vibrational frequency calculations at the B3LYP/6-311+G(d,p) level of theory. Geometry optimizations utilizing empirical dispersion corrections were also determined at the B3LYP-GD3BJ/6-311+G(d,p) level.[27] The $CdCl^+$(Ser) complexes went through the same geometry optimization procedure except the def2-TZVP basis set was used, where def2-TZVP is a size-consistent basis set for all atoms and includes triple-ζ + polarization functions with a small core (28 electron) effective

core potential (ECP) on Cd.[28,29] The def2-TZVP basis set and affiliated ECP were obtained from the EMSL basis set exchange.[30]

To determine the accurate relative energies of the isomers of the Zn (Cd) complexes at both 0 and 298 K, single-point energy calculations were carried out at the B3LYP, B3LYP-GD3BJ,[27] B3P86,[31] and MP2(full)[32] (where full indicates correlation of all electrons) levels using the 6-311+G(2d,2p) (def2-TZVPP) basis sets. For all species, zero point energy (ZPE) corrections and thermal corrections to free energies at 298 K utilized vibrational frequencies scaled by 0.989. The transition states (TSs) of the $[Zn(Ser\text{-}H)ACN]^+$ photofragmentation processes were found through a series of relaxed potential energy scans along the likely reaction coordinates at the B3LYP/6-31G(d) level.[25,33,34] Geometry optimizations and frequency calculations of the TSs and intermediates (INTs) were performed at the B3LYP/6-311+G(d,p) level. Here the vibrational frequencies of the TSs were found to have only one imaginary frequency, and all INTs were determined to be vibrationally stable.

For comparison to IRMPD experimental spectra, calculated frequencies were scaled by 0.975, as this factor leads to good agreement between the calculated and experimentally well-resolved peaks and is consistent with previous IRMPD studies of metal–amino acid complexes.[2,10,35–38] The calculated vibrational frequencies are broadened using a 30 cm^{-1} full width at half maximum Gaussian line shape for comparison with experimental spectra. This broadening accounts for the finite laser bandwidth, unresolved rotational structure of the ions (which are near room temperature), anharmonicity of the vibrational mode, and broadening as a result of the multiple photon absorption process.[19]

Results

IRMPD action spectroscopy

The IRMPD action spectra of $[Zn(Ser\text{-}H)ACN]^+$ and $CdCl^+(Ser)$ were examined from 550 to 1800 cm^{-1} (Fig. 1). The IRMPD action spectra shown here correspond to the fractional yield of the product ions as a function of free electron laser wavenumber. Dominant dissociation pathways for the photodissociation of $CdCl^+(Ser)$ resulted in the loss of H_2O and (H_2O + CO); whereas, for $[Zn(Ser\text{-}H)ACN]^+$, the photodissociation fragmentation corresponded only to the loss of CH_2O, agreeing with the IRMPD dissociation channel previously observed for the deprotonated serine anion $(Ser\text{-}H)^-$.[39] Notably, ACN loss was not observed and these fragmentation pathways differ from those observed for the IRMPD[8] and collision-induced dissociation (CID)[40] studies of $M^+(Ser)$ where $M^+ = Na^+$, K^+, Rb^+, and Cs^+, in which dissociation resulted in the loss of the intact ligand to form the atomic metal cation. Fragment mass channels of 167 and 151 *m*/*z* were also observed during the photodissociation of $[Zn(Ser\text{-}H)ACN]^+$; however, they were not included in the fractional yield spectrum in Fig. 1. These fragmentation mass channels are such that they cannot be from the parent complex as there are no Zn isotopes for either mass channel and their spectra are very different from that for the loss of formaldehyde from $[Zn(Ser\text{-}H)ACN]^+$. These fragments are most likely contaminants or formed from species that were above the selected SWIFT mass range.

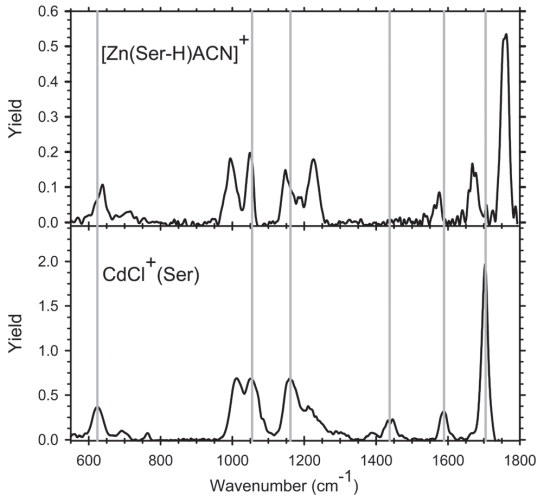

Fig. 1 IRMPD spectra of $[Zn(Ser\text{-}H)ACN]^+$ and $CdCl^+(Ser)$ complexes. Vertical lines at 624, 1013, 1052, 1159, 1432, 1586, and 1704 cm^{-1} are drawn to approximate COH wagging, COH stretching, NH_2 wagging, carboxylic COH bending, side-chain COH bending, NH_2 bending, and C═O stretching, respectively, of $CdCl^+(Ser)$.

Comparison of the spectra in Fig. 1 shows that the features observed for the intact amino acid and deprotonated system are similar in several respects. Particularly, $[Zn(Ser\text{-}H)ACN]^+$ and $CdCl^+(Ser)$ have parallel spectra for the low to middle wavenumber range, less than 1600 cm^{-1}, but obvious spectral differences appear in the higher frequency range associated with C═O stretching. Key differences between the Zn spectrum and that for Cd include: the intensity growth of the 1230 cm^{-1} band for Zn, the weakness of the 1430 cm^{-1} band for Zn, and most obviously, the two spectral features observed in the high frequency range from 1650–1760 cm^{-1} for Zn compared to only one for Cd. As will be documented below, this is indicative of multiple isomers present for the Zn complex.

Overview of theoretical results

As described above, the low-energy structures of $[Zn(Ser\text{-}H)ACN]^+$ and $CdCl^+(Ser)$ complexes were optimized at the B3LYP/6-311+G(d,p) and B3LYP/def2-TZVP levels of theory, respectively, with single point energies calculated using slightly larger basis sets and several levels of theory. Details of the calculated distinct low-lying conformers of $[Zn(Ser\text{-}H)ACN]^+$ and $CdCl^+(Ser)$ complexes are provided in the ESI† along with their corresponding optimized geometry structures, Fig. S1 and S2, respectively. The nomenclature used to identify the different structural isomers is based on that described in previous studies of metal–amino acid complexes.[1,8,9,11,40,41] Briefly, conformations are identified by their metal binding site in brackets, where backbone binding sites always precede side-chain binding. In cases where the binding site is ambiguous, ''s'' is used to specify a side-chain group. The binding site designation is followed by a description of the amino acid orientation by a series of dihedral angles.

The angles are denoted as "*c*" (*cis*) for angles $<45^\circ$, "*g*" (*gauche*) for angles between 45° and 135°, and "*t*" (*trans*) for angles $>135^\circ$. For charge-solvated (CS) structures, these dihedral angles start with the carboxylic acid hydrogen atom and proceed along the molecule to the terminal hydrogen of the amino acid side-chain, ∠HOCC, ∠OCCC, ∠CCCO, and ∠CCOH. The former or latter angles are missing if the carboxylic acid or hydroxyl has been deprotonated, respectively. The deprotonation site is designated by a negative ion symbol on the appropriate atom. In the case of salt-bridge (SB) structures, the proton originally on either the carboxylic acid or hydroxyl termini is attached instead to the nitrogen. For SB complexes deprotonated at the carboxylic acid, the first dihedral angle starts at this bridging proton, moves along the H-bond toward the deprotonated site, and then includes the same three dihedral angles as above.

Theoretical results for $[Zn(Ser-H)ACN]^+$

The optimized structures of select and distinctive low-lying conformations of $[Zn(Ser-H)ACN]^+$ are shown in Fig. 2a–d with their corresponding linear IR spectra. Energies at 0 and 298 K of the calculated conformations of these complexes relative to the ground structure (GS) calculated at four different levels of theory are given in Table 1. In all $[Zn(Ser-H)ACN]^+$ complexes, the acetonitrile ligand binds in a near linear configuration on the opposite side of the zinc cation away from the amino acid. All levels of theory predict that the lowest energy structure has deprotonated Ser binding in a tridentate fashion to Zn; however, the preferred site of deprotonation differs with the level of theory (Table 1). DFT levels of theory, including B3LYP with empirical dispersion corrections, find that the lowest energy structure at 0 and 298 K is $[N,CO,O^-]$tgg (Fig. 2a), Zn bound to the amino nitrogen and carbonyl of the Ser backbone with added complexation to the deprotonated side-chain hydroxyl. In contrast, the MP2(full) level of theory predicts that deprotonation occurs at the carboxylic acid terminus, $[N,CO^-,OH]$ggt (Fig. 2b), although this conformer is lower in free energy at 298 K by only 0.2 kJ mol^{-1}. Comparison of bond lengths in Table 2 reveals that the $[N,CO^-,OH]$ggt conformer has shorter M^{2+}–OC and M^{2+}–N bond distances than the $[N,CO,O^-]$tgg conformer by 0.29 and 0.07 Å, respectively. Conversely, the tridentate deprotonated side-chain hydroxyl, $[N,CO,O^-]$tgg, conformer binds more closely at the M^{2+}–O_s site by 0.29 Å. This shift in coordination distances between the two conformers can be clearly seen in the optimized structures provided in Fig. 2a and b.

The next lowest energy conformer of $[Zn(Ser-H)ACN]^+$ is the deprotonated tridentate $[N,CO,O^-]$cgg conformer (Fig. 2c). In the tgg GS, the carboxylic hydrogen forms an intramolecular hydrogen bond (H-bond) with the carbonyl oxygen. The cgg conformer

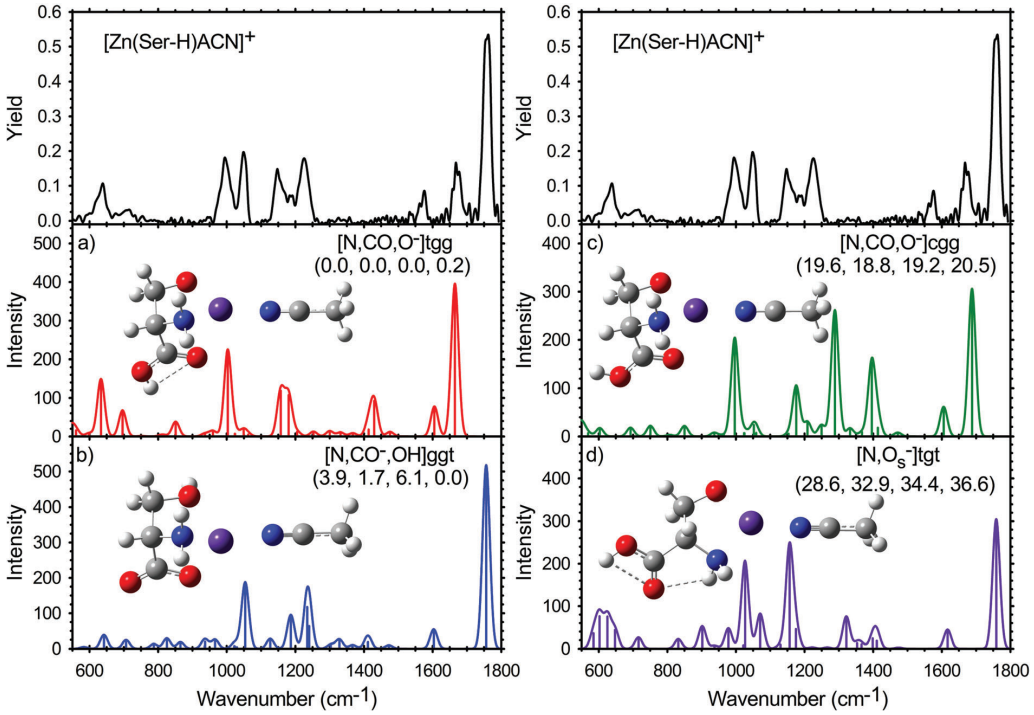

Fig. 2 Comparison of the experimental IRMPD spectrum of $[Zn(Ser-H)ACN]^+$ with IR spectra and structures of select low-lying conformers calculated at the B3LYP/6-311+G(d,p) level. Relative 298 K free energies in kJ mol^{-1} from Table 1 given in parentheses are calculated at the B3LYP, B3LYP-GD3BJ, B3P86, and MP2(full) levels with the 6-311+G(2d,2p) basis set. For structures: grey = C, red = O, blue = N, white = H, and purple = Zn. Dashed lines indicate hydrogen bonds.

Table 1 Relative enthalpies at 0 K and free energies at 298 K (kJ mol^{-1}) of [Zn(Ser-H)ACN]$^+$ conformers[a]

Structure	B3LYP	B3LYP-GD3BJ	B3P86	MP2(full)
[N,CO,O$^-$]tgg	0.0 (0.0)	0.0 (0.0)	0.0 (0.0)	1.1 (0.2)
[N,CO$^-$,OH]ggt	3.1 (3.9)	0.8 (1.7)	5.2 (6.1)	0.0 (0.0)
[N,CO,O$^-$]cgg	19.4 (19.6)	18.6 (18.8)	19.0 (19.2)	21.2 (20.5)
[N,O$_s^-$]tgt	30.3 (28.6)	34.5 (32.9)	36.0 (34.4)	39.1 (36.6)
[N,CO$^-$]tgt	31.0 (32.4)	34.9 (36.3)	36.9 (38.3)	38.6 (39.1)
[N,CO$^-$]gtt	35.1 (36.6)	38.8 (40.3)	41.2 (42.8)	43.2 (43.9)
[N,OH,O$^-$]tgg	37.0 (37.6)	35.7 (36.2)	40.6 (41.1)	35.5 (35.1)
[CO$^-$,O$^-$]ctc[b]	45.9 (46.4)	48.2 (48.7)	50.6 (51.1)	52.5 (52.1)
[CO,O$^-$]ctc	48.1 (48.7)	52.8 (53.4)	52.5 (53.1)	64.3 (64.0)
[N,CO$^-$]tgg	51.3 (52.1)	54.8 (55.7)	56.9 (57.7)	62.1 (62.0)
[N$^-$,CO,OH]tggt	51.9 (51.0)	53.1 (52.2)	54.3 (53.4)	50.5 (48.6)
[CO,O$^-$]tgg	52.5 (54.0)	58.2 (59.7)	60.6 (62.1)	70.3 (70.9)
[CO,O$^-$]tgg	52.9 (54.6)	58.9 (60.5)	61.0 (62.7)	70.0 (70.7)
[CO,O$^-$]ttg	53.7 (55.2)	58.1 (59.6)	62.1 (63.6)	71.7 (72.3)
[N$^-$,CO]tggg	58.2 (60.2)	63.7 (65.6)	63.4 (65.4)	66.3 (67.3)
[CO$_2^-$]ggg	66.9 (69.4)	78.4 (80.8)	74.7 (77.2)	80.8 (82.4)
[CO$_2^-$]ggt	68.9 (72.1)	81.8 (85.0)	78.2 (81.4)	82.0 (84.3)
[CO$^-$,O]cgt	71.5 (72.4)	72.6 (73.5)	77.8 (78.8)	78.1 (78.2)
[CO$_2^-$]gtg	73.4 (76.2)	86.5 (89.3)	81.5 (84.3)	92.9 (94.9)
[OH,O$^-$]tgg	103.3 (106.0)	108.1 (110.7)	115.8 (118.5)	116.8 (118.5)

[a] Free energies at 298 K are in parentheses. Calculations performed at the stated level of theory using a 6-311+G(2d,2p) basis set. Geometries and vibrational frequencies calculated at the B3LYP/6-311+G(d,p) level. Energies include ZPE corrections scaled by 0.989. s = side-chain. [b] Salt-bridge between NH_3^+ and COO^- groups.

Table 2 Bond distances (Å) and bond angles (°) for select low-energy conformers of metalated serine[a]

Complex	Structure	r(M–N)	r(M–OC)	r(M–OH$_s$)	∠NMO	∠NMO$_s$	∠OMO$_s$	∠NCCO
[Zn(Ser-H)ACN]$^+$	[N,CO,O$^-$]tgg	2.17	2.19	1.87	77.0	85.8	94.4	33.0
	[N,CO$^-$,OH]ggt	2.10	1.90	2.16	85.5	78.1	94.3	32.0
	[N,CO,O$^-$]cgg	2.19	2.15	1.87	75.9	84.8	95.7	33.4
	[N,O$_s^-$]tgt	2.08		1.83		90.4		14.9
	[N,CO$^-$]gtt	2.04	1.86		90.4			15.3
	[N,OH,O$^-$]tgg	2.13	2.37[c]	1.85	70.8	88.3	91.2	152.9
	[CO$^-$,O$^-$]ctc[b]		1.95	1.86			100.6	32.1
	[N$^-$,CO,OH]tggt	1.88	2.24	2.23	85.0	81.4	80.6	31.6
	[CO$_2^-$]ggg		1.99/1.97				67.0[d]	2.2
[Zn(Ser-H)]$^+$	[N,CO,O$^-$]tgg	2.21	2.10	1.86	78.1	86.7	95.8	34.5
	[N,CO$^-$,OH]ggt	2.06	1.89	2.08	89.2	81.0	100.1	34.6
	[N,CO,O$^-$]cgg	2.14	2.07	1.86	79.9	88.7	101.4	34.9
	[N,O$_s^-$]tgt	2.03		1.83		96.4		14.2
	[N,CO$^-$]ggt	1.99	1.84		97.0			7.2
	[N,OH,O$^-$]tgg	2.09	2.20[c]	1.85	75.2	92.7	97.4	150.1
	[CO$^-$,O$^-$]ctc[b]		1.88	1.84			109.8	32.0
	[N$^-$,CO,O]tggt	1.91	2.14	2.13	89.1	84.9	84.8	35.2
	[CO$_2^-$]ggg		2.04/2.03				65.3[d]	1.2

[a] Geometries calculated at the B3LYP/6-311+G(d,p) level for Zn-containing complexes. s = side-chain. [b] Salt-bridge between NH_3^+ and COO^- groups. [c] Hydroxyl of backbone carboxylic acid. [d] ∠OMO backbone carboxylate oxygens.

breaks this intramolecular bond, leading to a 19–21 kJ mol^{-1} increase in the free energy at 298 K relative to the tgg GS. The lowest energy bidentate species is the metal bound to the amine and deprotonated side-chain hydroxyl, [N,O$_s^-$]tgt (Fig. 2d), 29–37 kJ mol^{-1} above the GS. Additional higher energy structures located are shown in Fig. S1 (ESI†) and include [N,OH,O$^-$]tgg, [N$^-$,CO,OH]tggt, [N,CO$^-$]tgt, [CO$^-$,O$^-$]ctc, and various [CO$_2^-$] binding motifs.

Although the [Zn(Ser-H)]$^+$ species were not observed experimentally, it is valuable to compare the theoretical results for this complex with those for the species contaminated by ACN. Tables 2 and 3 provide direct comparison of the geometries and relative enthalpies, respectively, of low-lying ACN-free and ACN-contaminated deprotonated conformers. The [Zn(Ser-H)]$^+$ [N,CO$^-$,OH]ggt conformer is calculated to be 12–20 kJ mol^{-1} higher in free energy than the [N,CO,O$^-$] GS, meaning it could at most populate 0.8% of an ion population equilibrated at 298 K. In contrast, as seen in Table 1, the presence of the ACN ligand stabilizes the [N,CO$^-$,OH]ggt conformer such that it would populate between 8 and 52% of ions at 298 K. Zn^{2+} prefers to adopt a 4-coordinate geometry such that the addition of the ACN ligand binding to the metal stabilizes the complexes (as demonstrated experimentally by the inability to remove the ACN ligand when irradiated with a high power CO_2 laser).

Table 3 Relative enthalpies at 0 K and free energies at 298 K (kJ mol^{-1}) of low-lying conformers of [Zn(Ser-H)]$^{+}$ [a]

Structure	B3LYP	B3LYP-GD3BJ	B3P86	MP2(full)
[N,CO,O^{-}]tgg	0.0 (0.0)	0.0 (0.0)	0.0 (0.0)	0.0 (0.0)
[N,CO^{-},OH]ggt	16.1 (17.1)	14.5 (15.5)	18.9 (19.9)	11.1 (12.0)
[N,CO,O^{-}]cgg	21.8 (22.0)	21.3 (21.5)	21.3 (21.4)	22.0 (22.2)
[N,O$_s^{-}$]tgt	49.5 (50.5)	52.4 (53.4)	57.3 (58.4)	58.2 (59.2)
[N,CO^{-}]ggt	63.5 (65.2)	66.1 (67.8)	71.6 (73.2)	68.4 (70.0)
[N,OH,O^{-}]tgg	46.5 (47.1)	44.6 (45.2)	50.8 (51.4)	42.7 (43.3)
[CO^{-},O^{-}]ctc [b]	50.3 (51.3)	52.1 (53.0)	56.9 (57.8)	56.1 (57.1)
[CO,O^{-}]ctc	70.4 (71.3)	74.4 (75.3)	75.1 (76.0)	88.2 (89.1)
[N^{-},CO,OH]tggt	52.1 (53.3)	53.3 (54.5)	55.4 (56.6)	53.5 (54.6)
[CO$_2^{-}$]ggg	102.8 (106.7)	114.4 (118.3)	120.9 (124.8)	156.0 (159.9)

[a] Free energies at 298 K are in parentheses. Calculations performed at the stated level of theory using a 6-311+G(2d,2p) basis set. Geometries and vibrational frequencies calculated at the B3LYP/6-311+G(d,p) level. Energies include ZPE corrections scaled by 0.989. s = side-chain. [b] Salt-bridge between NH_3^+ and COO^- groups.

Interestingly, comparison of [Zn(Ser-H)ACN]$^{+}$ and [Zn(Ser-H)]$^{+}$ relative free energies (Tables 1 and 3) shows that the ACN containing conformers all have a lower free energy relative to the ground conformer than the corresponding ACN-free structures, although [N,CO,O^{-}]cgg and [N^{-},CO,OH]tggt are stabilized comparably to the GS. This phenomenon can be explained by examining the geometric effects of adding ACN to the [Zn(Ser-H)]$^{+}$ complexes, as seen in Table 2. For most complexes, the addition of ACN increases the metal–ligand bond lengths, a natural consequence of electron donation from acetonitrile to the metal center. In contrast, the Zn–N bond of both [N,CO,O^{-}]tgg and [N^{-},CO,OH]tggt decreases upon ACN addition as does the Zn–OC bonds of [CO$_2^{-}$]ggg, such that these structures benefit less from coordination of the fourth coordination site. With the exception of the [CO$_2^{-}$]ggg conformer, all of the complexes see a decrease in ligand binding site bond angles upon ACN attachment, again indicating that the metal generally moves away from the (Ser-H)$^{-}$ ligand. Overall, the addition of the ACN ligand results in the [N,CO^{-},OH]ggt conformer becoming comparable in energy to the [N,CO,O^{-}]tgg GS, with an inversion in the relative energies occurring at the MP2(full) level.

Theoretical results for CdCl^{+}(Ser)

The optimized structures of select and distinctive low-lying conformations of CdCl^{+}(Ser) with their corresponding linear IR spectra are shown in Fig. 3a–c with relative energies in Table 4. Calculations at all four levels of theory find that the charge-solvated tridentate [N,CO,OH]tggt structure is the ground structure (GS) for CdCl^{+}(Ser). As seen in Fig. 3a, in this conformer, Cd is bound to the amino nitrogen, r(Cd–N) = 2.33 Å, carbonyl oxygen, r(Cd–O) = 2.39 Å, and side-chain hydroxyl oxygen, r(Cd–O) = 2.51 Å, and the carboxylic hydrogen forms an intramolecular H-bond with the carbonyl oxygen. Similar to the deprotonated species, when this intramolecular bond is broken, as in the [N,CO,OH]cggt conformer, the relative free energy at 298 K is found to be 28–30 kJ mol^{-1} higher than the tggt conformer.

If the metal ion interaction with the hydroxyl side-chain is lost and only the backbone amino acid interaction is maintained, bidentate [N,CO] conformers are formed with tcgt, tgtt, and tgtg orientations. The lowest of these bidentate conformers is

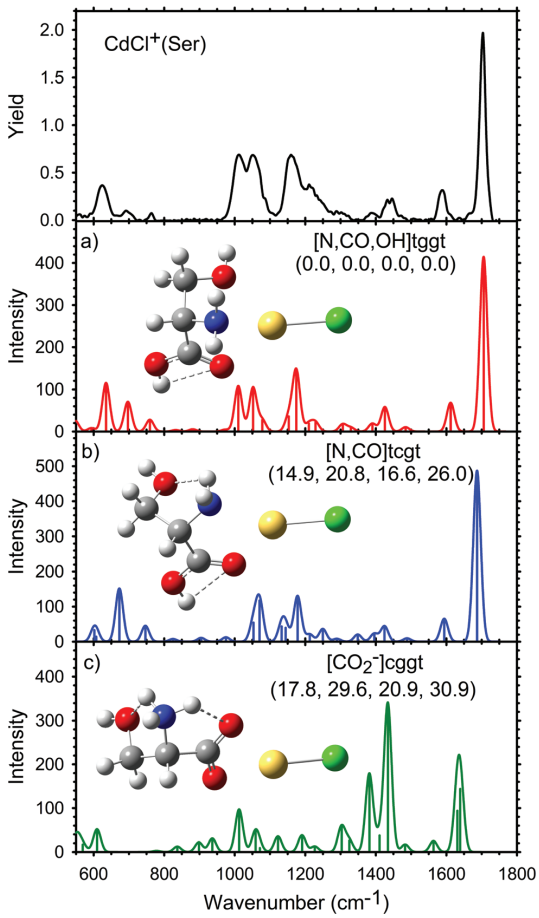

Fig. 3 Comparison of the experimental IRMPD spectrum of CdCl^{+}(Ser) with IR spectra and structures of select low-lying conformers calculated at the B3LYP/def2-TZVP level. Relative 298 K free energies in kJ mol^{-1} from Table 4 given in parentheses are calculated at the B3LYP, B3LYP-GD3BJ, B3P86, and MP2(full) levels with the def2-TZVPP basis set. For structures: grey = C, red = O, blue = N, white = H, green = Cl, and yellow = Cd. Dashed lines indicate hydrogen bonds.

Table 4 Relative enthalpies at 0 K and free energies at 298 K (kJ mol^{-1}) of $CdCl^+$(Ser) conformers[a]

Structure	B3LYP	B3LYP-GD3BJ	B3P86	MP2(full)
[N,CO,OH]tggt	0.0 (0.0)	0.0 (0.0)	0.0 (0.0)	0.0 (0.0)
[N,CO]tcgt	14.8 (14.9)	20.7 (20.8)	16.5 (16.6)	25.9 (26.0)
[CO_2^-]cggt[b]	17.1 (17.8)	28.9 (29.6)	20.2 (20.9)	30.2 (30.9)
[N,CO]tgtt	19.9 (20.2)	25.0 (25.2)	21.6 (21.8)	31.0 (31.3)
[CO_2^-]cgtt[b]	19.5 (20.6)	31.9 (33.0)	23.6 (24.7)	34.4 (35.6)
[N,CO]tgtg	21.9 (22.5)	26.6 (27.2)	23.5 (24.1)	34.1 (34.7)
[N,OH_s]tgtt	27.3 (27.7)	31.6 (31.9)	30.3 (30.6)	34.6 (34.9)
[N,CO,OH]cggt	28.5 (28.8)	28.1 (28.4)	28.2 (28.5)	30.0 (30.3)
[N,OH,OH]tggt	30.3 (30.5)	28.7 (28.9)	32.6 (32.8)	27.3 (27.5)
[N,OH_s]tttt	38.1 (38.7)	42.5 (43.1)	42.0 (42.6)	46.1 (46.8)
[CO,OH_s]cggt	43.9 (44.5)	50.4 (51.0)	46.4 (46.9)	62.2 (62.7)
[N,CO]tcgg	44.8 (45.6)	51.4 (52.2)	47.4 (48.2)	61.7 (62.4)
[COOH]cggt	49.3 (49.8)	62.2 (62.7)	51.6 (52.2)	69.8 (70.3)
[CO_2^-]cggg[b]	49.4 (50.6)	61.0 (62.1)	53.1 (54.3)	66.6 (67.8)
[N,OH]ttgt	56.4 (56.8)	60.6 (61.0)	60.2 (60.6)	62.2 (62.6)
[CO,OH_s]ggt[b]	60.4 (60.9)	65.6 (66.1)	61.7 (62.2)	73.9 (74.4)
[CO,OH_s]ttgt	60.0 (61.2)	65.9 (67.1)	66.7 (67.9)	80.8 (82.0)
[N,OH]tttt	60.8 (61.5)	65.6 (66.3)	65.4 (66.2)	68.0 (68.7)
[CO,OH_s]ctct	61.3 (61.5)	66.7 (66.9)	63.9 (64.1)	77.5 (77.7)
[CO,OH_s]tggt	60.0 (61.7)	67.3 (69.0)	66.3 (67.9)	80.4 (82.1)
[N,OH_s]cgtt	62.9 (63.2)	66.3 (66.6)	65.3 (65.6)	71.0 (71.4)
[O_s^-]cggt[c]	64.1 (63.8)	75.7 (75.5)	67.6 (67.3)	78.8 (78.5)
[OH_s]ttcc	103.1 (103.6)	115.3 (115.8)	107.9 (108.4)	128.5 (129.0)
[OH,OH]tggg	118.5 (120.9)	123.8 (126.1)	128.5 (130.8)	133.4 (135.7)
[OH_s]tggc	136.4 (137.8)	148.6 (150.0)	146.4 (147.8)	159.7 (161.1)

[a] Free energies at 298 K are in parentheses. Calculations performed at the stated level of theory using a def2-TZVPP basis set. Geometries and vibrational frequencies calculated at the B3LYP/def2-TZVP level. Energies include ZPE corrections scaled by 0.989. s = side-chain. [b] Salt-bridge between NH_3^+ and COO^- groups. [c] Salt-bridge between NH_3^+ and O_s^- groups.

[N,CO]tcgt (Fig. 3b), which lies 15–26 kJ mol^{-1} higher in energy than the tridentate GS (Table 4) and is stabilized by a NH·OH_s hydrogen bond. Although the loss of the side-chain interaction is less favorable energetically, it allows stronger binding interactions between the metal and the amino nitrogen and carbonyl oxygen, as evidenced by shortening these bond distances by 0.09 and 0.03 Å, respectively.

The lowest energy salt-bridge (SB) structure for $CdCl^+$(Ser) is the [CO_2^-]cggt conformer (Fig. 3c), which is 18–31 kJ mol^{-1} higher than the tridentate GS. Interestingly, this SB conformer is lower by 32–39 kJ mol^{-1} than its corresponding nonzwitterionic [COOH]cggt conformer (Table 4), where the H remains on the carboxylic acid rather than transferring to the amino nitrogen. Both of these structures are also stabilized by NH·OH_s H-bonds. Additional higher lying structures are shown in Fig. S2 (ESI†) and include [N,CO,OH]cggt, [N,OH,OH]tggt, [CO,OH_s]cggt, [CO,OH]tggt, and various [N,OH], [N,OH_s], and [CO_2^-] structures.

These results are analogous with our previous studies of the alkali metal cation interactions with Ser, where [N,CO,OH] ground conformers were found for M^+(Ser) where M^+ = Li^+, Na^+, and K^+.[8] The GS of $CdCl^+$(Ser) is also similar to the ground structure found for $CdCl^+$(CysOMe), [N,CO,S]tggg.[1]

Comparison of experimental and theoretical spectra: $[Zn(Ser-H)ACN]^+$

Fig. 2 shows the experimental IRMPD action spectrum compared to the calculated linear IR absorption spectra for selected low-energy conformers found for the $[Zn(Ser-H)ACN]^+$ complex. In making these comparisons, it should be taken into consideration that the calculated IR intensities are based on single photon absorption, which sometimes do not correspond directly to the multiphoton process of the action spectra.

The highest frequency band observed at 1762 cm^{-1} corresponds to the carbonyl stretch, which explains its large intensity. Interaction with the zinc dication results in red shift compared to that calculated for free Ser at 1791 cm^{-1}.[8] The [N,CO^-,OH]ggt conformer predicts this band lies at 1756 cm^{-1}, in good agreement with the action spectrum. In addition, the peaks observed at 1227 and 1047 cm^{-1} are consistent with the next most intense bands in the calculated IR spectrum of this conformer. Clearly, this conformer does not reproduce many of the other peaks observed experimentally. The peak observed at 1667 cm^{-1} suggests the presence of the [N,CO,O^-]tgg conformer, which theory predicts has a C═O stretch at 1665 cm^{-1} for the deprotonated carboxylic acid. The presence of this conformer is confirmed by reproduction of the peaks observed at 1147 and 992 cm^{-1}. Both low-energy conformers have vibrations in good agreement with the bands observed at 639 and 712 cm^{-1} associated with COH wagging. The band observed at 1577 cm^{-1} associated with the NH_2 bend motion is predicted to be at 1606 and 1604 cm^{-1} for the [N,CO,O^-]tgg and [N,CO^-,OH]ggt conformers, respectively. This vibrational mode is known to have especially strong anharmonic character in metallated amino acids accounting for the significant shift in the action spectra, as observed consistently in IRMPD amino acid studies.[7,38–40] For instance, the 28 cm^{-1} shift in this mode observed here is comparable to those seen for $[M(Cys-H)]^+$, between 26 and 30 cm^{-1},[1] and actually less than those observed for M^+(Ser) where M^+ = K^+, Rb^+, and Cs^+, which exhibit shifts up to 40 cm^{-1}.[8]

Overall, we conclude that the experimental spectrum can be explained nicely by a combination of the two lowest energy conformers. The appearance of multiple conformers is consistent with the relative enthalpies and free energies calculated for this system, Table 1. The relative intensities of the two C═O stretch bands suggest that [N,CO^-,OH]ggt has a higher abundance than the [N,CO,O^-]tgg conformer. This result is consistent with the relative free energies calculated at the MP2(full) level of theory, which indicates that [N,CO,O^-]tgg can account for 52% of an equilibrated ion population at 298 K.

Fig. 2 also includes the predicted spectra for two conformers that are next lowest in energy, Table 1. In both cases, all levels of theory place these structures sufficiently high in energy that they should not be populated if equilibrated at 298 K. The [N,CO,O^-]cgg spectrum has similarities to the [N,CO,O^-]tgg spectrum, particularly for the C═O stretch (1688 cm^{-1}), NH_2 bend (1606 cm^{-1}), and NH_2 wag (996 cm^{-1}) vibrational modes. However, it also predicts intense peaks at 1289 and 1396 cm^{-1} that are clearly absent from the experimental spectrum. The former band is unique to this [N,CO,O^-]cgg conformer as it is from HOCC bending motion centered at the carboxylic acid carbon, when there is no intramolecular bonding within the carboxylic acid. The bidentate [N,O_s^-]tgt spectrum also has a band at 1759 cm^{-1}, corresponding to the C═O stretch of an intact carboxylic acid but no longer coordinated to the metal cation.

The rest of the spectrum matches the experiment reasonably well in the wavenumber position, but not in relative intensity. Furthermore, the band near 630 cm^{-1} is much too broad compared to the experiment and peaks predicted between 1300 and 1450 cm^{-1} that are not observed experimentally.

Comparison of experimental and theoretical spectra: $CdCl^+$(Ser)

Compared with the experimental spectrum of $[Zn(Ser\text{-}H)ACN]^+$ (Fig. 1), the $CdCl^+$(Ser) spectrum retains most of the same characteristics but there is only one C=O stretch band and more intensity in the 1350–1500 cm^{-1} region. Fig. 3 shows the experimental IRMPD action spectrum of $CdCl^+$(Ser) compared with theoretical predictions for the three lowest energy conformations, Table 4. It is clear that the bands predicted for the consensus GS, [N,CO,OH]tggt, correspond well to the observed spectrum. All major bands are present with comparable theoretical and experimental frequencies. The largest difference can be found for the band at 1586 cm^{-1} where there is a 26 cm^{-1} shift to the blue in the predicted spectrum, a common anharmonic shift for the NH_2 bend motion, as noted above.

The intense carbonyl stretch band observed at 1704 cm^{-1} shows that that interaction of intact Ser with Cd^{2+} results in an even larger red shift from the free Ser C=O band compared to the interaction with Zn^{2+}. The [N,CO,OH]tggt conformer predicts this band at 1704 cm^{-1}, in excellent agreement with the observed band. The next lowest energy conformer, [N,CO]tcgt, predicts a red-shifted carbonyl stretch at 1687 cm^{-1}. The carboxylate C=O stretch band for the salt-bridge conformer, $[CO_2^-]$cggt, is shifted even further to 1637 cm^{-1}. The position of this band and other spectral discrepancies with the action spectrum confirm that the higher energy salt-bridge conformer is not present experimentally.

Except for the carbonyl stretch, the predicted spectrum of the higher energy bidentate conformer, [N,CO]tcgt, agrees reasonably with the observed action spectrum, although there are additional disagreements in diagnostic bands that unequivocally assign the $CdCl^+$(Ser) experimental spectrum as tridentate [N,CO,OH]tggt. Specifically, the 1013 and 1052 cm^{-1} bands, which are associated with the COH stretch and NH_2 wag, respectively, match the GS spectrum well, whereas the [N,CO]tcgt spectrum does not predict the COH stretch band and calculates that the NH_2 wag vibrational mode is shifted to the blue by 20 cm^{-1} compared to the experiment. Another diagnostic region is apparent in the sequence of three bands corresponding to carboxylic acid hydrogen wagging observed at 624, 691, and 764 cm^{-1}. The relative intensities as well as their positions are nicely predicted by the GS, whereas these three bands for the [N,CO]tcgt conformer are all red shifted and the relative intensity ratio is different from the experiment. Therefore, we assign the [N,CO,OH]tggt ground conformer as the only structure present experimentally. Although the possibility that small contributions from the [N,CO]tcgt conformer cannot be completely eliminated, its calculated relative energy suggests that its equilibrium 298 K population is less than 0.3%.

Notably, the $CdCl^+$(Ser) action spectrum has a band at ~1430 cm^{-1} band, which was not observed for $[Zn(Ser\text{-}H)ACN]^+$, Fig. 1. This vibrational band can be assigned to the intact carboxylic acid HOC bend. Because the experimental ion population of the Zn complex appears to be dominated by the deprotonated carboxylic acid conformer, which naturally lacks this vibrational mode, this comparison helps validate the conclusions regarding the relative populations discerned above.

Photofragmentation pathways

Reaction coordinate calculations were performed to elucidate the photodissociation pathways of $[Zn(Ser\text{-}H)ACN]^+$, as two sterically different parent ion conformers, $[N,CO,O^-]$tgg and $[N,CO^-,OH]$ggt, were present experimentally yet only one distinct fragment ion was observed. Interestingly, the only fragment ion observed corresponds to the loss of neutral formaldehyde, which can be imagined to be lost easily in a charge remote process from the $[N,CO,O^-]$tgg parent ion conformer (Fig. 2). However, as determined above, the $[N,CO^-,OH]$ggt conformer probably has a higher population. Therefore it needs to be investigated how the $[N,CO^-,OH]$ggt conformer loses formaldehyde and why other potential pathways, such as the loss of neutral carbon dioxide or the ACN ligand, are not observed.

To investigate the loss of neutral CO_2 from $[N,CO^-,OH]$ggt, a complete reaction coordinate path for this dissociation was investigated theoretically. Fig. 4 shows the potential energy surface generated for the loss of neutral CO_2 by a charge-remote process with relative energies at multiple levels of theory listed in Table 5. In this mechanism, the rate-limiting barrier TS_C corresponds to breaking the amino acid backbone C–C bond, 159–173 kJ mol^{-1} higher in energy than the $[N,CO,O^-]$tgg conformer. The loss of the M–OC interaction does not occur yet as the CO_2 ligand moves to stay coordinated with the metal ion in INT_C. The M–N coordination is lost in the process and now the metal coordinates to the newly formed anionic carbon, such that Zn remains 4-coordinate, $[C^-,OH][CO][ACN]$. Complete loss of CO_2 from the metal ion from INT_C requires an additional 12–23 kJ mol^{-1} energy.

The loss of neutral CH_2O from the $(Ser\text{-}H)^-$ parent ion has been observed in IRMPD[39] and CID[42] studies and investigated by molecular modeling.[43] It has been suggested that the loss of CH_2O from $(Ser\text{-}H)^-$ may occur by a charge-direct process.[44] In that study, the deprotonation site was the carboxylic acid and fragmentation was initiated by endothermic proton transfer from the side-chain hydroxyl to the carboxylate, resulting in a facile and exothermic anion-induced elimination of CH_2O. A similar process was found to be the lowest energy pathway in this study, where Fig. 4 shows the reaction coordinate for the loss of CH_2O from $[Zn(Ser\text{-}H)ACN]^+$ $[N,CO^-,OH]$ggt. (It can also be noted that we also located a higher energy charge-direct process for the loss of CH_2O.) In this mechanism, the first step is proton transfer from the side-chain hydroxyl to the carboxylate *via* $TS1_F$, which requires 84–91 kJ mol^{-1}. Facile rotation of the COOH group forms $INT1_F$, $[N,CO,O^-]$cgg, which rearranges to the other populated conformer, $INT2_F$ $[N,CO,O^-]$tgg, by rotation of the hydroxyl group over $TS2_F$ (51–54 kJ mol^{-1} above the GS). In $[N,CO,O^-]$tgg, the side-chain is positioned to allow the cleavage of the carbon–carbon bond to free CH_2O *via* $TS3_F$, which requires 74–99 kJ mol^{-1} energy. The CH_2O moves to stay

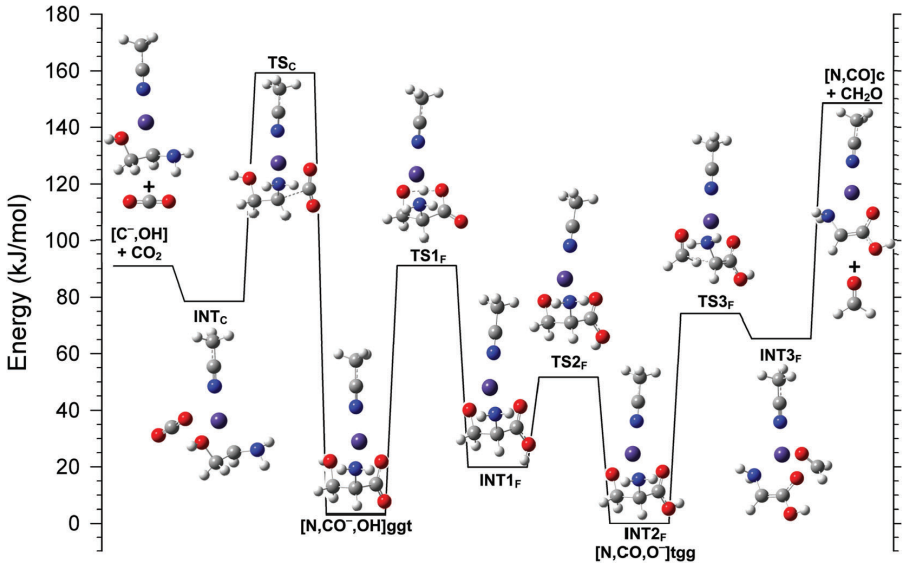

Fig. 4 The reaction coordinate for $[Zn(Ser-H)ACN]^+$ $[N,CO^-,OH]ggt$ and $[N,CO,O^-]tgg$ fragmenting to lose neutral CO_2 (subscript C, left) or CH_2O (subscript F, right). Single point energies are calculated at B3LYP/6-311+G(2d,2p)//B3LYP/6-311+G(d,p) levels of theory including zero point energy corrections and are relative to the $[N,CO,O^-]tgg$ conformer. Dashed lines show the bonds being broken in TS_C and $TS3_F$.

Table 5 Relative enthalpies at 0 K (kJ mol^{-1}) for intermediates (INTs) and transition states (TSs) along the reaction coordinates for the loss of neutral carbon dioxide and formaldehyde from $[Zn(Ser-H)ACN]^+$ [a]

Species	B3LYP	B3LYP-GD3BJ	B3P86	MP2(full)
$[N,CO,O^-]tgg$	0.0	0.0	0.0	1.1
$TS1_G$	51.3	50.9	52.1	54.3
$[N,CO^-,OH]ggt$	3.1	0.8	5.2	0.0
TS_C	159.1	161.1	172.7	164.3
INT_C	78.5	91.9	106.9	93.7
$[C^-,OH] + CO_2$	91.0	113.8	120.3	117.4
$[N,CO^-,OH]ggt$	3.1	0.8	5.2	0.0
$TS1_F$	90.8	86.6	84.1	84.0
$INT1_F$ $[N,CO,O^-]cgg$	19.4	18.6	19.0	21.2
$TS2_F$	86.2	85.8	101.5	111.1
$INT2_F$ $[N,CO,O^-]tgg$	0.0	0.0	0.0	1.1
$TS3_F$	73.9	74.6	90.9	98.6
$INT3_F$	65.3	73.1	87.4	91.6
$[N,CO]c + CH_2O$	148.5	170.5	174.9	192.4
$[N,CO^-] + CH_2O$	100.1	121.3	130.1	139.9
$[N,CO,O^-]tgg$ + ACN	221.1	231.5	227.8	234.7

[a] Calculations performed at the stated level of theory using a 6-311+G(2d,2p) basis set. Geometries and vibrational frequencies calculated at the B3LYP/6-311+G(d,p) level. Energies include ZPE corrections scaled by 0.989.

coordinated to the metal ion in $INT3_F$, $[N,CO]c[CH_2O][ACN]$, where here *c* indicates a *cis* COOH dihedral angle. Elimination of formaldehyde requires an additional 83–101 kJ mol^{-1} of energy after $INT3_F$. Note that this CH_2O loss mechanism forms the $[N,CO]c[ACN]$ product, rather than the lowest energy product conformer, $[N,CO^-][ACN]$ (Table 5), which requires proton transfer from COOH to the alpha-carbon radical. Mechanisms for this proton transfer were located but all contained a transition state lying >245 kJ mol^{-1} above reactants (see, for example, Fig. S3 of the ESI†).

Overall, the rate-limiting transition state for the loss of formaldehyde is the final products, a loose phase space limit (PSL) TS, which lie 148–192 kJ mol^{-1} above the GS. Theory predicts that this TS is below the rate-limiting TS_C for CO_2 loss by 11 kJ mol^{-1} at the B3LYP level, but 2–28 kJ mol^{-1} above at the other levels examined, Table 5. To examine how these relative energetics would influence the competition between these two competitive channels, we performed RRKM analysis for H_2CO and CO_2 loss using relative energy differences stipulated by all levels of theory. In all cases, the loose PSL TS for the loss of CH_2O dominated the tight TS for CO_2 loss (TS_C) by an order of magnitude or more at time scales relevant to the ICR detection ($\sim$100 ms). For CO_2 loss to be observed, we calculate that TS_C would need to be lower in relative energy by >34 kJ mol^{-1}, well over the difference predicted by any level of theory. Thus, proton transfer between the deprotonated side-chain hydroxyl and carboxylic acid sites over $TS1_F$ requires only 84–91 kJ mol^{-1}, well below either dissociation channel. Thus proton transfer is facile and permits the loss of formaldehyde from both $[N,CO,O^-]tgg$ and $[N,CO^-,OH]ggt$ conformers. The failure to remove the ACN ligand can also be understood as this requires much more energy (221–235 kJ mol^{-1}) than the decomposition routes shown in Fig. 4.

Discussion

Comparison with M^{2+}(Cys)

The amino acids cysteine and serine differ only by the substitution of sulfur for the oxygen in the side-chain and have

proven to exchange easily in proteins.[7,45] Comparison of the present work on Ser with the corresponding study of Cys[1] demonstrates that such equivalent amino acid exchange is not as facile upon interaction with metal dications. In the previous study of Cys and its methyl ester, CysOMe, the ESI source formed $[M(Cys\text{-}H)ACN]^+$, $[M(CysOMe\text{-}H)ACN]^+$ and $CdCl^+(CysOMe)$ for M = Zn and Cd. The ACN contamination ligand was easily removed from $[M(Cys\text{-}H)ACN]^+$ and $[M(CysOMe\text{-}H)ACN]^+$ by CO_2 laser irradiation, thereby forming stable 3-coordinate $[M(Cys\text{-}H)]^+$ and $[M(CysOMe\text{-}H)]^+$ complexes.[1] Comparably for histidine, both 3- and 4-coordinate systems, $[M(His\text{-}H)]^+$, $CdCl^+(His)$, and $M^{2+}(His)_2$, could be formed. Conversely, the equivalent $[M(Ser\text{-}H)]^+$ complexes could not be generated either in the source or by additional laser irradiation. Instead the acetonitrile ligand (for Zn^{2+}) or spectator ion (Cl^- for Cd^{2+}) needs to be present, and even after FELIX light irradiation, the $[M(Ser\text{-}H)]^+$ deprotonated species were never observed because fragmentation leads to the decomposition of the amino acid instead of the loss of the ACN ligand. The need to bind these non-amino acid ligands to the metal and the inability to remove these ligands by irradiation indicates that Ser binds less effectively to Zn^{2+} and Cd^{2+} than Cys and His.

Previously, comparison of experimental and theoretical IR spectra allowed us to conclude that Zn^{2+} and Cd^{2+} bind to deprotonated Cys in a tridentate $[N,CO,S^-]tgg$ configuration, with deprotonation occurring at the sulfur side-chain.[1] For $CdCl^+(CysOMe)$, a similar tridentate binding motif is found, [N,CO,S], and likewise $CdCl^+$ binds to intact Ser as [N,CO,OH]. These binding motifs are also found for alkali metal cations binding to Ser[40] and Cys.[8] The side-chain hydroxyl is polar and partially negative and thus interacts strongly with the metal dications, even in the presence of spectator ions and ligands as found in the present study. The $[Zn(Ser\text{-}H)ACN]^+$ complex is also found to have a tridentate ligand binding geometry, analogous to the deprotonated Cys systems. However, unlike the unambiguous assignment of deprotonation at the thiol for Cys, the site of deprotonation for Ser is mixed. Deprotonation at the carboxylic acid becomes competitive with the side-chain deprotonation for the lowest energy conformer, as demonstrated experimentally by the IR action spectrum. DFT levels of theory calculate that the $[N,CO,O^-]tgg$ conformer is more favorable than $[N,CO^-,OH]ggt$ by 2–6 kJ mol^{-1} at 298 K, and the reverse is found at the MP2(full) level (energy difference of only 0.2 kJ mol^{-1}). The relative intensities of diagnostic C=O stretch bands in the IRMPD action spectrum suggest that the latter level of theory is the most accurate for this study.

The relative propensities of these deprotonation sites can be understood by examining the thermodynamics for simple model systems. Heterolytic bond cleavage ($RH \rightarrow R^- + H^+$) of methanethiol requires 1496 kJ mol^{-1},[46] which is much lower than that for methanol, 1597 kJ mol^{-1}.[47] Thus, these relative deprotonation energies of SH and OH coincide with the relative probability of deprotonating at the side-chain SH of Cys over the side-chain OH of Ser. However, carboxylic acids are generally more acidic in the gas phase than simple thiols and alcohols,[48] *e.g.*, acetic acid has a deprotonation enthalpy of 1457 kJ mol^{-1}.[49] As such, one might expect the carboxylic acid to be the preferred site of deprotonation for both of these amino acids. However, as we have observed in this study, interaction with Zn^{2+} changes the relative probabilities for deprotonation as deprotonation of SH in Cys is highly favored and deprotonations of OH and COOH in Ser are competitive when binding to Zn^{2+}. One plausible rationale is that Zn^{2+} prefers bonding with more localized anion sites, O^- and S^-, over the delocalized CO_2^-, although the latter coordination site remains competitive because its deprotonation is enthalpically favored.

Theory can also be used to examine the relative energies of low-lying conformers of $[Zn(Ser\text{-}H)]^+$ (Table 3), which allows for a direct comparison with the previously studied $[Zn(Cys\text{-}H)]^+$ system.[1] Deprotonation at the side-chain is predicted to be the ground conformer for both Cys and Ser interacting with zinc, finding each species to have a tridentate $[N,CO,X^-]tgg$ ground conformer, where X = S or O. For Cys, all levels of theory find that this structure is lower in energy than all other structures by >25 kJ mol^{-1} with deprotonation at the carboxylic acid, $[N,CO^-,S]ggg$, being $\sim$42 kJ mol^{-1} less favorable at 298 K. In contrast, for Ser, Table 3 shows that this gap is 12–20 kJ mol^{-1}, with decarbonylation at the carboxylic acid, $[N,CO^-,OH]ggt$, lying closest in energy. Furthermore, this energy difference is dramatically reduced upon coordination by a fourth ligand, as in the experimentally observed $[Zn(Ser\text{-}H)ACN]^+$ system.

Overview

The IRMPD action spectra of cationized serine have been obtained in the region of 550–1800 cm^{-1} for complexes with Zn^{2+} and Cd^{2+}. Experimental spectra compared with IR spectra calculated at the B3LYP/6-311+G(d,p) level for Zn^{2+} and at the B3LYP/def2-TZVP level for Cd^{2+} containing complexes allow the identification of conformations present in the experiment. Action spectra were collected for complexes of Zn^{2+} with deprotonated serine and a metal bound acetonitrile spectator ligand and Cd^{2+} with a chlorine spectator anion interacting with intact serine. Thus, in both cases, only 4-coordinate systems are formed for the Ser ligand. Comparison of experimental and theoretical IR spectra show that both metal dications (Zn and Cd) bind to Ser in a tridentate motif coordinated to the amine and carbonyl groups of the amino acid backbone and the hydroxyl group of the side-chain. Our study finds that the $CdCl^+(Ser)$ complex can be assigned as the predicted ground conformer, [N,CO,OH]tggt; whereas both $[N,CO,O^-]tgg$ and $[N,CO^-,OH]ggt$, the two lowest energy conformers, were observed for the $[Zn(Ser\text{-}H)ACN]^+$ complex. Relative intensities of the diagnostic C=O stretch bands in the $[Zn(Ser\text{-}H)ACN]^+$ action spectra suggest deprotonation at the carboxylic acid conformer is the more populated conformer, in agreement with the results at the MP2(full) level of theory. Deprotonation at this site differs from the previously studied deprotonated cysteine complexes, where the site of deprotonation for both Zn^{2+} and Cd^{2+} was assigned unambiguously to be the thiol side-chain.[1] Although not experimentally observed, *ab initio* calculations of the $[Zn(Ser\text{-}H)]^+$ complex show that the conformer with deprotonation of the carboxylic acid is stabilized by the addition of the acetonitrile ligand yielding a desirable 4-coordinate complex.

The ACN ligand pulls electron density away from the metal, thereby relaxing the coordination of the amino acid ligand.

The types of complexes for amino acids interacting with metal dications, Zn^{2+} and Cd^{2+}, that can be experimentally generated change from 3-coordinate for Cys and His to 4-coordinate complexes for Ser, indicating that stabilization of the Ser complex requires the extra ligand. As noted above, it is energetically more favorable for the acidic side-chain thiol of Cys to undergo deprotonation to bind with the metal dication, than to deprotonate the hydroxyl side-chain of Ser. To compensate for this energetic cost, deprotonated Ser binds to Zn only in the presence of the adventitious ACN ligand, which binds much more tightly than in the comparable deprotonated Cys complex. This result parallels the observation that the metal–amino acid interaction is lost when Ser replaces Cys in zinc-finger protein studies.[7] The results presented here provide valuable information for expanding our understanding of the fundamental aspects of metal–amino acid preferential binding phenomena in metal-dependent proteins.

Acknowledgements

Financial support for this work was provided by the National Science Foundation, Grants CHE-1359769 and PIRE-0730072. The FELIX Laboratory is supported by the Stichting voor Fundamenteel Onderzoek der Materie (FOM). A grant of generous allocation of computing time from the Center for High Performance Computing at the University of Utah is gratefully acknowledged. In addition, the skilled assistance of the FELIX staff is highly appreciated.

References

1 R. A. Coates, C. P. McNary, G. C. Boles, G. Berden, J. Oomens and P. B. Armentrout, *Phys. Chem. Chem. Phys.*, 2015, **17**, 25799–25808.
2 T. E. Hofstetter, C. Howder, G. Berden, J. Oomens and P. B. Armentrout, *J. Phys. Chem. B*, 2011, **115**, 12648–12661.
3 J. M. Berg and Y. Shi, *Science*, 1996, vol. 271, pp. 1081–1085.
4 M. Huang, D. Krepkiy, W. W. Hu and D. H. Petering, *J. Inorg. Biochem.*, 2004, **98**, 775–785.
5 A. D. Frankel, J. M. Berg and C. O. Pabo, *Proc. Natl. Acad. Sci. U. S. A.*, 1987, **84**, 4841–4845.
6 G. C. Boles, R. A. Coates, G. Berden, J. Oomens and P. B. Armentrout, *J. Phys. Chem. B*, 2015, **119**, 11607–11617.
7 I. Baglivo, L. Russo, S. Esposito, G. Malgieri, M. Renda, A. Salluzzo, B. Di Blasio, C. Isernia, R. Fattorusso and P. V. Pedone, *Proc. Natl. Acad. Sci. U. S. A.*, 2009, **106**, 6933–6938.
8 P. B. Armentrout, M. T. Rodgers, J. Oomens and J. D. Steill, *J. Phys. Chem. A*, 2008, **112**, 2248–2257.
9 M. Citir, E. M. S. Stennett, J. Oomens, J. D. Steill, M. T. Rodgers and P. B. Armentrout, *Int. J. Mass Spectrom.*, 2010, **297**, 9–17.
10 M. Citir, C. S. Hinton, J. Oomens, J. D. Steill and P. B. Armentrout, *J. Phys. Chem. A*, 2012, **116**, 1532–1541.
11 A. L. Heaton, V. N. Bowman, J. Oomens, J. D. Steill and P. B. Armentrout, *J. Phys. Chem. A*, 2009, **113**, 5519–5530.
12 D. Oepts, A. F. G. van der Meer and P. W. van Amersfoort, *Infrared Phys. Technol.*, 1995, **36**, 297–308.
13 N. C. Polfer, J. Oomens, D. T. Moore, G. von Helden, G. Meijer and R. C. Dunbar, *J. Am. Chem. Soc.*, 2006, **128**, 517–525.
14 J. J. Valle, J. R. Eyler, J. Oomens, D. T. Moore, A. F. G. van der Meer, G. von Heldon, G. Meijer, C. L. Hendrickson, A. G. Marshall and G. T. Blakney, *Rev. Sci. Instrum.*, 2005, **76**, 023103.
15 N. C. Polfer and J. Oomens, *Phys. Chem. Chem. Phys.*, 2007, **9**, 3804–3817.
16 R. C. Dunbar, *J. Chem. Phys.*, 1989, **90**, 7369–7375.
17 A. G. Marshall, T. C. L. Wang and T. L. Ricca, *J. Am. Chem. Soc.*, 1985, **107**, 7893–7897.
18 S. H. Guan and A. G. Marshall, *Int. J. Mass Spectrom. Ion Processes*, 1996, **158**, 5–37.
19 N. C. Polfer, *Chem. Soc. Rev.*, 2011, **40**, 2211–2221.
20 J. Oomens, B. G. Sartakov, G. Meijer and G. von Helden, *Int. J. Mass Spectrom.*, 2006, **254**, 1–19.
21 J. Lemaire, P. Boissel, M. Heninger, G. Mauclaire, G. Bellec, H. Mestdagh, A. Simon, S. Le Caer, J. M. Ortega, F. Glotin and P. Maitre, *Phys. Rev. Lett.*, 2002, **89**, 273002.
22 S. J. Ye and P. B. Armentrout, *J. Phys. Chem. B*, 2008, **112**, 10303–10313.
23 R. M. Moision and P. B. Armentrout, *J. Phys. Chem. A*, 2002, **106**, 10350–10362.
24 M. J. Frisch, G. W. Trucks, H. B. Schlegel, G. E. Scuseria, M. A. Robb, J. R. Cheeseman, G. Scalmani, V. Barone, B. Mennucci, G. A. Petersson, H. Nakatsuji, M. Caricato, X. Li, H. P. Hratchian, A. F. Izmaylov, J. Bloino, G. Zheng, J. L. Sonnenberg, M. Hada, M. Ehara, K. Toyota, R. Fukuda, J. Hasegawa, M. Ishida, T. Nakajima, Y. Honda, O. Kitao, H. Nakai, T. Vreven, J. A. Montgomery, J. E. Peralta, F. Ogliaro, M. Bearpark, J. J. Heyd, E. Brothers, K. N. Kudin, V. N. Staroverov, R. Kobayashi, J. Normand, K. Raghavachari, A. Rendell, J. C. Burant, J. M. Millam, S. S. Iyengar, J. Tomasi, M. Cossi, N. Rega, J. M. Millam, M. Klene, J. E. Knox, J. B. Cross, V. Bakken, C. Adamo, J. Jaramillo, R. Gomperts, R. E. Stratmann, O. Yazyev, A. J. Austin, R. Cammi, C. Pomelli, J. W. Ochterski, R. L. Martin, K. Morokuma, V. G. Zakrzewski, G. A. Voth, P. Salvador, J. J. Dannenberg, S. Dapprich, A. D. Daniels, O. Farkas, J. B. Foresman, J. V. Ortiz, J. Cioslowski and D. J. Fox, *Gaussian 09, Revision A.02*, Gaussian Inc., Pittsburgh, PA, 2009.
25 A. D. Becke, *J. Chem. Phys.*, 1993, **98**, 5648–5652.
26 R. Ditchfield, W. J. Hehre and J. A. Pople, *J. Chem. Phys.*, 1971, **54**, 724–728.
27 S. Grimme, S. Ehrlich and L. Goerigk, *J. Comput. Chem.*, 2011, **32**, 1456–1465.
28 F. Weigend and R. Ahlrichs, *Phys. Chem. Chem. Phys.*, 2005, **7**, 3297–3305.
29 D. Andrae, U. Haeussermann, M. Dolg, H. Stoll and H. Preuss, *Theor. Chim. Acta*, 1990, **77**, 123–141.
30 K. L. Schuchardt, B. T. Didier, T. Elsethagen, L. Sun, V. Gurumoorthi, J. Chase, J. Li and T. L. Windus, *J. Chem. Inf. Model.*, 2007, **47**, 1045–1052.
31 J. P. Perdew, *Phys. Rev. B: Condens. Matter Mater. Phys.*, 1986, **33**, 8822–8824.
32 C. Möller and M. S. Plesset, *Phys. Rev.*, 1934, **46**, 618–622.

33 C. Lee, W. Yang and R. G. Parr, *Phys. Rev. B: Condens. Matter Mater. Phys.*, 1988, **37**, 785–789.

34 R. Ditchfield, W. J. Hehre and J. A. Pople, *J. Chem. Phys.*, 1971, **72**, 5639.

35 R. C. Dunbar, A. C. Hopkinson, J. Oomens, C.-K. Siu, K. W. M. Siu, J. D. Steill, U. H. Verkerk and J. Zhao, *J. Phys. Chem. B*, 2009, **113**, 10403–10408.

36 J. S. Prell, J. T. O'Brien, J. D. Steill, J. Oomens and E. R. Williams, *J. Am. Chem. Soc.*, 2009, **131**, 11442.

37 J. T. O'Brien, J. S. Prell, J. D. Steill, J. Oomens and E. R. Williams, *J. Phys. Chem. A*, 2008, **112**, 10823–10830.

38 R. C. Dunbar, N. C. Polfer and J. Oomens, *J. Am. Chem. Soc.*, 2007, **129**, 14562–14563.

39 J. Oomens, J. D. Steill and B. Redlich, *J. Am. Chem. Soc.*, 2009, **131**, 4310–4319.

40 S. J. Ye, A. A. Clark and P. B. Armentrout, *J. Phys. Chem. B*, 2008, **112**, 10291–10302.

41 D. R. Carl, T. E. Cooper, J. Oomens, J. D. Steill and P. B. Armentrout, *Phys. Chem. Chem. Phys.*, 2010, **12**, 3384–3398.

42 J. H. Bowie, C. S. Brinkworth and S. Dua, *Mass Spectrom. Rev.*, 2002, **21**, 87–107.

43 C. S. Brinkworth, S. Dua and J. H. Bowie, *Eur. J. Mass Spectrom.*, 2002, **8**, 53–56.

44 A. Reiter, L. M. Teesch, H. Zhao and J. Adams, *Int. J. Mass Spectrom. Ion Processes*, 1993, **127**, 17–26.

45 M. J. Betts and R. B. Russell, in *Bioinformatics for Geneticists*, ed. M. R. Barnes and I. C. Gray, John Wiley & Sons, Ltd, 2003, pp. 289–316.

46 R. L. Schwartz, G. E. Davico and W. C. Lineberger, *J. Electron Spectrosc. Relat. Phenom.*, 2000, **108**, 163–168.

47 M. J. Nee, A. Osterwalder, J. Zhou and D. M. Neumark, *J. Chem. Phys.*, 2006, **125**, 014306.

48 S. G. Lias and J. E. Bartmess, National Institute of Standards and Technology, Gaithersburg MD, 20899 (http://webbook.nist.gov). 2000, vol. NIST Standard Reference Database Number 69.

49 L. A. Angel and K. M. Ervin, *J. Phys. Chem. A*, 2006, **110**, 10392–10403.

PCCP

CORRECTION

View Article Online
View Journal | View Issue

Cite this: *Phys. Chem. Chem. Phys.*, 2017, **19**, 18100

Correction: Zn^{2+} and Cd^{2+} cationized serine complexes: infrared multiple photon dissociation spectroscopy and density functional theory investigations

Rebecca A. Coates,[a] Georgia C. Boles,[a] Christopher P. McNary,[a] Giel Berden,[b] Jos Oomens[bc] and P. B. Armentrout[a]

DOI: 10.1039/c7cp90143g

rsc.li/pccp

Correction for 'Zn^{2+} and Cd^{2+} cationized serine complexes: infrared multiple photon dissociation spectroscopy and density functional theory investigations' by Rebecca A. Coates *et al.*, *Phys. Chem. Chem. Phys.*, 2016, **18**, 22434–22445.

Although the overall conclusions of the original article remain unaffected (no experimental or theoretical IR spectra are changed, nor is any calculated thermochemistry at 0 K), the thermal corrections to the Gibbs free energy at 298 K were mistakenly overestimated. Corrected 298 K free energies are given below in Tables 1, 3 and 4 from the original manuscript. Because the 298 K values were only slightly modified from the published values, we have not corrected the many references to relative energies in the text, except those noted below. Using the correct values, the ion population analysis for the two lowest energy isomers of the $[Zn(Ser\text{-}H)ACN]^+$ complex is altered. Using the correct 298 K ion population analysis, the following corrections are made to the publication.

Table 1 Relative free energies at 298 K kJ mol^{-1} of $[Zn(Ser\text{-}H)ACN]^+$ conformers[a]

Structure	B3LYP	B3LYP-GD3BJ	B3P86	MP2(full)
$[N,CO,O^-]$tgg	0.0	0.0	0.0	1.7
$[N,CO^-,OH]$ggt	2.4	0.2	4.5	0.0
$[N,CO,O^-]$cgg	25.0	24.2	24.6	27.4
$[N,O_s^-]$tgt	38.4	42.6	44.1	47.9
$[N,CO^-]$tgt	37.5	41.4	43.5	45.1
$[N,CO^-]$gtt	35.6	39.3	41.7	44.4
$[N,OH,O^-]$tgg	41.2	39.8	44.8	40.3
$[CO^-,O^-]$ctc[b]	49.2	51.5	54.0	56.5
$[CO,O^-]$ctc	56.6	61.5	61.1	66.6
$[N,CO^-]$tgg	54.4	57.9	60.0	65.1
$[N^-,CO,OH]$tggt	58.0	59.2	60.5	57.2
$[CO,O^-]$tgg	58.8	64.5	66.9	77.2
$[CO,O^-]$tgg	59.3	65.2	67.3	77.0
$[CO,O^-]$ttg	59.5	63.9	67.9	78.1
$[N^-,CO]$tggg	65.0	70.5	70.2	73.7
$[CO_2^-]$ggg	73.9	85.4	81.7	88.5
$[CO_2^-]$ggt	77.0	89.9	86.3	90.7
$[CO^-,O]$cgt	72.8	73.9	79.1	80.2
$[CO_2^-]$gtg	80.6	93.8	88.8	100.9
$[OH,O^-]$tgg	112.3	117.1	124.8	126.4

[a] Calculations performed at the stated level of theory using a 6-311+G(2d,2p) basis set. Geometries and vibrational frequencies calculated at the B3LYP/6-311+G(d,p) level. s = side-chain. [b] Salt bridge between NH_3^+ and COO^- groups.

[a] *Department of Chemistry, University of Utah, Salt Lake City, UT 84112, USA*
[b] *Radboud University, Institute for Molecules and Materials, FELIX Laboratory, Toernooiveld 7c, NL-6525ED Nijmegen, The Netherlands*
[c] *van't Hoff Institute for Molecular Sciences, University of Amsterdam, Science Park 904, NL-1098XH Amsterdam, The Netherlands*

Table 3 Relative free energies at 298 K kJ mol^{-1} of low-lying conformers of [Zn(Ser-H)]$^{+a}$

Structure	B3LYP	B3LYP-GD3BJ	B3P86	MP2(full)
[N,CO,O$^-$]tgg	0.0	0.0	0.0	0.0
[N,CO$^-$,OH]ggt	15.0	13.4	17.9	10.0
[N,CO,O$^-$]cgg	21.7	21.2	21.2	21.9
[N,O$_s^-$]tgt	45.7	48.6	53.6	54.4
[N,CO$^-$]ggt	58.1	60.7	66.1	63.0
[N,OH,O$^-$]tgg	45.5	43.7	49.8	41.7
[CO$^-$,O$^-$]ctc^b	47.6	49.3	54.1	53.4
[CO,O$^-$]ctc	66.8	70.8	70.8	84.6
[N$^-$,CO,OH]tggt	51.1	52.4	54.4	52.5
[CO$_2^-$]ggg	95.1	106.6	113.2	148.2

^{a} Calculations performed at the stated level of theory using a 6-311+G(2d,2p) basis set. Geometries and vibrational frequencies calculated at the B3LYP/6-311+G(d,p) level. s = side-chain. ^{b} Salt bridge between NH_3^+ and COO^- groups.

Table 4 Relative free energies at 298 K kJ mol^{-1} of CdCl$^+$(Ser) conformers^a

Structure	B3LYP	B3LYP-GD3BJ	B3P86	MP2(full)
[N,CO,OH]tggt	0.0	0.0	0.0	0.0
[N,CO]tcgt	12.0	17.8	13.7	23.1
[CO$_2^-$]cggt^b	13.9	25.6	16.9	27.0
[N,CO]tgtt	17.4	22.4	19.0	28.5
[CO$_2^-$]cgtt^b	15.7	28.0	19.7	30.6
[N,CO]tgtg	19.0	23.7	20.6	31.2
[N,OH$_s$]tgtt	24.5	28.8	27.5	31.8
[N,CO,OH]cggt	28.2	27.8	27.8	29.6
[N,OH,OH]tggt	29.4	27.8	31.7	26.4
[N,OH$_s$]tttt	33.7	38.1	37.6	41.7
[CO,OH$_s$]cggt	41.9	48.4	44.3	60.2
[N,CO]tcgg	43.6	50.2	45.3	59.7
[COOH]cggt	45.6	58.6	48.0	66.2
[CO$_2^-$]cggg^b	45.3	56.8	49.0	62.5
[N,OH]ttgt	53.6	57.8	57.4	59.4
[CO,OH$_s$]ggt^b	58.0	63.2	59.3	71.5
[CO,OH$_s$]ttgt	57.6	63.5	64.3	78.3
[N,OH]tttt	58.0	62.7	62.6	62.5
[CO,OH$_s$]ctct	59.7	65.1	62.3	75.9
[CO,OH$_s$]tggt	56.0	63.3	62.3	76.4
[N,OH$_s$]cgtt	60.8	64.2	63.2	68.9
[O$_s^-$]cggt^c	60.8	72.4	64.3	75.5
[OH$_s$]ttcc	99.0	111.1	103.8	124.4
[OH,OH]tggg	112.7	117.9	122.7	127.5
[OH$_s$]tggc	131.3	143.5	141.3	154.6

^{a} Calculations performed at the stated level of theory using a def2-TZVPP basis set. Geometries and vibrational frequencies calculated at the B3LYP/def2-TZVP level. s = side-chain. ^{b} Salt bridge between NH_3^+ and COO^- groups. ^{c} Salt bridge between NH_3^+ and O_s^- groups.

Page 22438, second paragraph, corrected: ''In contrast, as seen in Table 1, the presence of the ACN ligand stabilizes the [N,CO$^-$,OH]ggt conformer such that it would populate between 14–48% of ions at 298 K.''

Page 22440, seventh paragraph, corrected: ''This result is consistent with the relative free energies calculated at the MP2(full) level of theory, which indicate that [N,CO,O$^-$]tgg can account for 33% of an equilibrated ion population at 298 K.'' In the published manuscript, we concluded that a superposition of the [N,CO,O$^-$]tgg and [N,CO$^-$,OH]tgg linear IR spectra best agreed with the experimental spectrum, a conclusion that still holds true. Indeed, as the previous [N,CO,O$^-$]tgg ion population was calculated to be 52%, the corrected value of 33% agrees more favorably with the relative intensities observed in the experimental spectrum.

The Royal Society of Chemistry apologises for these errors and any consequent inconvenience to authors and readers.